

SANDIA REPORT

SAND2005-7142

Unlimited Release

Printed August 2007

A Vadose Zone Transport Processes Investigation within the Glacial Till at the Fernald Environmental Management Project

J. Brainard, R.J. Glass, C. Roepke, M. Mann, K. Kriel, R. Holt

Prepared by
Sandia National Laboratories
Albuquerque, New Mexico 87185 and Livermore, California 94550

Sandia is a multiprogram laboratory operated by Sandia Corporation, a Lockheed Martin Company, for the United States Department of Energy under Contract DE-AC04-94AL85000.

Approved for public release; further dissemination unlimited.



Sandia National Laboratories

Issued by Sandia National Laboratories, operated for the United States Department of Energy by Sandia Corporation.

NOTICE: This report was prepared as an account of work sponsored by an agency of the United States Government. Neither the United States Government, nor any agency thereof, nor any of their employees, nor any of their contractors, subcontractors, or their employees, make any warranty, express or implied, or assume any legal liability or responsibility for the accuracy, completeness, or usefulness of any information, apparatus, product, or process disclosed, or represent that its use would not infringe privately owned rights. Reference herein to any specific commercial product, process, or service by trade name, trademark, manufacturer, or otherwise, does not necessarily constitute or imply its endorsement, recommendation, or favoring by the United States Government, any agency thereof, or any of their contractors or subcontractors. The views and opinions expressed herein do not necessarily state or reflect those of the United States Government, any agency thereof, or any of their contractors.

Printed in the United States of America. This report has been reproduced directly from the best available copy.

Available to DOE and DOE contractors from
U.S. Department of Energy
Office of Scientific and Technical Information
P.O. Box 62
Oak Ridge, TN 37831

Telephone: (865)576-8401
Facsimile: (865)576-5728
E-Mail: reports@adonis.osti.gov
Online ordering: <http://www.doc.gov/bridge>

Available to the public from
U.S. Department of Commerce
National Technical Information Service
5285 Port Royal Rd.
Springfield, VA 22161

Telephone: (800)553-6847
Facsimile: (703)605-6900
E-Mail: orders@ntis.fedworld.gov
Online ordering: <http://www.ntis.gov/ordering.htm>



SAND2005-7142
Unlimited Release
Printed August 2007

A Vadose Zone Transport Processes Investigation within the Glacial Till at the Fernald Environmental Management Project

C. Roepke, R.J. Glass, J. Brainard, M. Mann, K. Kriel, R. Holt
Geohydrology Department 6115
Geosciences Division
Sandia National Laboratories
P.O. Box 5800
Albuquerque, New Mexico 87185-1324

J. Schwing
FERMCO
Technology Development
Cincinnati, Ohio 45256

Abstract

This report describes a model Transport Processes Investigation (TPI) where field-scale vadose zone flow and transport processes are identified and verified through a systematic field investigation at a contaminated DOE site. The objective of the TPI is to help with formulating accurate conceptual models and aid in implementing rational and cost effective site specific characterization strategies at contaminated sites with diverse hydrogeologic settings. Central to the TPI are Transport Processes Characterization (TPC) tests that incorporate field surveys and large-scale infiltration experiments. Hypotheses are formulated based on observed pedogenic and hydrogeologic features as well as information provided by literature searches. The field and literature information is then used to optimize the design of one or more infiltration experiments to field test the hypothesis. Findings from the field surveys and infiltration experiments are then synthesized to formulate accurate flow and transport conceptual models. Here we document a TPI implemented in the glacial till vadose zone at the Fernald

Environmental Management Project (FEMP) in Fernald, Ohio, a US Department of Energy (DOE) uranium processing site. As a result of this TPI, the flow and transport mechanisms were identified through visualization of dye stain within extensive macro pore and fracture networks which provided the means for the infiltrate to bypass potential aquatards. Such mechanisms are not addressed in current vadose zone modeling and are generally missed by classical characterization methods.

Acknowledgment

We are very grateful to the supporting staff at the Fernald Environmental Restoration Management Corporation (FERMCO) who in one way or another made it possible for us to bring this project to fruition. Kim Nuhfer of FERMCO provided administrative, logistical, and planning support and Cliff Lee of FERMCO aided in geological sampling and sensor installation support. The effort of the Site Sampling Team deserves particular mention for their efforts in performing many difficult and laborious tasks on hot, muggy days. Among these outstanding individuals are team leaders Mike Stott and, Tim Smith, as well as team members Nick Jansen, Bill Neyer, Jenny Milchert, and Andy Cleeter. Without the dedication and hard work of these individuals, the scale and complexity of this project would have been significantly less. We also appreciate the financial support by the DOE Office of Technology Development Landfill Focus Area program.

This page intentionally left blank.

Contents

Acknowledgment.....	5
Nomenclature	9
1. Introduction.....	11
2. Implementation of the Transport Processes Investigation Test at the Fernald Environmental Management Plan (FEMP).....	15
2.1 The Exploratory Phase At the FEMP.....	15
2.1.1 Background.....	15
2.1.2 Hydrogeologic Characterization	15
2.1.3 Site Selection	18
2.2 Hypothesis Testing Phase – Design and Implementation of the TPC	18
2.2.1 Background.....	18
2.2.2 Infiltration System, Data Acquisition Systems and Sensor Arrays	20
2.2.3 Infiltration	22
2.2.4 Colloid Tracer	23
2.2.5 Chloride Tracer	23
2.2.6 Dye Tracer and Excavation of the Clay Site.....	23
2.3 Analysis of the TPC	24
2.3.1 Infiltration	24
2.3.2 Pressure Head Field	25
2.3.3 Chloride Tracer Measurements.....	25
2.3.4 Dye Pulse and Excavation	33
3. Conclusions.....	37
3.1 Transport Processes, Controls and Connectivity	37
4. Further Investigation.....	39
References.....	41
Appendix A. Geology	43
Appendix B. Infiltration	77
Appendix C. Sensor Design and Array	83
Appendix D. Colloid and Chloride Tracers.....	91
Appendix E: Pressure Field	179
Appendix F. Dye Pulse and Site Excavation.....	223
Appendix G. Plates.....	231

Figures

Figure 1. Ohio State Map Showing the location of the Fernald Environmental Management Project (FEMP).....	12
Figure 2. Detailed Site Map of the FEMP showing the location of the Infiltration Study Area relative to major landmarks.	16

Figure 3. Schematic of the major hydrostratigraphic units found within the study area.	17
Figure 4. Study Area site map showing the location of the preliminary infiltration test sites from the previous year, exploratory borings, candidate test sites, and the sites chosen for this study (Sand and Clay Sites).....	19
Figure 5. Plan-view map of the Clay and Sand Site Sensor Array.....	21
Figure 6. Schematic of the arrangement of sensors installed in the sensor pack.....	22
Figure 7. Plot of infiltration rates for the Clay and Sand Sites.....	26
Figure 8. Plot showing the mimicking of infiltration rates by tensiometer measured pressure head.	26
Figure 9a and b. Plot showing rainfall spikes in tensiometer data at the Sand (top) and Clay (bottom) Sites.....	27
Figure 10a and b. Plots contrasting a fast (top) and slow (bottom) return of pressure head to pre-sampling conditions.....	28
Figure 11. Plots comparing breakthrough curves obtained from TDR measurements and samples collected from suction samplers where the TDR measurements record oscillations and an earlier arrival.	29
Figure 12. Plots comparing breakthrough curves obtained from TDR measurements and samples collected from suction samplers where the suction samplers record an earlier arrival time.....	29
Figure 13. Plots comparing breakthrough curves obtained from TDR measurements and samples collected from suction samplers where arrival time and the peaks occur at the same time.	30
Figure 14a. Schematic of sand pack showing the hypothesized location of a macropore that may result in a earlier arrival time for TDR measured breakthrough curves.	30
Figure 14b. Schematic of sand pack showing the hypothesized location of a macropore that may result in a earlier arrival time for suction sampler derived breakthrough curves.....	31
Figure 15. Plots of TDR measured and suction sampler derived breakthrough curves showing a second breakthrough peak.	32
Figure 16. Plan-view contour plots of the Clay and Sand sites showing interpolated Cl ⁻ relative concentrations at 2 m depth at 120 hours. Cl ⁻ tracer concentrations distribution at the 2 m level of the Clay and Sand Sites 119 and 120 hours after start of the Cl ⁻ pulse.....	32
Figure 17. Schematic plan view of the Clay Site showing the approximate lateral extent excavation along with major occurrences of macropore, fracture, and preferential flow as evidenced by the presence of dye stain	34

Tables

Table 1. Infiltration Schedule	23
--------------------------------------	----

Nomenclature

CS	Cross-section
Cl ⁻	Chloride
C/Co	Relative concentration
DOE	Department of Energy
FD&C	(Federal) Food, Drug and Cosmetic (Act)
FEMP	Fernald Environmental Management Project
FERMCO	Fernald Environmental Restoration Management Corporation
hr	hour
hrs	hours
HS	Hydrostratigraphic
m	meters
ns	nanosecond
mg/l	milligram per liter
TDR	time domain reflectometry
TPC	Transport Processes Characterization
TPI	Transport Processes Investigation

This page intentionally left blank.

1. Introduction

In many cases, site characterization has been driven by legal and regulatory mandates requiring locating and monitoring of contaminant concentrations and distributions with little emphasis being placed on the need to understand the geologic, chemical, and hydrologic processes that impact contaminant fate and transport. As a result, conceptual models are not always fully formulated and predictive simulations based upon flawed conceptual models fail to correctly forecast contaminant transport (Lewis and Goldstein, 1982; Pearson and Konikow, 1986; Andersen and Woessner, 1992).

In this report, an approach is described that provided the ability to identify flow and transport processes at a US Department of Energy (DOE) contaminated site through the use of infiltration experiments that incorporated a salt tracer and dye pulse. This approach is called the Transport Processes Investigation (TPI), a systematic approach where information from a number of activities helps to formulate an accurate conceptual model accounting for important flow and transport mechanisms. This TPI was initiated in the summer of 1993 with a preliminary geologic survey of nearby outcrops and implementation of the “Preliminary Infiltration Tests” performed to gain some experience and insight for the design for the planned follow-up infiltration test documented in this report and performed in 1995. See Brainard et al., 2005 for a description of the Preliminary Infiltration Test. The preliminary and the infiltration tests covered in this report were implemented within a short distance of each other. These tests were designed to identify hydrologic flow processes and the features that control these processes within the glacial tills that underlie the Fernald Environmental Management Project (FEMP) in Fernald, Ohio (see the state map in Figure 1 for the location of the FEMP) where soluble species of uranium have been identified in the near surface soils (Tidwell, 1993) and underlying aquifers (ITT, 1990).

The TPI process as implemented at the FEMP involved three distinct project phases.

1. **Exploratory Phase:** During this phase, information is collected to develop site-specific hypotheses concerning flow and transport mechanisms and identifying potential field sites where large-scale infiltration experiments can be implemented. Hypotheses formulation is based on integrated information from literature reviews, site-specific documents, other resources that may be unique to the site, and surveys of the local hydrogeology. These sources are used to identify hydrostratigraphic units and optimize the design of infiltration experiments that interrogate flow and transport processes at critical locations at the site. This phase may also include performing small-scale, simple experiments to aid with both hypothesis building and designing field scale experiments.
2. **Hypothesis Testing Phase:** In this phase, the methods for testing the hypotheses are implemented by conducting Transport Processes Characterization (TPC) tests. At the FEMP, two large-scale infiltration experiments were performed using nontoxic chemical and dye tracers infiltrated under controlled conditions while monitoring the subsurface with dense arrays of sensors. The subsequent excavation of the infiltration site provided the means to identify flow mechanisms through visually observing and subsequent mapping of dye stain. The excavation also provided the ability to make detailed hydrogeologic observations and to collect samples for further laboratory analysis of hydraulic properties. This phase also offers

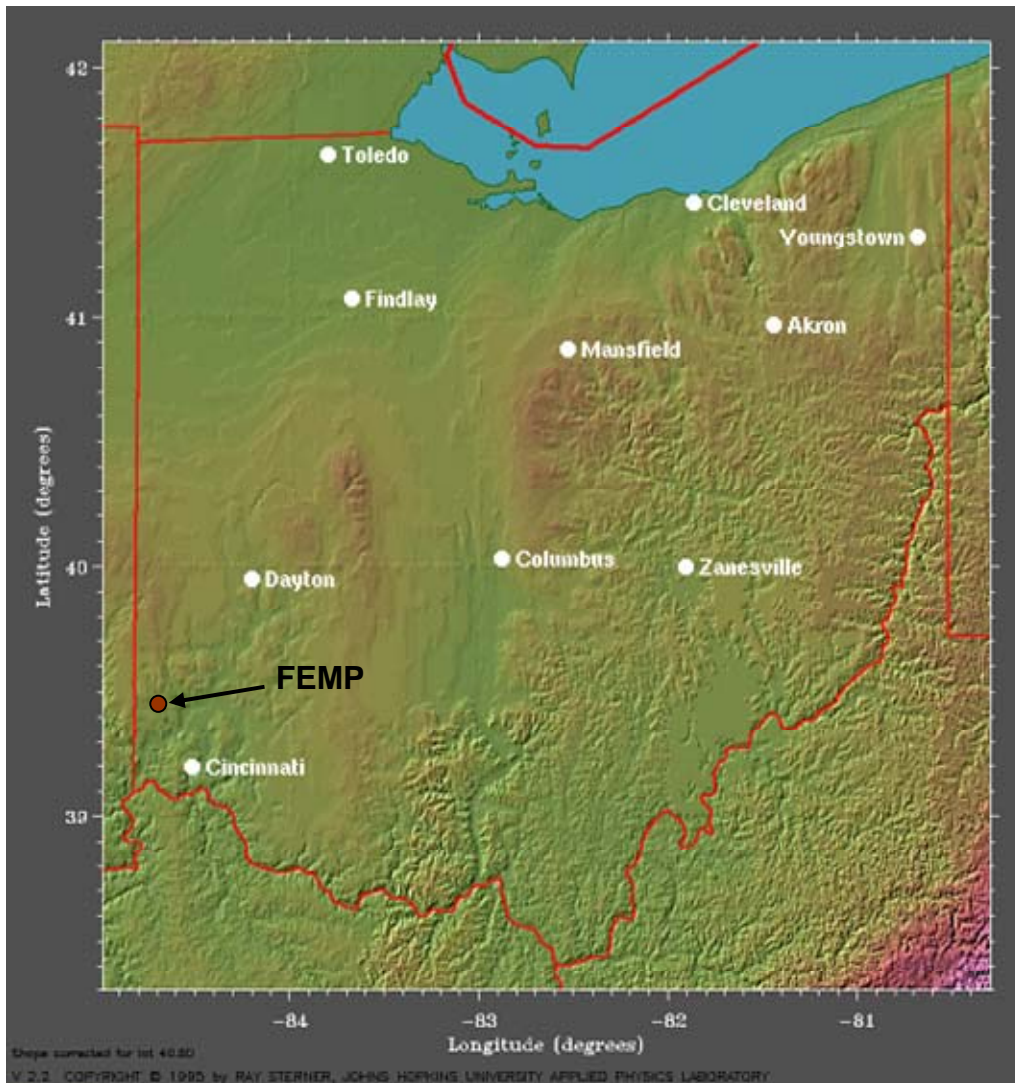


Figure 1. Ohio State Map Showing the location of the Fernald Environmental Management Project (FEMP).

the opportunity to test new monitoring technologies. Here we applied Time Domain Reflectometry (TDR) to salinity concentration measurements with the promise of obtaining temporally dense breakthrough curves as compared to that obtained with suction samplers.

3. **Transport Processes Characterization Test Analysis:** The final phase involves an analysis of TPC results that either confirms or refutes the hypothesized conceptual model and determines whether the transport processes at the site are understood.

This report contains a main section where the TPI as implemented at the FEMP are discussed in sufficient detail to provide the reader with an overview of the findings from the three TPI project phases as presented above. Each of the appendices is written as stand-alone sections detailing the various aspects of the TPI discussed in the main section.

Appendix A discusses the regional geology and presents findings from local outcrop surveys, borehole sampling, and site excavation. Appendix B describes the infiltration system, infiltration monitoring systems, as well as infiltration initiation and maintenance procedures, and the infiltration rate calculation methods. Appendix C includes complete details of sensor design, sensor arrays, and installation procedures. Appendix D contains a description of colloid and chloride (Cl⁻) tracer pulses, soil water sampling of Cl⁻ tracer solutions, time domain reflectometry (TDR) measurement of Cl⁻ tracer concentrations, and the complete set of plots of Cl⁻ concentrations obtained from both the TDR measurement system and analysis of water samples collected from the suction samplers. Appendix E describes the tensiometers, data acquisition systems, data reduction methods and results, and pressure field data. Appendix F describes the dye pulse implementation procedures. Appendix G contains Plates 1 through 110 that provide a photographic record of the implementation of the infiltration/tracer tests and the excavation of one of the two infiltration sites.

This page intentionally left blank.

2. Implementation of the Transport Processes Investigation Test at the Fernald Environmental Management Plan (FEMP)

2.1 The Exploratory Phase at the FEMP

2.1.1 Background

During the exploratory phase, information from a literature search, a survey of local outcrops, and results from a preliminary infiltration study at the FEMP performed during the previous summer (Brainard et al., 2005) was integrated into the plan for the current study.

The literature search revealed potential flow and transport processes common to glacial tills and provided background on the regional geologic setting (see Appendix A for a geologic description of the site). Among the potential processes at the FEMP is flow through macropores of biologic origins (biological macropores) and fractures (Beven and German, 1982; Tipcotter, 1983; Smetten and Collis-George, 1985; Glass et al., 1988 and from formation heterogeneities such as contrasts between bedding (Nielsen et al., 1973; Vieira et al., 1981; and Waganet et al., 1984). These processes may produce fast transport pathways to underlying aquifers. Diffusive flow through massive clays in glacial tills may also occur (Jones et al., 1992).

Numerous well-exposed outcrops at cut-banks along Paddys Run, an incised intermittent stream crossing the FEMP site for 2.5 km (Figure 2), allowed local stratigraphic and hydrologic features to be easily observed. Outcrop observations led to hypotheses concerning the impact of the stratigraphy on the local hydrology. For instance, seeps in the cut-banks provided insight on likely stratigraphic controls on ground water flow processes, while fractures and channel sands with brown oxidation/reduction halos within a pervasive deposit of gray clay provided evidence of flow through this dense clay unit. Additionally small-scale dye infiltration experiments implemented on cut banks provided direct evidence for flow in macropores such as worm burrows and root casts (biological macropores) and fractures (See Brainard et al., 2005).

The Preliminary Infiltration Tests involved several small infiltration tests implemented with a tension infiltrometer and three large-scale ponded infiltration tests, one of which incorporated a salt tracer experiment for investigating the connection of infiltrated surface water with seeps in a nearby cutbank in Paddys Run (Brainard et al., 2005). The ponded infiltration experiments performed by Brainard et al., 2005 provided information on the likely infiltration rates while the tracer study confirmed hydrologic connection between the surface and the seeps and afforded the opportunity to test the water supply systems, sensors, and data acquisition systems for potential use for this project.

2.1.2 Hydrogeologic Characterization

The outcrop survey resulted in a stratigraphic model composed of six hydrostratigraphic units. The hydrostratigraphic units are designated HS Units to emphasize the difference between these units and the Cross-section Units (CS Units) described from borehole samples. Both types of units are described in detail in Appendix A. The six HS units are described below:

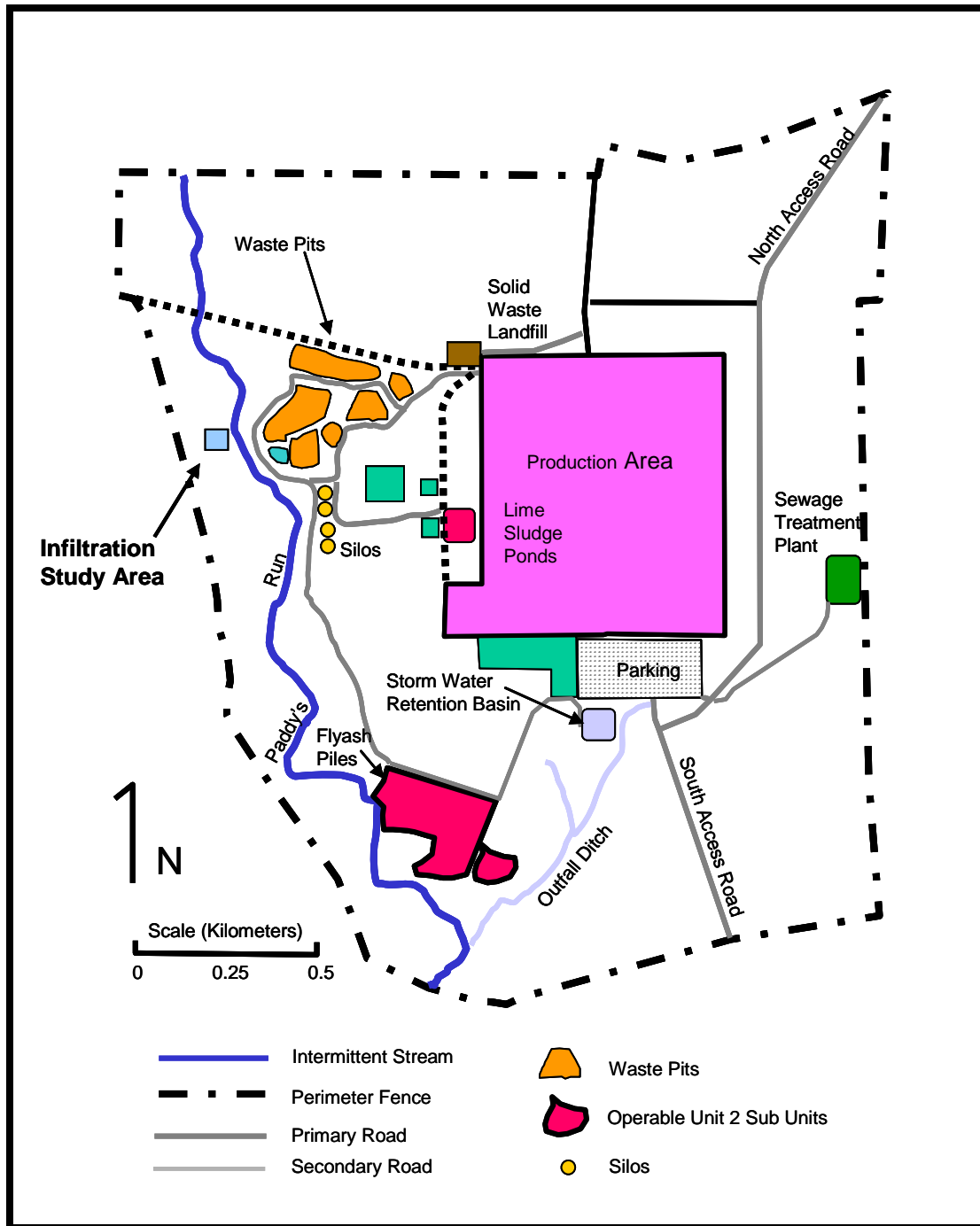


Figure 2. Detailed Site Map of the FEMP showing the location of the Infiltration Study Area relative to major landmarks.

- Found throughout the outcrops along Paddy's Run were numerous lenses of poorly indurated sand and gravel diamicts with thicknesses up to 2 m and extending laterally up to 5 m and occasionally more. These lenses were found in all but the uppermost HS Unit 5, described below. For ease of discussing these widely distributed but discontinuous deposits, they are referred to as HS Unit 6.

- HS Unit 5 is the uppermost unit and contains the topsoil and silty loess comprising the bulk of the root zone. It was hypothesized that flow through this unit would be controlled by plant material, root holes, and wormholes.
- HS Unit 4 consists of blocky, structured silty clays and sandy silts. Flow in this unit was hypothesized to occur through the vertical fracture networks.
- HS Unit 3 is composed of bedded and fractured brown (oxidized) clays and silty clays. Both horizontal and vertical flow was hypothesized to occur in this unit: horizontally along bedding planes and laminae and downward through fractures.
- HS Unit 2 is composed of layered and bedded gray (unoxidized) clays. It was hypothesized that horizontal and vertical fracture surfaces and bedding planes would provide avenues for flow.
- HS Unit 1 is composed of gray (unoxidized) clay with frequent and irregular spatial distributions of what appeared to be channel deposits of sandy gravels and fractures. Both types of features were consistently rimmed with brown oxidation/reduction halos. This "gray clay" has often been modeled as a barrier to flow in the Fernald area.

A schematic of these hydrostratigraphic units is presented in Figure 3. A more comprehensive description of the stratigraphy is presented in Appendix A.

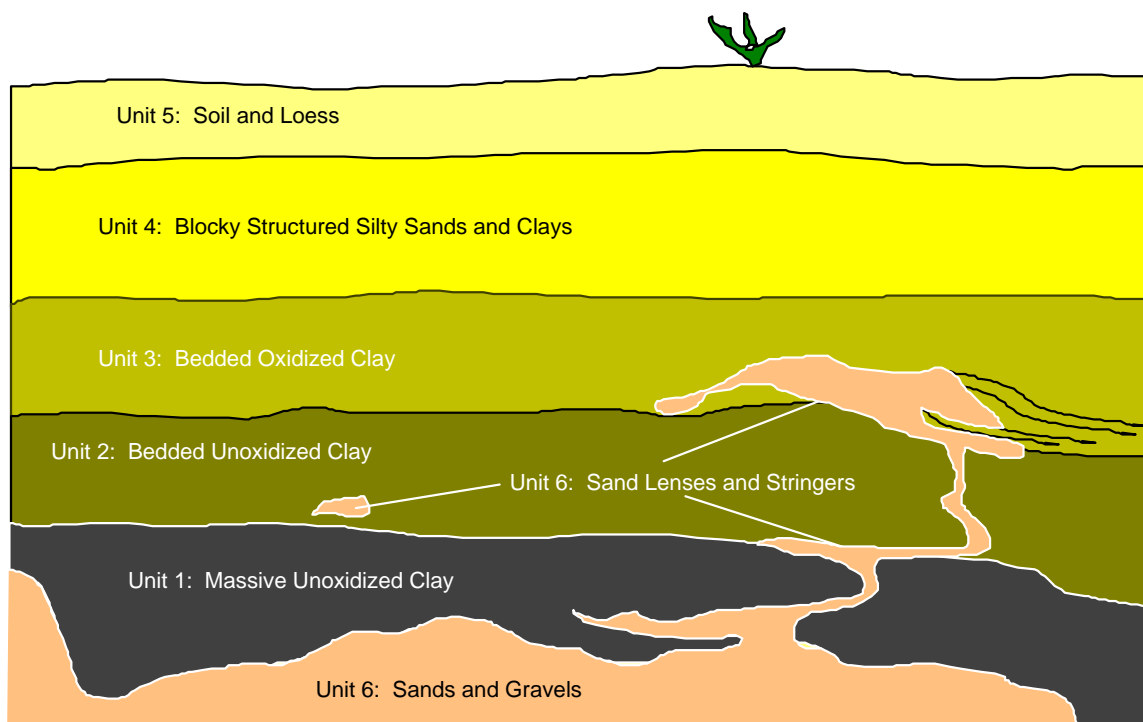


Figure 3. Schematic of the major hydrostratigraphic units found within the study area.

Field data collected during the exploratory phase resulted in identification of the near-surface geologic units at the FEMP, the stratigraphic sequence of these units, and recognition of features within these deposits that very likely play a major role in transporting contaminants to the underlying aquifers.

2.1.3 Site Selection

Once the outcrop exploratory phase was complete, site selection for a series of infiltration tests commenced. Since performing infiltration experiments within contaminated areas is not cost-effective or desired due to the possibility of enhancing contaminant migration, a 90-hectare field used as a cow pasture outside the contaminated area was selected as the study area. The field was located within 500 m of the main processing facilities and within 250 m of several locations with known uranium contamination. It was separated from these sites to the east by an 8 m deep incised stream bed called Paddys Run (Figure 2). The incised channel provided assurance that the near surface deposits in the study area were not contaminated due to a lack of hydraulic connection with the contaminated sites. Several candidate sites were selected across the field based on geologic samples collected during exploratory augering. Comparisons between stratigraphic columns constructed from augered sample descriptions resulted in the selection of two TPS sites. The two sites had distinct stratigraphic sequences and together they contained all of the hydrostratigraphic units described above. The descriptive terms Sand Site and Clay Site were used to identify the sites. The Sand Site was composed of top soils and loess (HS Unit 5) overlying blocky, structured clays (HS Unit 4). Underlying HS Unit 4 was a large unconsolidated body of muddy sand and gravel (HS Unit 6). Bedded clays (HS Units 2 and 3) were encountered at the Sand Site only in isolated lenses above HS Unit 6. A plan-view map of the study area showing the locations of the candidate and chosen sites is given in Figure 4.

The Clay Site contained HS Units 2 through 5, described above, as well as horizontal beds of oxidized and unoxidized clays (brown and gray clays respectively) (HS Units 3 and 2) extending across the site and overlying the massive unoxidized gray clay (HS Unit 1). The sands and gravels of HS Unit 6 were present in small lens stringers and a larger lens in contact with HS Units 2 through 1, but not nearly extensively as those present in the Sand Site.

2.2 Hypothesis Testing Phase – Design and Implementation of the TPC

2.2.1 Background

Increased saturated conditions within the study area were observed during a spring site survey. Evidence for this included numerous seeps along the cut banks in Paddys Run that disappeared in late summer. This observation is important because spring saturated conditions may provide the worst-case scenario for transport of dissolved uranium off the FEMP site. Additionally, it was hypothesized that the dominant active transport processes would be (1) macropore flow through worm burrows and root casts (biological macropores), (2) flow through bedding planes and fractures, and (3) preferential flow through highly transmissive sand and gravel channels within less permeable till deposits.

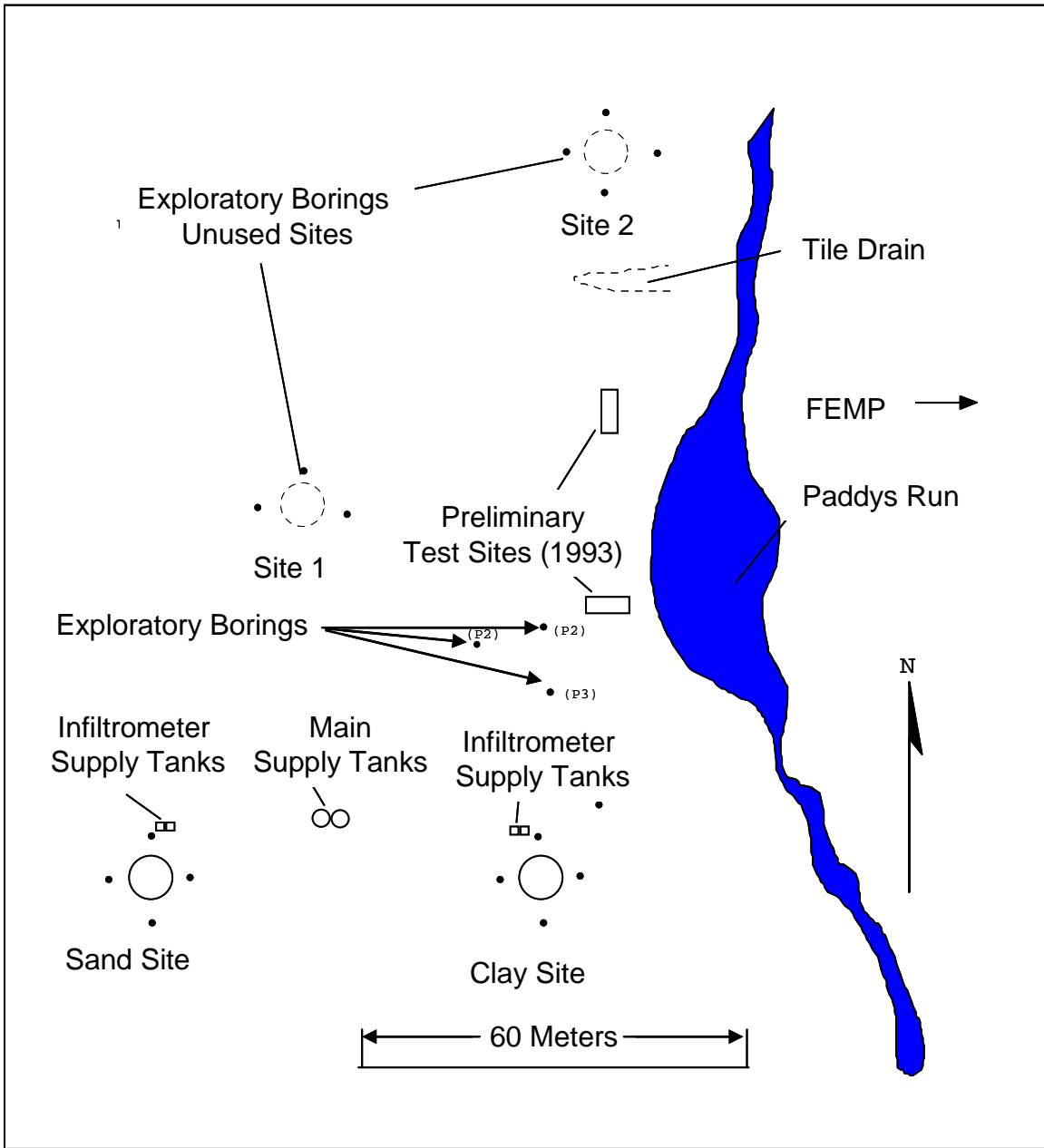


Figure 4. Study Area site map showing the location of the preliminary infiltration test sites from the previous year, exploratory borings, candidate test sites, and the sites chosen for this study (Sand and Clay Sites).

To test these hypotheses, we designed two infiltration tests to be performed at locations with contrasting geology (see Section 2.1.3 for a description of the geology at these infiltration sites) and to be implemented during the summer months when the seeps in Paddys Run were greatly diminished (see Plates 1 through 14 in Appendix G for photographs of the outcrops in Paddys run). The decision to implement two infiltration tests was based on knowledge gained from exploratory augering of the field adjacent to Paddys Run (described in Section 3.1.2). Augering revealed that the subsurface consisted mostly of clay deposits near Paddys Run, while across the

field to the west of Paddys Run, sandy deposits predominated. See Appendix A for a detailed geologic description of the Sand and Clay Sites.

2.2.2 Infiltration System, Data Acquisition Systems and Sensor Arrays

Other than the difference in the subsurface deposits, the two infiltration tests were identical in that both tests incorporated duplicate water supply systems and ponded infiltrometers (see Appendix B and Appendix G, Plate 11), data acquisition systems (see Appendix C), sensors, and sensor array layouts (see Appendix C). However, due to insufficient data acquisition systems, the Sand Site had 32 sensor packs while the Clay Site had 44. The sensors in these packs monitored hydrostatic pressure (pressure head) and Cl^- tracer concentration which allowed for collection of water samples for both laboratory analyses of Cl^- and analog colloid tracer concentrations. In plan view, the sensor packs formed two rings around the infiltrometer; one at a radius of 2.5 m and the other at 5 m from the center of the infiltrometer. Both sites had the same sensor geometry except for missing sensor packs at the Sand Site explained below. See Figure 5 for the plan view maps of the Clay and Sand Site sensor arrays. The emplacement depth of the upper and lower sensor packs was based on the stratigraphy as determined from augered samples. At the Clay Site, the upper packs were installed within the layered clays (HS Units 2 or 3) approximately 2 m below ground surface, with the lower packs located at the upper surface of the massive unoxidized clay (HS Unit 1) at approximately 3 m depth. At the Sand Site, the upper-level sensor packs were located in the blocky-structured silty clays (HS Unit 4) at approximately 1.1 m depth, while the lower level packs were contained in the underlying sands and gravels (HS Unit 6) at approximately 2.1 m depth. The shallow installation depth of the deeper sensors at the Sand Site relative to the Clay Site was due to cave-in within the saturated sands during augering. For the reason mentioned above, some of the corresponding sensor pack locations at the Clay Site were not installed at the Sand Site. Missing at the Sand Site were all but the east upper sensor pack in the outer upper ring, and the South-southwest and West-northwest angled sensor packs (Figure 5).

Each sensor pack consisted of pressure transducer-equipped tensiometers, solution and colloid samplers, and TDR probes (Figure 6). TDR was implemented here to monitor the electrical conductivity of the solution within sensor packs through analysis of reflected signal attenuation. Calibration provided the conversion between the magnitudes of signal attenuation to solute concentration. Appendix D provides details on TDR measurement theory as applied here. Through the use of a multiplexed automated data acquisition system, TDR provided much higher temporal resolution measurement of solute concentrations than possible with manual sampling of suction samplers. The TDR system was also used to monitor the degree of saturation of the sand within the sensor packs. Automated multiplexed dataloggers also monitored the tensiometer pressure transducers and pressure transducers in the bottom of the water supply tanks from which flow rates and were obtained, as well as a tipping bucket rain gage.

Water samples were collected from the suction samplers one to three times per day while the TDR system monitored solute concentrations at 15 minute intervals during early infiltration times to one-hour intervals as infiltration progressed (See Appendices C and D).

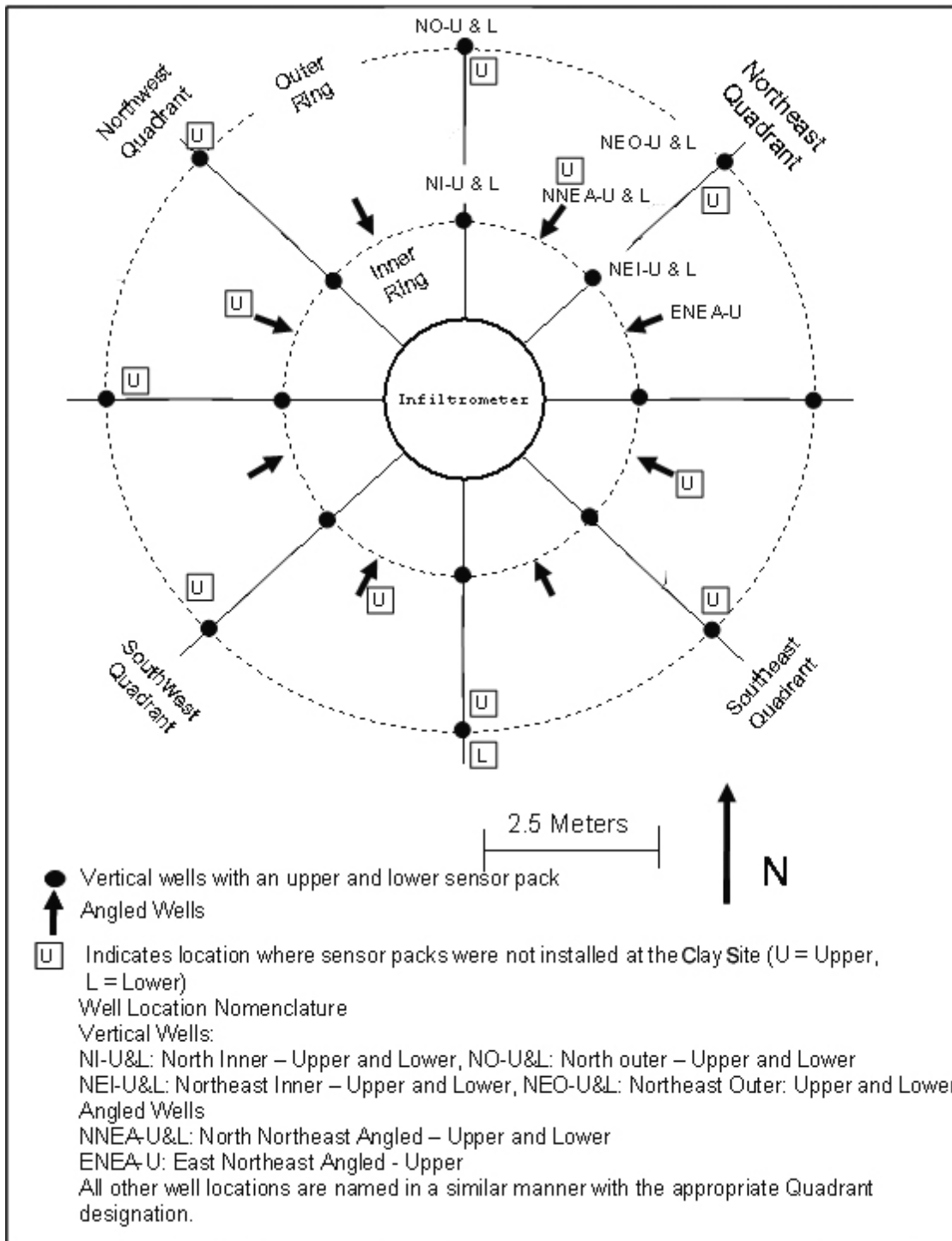


Figure 5. Plan-view map of the Clay and Sand Site Sensor Array.

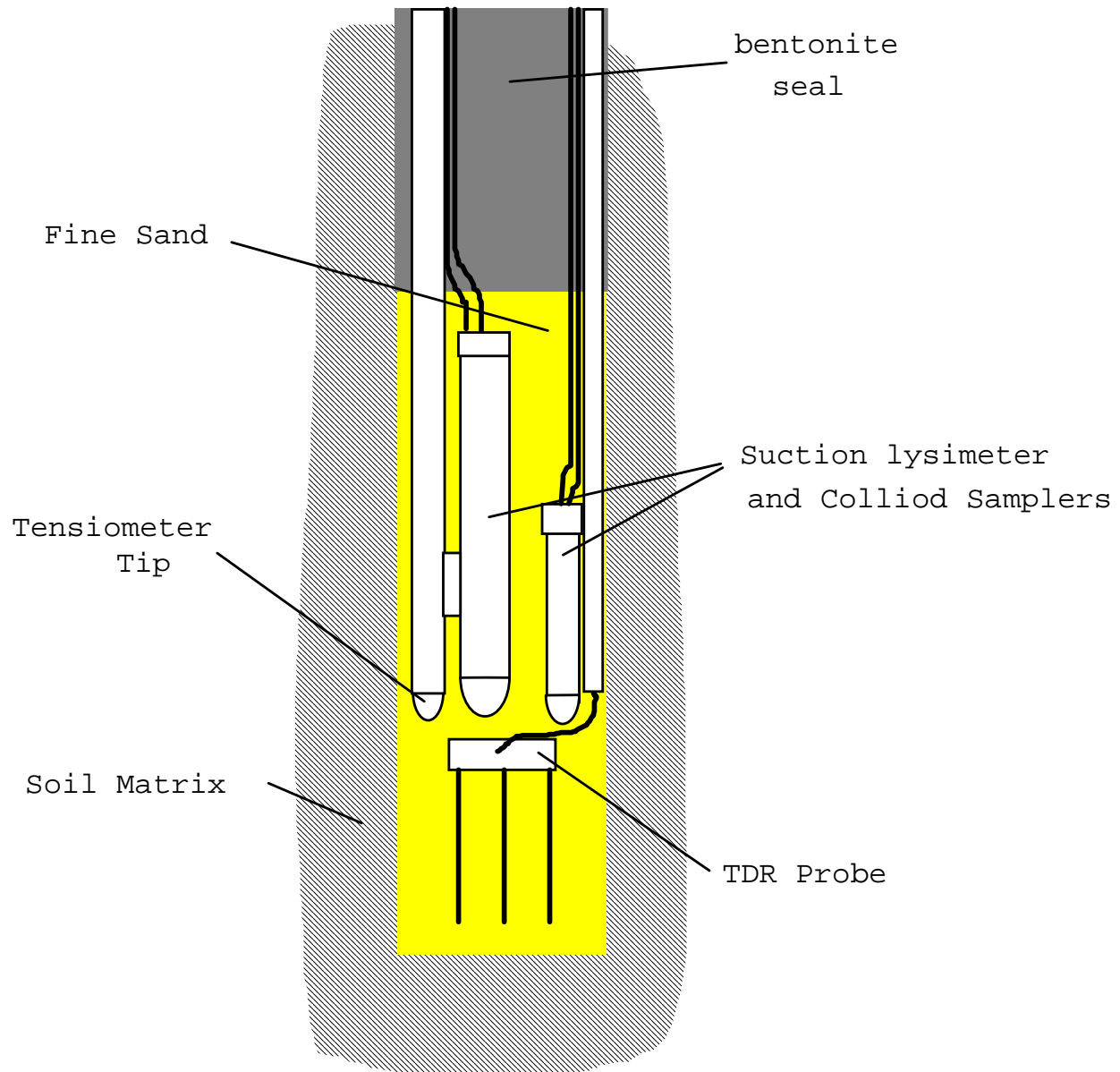


Figure 6. Schematic of the arrangement of sensors installed in the sensor pack

2.2.3 Infiltration

Infiltration was initiated in mid-June 1994 at both the Clay and Sand Sites simultaneously by pouring water into the infiltrometers and opening the water supply valves. This resulted in an instantaneous ponded head of 5 cm. Infiltration was terminated at both sites in late August, 1994. Table 1 details the length of each infiltration phase at both sites.

Infiltration at both sites started with potable water and followed with the addition of fluorescent microspheres (a colloid analog) and salt tracer of CaCl_2 . The fluorescent microspheres were used to determine the extent of colloid transport at the site, while the CaCl_2 tracer was implemented to obtain breakthrough curves through the suction sampler and TDR probe arrays.

After the tracer pulses were infiltrated, FD&C food coloring was added to the water supply system at the Clay Site to provide a means to visualize flow paths during subsequent excavation. All of these tracer pulses occurred in sequence without interrupting flow to the infiltrometers. In summary, infiltration followed the schedule in Table 1 which also shows the Appendix where detailed information is given on these infiltration periods and the sensors used to measure colloid and salt concentrations.

Table 1. Infiltration Schedule

Infiltration Event	Clay Site (days)	Sand Site (days)	Appendix Number
Potable water	5	6	B
Microspheres	1	1	D
CaCl ₂	55	54	D
Dyed water (FD&C food coloring)	2.0	2.2	F and G

2.2.4 Colloid Tracer

Analog colloid tracers composed of 260 ml (2% solids) of 1 μm blue fluorescent *Interfacial Dynamics Corporation's* latex microspheres and 25 ml (2% solids) of .2 μm yellow fluorescent microspheres were introduced into the Clay Site infiltrometer five days after the start of infiltration when steady-state conditions had been attained. The water supply to the infiltrometer was shut off upon introduction of the analog colloids and resumed after the water infiltrometer water level had dropped to the ground surface inside the infiltrometer. A pulse of 25 ml (2% solids) of *Interfacial Dynamics Corporation* .2 μm yellow fluorescent microspheres was introduced in the same manner to the Sand Site infiltrometer on the following day.

Soil water samples were collected from the colloid samplers transported to Los Alamos National Laboratory for analysis. An analysis of the samples did not detect the analogue colloids. It was hypothesized that either the fluorescent materials had degraded to the extent that they could not be detected or the colloids were not present in the samples.

2.2.5 Chloride Tracer

Six days after the start of infiltration with potable water and one day after the analog colloid pulse, a 0.1M CaCl₂ tracer pulse was introduced through the Clay Site infiltrometer. On the following day, the same concentration of CaCl₂ was introduced at the Sand Site. The Cl⁻ tracer pulse at the Clay Site was terminated 48 hours after infiltration of 1,534 liters, while at the Sand Site, infiltration was stopped after 53 hours and 1,209 liters.

2.2.6 Dye Tracer and Excavation of the Clay Site

After 61 days of potable water infiltration, FD&C Red #3 dye was added to the Clay Site infiltrometer supply tanks. Four days later after infiltration of 400 gallons of dye tainted water, all infiltration stopped at the Clay Site. At the same time, infiltration was halted at the Sand Site.

The excavation of the Clay Site down to and including the lowermost massive gray clay (HS Unit 1) was accomplished using both a large trackhoe and hand tools. Typically, the trackhoe would remove layers of material one to two feet at a time and hand tools were used to remove small quantities of material necessary to see features in detail. A set of photographs documenting the Clay Site excavation and a full discussion of the excavation process and results are contained in Appendix G.

2.3 Analysis of the TPC

Results from each type of measurement obtained during the TPC tests confirmed the validity of the hypothesized transport processes and provided additional insights. The major results are presented in this section. Complete results and discussions are presented in the applicable Appendices.

2.3.1 Infiltration

Infiltration rates versus time for both the Clay and the Sand Site are plotted in Figure 7. The maximum daily average infiltration rate at the Clay Site was 2.23 cm/hr, attained approximately 570 hours after the start of infiltration (430 hours after the start of the CI tracer pulse). From this point, infiltration asymptotically declined to 0.74 cm/hr which is taken as the steady-state infiltration rate. The maximum daily average infiltration rate for the Sand Site was 2.85 cm/hr, attained after approximately 514 hours of infiltration (350 hours after the start of the CI tracer pulse). After reaching this maximum, the infiltration rate declined to a steady state rate of approximately 0.73 cm/hr. During the dye pulse, the infiltration rate at the Clay Site again experienced a decline from 0.74 cm/hr to 0.57 cm/hr. The dye pulse was initiated by infiltrating adding a thick solution of dissolved powdered dye to the infiltrometer resulting in a fairly concentrated mix of water and dye in the infiltrometer. It was hypothesized that near surface deposition of the dye was clogging fractures and small biological macropores. This hypothesis was borne out during excavation (see Appendix G, Plates 15 through 103) when most of the dye appeared to be deposited in the uppermost 2 to 3 m immediately below the infiltrometer (see Plate 19). A full discussion of the implications of the pattern of infiltration rate change in time is given in Appendix B.

Based on published values, the probable saturated hydraulic conductivities of clay rich deposits ranges from 10^{-5} cm/s to 10^{-11} cm/s (Freeze, and Cherry, 1979). However, infiltration rates at both the Sand and Clay Sites approached 10^{-3} cm/s, exceeding these published values by two to eight orders of magnitude. This was the first indication that infiltration rates were controlled by the carrying capacity of the biological macropores and fractures and not by flow through the matrix alone.

Over the 66 day infiltration period, 61,000 liters of water were infiltrated through the system at the Clay Site and 78,000 liters of water at the Sand Site. Other indications that macropore flow significantly influenced the flow field include the lack of saturated deposits at the surface anywhere outside the infiltrometer during infiltration and the absence of mud found at depth during excavation of the Clay Site.

2.3.2 Pressure Head Field

Pressure head measurements at both sites mimicked the infiltration rate as seen in Figure 8 where the two variables are plotted. The increase in pressure head below the infiltrometer is probably due a build up of water from the infiltrometer. The mimicking of infiltration rate and pressure heads is further evidence for a direct hydraulic connection with the surface. Additional evidence comes from rapid tensiometer response to rainfall events at both the Sand and Clay Sites (Figures 9 and 10). During the rainfall events, the rise in head was typically almost 10 times the amount of precipitation. However, some sampling points displayed neither rapid nor large rises in head indicating that the surface to subsurface hydraulic connection is variable across the site.

Most tensiometers recorded an abrupt drop in pressure during suction sampler sampling, some with a fast return to the pre-sampling pressure and others with a much slower return (Figure 10). This rate of return is probably related to how easily water displaced to the suction sampler during sampling is replaced with water from outside the sensor pack. Thus, a fast return may indicate a hydraulic connection between the sand pack and macropores.

2.3.3 Chloride Tracer Measurements

As previously discussed, Cl^- concentrations were monitored with both TDR and suction samplers where water samples collected from the suction samplers were analyzed in the laboratory. An obvious rout for analyzing the TDR and suction sampler data is to compare breakthrough data from the two measurement systems. For this analysis, an important point to consider is that the suction sampler monitoring process is active (the measurement process creates a pressure gradient which impacts the flow field and hence the measured result) while the TDR monitoring process is passive (the measurement process does not impact the measured result). In Figures 11, 12, and 13, paired breakthrough data (one from TDR and the other from solution samples) from three separate sensor packs are plotted. In all three data sets, the chloride concentrations rise from background levels and gradually decrease over time. In Figure 11, the rise in concentration as measured with TDR shows some rapid oscillations before the peak where as the suction sampler data does not. Other than this anomaly, all three data pairs in Figures 11, 12, and 13 duplicate each other fairly well, albeit with an obvious vertical offset and slight arrival time discrepancy. In Figure 11 the solution samples recorded an earlier arrival time and peak than that of the TDR, while in Figure 12, the opposite is observed, while in Figure 13 the peaks appear at the same time. As indicated in the schematics in Figure 14a & 14b, the relative timing of the peaks could be explained by the relative location of a macro pore providing a conduit between the infiltrometer and the sensor pack. If a macropore intersects the sensor pack above the TDR probe, as depicted in Figure 14a, then the pressure gradient imposed by the suction sampler would draw the solution out of the macropore causing the salt pulse to at least initially bypass the TDR probe. This would result in an earlier suction sampler arrival time and peak. An intersection lower in the sensor pack as depicted in the Figure 14b would draw water out of the macropore and force it through the TDR probe sample volume resulting in an earlier TDR arrival time and peak.

Since the units forming the upper several meters of the Sand Site and the full depth of the Clay Site exhibited bedded heterogeneities, it is possible that layers with strongly contrasting

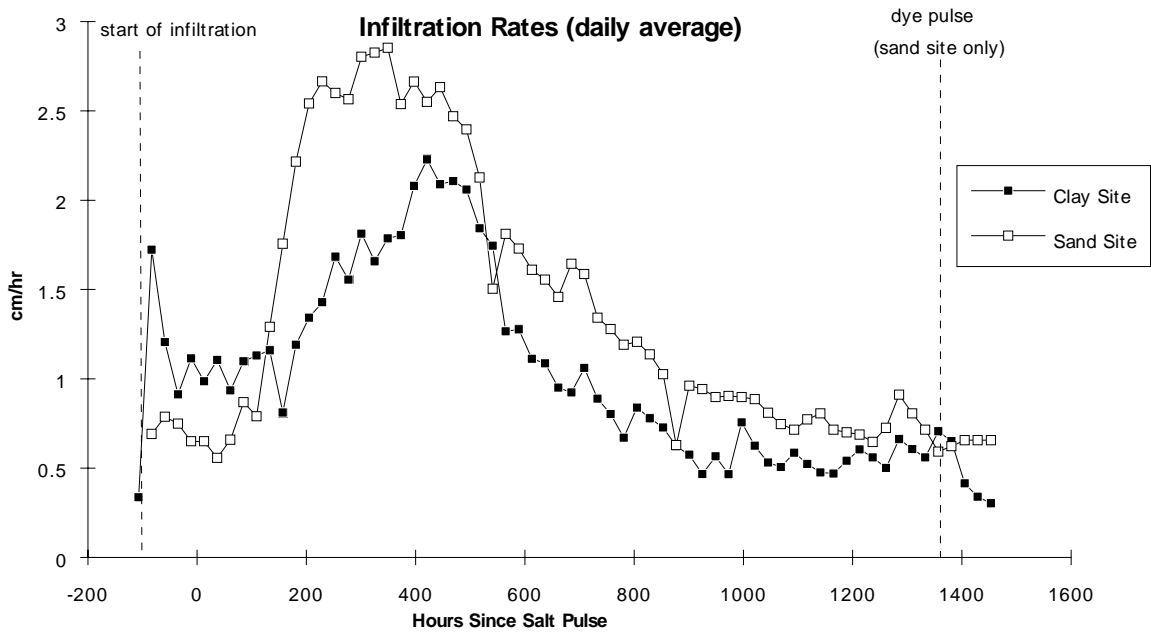


Figure 7. Plot of infiltration rates for the Clay and Sand Sites.

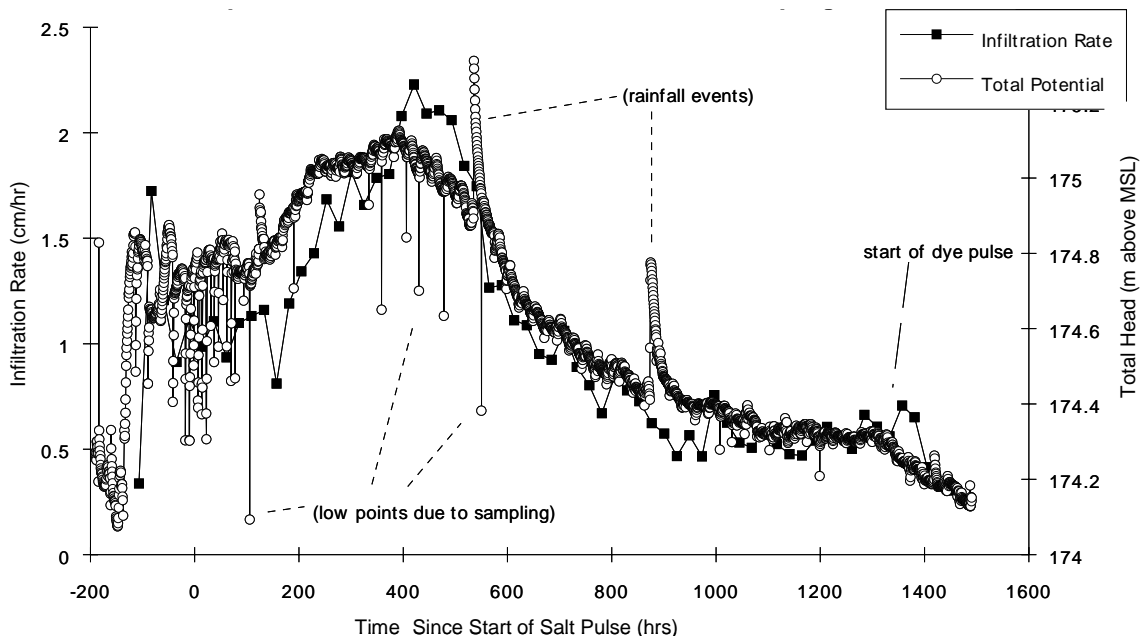


Figure 8. Plot showing the mimicking of infiltration rates by tensiometer measured pressure head.

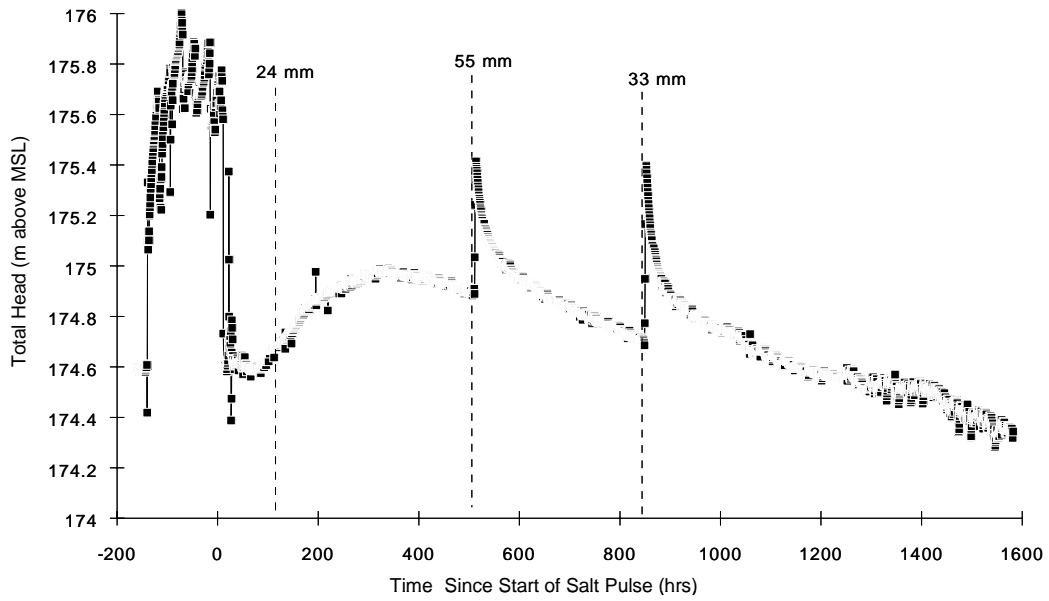
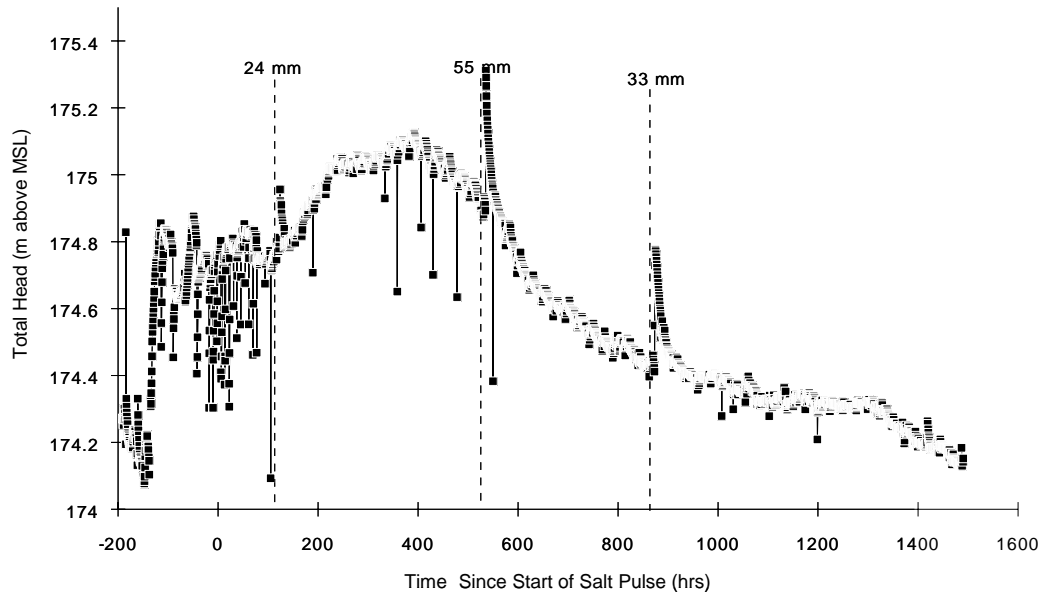


Figure 9a and b. Plot showing rainfall spikes in tensiometer data at the Sand (top) and Clay (bottom) Sites.

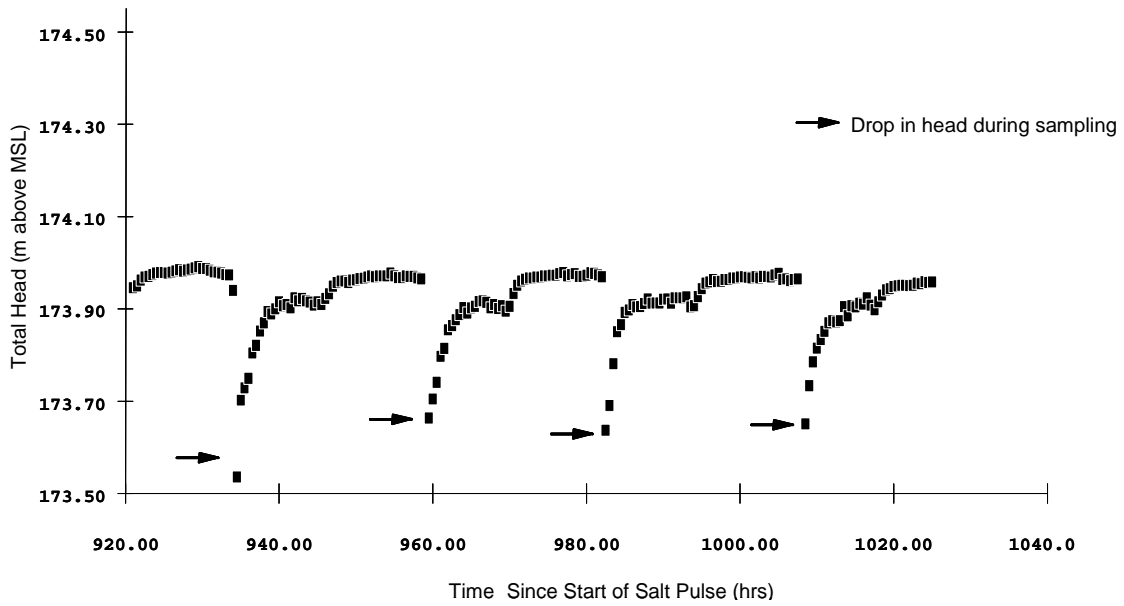
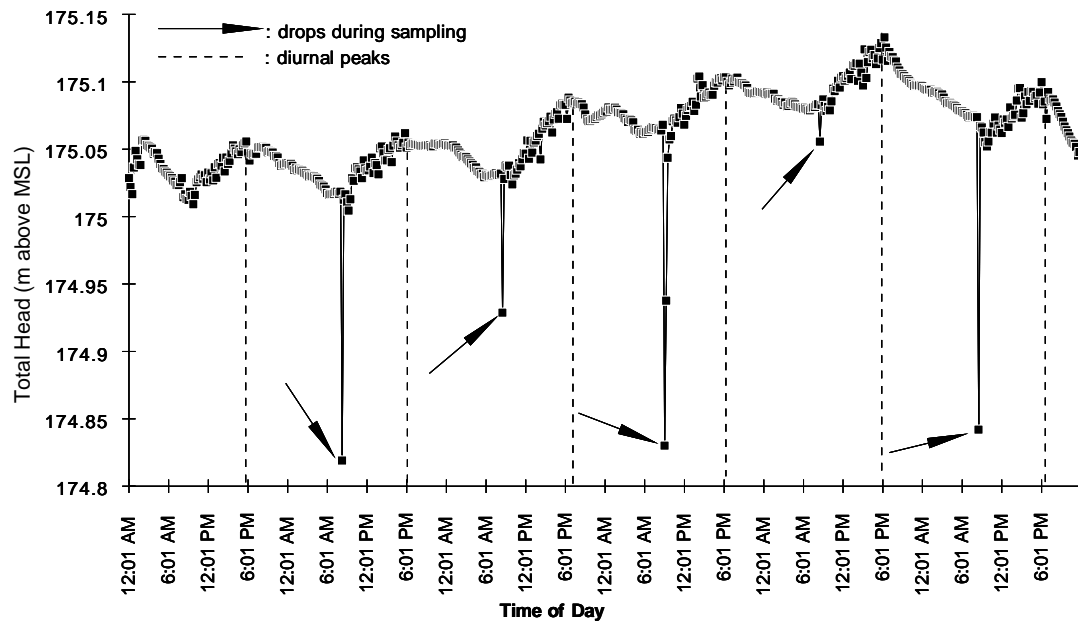


Figure 10a and b. Plots contrasting a fast (top) and slow (bottom) return of pressure head to pre-sampling conditions.

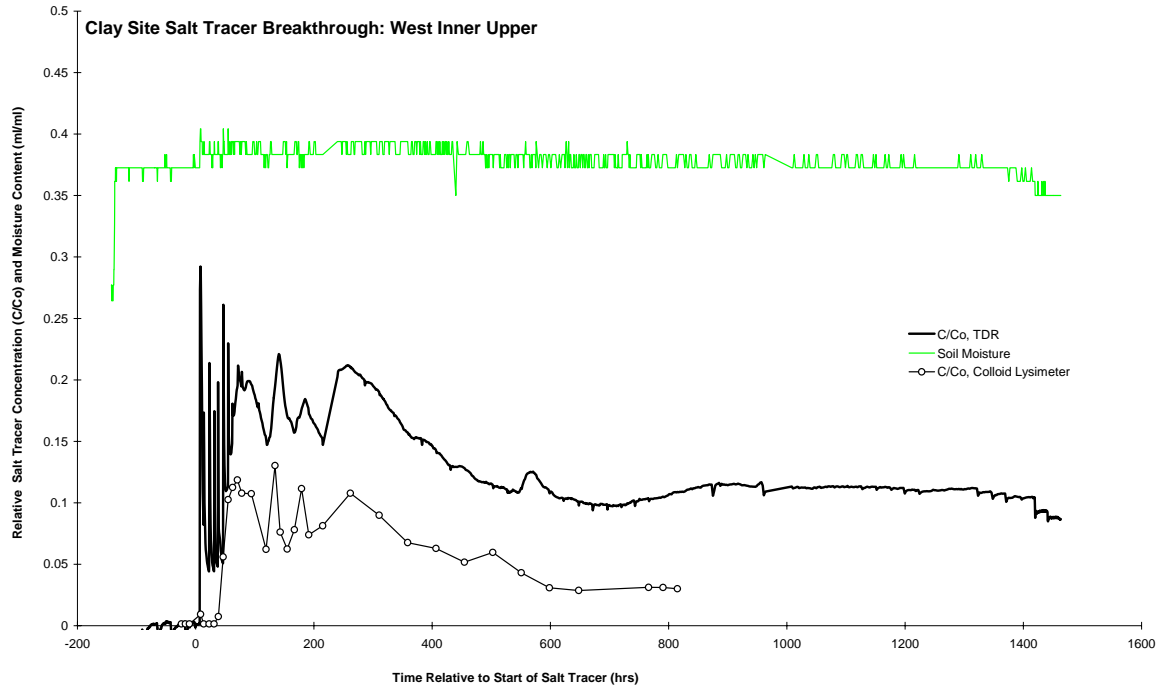


Figure 11. Plots comparing breakthrough curves obtained from TDR measurements and samples collected from suction samplers where the TDR measurements record oscillations and an earlier arrival.

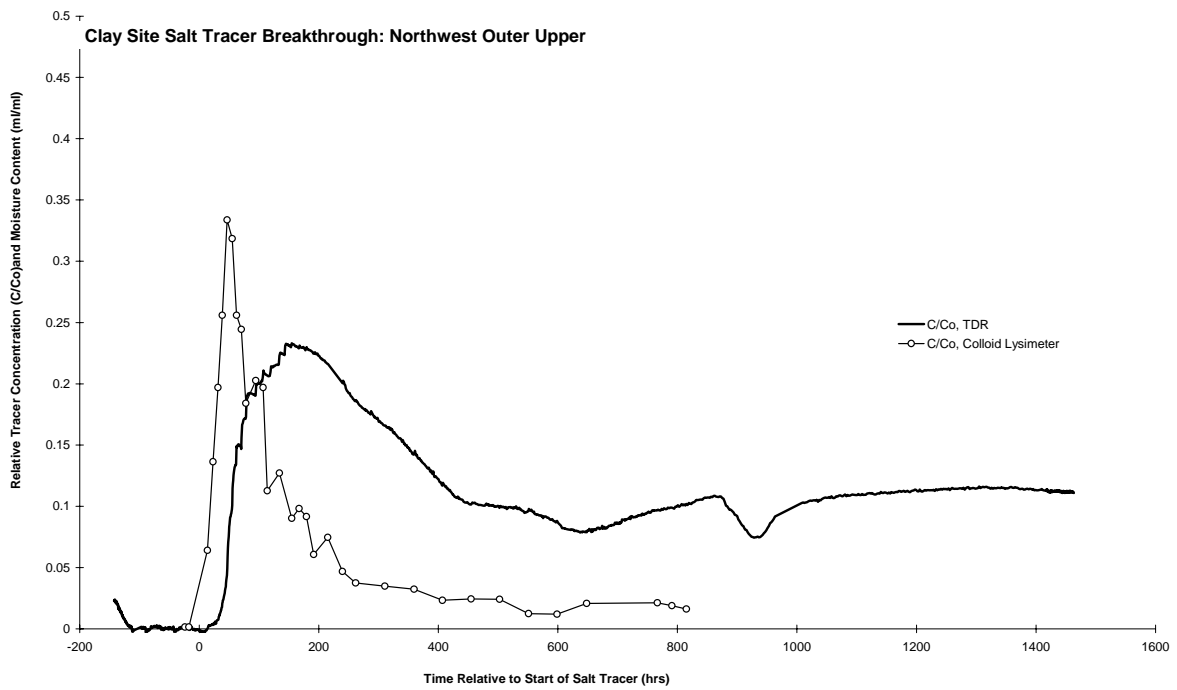


Figure 12. Plots comparing breakthrough curves obtained from TDR measurements and samples collected from suction samplers where the suction samplers record an earlier arrival time.

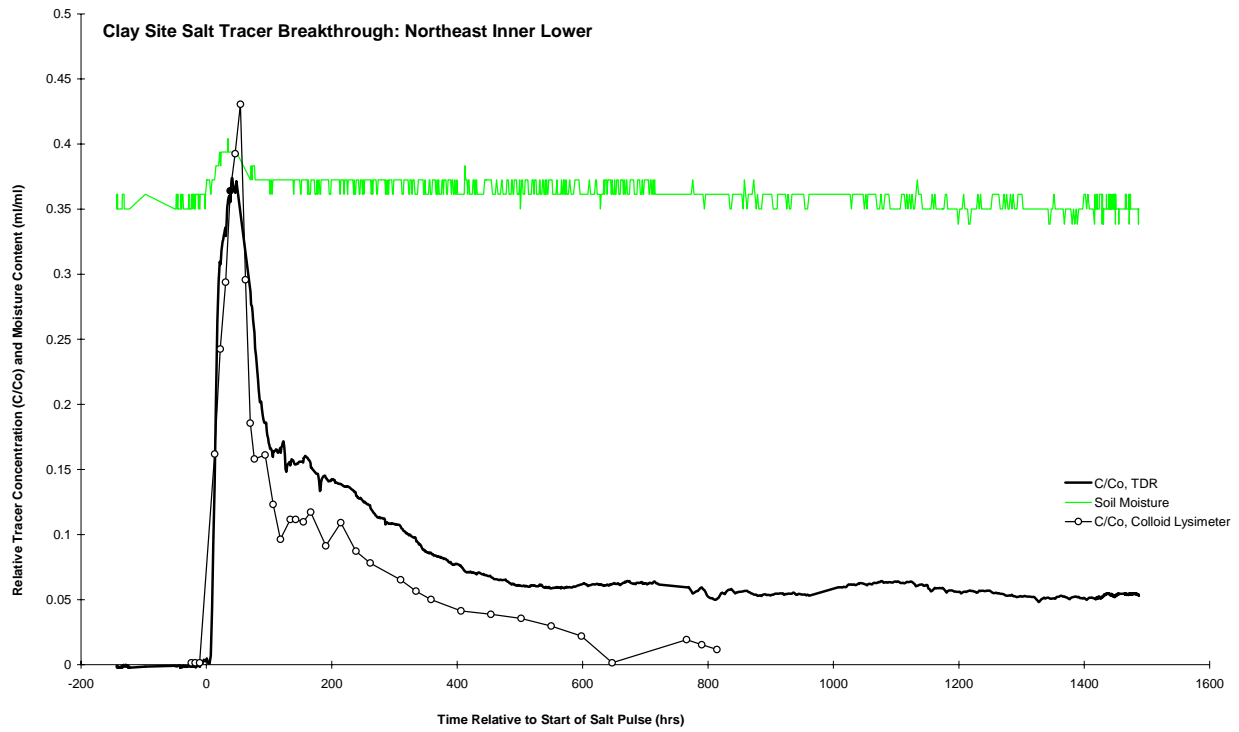


Figure 13. Plots comparing breakthrough curves obtained from TDR measurements and samples collected from suction samplers where arrival time and the peaks occur at the same time.

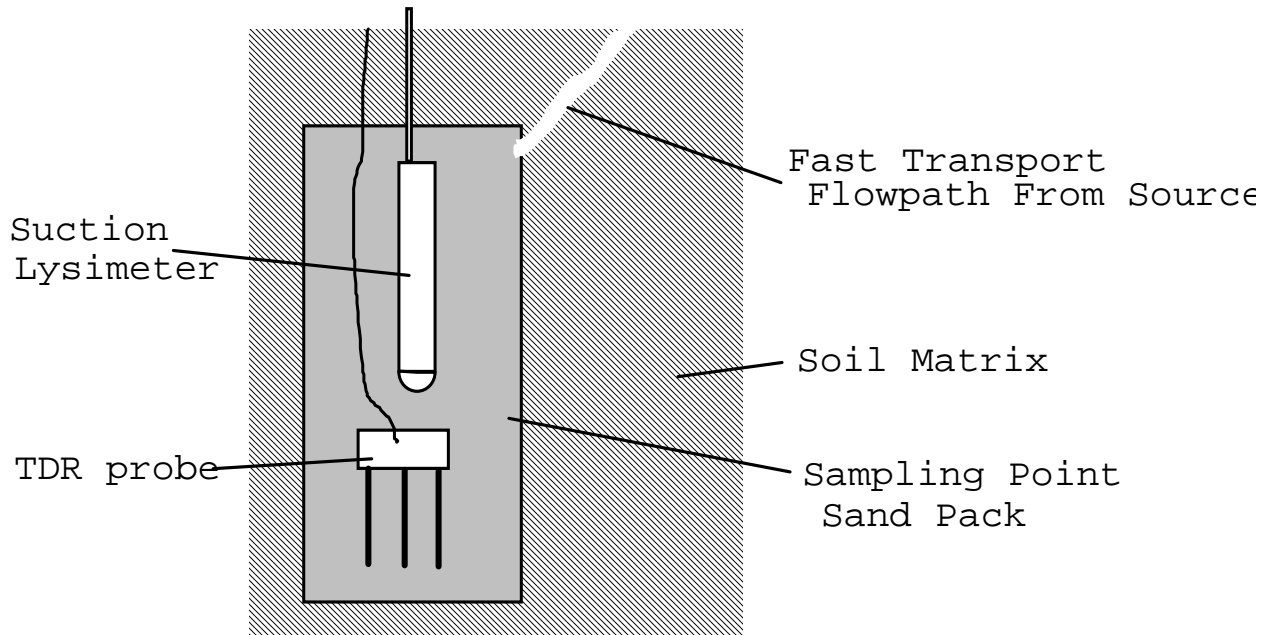


Figure 14a. Schematic of sand pack showing the hypothesized location of a macropore that may result in an earlier arrival time for TDR measured breakthrough curves.

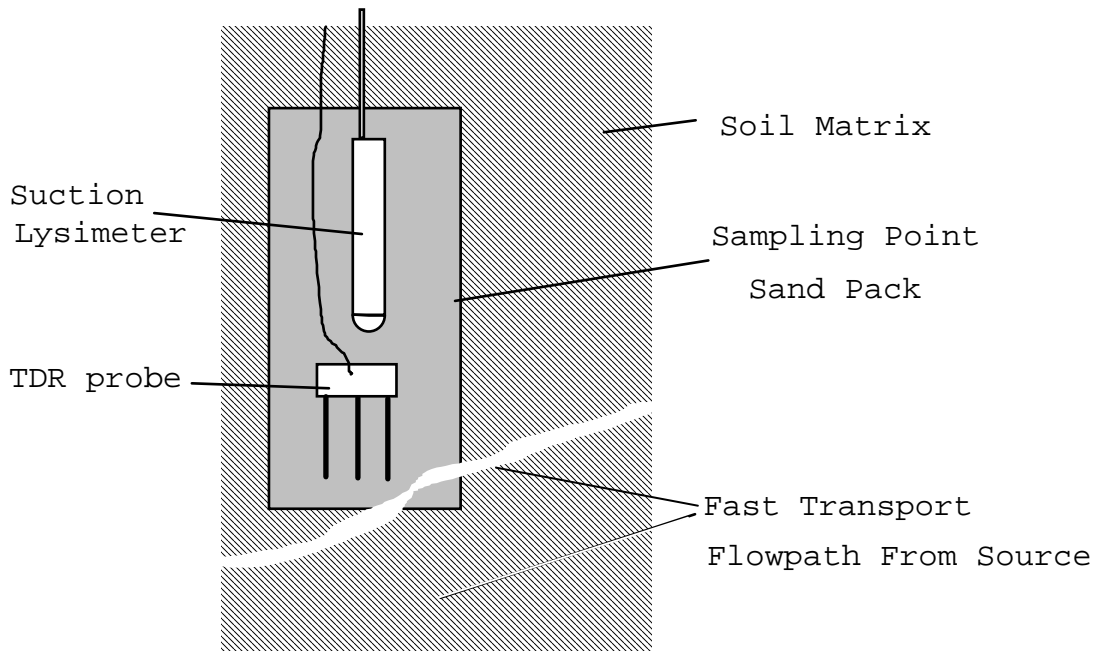


Figure 14b. Schematic of sand pack showing the hypothesized location of a macropore that may result in a earlier arrival time for suction sampler derived breakthrough curves.

hydraulic conductivities almost duplicating the hydraulic conditions depicted in Figure 14 a & b could generate the same plots shown in Figures 13 and 14. However, a significant piece of evidence for significant macropore flow is the abrupt and repeated peaks displayed in the TDR data in Figure 13. These peaks correspond exactly to soil water sampling times and most likely result from flushing the sand pack with tracer solution from a macropore.

Repeated peaks were observed in the TDR measured breakthrough curves (Figure 15) and may result from arrival of the tracer in two waves. Since only one tracer pulse was infiltrated, it is likely that the double peaks are the result of two pathways operating independently of each other. Based on previous outcrop surveys in Paddys run, the numerous fractures observed in most of the units could be responsible for the fast arrival of the first peak, but the flow path responsible for the second peak could not be explained with much certainty based on outcrop information alone.

A sense of the lateral direction of Cl⁻ tracer transport at both the Sand and Clay Sites can be seen in the plan-view contour plots Cl⁻ concentration interpolated from data collected at 120 hours after start of the pulse (Figure 16). White dots are operational sampling points. The 2.2 m diameter surface infiltrometer is centered in the figure. The flow to the upper left at the Clay Site is moving through a transmissive body of sandy silts deposited by glacial processes among the clays normally encountered at that depth. At the Clay Site the Cl⁻ tracer seems to flow to the northeast off of the site while at the sand site the tracer appears to have considerably less lateral movement and is limited to the region inside the inner ring sensor packs. Considering what was known about the potential for preferential flow through macropores, these plots can not be interpreted literally in that the plotted concentration gradients are, of course, the result of the interpolation of data between widely scattered points. Without further evidence for macropore flow however, the validity of the contour plots could not be seriously challenged.

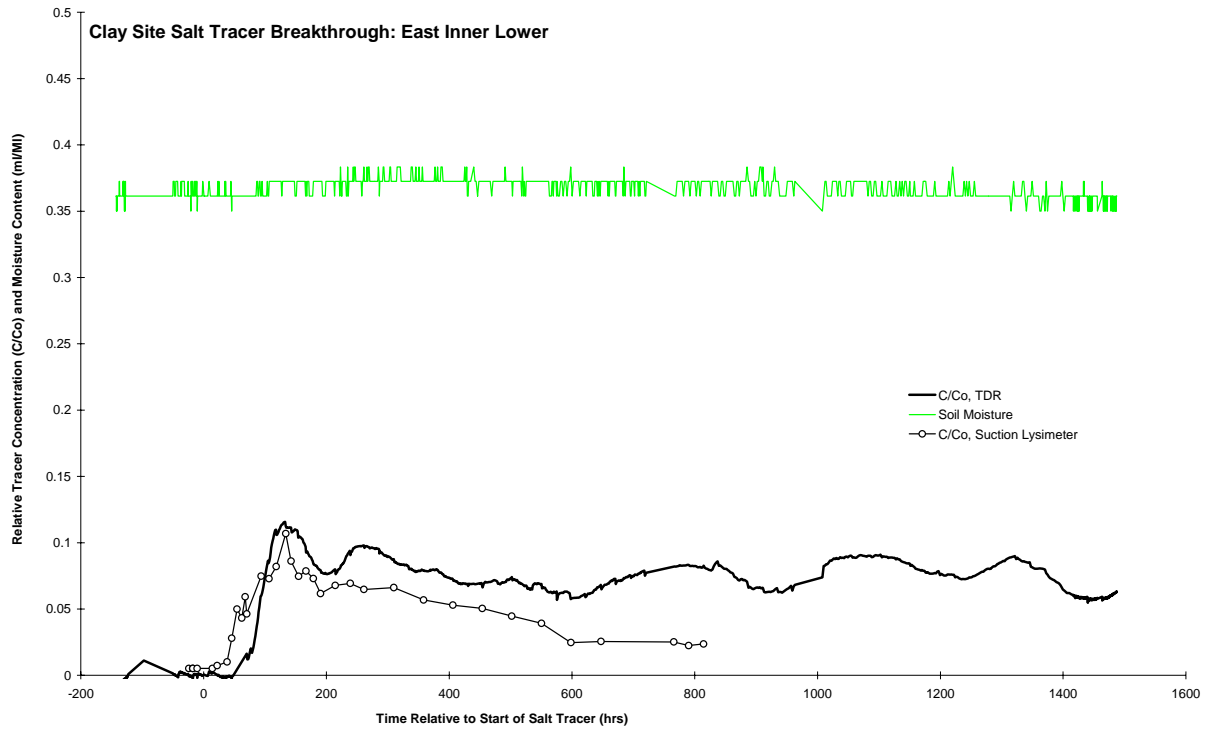


Figure 15. Plots of TDR measured and suction sampler derived breakthrough curves showing a second breakthrough peak.

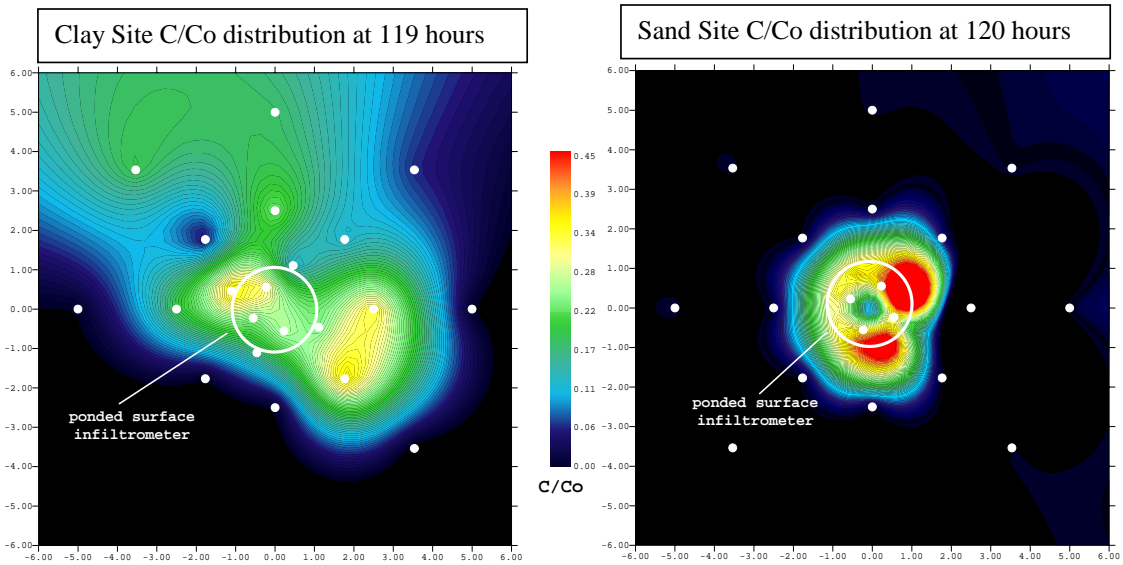


Figure 16. Plan-view contour plots of the Clay and Sand sites showing interpolated Cl^- relative concentrations at 2 m depth at 120 hours. Cl^- tracer concentrations distribution at the 2 m level of the Clay and Sand Sites 119 and 120 hours after start of the Cl^- pulse. White dots are operational sampling points. The 2.2 m diameter surface infiltrrometer is centered in the figure. The flow to the upper left at the Clay Site is moving through a transmissive body of sandy silts deposited by glacial processes among the clays normally encountered at that depth.

Notwithstanding the above complications, the following observations can be made. Arrival times of peak concentrations of Cl^- occurred less than one hour from start of the tracer pulse at some sampling points in the Clay Site. This fact also reinforces the hypothesis that macropores provide rapid transport paths. Based on timing of peak Cl^- concentration from the TDR data, overall tracer movement at both sites was initially vertical downward, then radially outward. Radial transport of the salt tracer began sooner at the Clay Site than at the Sand Site and resulted in a greater radial dispersal of the tracer.

2.3.4 Dye Pulse and Excavation

The dye pulse and subsequent excavation of the Clay Site afforded striking visualization of flow and transport pathways and helped to confirm many of the hypotheses that arose during the outcrop survey and sensor data analysis. Plates 13 and 14 (all Plates can be found in Appendix G) show the dye replacing clear water in the infiltrometer while Plates 16 through 103 documents the excavation process. Excavation involved removing large quantities of dirt with the trackhoe and removing small quantities of dirt by hand to allow for detail observations.

Dye stain was prevalent in the uppermost layer of top soils and loess (Plate 19) where it concentrated in root casts and worm burrows (biological macropores) and fractures indicating that these features served as the main pathways for dye transport of dye tracer through HS Units 5 and 4 (Plates 29 to 39). The matrix of HS Unit 4 was stained only in the immediate vicinity of dye-stained biological macropores and fractures. The lack of staining in the bulk of the HS Unit 4 matrix indicated that matrix flow through these deposits did not occur (Plate 34). As hypothesized, lateral transport along horizontal fractures and bedding planes as well as vertical fractures occurred in the oxidized bedded clays of HS Unit 3 and in the unoxidized bedded clays of HS Unit 2 as indicated by a very light dye stain – too light to show up in photographs – in scattered locations (Plates 45, 47, 50, 51, 54 and 58). Macropores were noticeably missing from the unconsolidated sands and gravels of HS Unit 6.

A sand stringer 2.8 m below the ground surface that discharged dyed water was discovered in close proximity to sampling point West Outer Lower in the oxidized clays of HS Unit 3 (see Figure 3 and Plate 77). Further excavation revealed a connection to a large silty sand body (mixture of HS Units 6 and 4) in the northwest quadrant of the site, truncating the beds of oxidized silty clays of HS Unit 3 (Figure 3 and Plate 76).

In addition to these dye-stained features, an unexpected network of tubes approximately 2 to 3 cm in diameter were found in the topsoil down to the unoxidized clays of HS Unit 2. These tubes (Plates 35, 40, 80 to 84) were later identified as crayfish burrows. Dye stain in many of the burrows confirmed that they provided a conduit for transporting water away from the infiltration site and in some cases providing a direct flow path to bedding planes and fractures. After completion of the excavation, three instances of crayfish burrows were discovered during a cursory 15-minute inspection of the surrounding field (Plates 104 to 109).

The large number of dye-stained burrows in the southern portion of the Clay Site (See the map in Figure 17) may explain the lack of measurable tracer concentrations by the sensor array in that these burrows provided a path of least resistance allowing most, if not all of the infiltrate to pass

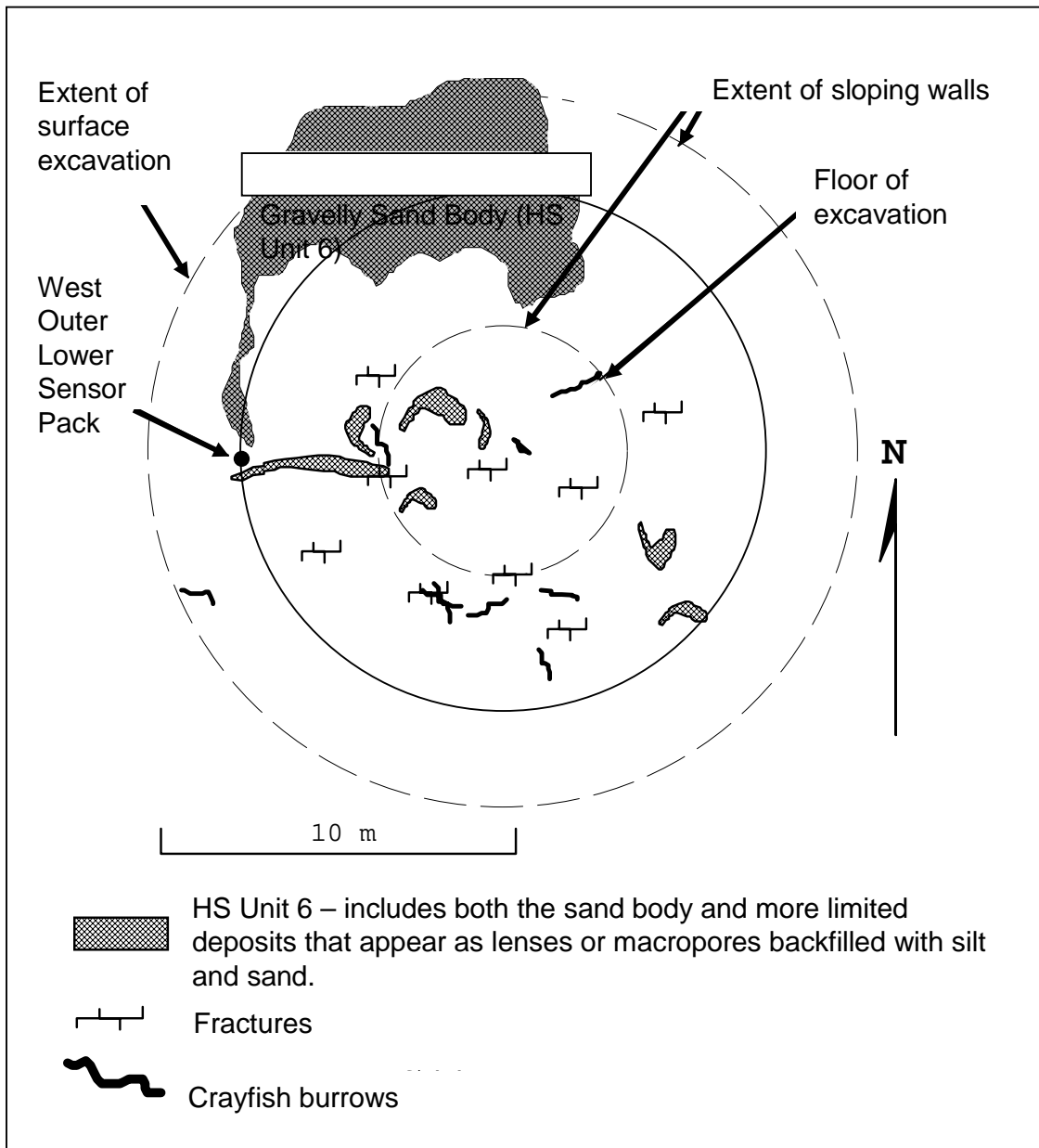


Figure 17. Schematic plan view of the Clay Site showing the approximate lateral extent excavation along with major occurrences of macropore, fracture, and preferential flow as evidenced by the presence of dye stain. The dye stained features are integrated over the full 6 meter deep excavation.

the fracture networks as well as the sensors. Burrows and vertical fractures were not observed within the lower part of the unoxidized layered clays of HS Unit 2.

Sand and gravel stringers and channels were observed at all depths and even penetrated the massive gray clays of HS Unit 1 (Plate 102). Unfortunately, at the top of HS Unit 1 (3 to 5 m in depth), the dye pulse was diluted to the extent that it was difficult to visualize the dye stain. Thus it is uncertain if the sand stringers within the massive gray clays any contained dye. To further our knowledge concerning flow and transport in HS Unit 1, an impromptu dye tracer

experiment was performed in the bottom of the pit within the top 1 to 2 m of this unit (see plate 55). The pond was approximately 3 by 3 m, 0.2 m deep, and was allowed to infiltrate for 24 hours. The pit was then covered with a tarp to allow excavation and sample collecting from around the site without impacting the pit (Plate 59). Trackhoe-excavated samples of HS Unit 1 often parted along planes that appeared to be bedding features similar to those observed in HS Unit 2 and shown in Plate 66. These planes were typically delineated with a thin layer of fine sand. Excavated samples within a few centimeters of the dye pit contained dye stain within the sandy partings as well as fractures indicating that these features may provide a pathway for contaminant migration in HS Unit 1 (Plate 103).

This page intentionally left blank.

3. Conclusions

3.1 Transport Processes, Controls and Connectivity

The TPI was effective in identifying important flow processes and the features that control those processes. Information gleaned from outcrop studies, data from sensors, and infiltration rates provided the opportunity to formulate hypothesis explaining the observations. The dye transport study and excavation resulted in visual evidence that confirmed the importance of biological macropore and fracture flow at the site and revealed an unexpected pathway through a network of crayfish burrows. Additionally the dye tracer and excavation contradicted the assumption of dispersion of the salt pulse through the media as suggested by the interpolated plots in Figure 16.

We conclude that a useful conceptual model for the near surface vadose zone at the Fernald Site must take into consideration the following processes and controls:

- (1) The dominant flow and transport pathways through the topsoil to the bedded clays are biological macropores and fractures. These pathways are capable of rapid transport in significant quantities, especially during saturated conditions such as that caused by spring runoff or intense rainfall events.
- (2) The bedded clays support a pervasive network of very transmissive horizontal and vertical fractures and are connected to the surface by these features as well as biological macropores in overlying deposits. Some crayfish burrows are continuous from the surface to the bedded clays while the entire network is likely hydraulically connected to the fracture network found in much of the clay deposits. Crayfish burrows may provide the dominant transport pathways in some areas, allowing contaminants to bypass much of the near surface deposits.
- (3) Hydraulic connection of the interconnected fracture and biological macropore networks with sand stringers and larger sandy-gravelly channel deposits results in surface water (and contaminants) reaching these highly transmissive channel deposits. These sand stringers and channels deposits appear to be ubiquitous in HS Unit 1 and likely provide conduits to the underlying aquifers.
- (4) Infiltration rates and changes in the pressure field support our findings that the near surface deposits have a significant infiltration potential, are well drained, and have a significant potential for transport of contaminants to the underlying deposits.

The transport processes delineated by the TPI can account for the vertical migration of uranium into perched groundwater, as noted in the Remedial Investigation Report for Operable HS Unit 3 (ITT, 1990), and may provide a means for migration through the glacial tills into the underlying Great Miami Aquifer.

This page intentionally left blank.

4. Further Investigation

The connectivity of transport pathways from the surface to near surface geologic units has been demonstrated at the field scale by implementation of a surface infiltration tracer experiment. However, the nature of the connectivity between the near-surface deposits and the underlying aquifers remains speculative and more investigation is required to gain a better understanding of this connection. The other area of need is the development of a method to model the behavior of this complicated hydrologic system and to design sampling strategies to characterize the deeper subsurface.

This page intentionally left blank.

References

- Andersen, M. P. and Woessner, W. W. 1992, *Applied Groundwater Modeling*. Academic Press, Inc, San Diego
- Beven, K, and P. Germann. 1982. "Macropores and Water Flow in Soils." *Water Resour. Res.*, vol. 18: 1311–1325.
- Dasberg, S., and F. N. Dalton, 1985, Field Measurement of Soil Water Content and Bulk Electrical Conductivity with Time-Domain Reflectometry. *Soil Sci. Am. J.* vol. 49: 293–297.
- Freeze, R. A., and J. A. Cherry, 1979, *Groundwater*, Prentice-Hall, Inc, Englewood Cliffs, New Jersey.
- Glass, R.J., J. Brainard, C. Roepke, M. Mann, and J. Schwing, Preliminary vadose zone transport pathway characterization test within glacial till at Fernald, Ohio: Data report, summer 1993, Uranium in Soils Project Report, 84 pgs, 1995 (SNL paper SAND95-R2938).
- Glass, R. J., T. S. Steenhuis, and J. Y. Parlange, 1988, Wetting Front Instability as a Rapid and Far-Reaching Hydrologic Process in the Vadose Zone. *J. Contam. Hydrol.* vol. 3: 207–226.
- ITT Industries. 1990. *Remedial Investigation Report for Operable Unit 3. Feed Materials Production Center, Fernald, Ohio*. White Plains, NY.
- Jones, L., Lemar, T., and T. Chin-Ta 1992. Results of Two Pumping Tests in Wisconsin Age Weathered Till in Iowa. *Groundwater*, vol. 30(4).
- Kachanoski, R. G., E. Pringle, and A. Ward. 1992. Field Measurement of Solute Travel Times Using Time Domain Reflectometry. *Soil Sci. Soc. Am. J.* vol. 56: 46–52.
- Lewis, B. D. and F. S. Goldstein. 1982. Evaluation of a Predictive Ground-Water Solute-Transport Model at the Idaho National Engineering Laboratory, Idaho, USGS, Water Resources Investigations Report 86-4022, 71 p, U.S. Geological Survey, Washington, D.C.
- Muckel, D. C. 1959. Replenishment of Ground Water Supplies by Artificial Means, U. S. Dept. of Agric., *Agric. Res. Service Tech. Bull.* 1195.
- Nadler, A., Dasberg, S. and I Lapid. 1991. Time Domain Reflectometry Measurements of Water Content and Electrical Conductivity of Layered Soil Columns. *Soil Science Society of America Journal.* vol. 55: 938–943.
- Nielsen, D. R., and J. W. Biggar, and K. T. Erh 1973. Spatial Variability of Field-Measured Soil-Water Properties. *Hilgardia* vol. 42: 215–259.
- Smettem, K. R. J. and N. Collis-George. 1985. Statistical Characterization on Soil Biopores Using a Soil Peel Method, *Geoderma*, vol. 36: 27–36.

- Tidwell, V. C., Cunnane, J. C., Gill, V. R., Lee, S. Y., Morris, D. E., Nickleson, M. D., and D. L. Perry. 1993. *Uranium in Soils Integrated Demonstration Project: Soil Characterization Project Report*. Sandia National Laboratories, Albuquerque, NM.
- Vieira, S. R., D. R. Nielsen, and J. W. Biggar. 1981. Spatial Variability of Field Measured Infiltration Rate. *Soil Sci. Soc. Am. J.* 45: 1040–1048.
- Wagenet, R. J., R. E. Knighton, and E. Bressler. 1984. Soil Chemical and Physical Effects on Spatial Variability of Hydraulic Conductivity. *Soil Sci.*, 137: 252–262.
- Wraith, J. M., S. D. Comfort, B. L. Woodbury, W. P. Inskeep. 1993. A Simplified Wave Form Analysis Approach for Monitoring Solute Transport Using Time-Domain Reflectometry. *Soil Sci. Soc. Am. J.* 57:637–642.

Appendix A. Geology

<u>Section</u>	<u>Page</u>
A.1 Introduction and Regional Geology	44
A.2 Outcrop mapping of Paddys Run	46
A.3 Test Site Geology	51

A.1 Introduction and Regional Geology

The Fernald site is located in the New Haven Trough, a classic paleo-glacial valley cut into Ordovician Age bedrock of shale and limestone. The ancestral Ohio River eroded into the bedrock of the New Haven Trough. A later ice sheet advance diverted its original flow, and the abandoned drainages filled with fluvial sands and gravels. These sands and gravels form the present-day Great Miami Aquifer, the major source of groundwater in the Fernald region. These sand and gravel deposits underlying the FEMP typically range from 40 to 60 m in thickness. During the glacial fluctuations, these aquifer deposits were covered by heterogeneous deposits of loess, clays, silts, sands, and gravels typical of glaciofluvial and glaciolacustrine environments.

The deposits encountered during mapping, sampling, and excavation at the FEMP, were divided into six hydrostratigraphic units. These hydrostratigraphic units are grouped according to their assumed hydrologic flow and transport characteristics and may cut across contacts and geologic units identified in other parts of this report. A schematic illustrating the general relationship of the six units at Clay Site is shown in Figure A-1. The Plates, referred to below, are in Appendix G.

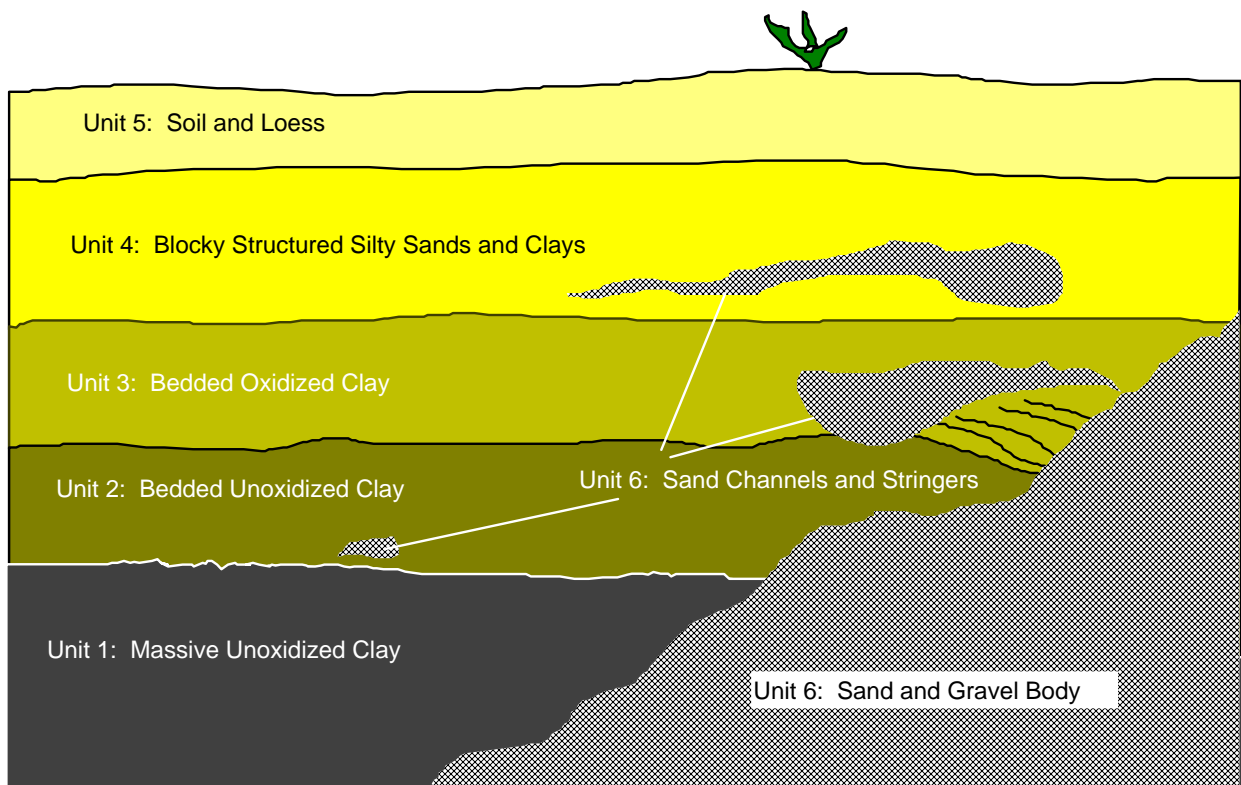


Figure A-1. General relationship of hydrostratigraphic units.

Table A-1. Hydrostratigraphic Units and Associated Transport Processes

Unit	Composition	Hypothesized Transport Processes and Controls
6	Sand and gravels	Highly transmissive matrix flow
5	Top soils and loess	Matrix flow, biological macropore and fracture flow, adsorption of colloids to organic material
4	Blocky structured silty clays	Matrix, fracture, and biological macropore flow
3	Oxidized bedded clays	Flow horizontally along bedding planes, vertically through fractures, transport by diffusion only through matrix
2	Unoxidized bedded clays	Flow through fractures, slight flow possible along tight bedding planes, diffusive flow only through matrix
1	Massive unoxidized (gray) clays	Flow through sand and gravel channels, along structural deformation, through matrix by diffusion only

HS Unit 6 is composed of sand and gravel diamicts of varied glaciofluvial, glaciolacustrine, fluvial, and lacustrine origin. All of the units below except HS Unit 5 were intersected at some location by channels or stringers of HS Unit 6 (Plates 77, 78, and 102). The sands and gravels of this unit were generally loosely compacted and provided the most transmissive avenue for transport through any unit matrix.

HS Unit 5 is the uppermost unit and consists of the topsoil and silty loess comprising the bulk of the rooted zone. Flow through this unit is controlled primarily by biological macropores providing avenues for fast transport of water and tracers (Plate 31), while plant and other organic matter absorbed much of the dye tracer (Plate 19) and perhaps much of the colloid tracers also.

HS Unit 4 consisted of blocky structured silty clays and sandy silts, apparently derived from paleosols. Flow in this unit was primarily vertical and aided by biological macropores as well as those formed by a pervasive system of interconnected fractures (Plates 20 and 38).

HS Unit 3 was composed of bedded and laminated oxidized clays and silty clays (Plate 47). The first significant radial flow was noticed in this unit, along bedding planes and laminae. Layers of rich in very soft carbonate nodules were apparent at some levels (Plate 36). Bedding planes, fractures, and laminae in this unit were heavily stained with iron and manganese oxides (Plate 54). Sand and gravel inclusions were encountered, providing zones of both radial and vertical preferential flow (Plate 44). Additionally, wormholes penetrated the unit as did the majority of observed crayfish burrows (Plate 40).

HS Unit 2 was composed of layered and bedded unoxidized clays. Although appearing massive during cursory sample examination, hand excavation and thorough sample examination revealed this unit to be heavily bedded and laminated (Plate 68). Horizontal and vertical fracture surfaces and bedding planes were often oxidized implying that these features have been active conduits (Plate 50). Large vertical fractures (~ 1 cm width) were commonly filled with sand. Crayfish burrows were not found beneath this unit.

HS Unit 1 consists of massive unoxidized clay with a frequent and irregular scattering of meter scale and larger sandy gravelly channels deposits and smaller scale sandy stringers. When excavated with the trackhoe, large masses fractured along what could have been remnant

bedding planes. Dye tracer was observed in these bedding planes (Plates 102 and 103), however, the primary mode of transport is likely through the channel deposits and sandy stringers.

Sensible geologic mapping of outcrops and the infiltration site required that these units be subdivided at the site scale and sometimes combined at the local outcrop scale. Over the entire study area, proportions of sands, silts, and clays were not constant in most units, especially in HS Units 4 and 5 where they were highly variable.

Available references on the geology and hydrology of the glacial tills include the *Remedial Investigation Report for Operable Unit 3* (ITT, 1990) and the summary report from the FEMP Industrial Workshop on Characterization on the Vadose Zone.

A brief geologic history of the FEMP site is given in the Remedial/Investigation Report (ITT, 1990) as well as general descriptions of the Great Miami Aquifer. *The Preliminary Subsurface Transport Pathway Characterization Test: Data Report Summer 1993* summarizes the geology at a test site located 50 m to the northeast of Clay Site.

A.2 Outcrop Mapping of Paddys Run

As part of the subsurface TPC test at Fernald, exposures of Wisconsin Age glacial deposits (Shelbyville Till) in Paddys Run were geologically mapped in mid-August, 1994. All accessible outcrops of usable size were mapped and described. In general, the exposures showed considerable geologic heterogeneity. The mapping unit geometry was complex. Only four outcrops (Outcrops #5, #8, #12, and #13, Figure A-2), showed complete or nearly complete sequences of the Shelbyville Till. The remaining outcrops are not complete because they were eroded during the development of the Paddys Run terrace. During the geologic mapping, nine lithofacies of the six hydrostratigraphic units were identified. Seeps, seepage face conditions, and locations were observed. The lithofacies encountered are briefly described below. Maps and complete descriptions of these outcrops are presented in the next section. Colors are described according to the Munsell Color System (Munsell soil color charts).

Matrix-Supported, Argillaceous Diamict (Hydrostratigraphic HS Unit 1)

The matrix-supported, argillaceous diamict (Dma) lithofacies is a calcareous, matrix supported deposit containing angular, blocky to tabular pebbles and cobbles of fossiliferous limestone and dolomite. The matrix consists of poorly sorted, sandy mud. The Dma lithofacies is usually massive or structureless (Dma-m). Stratification (Dma-s) is rare within the matrix, although irregular, discontinuous, and deformed interbeds of sand and laminae of silt are common. Sand interbeds vary in thickness from a less than an inch (2 cm) to over 1.4 m, but most are a few inches (cm) thick. Some thin beds of sand contain clay inter laminae. Planar features, marked by a pavement of limestone and dolomite cobbles wedged into the deformed underlying Dma, are persistent across several outcrops. Some of these cobbles show a weak imbrication toward the south. The Dma is light gray (5 Y 7/1 to 5 Y 7/2) when dry. It is gray (5 Y 6/1 to 10 YR) 5/1) or light olive gray (5 Y 6/2) when moist. Along the upper contacts and some internal contacts with sand interbeds, the Dma is light olive brown (2.5 Y 5/3 to 2.5 Y 5/6), pale yellow (2.5 Y 7/2), or brown (10 YR 5/3).

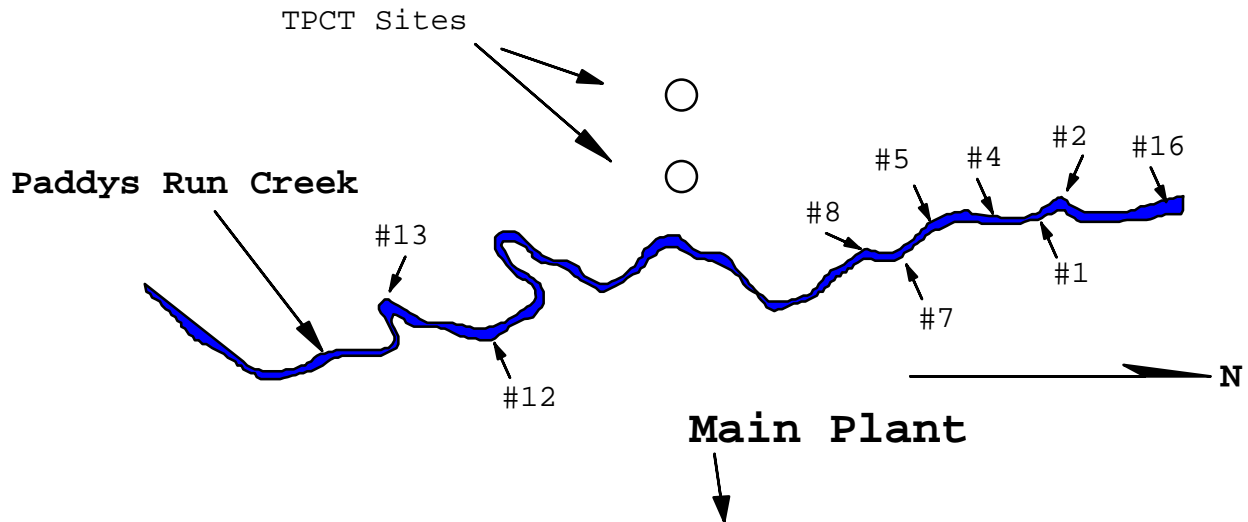


Figure A-2. Outcrop locations along Paddys Run.

Deformation structures are common within the Dma. Strata and interstrata, when present, are often deformed into flame structures or contorted drag folds indicating shear toward the south. Shear planes showing separation and displacement are common. At some outcrops (e.g., Outcrops #5 and #8), series of reverse faults with over 1.5 m of slip are over thrust toward the south indicating horizontal compression in the north-south direction.

The Dma is typically massive and breaks along irregular planes forming a blocky surface. Sub vertical fractures are common locally and the matrix material along the fractures is often light olive brown (2.5 Y 5/3 to 2.5 Y 5/6), pale yellow (2.5 Y 7/2), or brown (10 YR 5/3), indicating possible oxidation and the potential for flow and transport.

Both the upper and lower contacts of the Dma are spatially variable, and the Dma is not uniformly distributed along Paddys Run. In the northernmost outcrops (e.g., Outcrops #16, #3, and #2), the Dma is overlain by a stratified gravel lithofacies. In this area the upper contact is erosional and slightly undulatory, and local channels 10s of feet wide and up to 1 m deep are down cut into the Dma. The erosional surface truncates shear surfaces and probable over thrust faults. The Dma is truncated erosionally by the stratified gravel lithofacies in the northern part of Outcrop #2. Channels within the stratified gravel lithofacies occur at the northern or southern edge of the outcrops, and it is possible that the channels cut through most of the Dma and that topographic highs (outcrops) are only present where channels do not occur. North of the study area, the Dma overlies the stratified sandy diamict and massive sandy diamict lithofacies. The lower contact is deformed and undulatory over 0.75 m and shows load deformation.

Further to the south (Outcrops #1 and #4), the Dma is overlain by a gravel lag and massive sandy silt lithofacies, and the upper contact is erosional, sharp, and undulates over 0.75 m. Along the north edge of Outcrop #1, a channel in the stratified gravel lithofacies significantly thins the Dma. The Dma overlies the sand and silt lithofacies.

At Outcrop #5, the Dma is overlain by a complicated and deformed mix of sandy diamict, gravel, and pebbly sand lithofacies. A highly deformed unit of Dma interbedded with sand overlies

massive Dma along the south side of the Outcrop #5. Complications at Outcrop #5 are due to preserved shear structures and over thrust faults affecting the upper contact of the Dma and the overlying materials. The lower contact of the Dma lithofacies is not visible at Outcrop #5.

At Outcrop #6, the Dma is absent. At Outcrop #7, the Dma is again overlain by the gravel lithofacies and the upper contact is erosional. The Dma overlies the sandy diamict lithofacies, and the lower contact is sharp, undulatory and shows load deformation.

Further south (Outcrop #8), the Dma lithofacies again shows complicated relationships with the overlying materials. Shear structures (over thrusts or flame structures) display over 1.2 m of vertical displacement. A lenticular zone of cross laminated sand is surrounded by Dma and appears to have been wedged into the Dma as a solid mass. A very thick bed of sand, over 0.75 m to 0.15 m thick, subdivides the Dma lithofacies. The Dma overlies the Great Miami Aquifer, but the contact zone is obscured.

The southernmost exposures of the Dma occur at Outcrops #12 and #13. In these locations, the Dma lithofacies directly overlies the GMA and underlies sandy diamict and sand. The upper contacts are sharp and undulatory.

Matrix Supported, Sandy Diamict Lithofacies (Hydrostratigraphic HS Unit 6)

The matrix supported, sandy diamict lithofacies (Dms) consists of poorly sorted, sand dominated matrix with sub rounded to subangular granules, pebbles, and cobbles, including limestone, dolomite, and siliclasts. The Dms lithofacies rarely displays structure and is described as massive, although some clasts show alignment along deformation at the basal contact. The Dms is typically brown (10 YR 4/3) when wet.

The Dms lithofacies has a limited distribution within Paddys Run, and is confined to two northern outcrops: Outcrops #2, and #3. In Outcrop #3, the Dms lithofacies occurs at the base of the outcrop and is overlain by the Dma lithofacies. The upper contact is sharp and undulatory. Evidence of erosion is not present. In Outcrop #2, the Dms lithofacies is bounded on the top by the gravel lithofacies and on the bottom by the clast supported, sandy diamict lithofacies. Along the north side of Outcrop #2, a thin tongue of Dma overlies the Dms. The upper contact is clearly erosional and local channels down cut into the Dms. The basal contact of the Dms is deformed from loading and undulatory over 1 m.

Clast Supported, Sandy Diamict Lithofacies (Hydrostratigraphic HS Unit 6)

The clast supported, sandy diamict (Dcs) is calcareous and displays a poorly sorted sand matrix with sub rounded to subangular granules, pebbles, and cobbles. Locally, some clasts are tabular and very angular. The Dcs displays horizontal to subhorizontal parallel very thin to thin beds (Dcs-h), planar cross-beds (Dcs-p), and trough cross-beds. Strata packages show lenticular bounding surfaces and are up to 0.6 m thick. Low angle cross cutting relationships are common at bounding surfaces. Some bar forms are almost completely exposed and are over 12 m long in the outcrop plane. The Dcs ranges from reddish yellow (7.5 YR 6/6) to light yellowish brown (2.5 Y 6/4) when dry.

The Dcs occurs at the base of Outcrops #2 and #7. At these locations, the lower contact is not observed. The upper contacts show load deformation and undulate over 1.2 m. The Dcs is

overlain by Dms at Outcrop #2 and Dma at Outcrop #7. At Outcrop #5, Dcs is weakly stratified, overlies the Dma, and is associated with deformed and sheared areas with over thrust.

Interbedded Matrix Supported, Argillaceous Diamict/Sand Lithofacies (Hydrostratigraphic HS Units 1 and 6)

The interbedded matrix supported, argillaceous diamict/sand (Dma/S) lithofacies consists of Dma (major component) with up to 8 cm thick interbeds of silt, very fine to very coarse sand with some granules and pebbles. Structure was not observed in the sandy component of the lithofacies. The Dma component contains some sub horizontally oriented planar surfaces marked by pebbles and cobbles of limestone and dolomite. The Dma breaks along blocky, slickenside surfaces. The Dma/S is generally grayish brown (10 YR 5/2) when wet.

The Dma/S lithofacies is a major part of the exposure at Outcrop #5. Dma/S overlies Dma, and the contact was partly obscured.

Pebbly Sand Lithofacies (Hydrostratigraphic HS Unit 6)

The pebbly sand (Sp) lithofacies consists of poorly sorted sand and subangular to sub rounded pebbles. It typically displays planar cross beds and horizontal laminae to very thin beds. Low angle cross cutting relationships are evident in some exposures. Frequently contains interbeds of silt and clay to 5 cm thick. The color varies from yellowish brown (10 YR 5/4) to light gray (5 Y 7/2) when dry. The silt component is light yellowish brown (2.5 Y 6/3) when wet.

The Sp lithofacies occurs as tilted, angular wedges within the Dms lithofacies at north part of Outcrop #5 and between the laminated mud lithofacies (top) and Dma lithofacies (bottom) at the south part of Outcrop #5. A lens-shaped form of Sp, with dipping strata, occurs near the top of Outcrop #8 and is bounded on all sides by Dma.

Sand Lithofacies (Hydrostratigraphic HS Unit 6)

The sand lithofacies encompasses a variety of mapping units showing different sedimentary structures. Typically, the sand is poorly sorted and calcareous. Grain sizes vary but the sand lithofacies usually consists of very fine to coarse sand. Sand may display horizontal laminations (Sh) and contain interbeds of silt to 4 cm thick when associated with the Dma lithofacies. Structureless and mottled sand (Sm) is laterally equivalent to Dcs and Dms at Outcrop #1. Sand stringers and interbeds within the Dma units may be considered small scale examples of the Sl lithofacies.

At Outcrop #13, sand is rippled (Sr). The Sr lithofacies consists of interbedded poorly sorted sand, well sorted sand, and silt. The lower 3 to 6 in. of Sr consists of granule and pebbly sand with wavy to contorted thin laminae that show some soft sediment deformation and shear. Well sorted, fine sand showing ripple cross laminae sets to 1 to 3 cm high and ripple drift cross laminae with stoss and lee preservation. Ripple sets are typically capped by clay drapes. Soft sediment deformation due to loading is abundant including flame structures and cm scale shear displacements.

The sand lithofacies is present in various locations within Paddys Run. At Outcrop #1, Sm occurs at the base of the outcrop and is overlain by Dma. At Outcrop #7, a thin bed of Sm is overlain by the sand and gravel lithofacies and underlain by the Dma lithofacies. Sl overlies

Dma and underlies the Sp lithofacies and the laminated mud lithofacies at Outcrop #8. At Outcrop #13 and possibly Outcrop #12, Sr and Sl with soft sediment deformation and shear directly underlay the laminated mud lithofacies and overlie the Dma at Outcrop #13 and the Sp or Dms lithofacies at Outcrop #12.

Laminated Mud Lithofacies (Hydrostratigraphic HS Units 2 and 3)

The laminated mud lithofacies (Fl) consists of horizontally laminated to thinly laminated silt and clay couplets. In general, strata are flat, parallel to wavy, and locally contorted and disrupted. The lower few cm of Fl are often slightly brecciated. Adhesion ripples are present locally. The color of Fl ranges from grayish brown (10 YR 5/2) to light gray (10 YR 7/2 to 2.5 Y 7/1).

The Fl lithofacies are only present at Outcrops #5, #8, #12, and #13 and overly a variety of other lithofacies. At Outcrop #5, only a small erosional remnant of the Fl lithofacies is preserved, and it overlies the Dms and Dcs lithofacies. At Outcrop #13, the Fl lithofacies overlies the Sr lithofacies.

Sand and Gravel Lithofacies (Hydrostratigraphic HS Unit 6)

The sand and gravel (S/G) lithofacies consists of matrix supported, massive (Sm/Gm), horizontally stratified (Sh/Gh), planar cross stratified (Sp/Gp), or trough cross-stratified (St/Gt) pebble to cobble gravel interbedded with poorly sorted sand. Most clasts tabular and vary from angular to sub rounded. Many clasts show strong imbrication toward the south. Packages separated by erosional bounding surfaces show distinct bar morphology. Strata within some sand interbeds drape over channel forms cut into the underlying gravel. Sand interbeds display flat strata, low angle tangential cross strata, and planar cross strata. Where sand dominates, gravel occurs as lags. In general, the sand and gravel lithofacies appears to fine upward as the gravel content decreases. The lower contact of this lithofacies is sharp and erosional, and channel forms are frequent along the edges of outcrops.

Except for Outcrops #8, #12, and # 13, the sand and gravel lithofacies is present at all outcrops mapped. These outcrops occur where the river bank has cut into the first terrace of Paddys Run. In the southern most outcrops, the lithofacies displays less gravel.

Blocky Structured Silt/Sand Lithofacies (Hydrostratigraphic HS Unit 4)

The silt/sand (Si/S) lithofacies consists of argillaceous silt and sand. It is frequently mottled, shows a blocky texture, and may display peds. Strata are evident locally but are poorly preserved. The lower contact may show a pebble lag. The unit typically grades upward into the root zone.

The Si/S lithofacies is present at all mapped outcrops in Paddys Run. In some circumstances, it is completely incorporated into the root zone. It appears to blanket a variety of lithofacies, and is the youngest outcrop deposit mapped. Strata occur infrequently in topographically low areas.

Seepage Face Locations in Paddys Run

During the mapping of Paddys Run, seepage faces were observed only in Outcrops #5 and #8. Seeps were observed at the upper contact of the Dma lithofacies and along sand interbeds within the Dma lithofacies. Because of local cover and slump, the volumetric flux from these seeps could not be estimated. Seeps do not always occur within oxidized sediments. At Outcrop #5,

seeps occur from gray (presumably reduced) sand in gray Dma. In addition, many oxidized fracture surfaces show no seepage. Therefore, the reduction/oxidation status of the sediment is not always a definitive indicator of modern flow paths. Seeps along the upper contact of the Dma occurred in topographically low areas where sands were in contact with the Dma. These topographically low areas display features consistent with large scale shear, over thrusting, or emplacement of frozen blocks by sub glacial processes. The three-dimensional geometry of these features is unknown, but it is clear they provide paths for preferential groundwater flow and transport.

A.3 Test Site Geology

In an effort to obtain information on the geology of the near surface vadose zone in the glacial deposits within the study area, 17 geologic cross-sections, six at each infiltration site, three between the infiltration sites, and two from unused candidate Transport Processes Characterization (TPC) tests were constructed from descriptions of approximately 800 hand-augered samples collected at one foot intervals the test site. Additional geological insight came from excavation of the Clay Site –one of two sites chosen for one of the TPC tests. Eight lithofacies were identified and mapped in geologic cross-sections. These lithofacies are designated cross-section units (CS Unit #) and are described independently of the lithofacies in the Outcrop Mapping section above.

TPC Site Geology

Exploratory augering throughout the study area was undertaken to locate two suitable TPC test sites. The final selection of sites was based on completeness of the stratigraphy relative to that identified in Paddys Run, and on the marked difference in the deposits at two nearby locations. One of the sites was underlain by clay deposits and the other by a sand and gravel deposit. The sites were named the Clay and Sand Sites. The Clay Site consists of eight distinct clay lithofacies in the upper 3.5 m while the Sand Site consists of 2 to 3 clay lithofacies overlying saturated silty sands and gravels. The sites were located approximately 45 m apart on an approximate east west line. A plan view map of the study area showing the two chosen infiltration sites, exploratory augered borings, and unused candidate sites is given in Figure A-3. Plan view maps illustrating sample locations and cross-sections of, and between the Sand and Clay sites are given in Figure A-4, while the map showing the sampling locations at these two sites is given in Figure A-5. All cross-sections discussed below are given in Figures A-7 through A-23 at the end of this appendix.

For each site, two circular cross-sections (Figures A-6 through A-9) along the inner and outer rings (see figure A-5) and four radial cross-sections (Figures A-10 through A-17) running through the center of each infiltrometer were constructed from information gained from samples taken during well augering sensor pack installation. The circular cross sections are designated inner and outer rings while radial sections are designated according to their compass direction (East-West, Northwest-Southeast, North-South, and Northeast-Southwest). Additional borings were augered around each site exclusively for the purpose of extending radial cross-sections. Three East-West cross-sections were constructed from three rows of augered borings between the two TPC test sites. The cross-sections from these borings are designated North Medial (Figure A-18), Central Medial (Figure A-19), and, South Medial (Figure A-20).

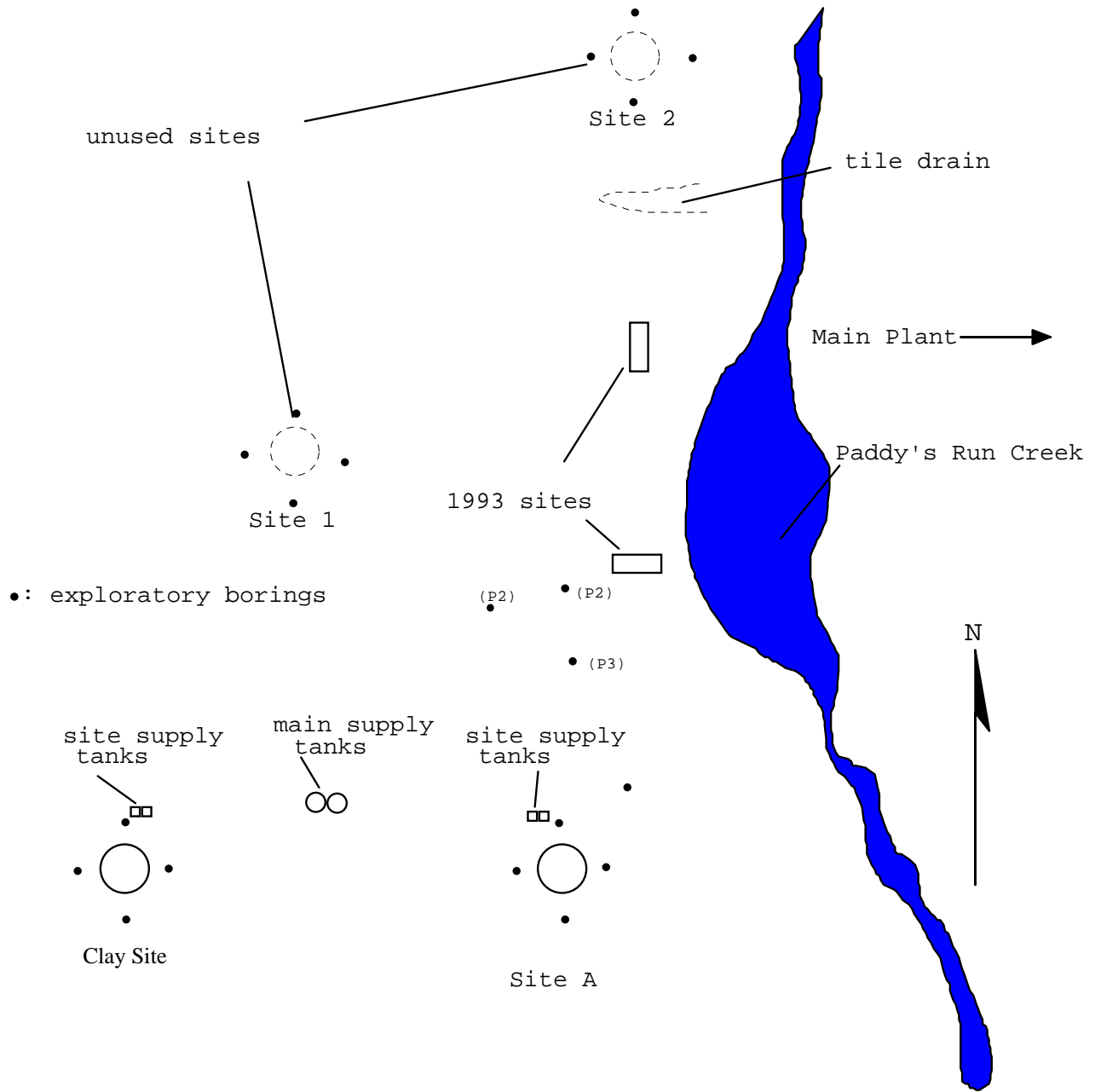


Figure A-3. Location of 1994 Infiltration Stress Tests sites.

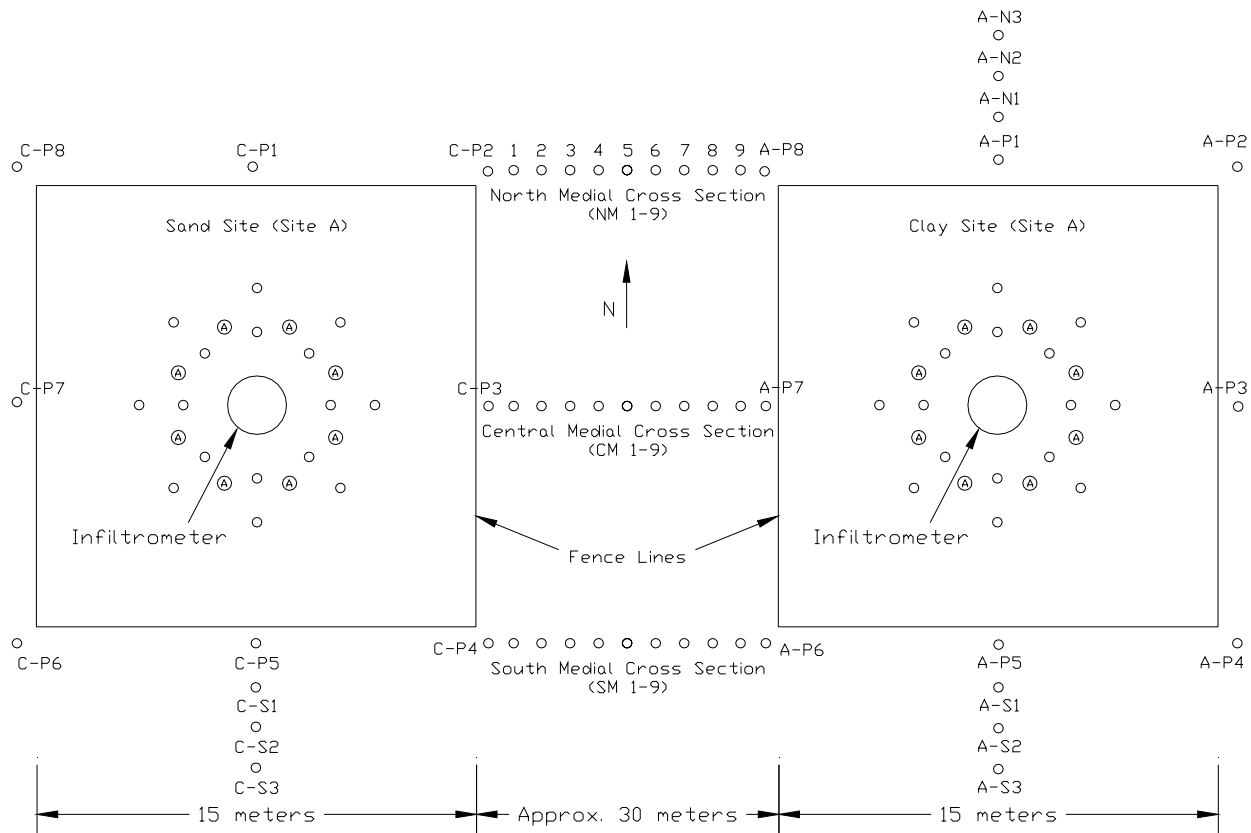


Figure A-4. Plan view of sampling borings.

Other cross-sections were constructed from samples collected from four borings at two other candidate infiltration sites (Figures A-21 and A-22). The four wells at each candidate site were augered 5 m distant from a common center and the wells correspond with the north, south, east, and west borings on the outer ring of Clay and Sand Site. Three other borings, P-1, P-2, and P-3 were augered between the 1993 site and the clay site (Figure A-3). The stratigraphy from these three wells is shown in Figure A-23. The geologic cross-sections associated with the infiltration sites document the contrasting geology of the two infiltration sites as well as the transition between the sites.

Sample Description and Categorization Methods

The cross-sections cited above were derived from tables where each sample description was recorded and the sample assigned a unit number. Because of the similar textures displayed by many samples, other features were used for identifying units. At shallow depths, where weathered clays predominated and original geological features could not be discerned, the Munsell Color System (soil color charts) was used as the primary criteria. At intermediate depths at the clay site and along the medial cross-sections, the Munsell color, bedding pervasiveness and thickness, texture, and soft carbonate nodules aided in identification. Details of this classification system as well as the descriptive tables which summarize the sample descriptions are given next. Using the criteria cited above, eight distinct lithofacies were identified from which the cross-sections were constructed. Subunits were identified in all but the

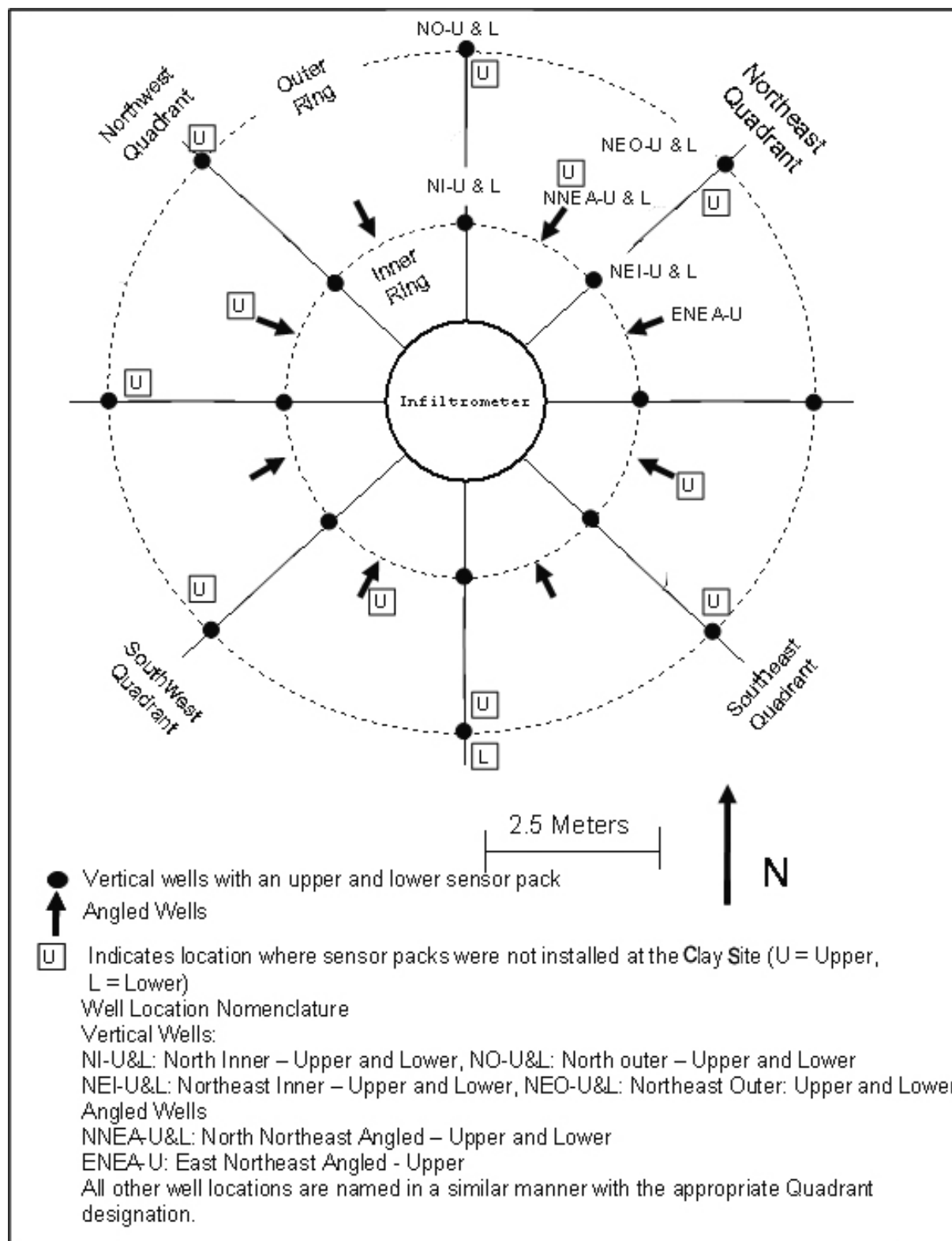


Figure A-5. Location of sampling borings at the Clay and Sand TPC Test sites. The samples were collected during augering of the vertical boreholes in which sensor packs were eventually installed.

deepest lithofacies. All Units and subunits are described in Table A-1 while Table 2 lists abbreviations used in the descriptive tables (Tables 3 - 20). A description of the CS Units is given below beginning with the Clay Site. The geology at the Sand Site as well as the transition between the sites is then contrasted to that of the Clay Site. The field scale geology is then discussed in light of the descriptions at, and between the infiltration sites.

Clay Site Geology

Identification of lithofacies at the clay site was greatly aided by the excavation of the site (Appendix F). The excavation was carried out by alternating excavation with the trackhoe with a backhoe attachment and by hand (Plates 16 through 103). The trackhoe had a long reach so that a 10 m diameter by 4 m deep well could be excavated without impacting the deposits. All aspects of the pit were exposed except one section where a dirt ramp was built for trackhoe access (Plate 87). Seven geologic lithofacies were identified from the excavation and hand augered samples from the Clay Site. Five of the units form a layer cake (Figure A-6), while the sixth (HS Unit 6) forms an anomalous silty sand body in the northwest section of the infiltration site and is present in one sand and gravel channel and several smaller scale stringers. The following seven cross-sectional lithofacies were used to guide construction of the Clay Site cross-sections as discussed above.

Soil and Loess (CS Unit 1, HS Unit 5)

The upper most unit (classified 1A in the description tables) consists of yellowish-brown silty clay (loamy) which in augered samples consisted of very fine to medium (< 20 mm) crumbs. As viewed from the exposures in the pit, the thickness of this unit varied from 15 to 20 cm.

Blocky Structured Silty Clays (CS Unit 2, HS Unit 4)

The next CS Unit consists of 1 to 1.5 m of predominantly blocky silty clays with occasional 1- to 4 cm-thick beds of sands. No primary geologic structure could be discerned in this unit, but the blocky structure was readily observable in pit exposures. Subtle mottles of gold, grays, and greens could be discerned when the samples were viewed closely without a hand lens. When viewed at arms length, the mottles could not be discerned and the color of the sample matched the Munsell soil color charts fairly well. Augered samples typically contained medium to coarse blocks which roughly correspond to the size of blocks observed in the pit exposures. Manganese deposits, which appear as black speckles, are found in many of the augered samples and are probably more common than indicated in the cross-section tables.

Two continuous color bands could be discerned in this lithofacies in the pit exposure: a lighter upper band and slightly darker lower band of approximately equal thickness. Augered samples from the upper band have a Munsell soil color of 10YR hue while the lower have a 2.5Y hue. Both colors were not consistently observed in the augered samples.

Interbedded/Laminated Oxidized Silty Clays (CS Unit 3, HS Unit 3)

The third lithofacies consists of a 2 to 3 m-thick sequence of bedded silty clay. Bedding characteristics in this unit change with depth. In the upper part of this lithofacies, beds 1 to 3 cm-thick and interbedded laminations are apparent, while towards the bottom, the laminations give way to diffuse layering and the beds thicken to 3 to 7 cm. In general, the beds are comprised of light gray, pale brown, pale yellow, to white mottled silty clay containing variable amounts of soft calcium carbonate nodules. In many locations, the fractures as well as bedding

planes are heavily stained with iron oxide and magnesium (Plate 54). Numerous vertical fracture planes connect planer surfaces of the well defined beds.

Bedded Oxidized Silty Clay (CS Unit 4, HS Unit 3)

The next lower cross-sectional unit consists of bedded brown silty clay distinguished from the interbedded deposits of CS Unit 3 by the lack of laminations and thicker beds (generally 4 to 8 cm-thick) with less color variation, and by lack of obvious calcium carbonate nodules. In general, these beds show a slight change in hue from the overlying beds although comparison with the Munsell soil color charts failed to reveal a consistent color change.

Bedded Oxidized to Unoxidized Silty Clays (CS Unit 5 and 6, HS Units 3 and 2)

CS Unit 5 marks the transition to between the overlying “weathered” deposits and the underlying “gray clay.” Samples from CS unit 5 are generally olive brown while those from CS Unit 6 are dark gray to dark grayish brown. These lithofacies are combined because excavation revealed that the transition between the oxidized (as indicated by brown colors) and the unoxidized deposits (gray colors) is gradational.

Both of these lithofacies are bedded to varying degrees, the bedding being defined by thin silt layers (<1mm). Stained partings (iron oxide and manganese oxide) are found in hand samples through out both of these lithofacies. Thin sand and pebble lenses are occasionally encountered in the lower part of this unit.

Sandy Clay to Clayey Sand (CS Unit 7*, HS Unit 6)

Upon excavation, an anomalous sand body was intersected on the northeast sector of the infiltration site (Plates 74, 75, 76, and 87). In general, this lithofacie contains lightly compacted sandy clay and clayey sand. Sandy deposits were found at other locations, but the dark brown color sharply contacts with surrounding lithofacies and the cohesive nature of the matrix is unique. This CS Unit is designated 7* because of its similarity to CS Unit 7 described in other sections below, with the most obvious exception being that CS 7* truncates several other units whereas when CS 7 is present, it consistently appears as a bed below the overlying unit without truncating it.

Clay Site Excavation

Correlation between the cross-sections constructed from samples at the Clay Site (See Cross-Sections and Descriptive Tables) and the geology observed in the pit is good, except in the northeast corner where the anomalous sand body was exhumed during excavation. This sand body forms sharp contacts with the surrounding lithofacies and truncates the Bedded/laminated deposits. It thickens to the north (Plate 87) where the upper contact becomes parallel to the bedding of Unit 3. A stringer from this body extended to the West Outer Lower sensor pack (Plate 77).

Deeper excavation of the central part of the pit revealed extensive areas of stained (presumed to be oxidized gray clay) partings in the gray clay (Plate 103). Non-stained silt-filled partings were also observed. A final excavation in the bottom of the pit in the form of a 2 m deep gouge exposed massive gray clay (Plate 102).

Sand Site Geology

Of the lithofacies found at the Clay Site, only CS Units 1, 2, and 7 were observed in the samples collected from the Sand Site. Here, CS Units 1 and 2 overlaid a large sand and gravel deposit identified as CS Units 7 and 8).

Soil and Loess (CS Unit 1, HS Unit 5)

The top soil encountered at the sand site was also encountered at the clay site. However, the soil and loess at the Sand Site exhibited a slightly darker Munsell hue (10YR versus 2.5YR) than at the clay site.

Blocky-Structured Silty Clay (CS Unit 2, HS Unit 4)

Samples comprising this unit were similar to lithofacies at the Clay Site except that the subtle mottle of gold, grays, and greens were more intense.

Interbedded/Laminated Oxidized Silty Clays (CS Unit 3, HS Unit 3)

The interbedded deposits found at the Clay Site were not readily apparent the Sand Site. However, when calcium carbonate nodules were observed in augered samples, they were classified as CS Unit 3.

Sands and Gravels (CS Unit 7 and 8, HS Unit 6)

These lithofacies are grouped together because they generally grade from silty, sandy, clayey deposits (CS Unit 7) in the upper part to sands and gravels (CS Unit 8) towards the bottom. All samples collected from both of these lithofacies were fully saturated. Samples from these lithofacies were typically monochromatic and matched the indicated Munsell soil color almost exactly. In contrast to the clayey sands of the anomalous sand body at (CS Unit 7*), samples from this unit are much lighter in color and have a much softer consistency.

Sand Site Cross-Sections

As indicated by the inner and outer ring Sand Site Cross-Sections, the infiltrometer was placed directly over a saturated zone with intervening CS Unit 1 and CS Unit 2. CS Units 3, 5, and 6 are missing in all samples taken from the sensor wells except at the C-3 well where CS Unit 3 is present. CS Units 3, 5, and 6 do reappear to the south of the site in the North-South cross-section. CS Unit 3 appears in the two farthest east sampling locations on the East-West Cross-Section (C-3 Outer and C-P3). CS Unit 3 also appears at the southwest corner in the Northeast-Southwest Cross-Section (C-P6).

Comparison of Geology between Sites A and C

In comparing the Sand and Clay Site Cross-Sections, several differences are obvious. First, the blocky structured silty clay deposits of CS Unit 2 are generally thicker at the Sand Site than it is at the Clay Site. Secondly, saturated deposits of sands and gravels were encountered at a fairly shallow depth at the Sand Site, but not at the Clay Site. Finally, several lithofacies identified at the Clay Site are missing at the Sand Site, especially within the inner and outer ring sampling locations.

Medial Cross-Section Geology

The medial cross-sections were constructed from sample borings located approximately 3 m apart (Figure A-4). These cross-sections reveal that saturated deposits of clays, sands, and

gravels (CS Units 7 and 8) are common between the two sites. Less common is the brownish to gray clay at the depths augered. The bedded and laminated clays (CS Unit 3), on the other hand, tend to be present between the infiltration sites while thickly bedded deposits (CS Unit 4) appear to pinch out completely. Also the blocky-structured silty clays of CS Unit 2 appear to maintain an approximate thickness of 0.6 m between the sites.

Field Scale Geology

Inspection of the preliminary test well geology shows that the lithofacies described at the Clay Site may be found up to 50 m north of the infiltration sites in test borings P2 and P3. Farther to the north of the infiltration sites, samples from candidate test sites exhibit the same lithofacies as found at the Sand Site (Figure A-3).

Summary of TPC Test Site Geology

The subsurface at, and between the infiltration sites vary considerably in the upper 3 to 4 m. All lithofacies, except the anomalous sand body at the Clay Site, were observed either at the candidate test sites or the preliminary augering sites. Correlations between the two infiltration sites were made possible with the three cross-sections spanning the distance between them, but correlations on larger scales may be impossible because of strong heterogeneities commonly present in glacial deposits. The variable nature of the deposits at the FEMP is evidenced by outcrops in Paddys Run and by the presence of the anomalous sand body at the Clay Site.

Clay Site: Inner Ring Cross-section

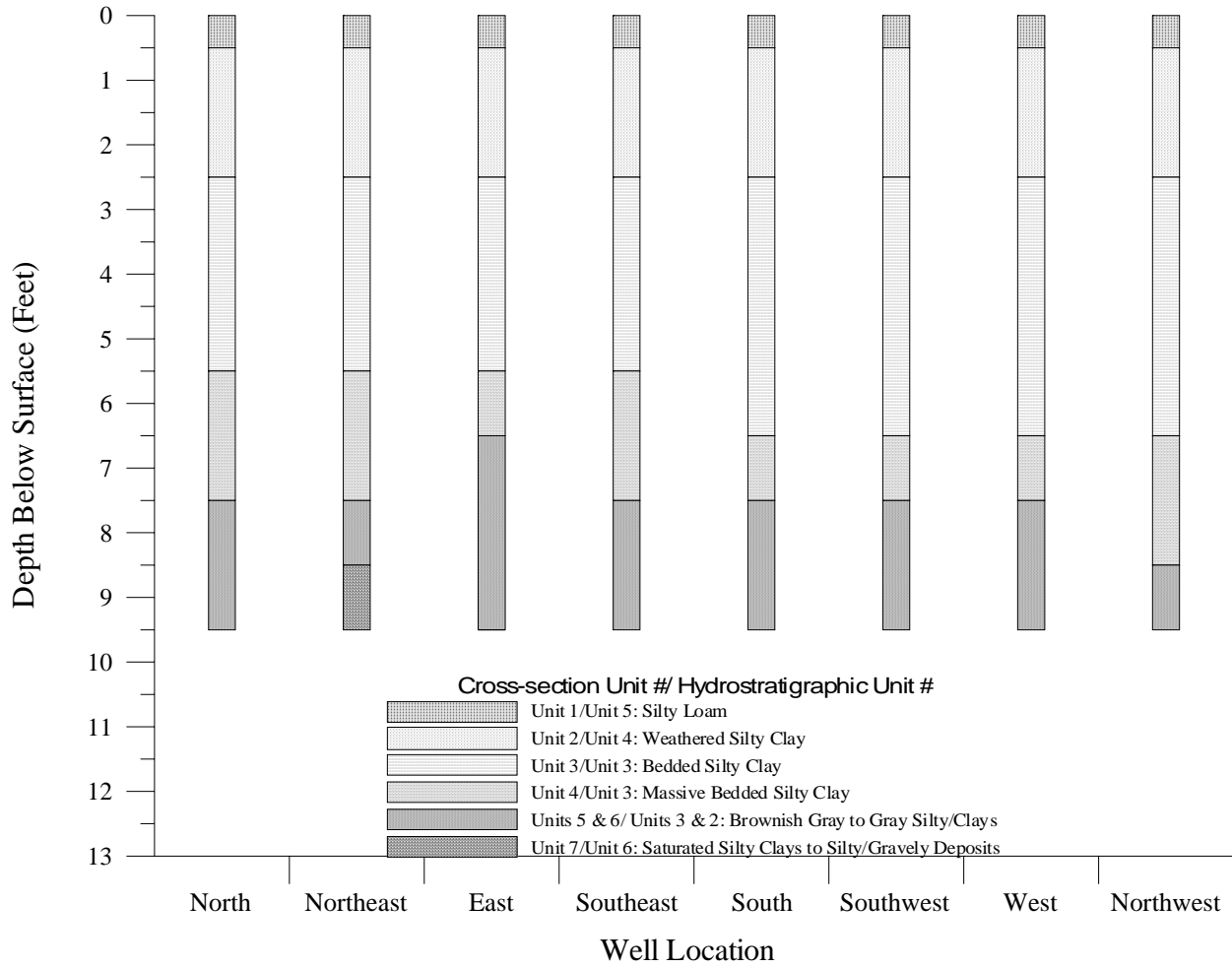


Figure A-6. Clay Site: Inner Ring Cross-section.

Clay Site: Outer Ring Cross-section

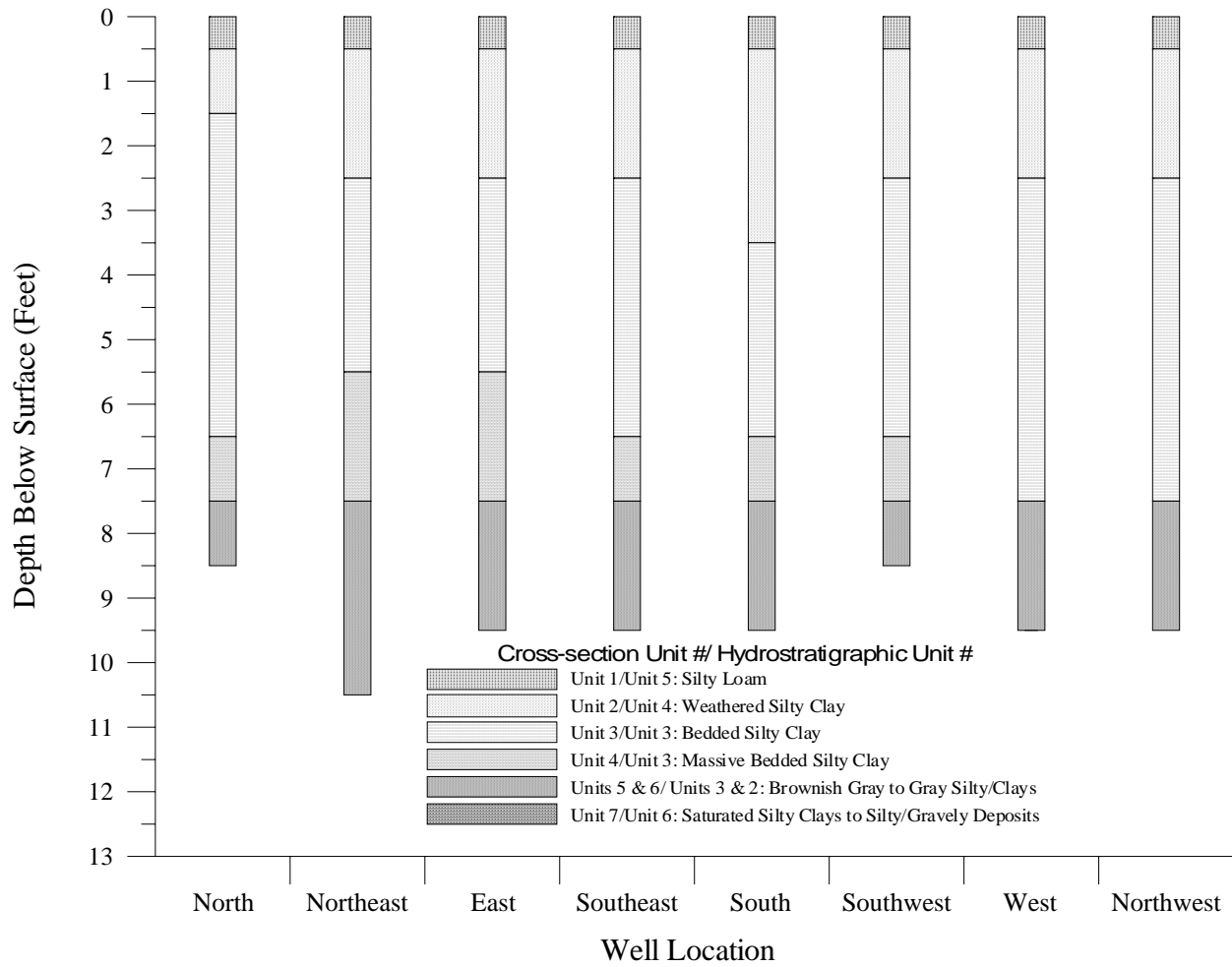


Figure A-7. Clay Site: Outer Ring Cross-section.

Clay Site: North-South Cross-section

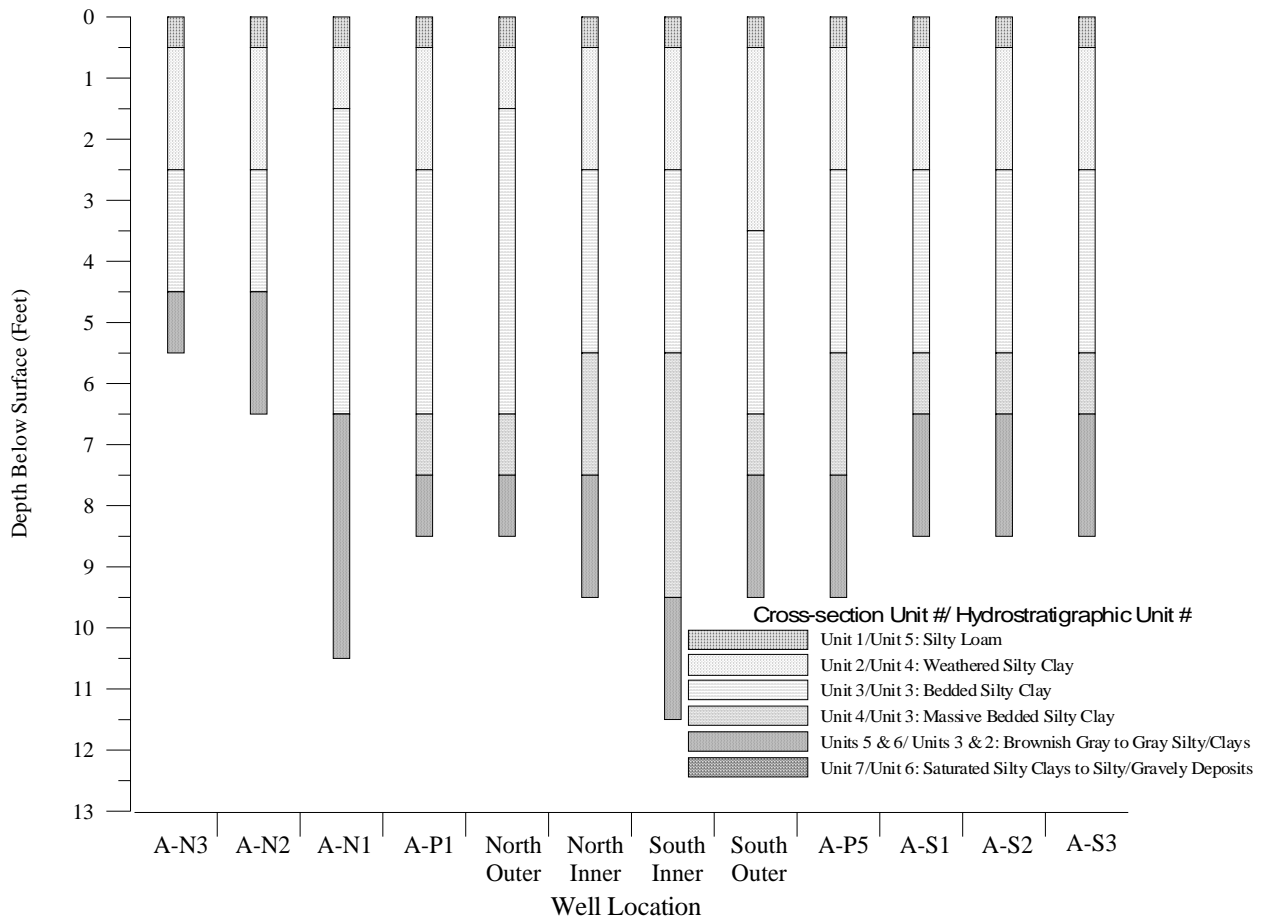


Figure A-8. Clay Site: North-South Cross-section.

Clay Site Northeast-Southwest Cross-section

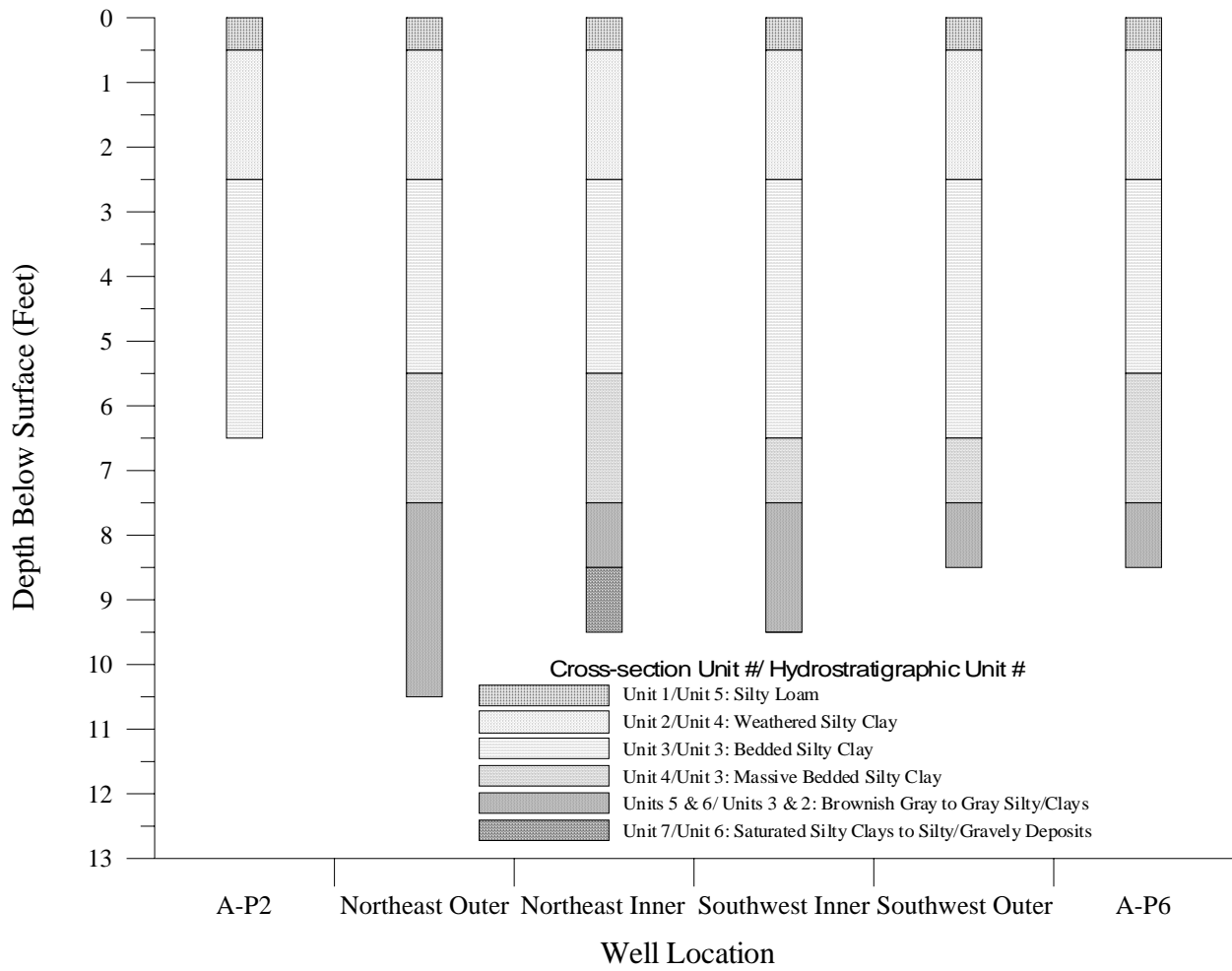


Figure A-9. Clay Site: Northeast-Southwest Cross-section.

Clay Site: East-West Cross-section

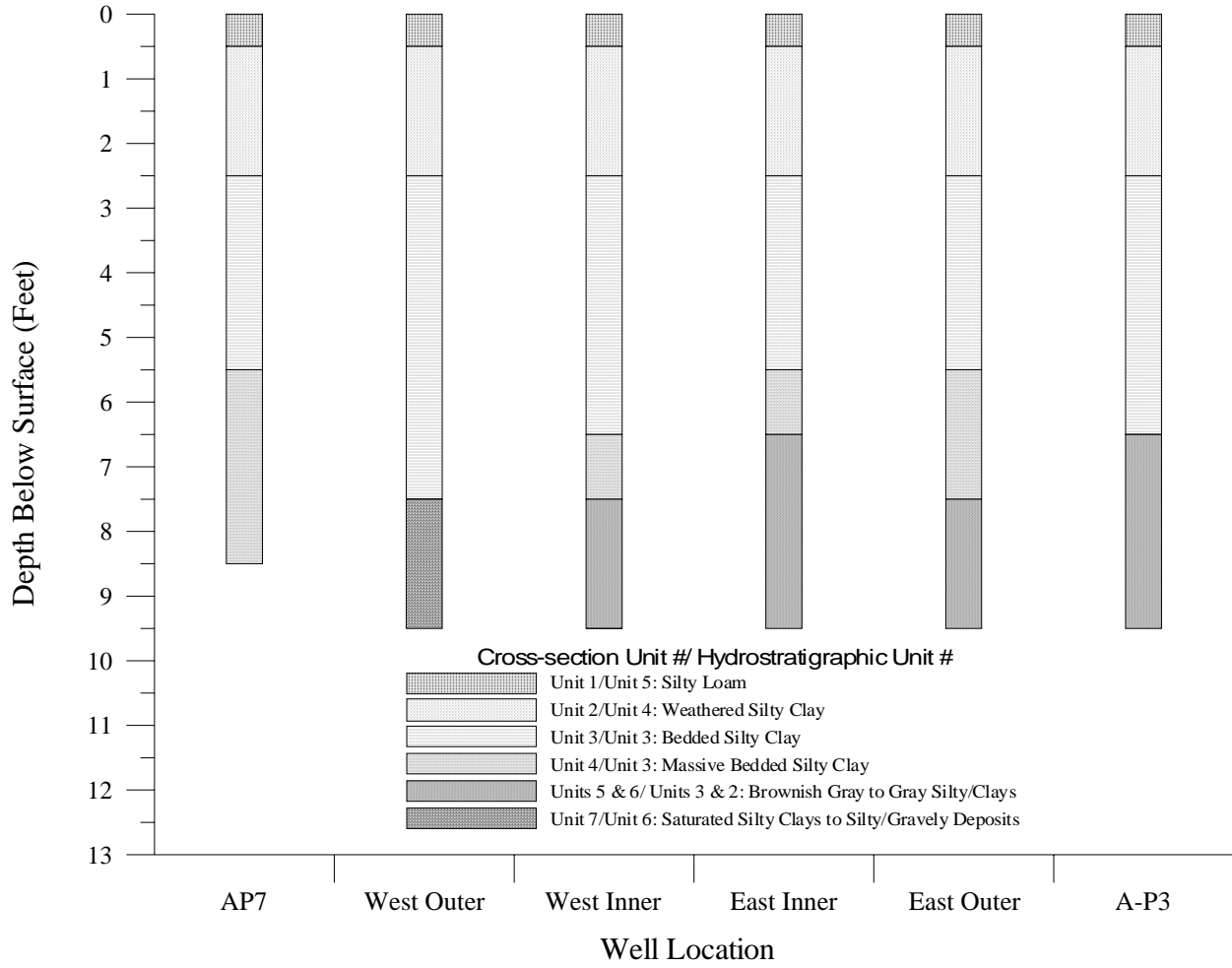


Figure A-10. Clay Site: East-West Cross-section.

Clay Site Northeast-Southwest Cross-section

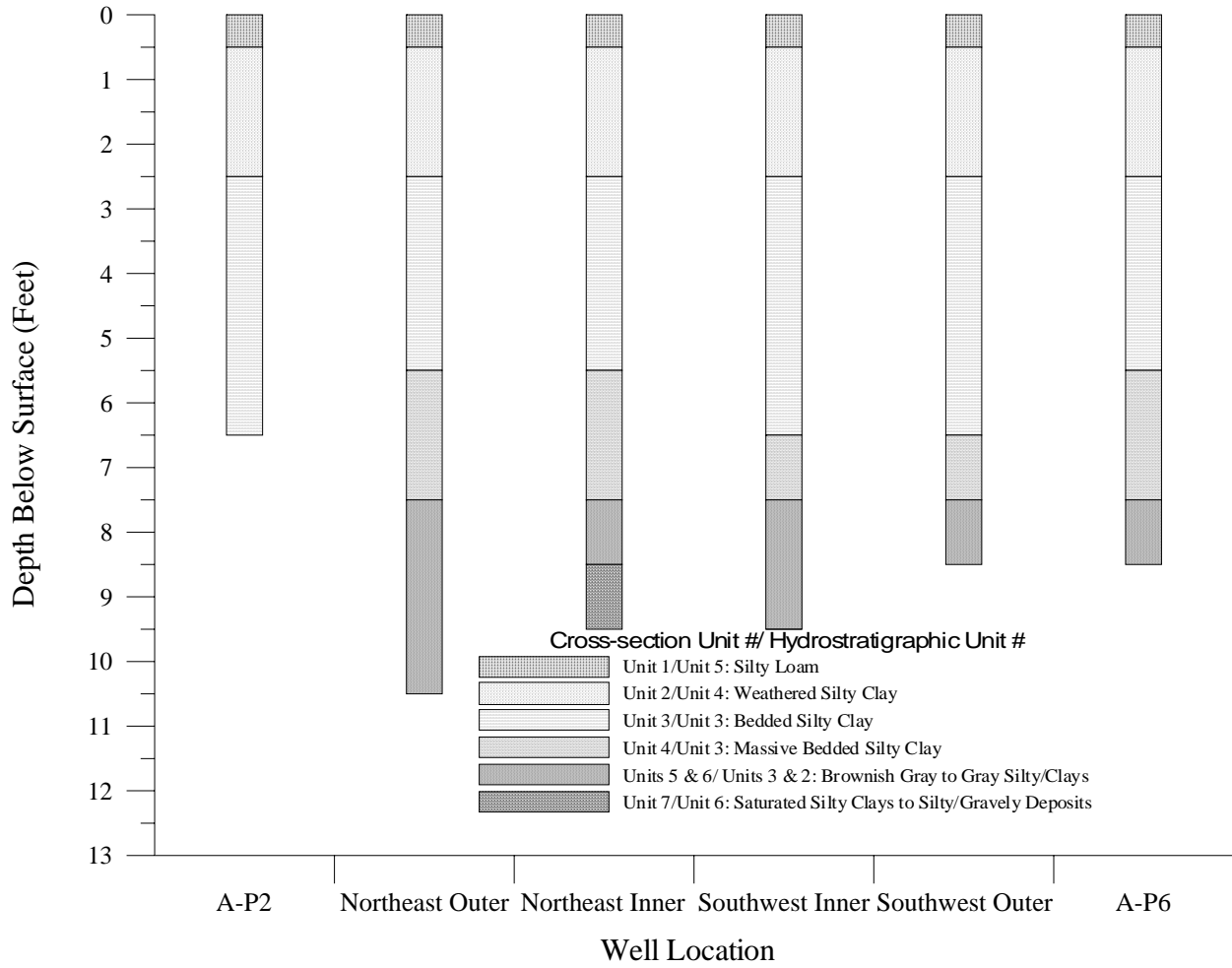


Figure A-11. Clay Site: Northeast-Southwest Cross-section.

Sand Site: Inner Ring Cross-section

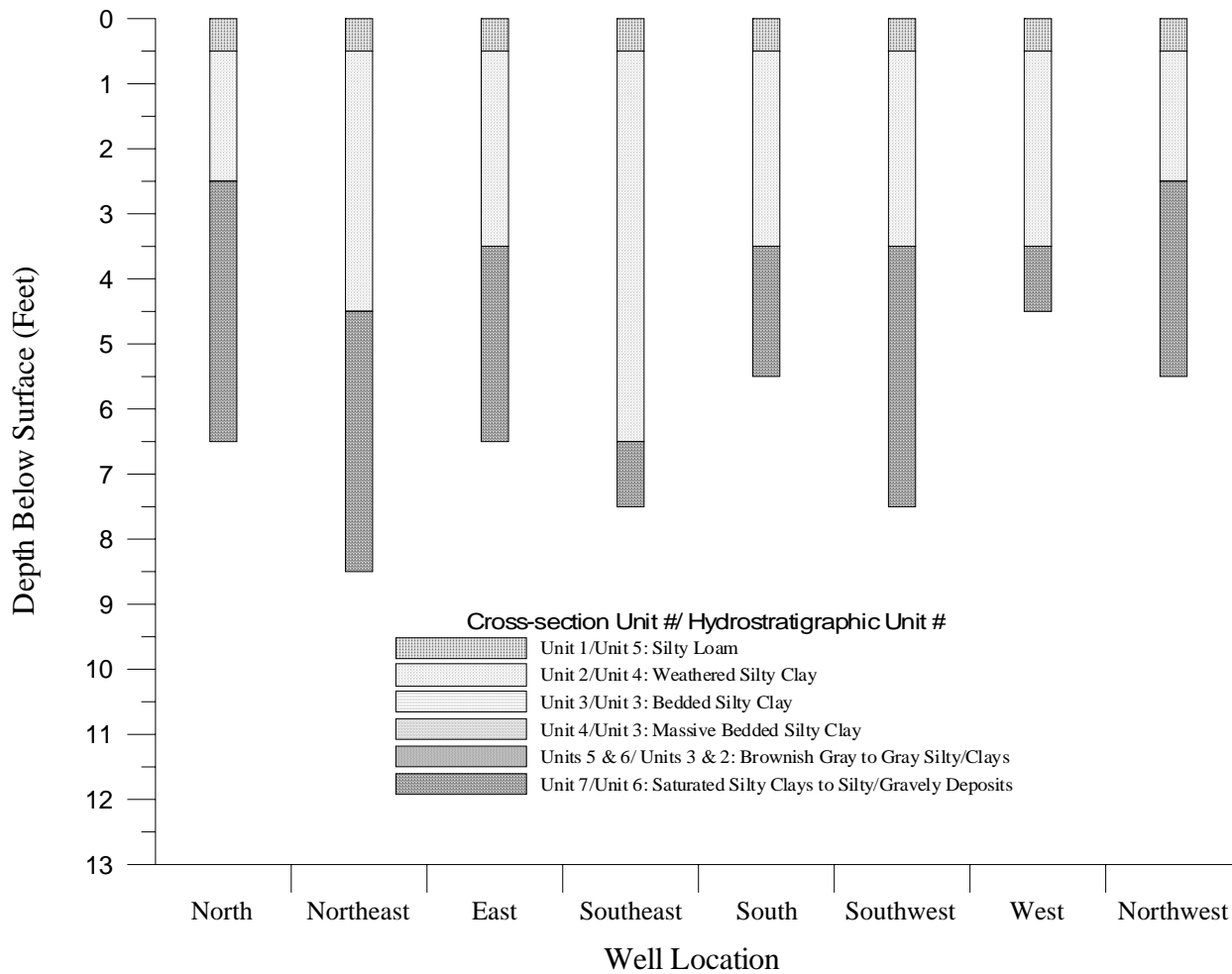


Figure A-12. Sand Site: Inner Ring Cross-section.

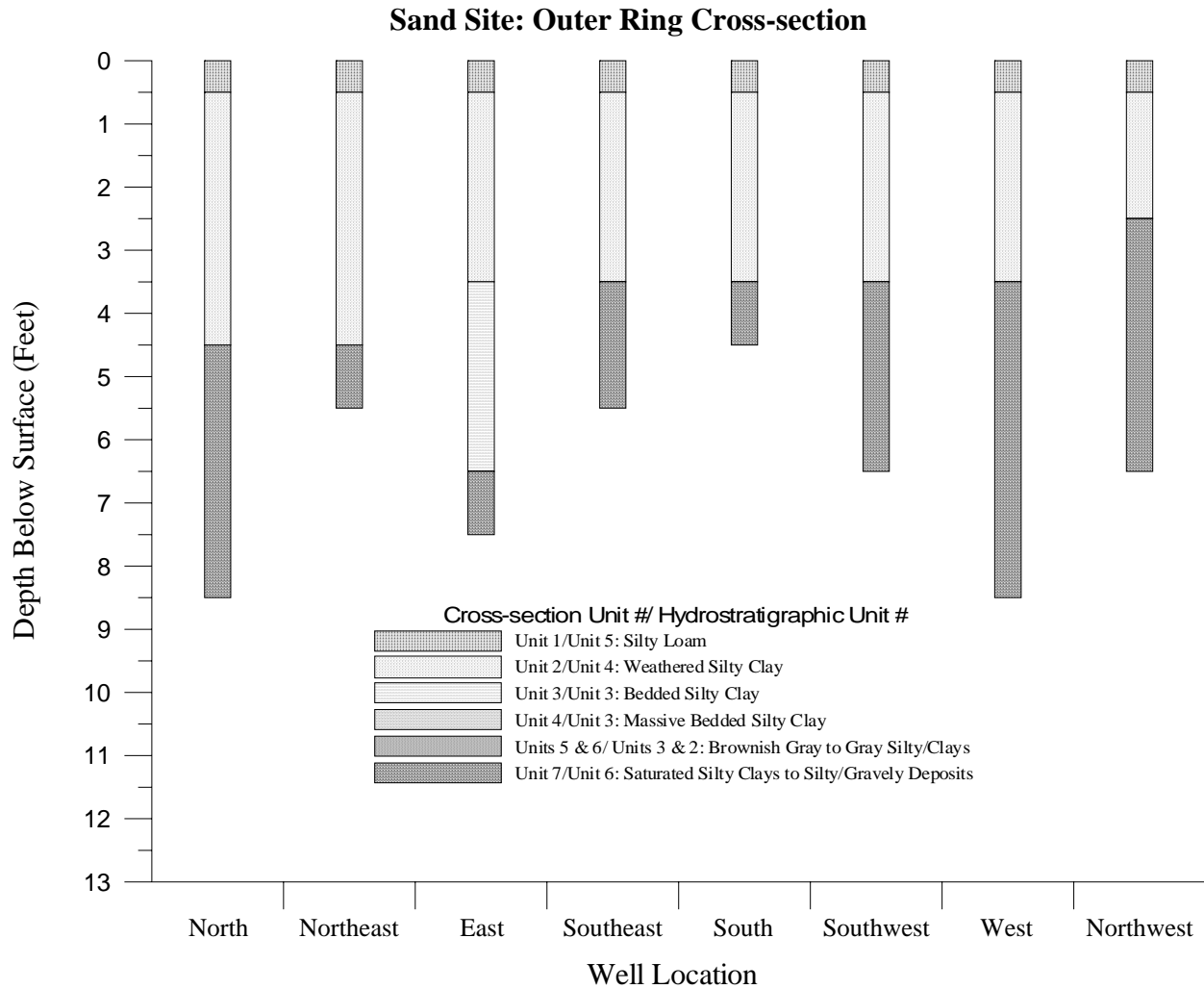


Figure A-13. Sand Site: Outer Ring Cross-section.

Sand Site: North South Cross-section

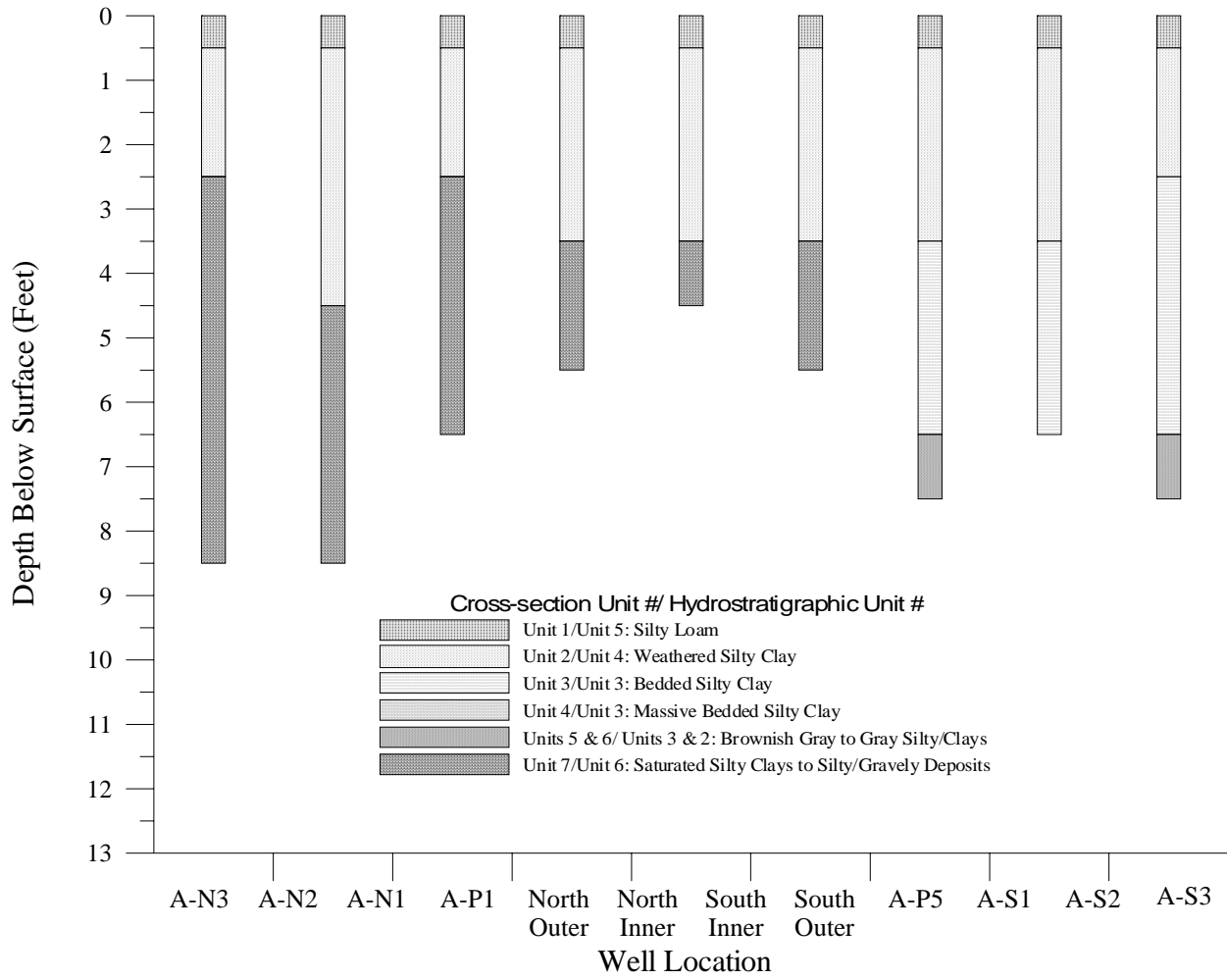


Figure A-14. Sand Site: North South Cross-section.

Sand Site: Northwest-Southeast Cross-section

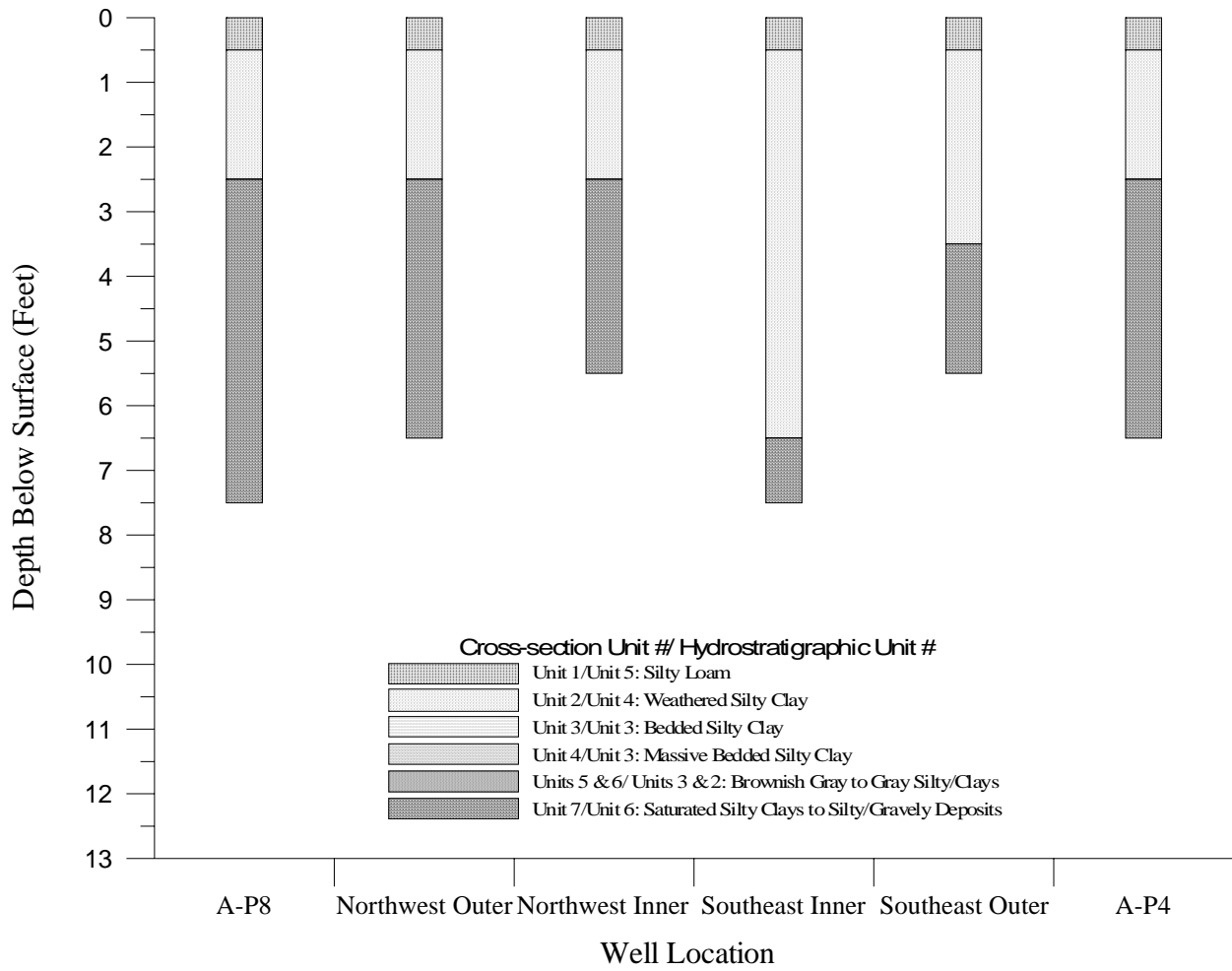


Figure A-15. Sand Site: Northwest-Southeast Cross-section.

Sand Site: East-West Cross-section

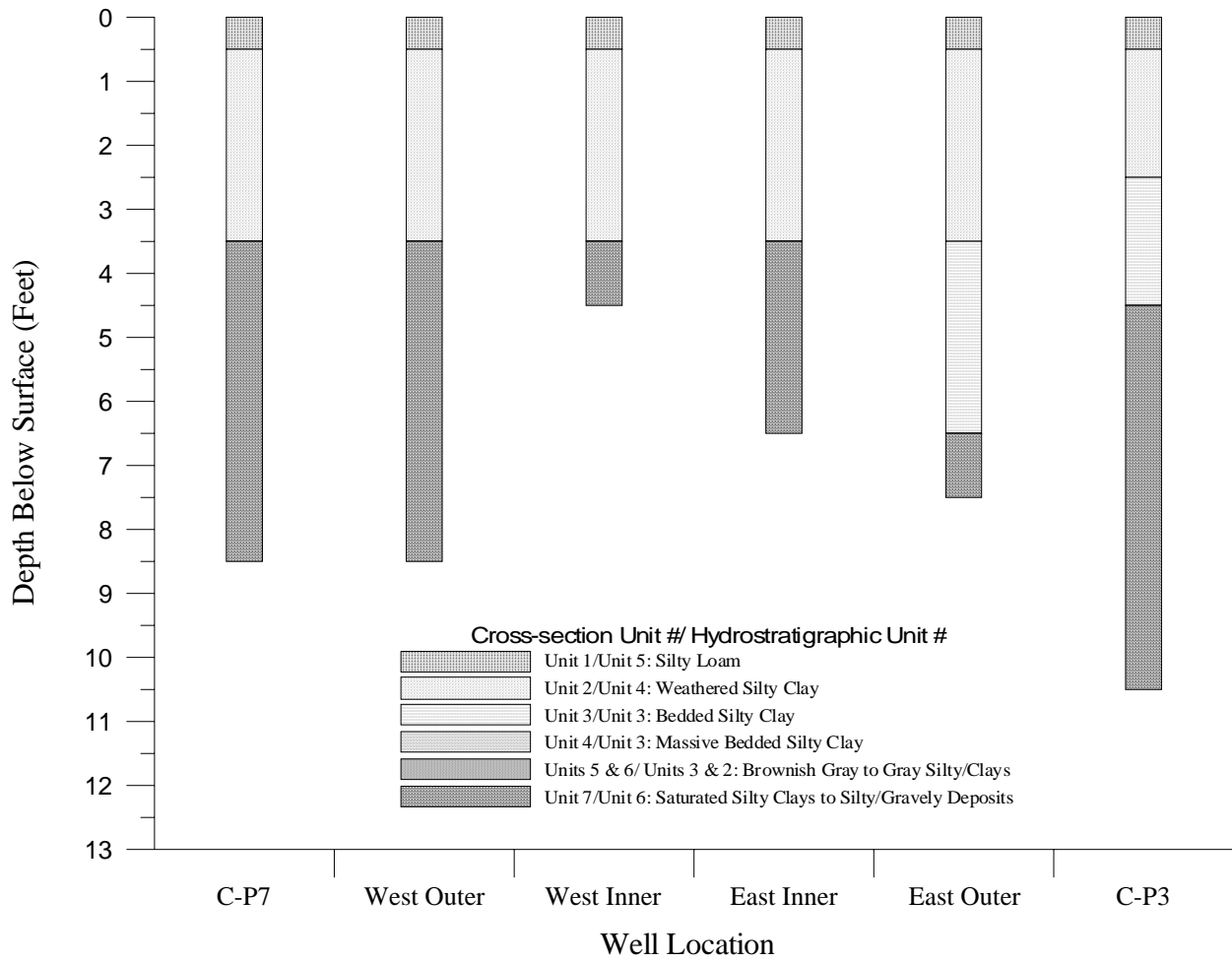


Figure A-16. Sand Site: East-West Cross-section.

Sand Site: Northeast-Southwest Cross-section

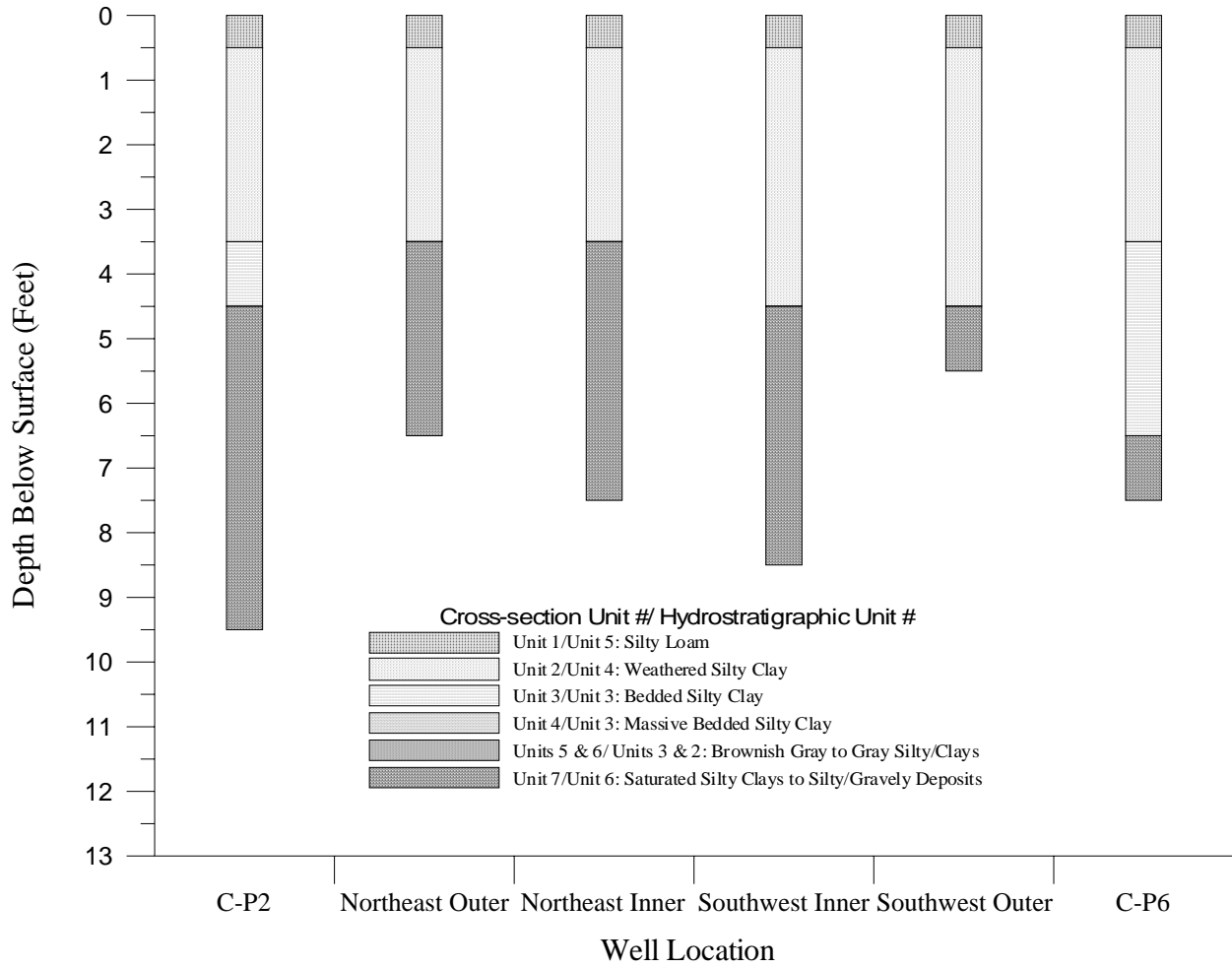


Figure A-17. Sand Site: Northeast-Southwest Cross-section.

North Medial Cross-section

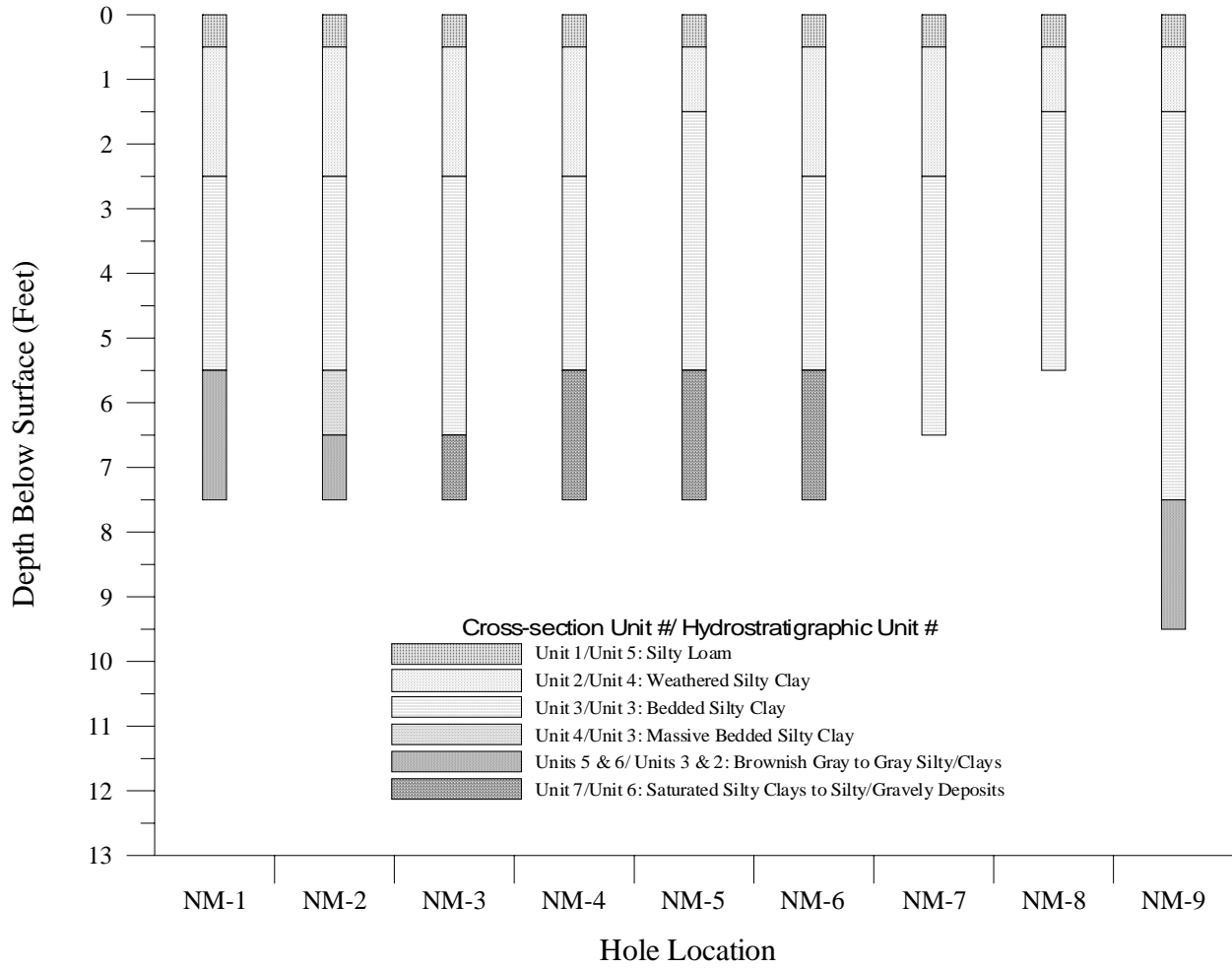


Figure A-18. North Medial Cross-section.

Central Medial Cross-section

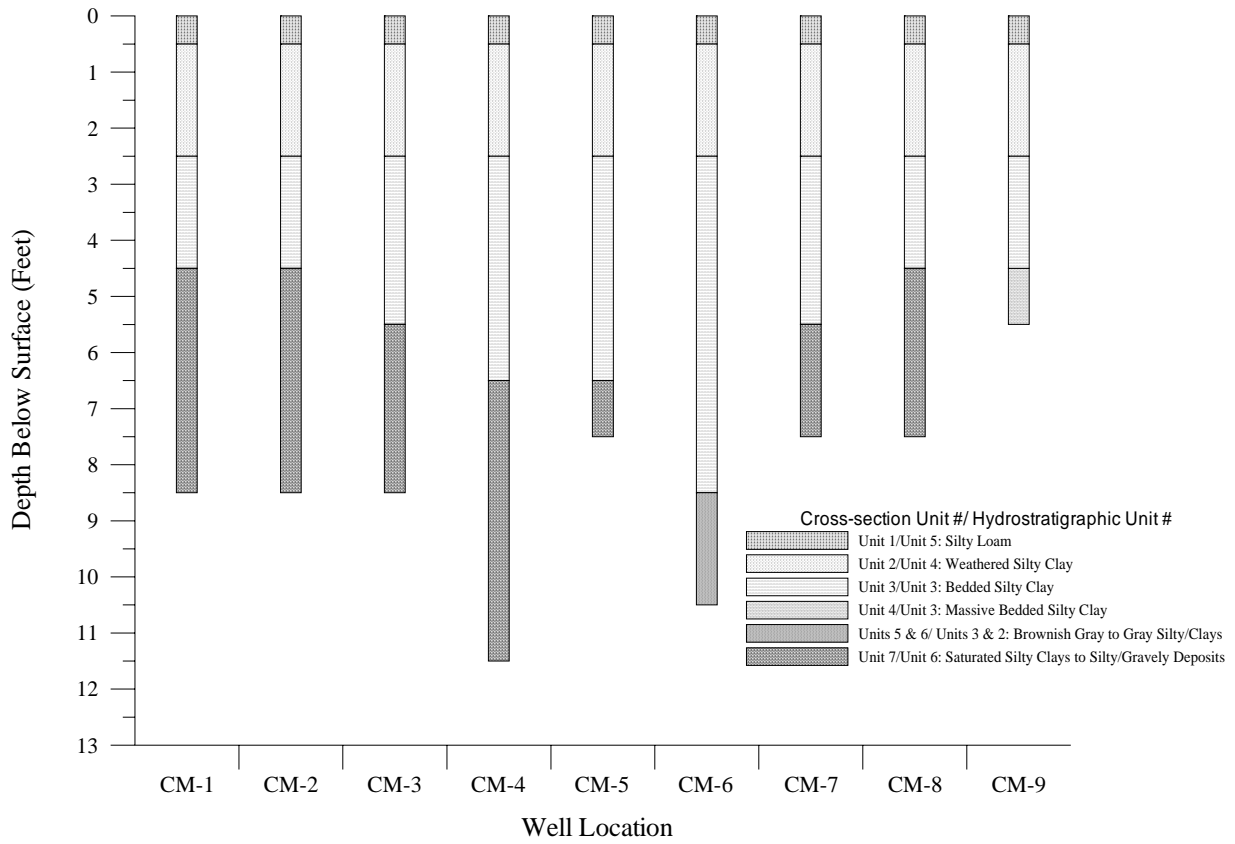


Figure A-19. Central Medial Cross-section.

South Medial Cross-section

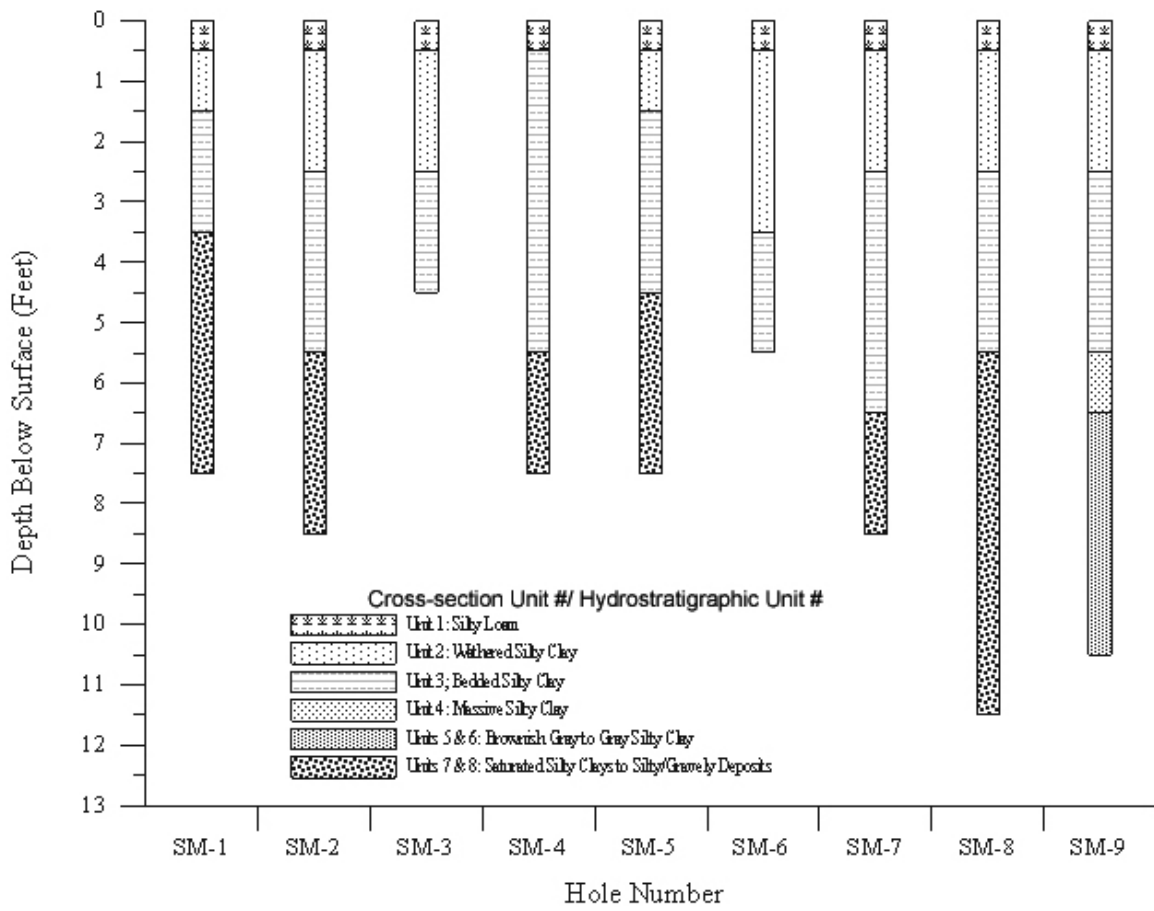


Figure A-20. South Medial Cross-section.

Test Site 1 Outer Ring Cross-section

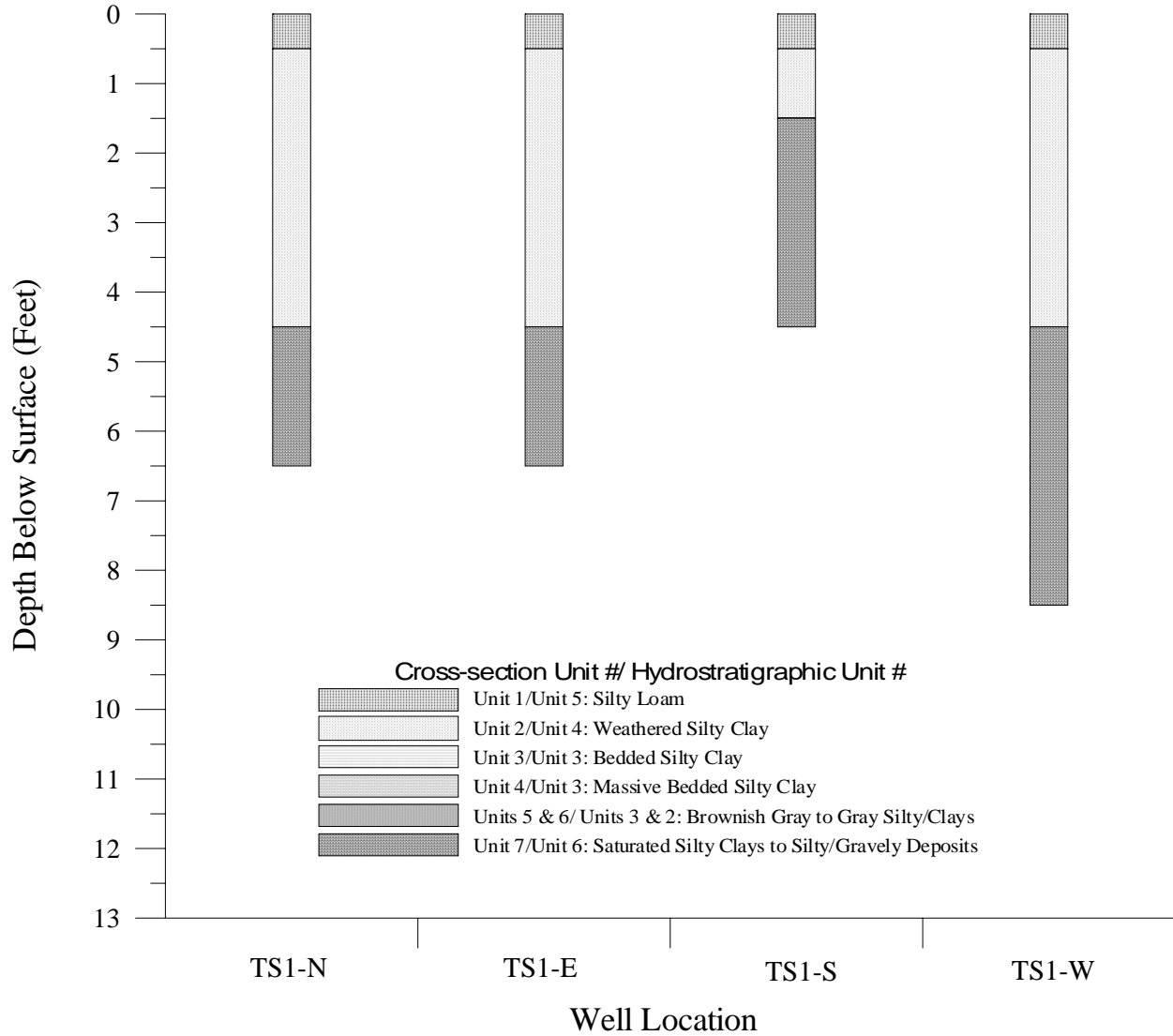


Figure A-21. Test Site 1 Outer Ring Cross-section.

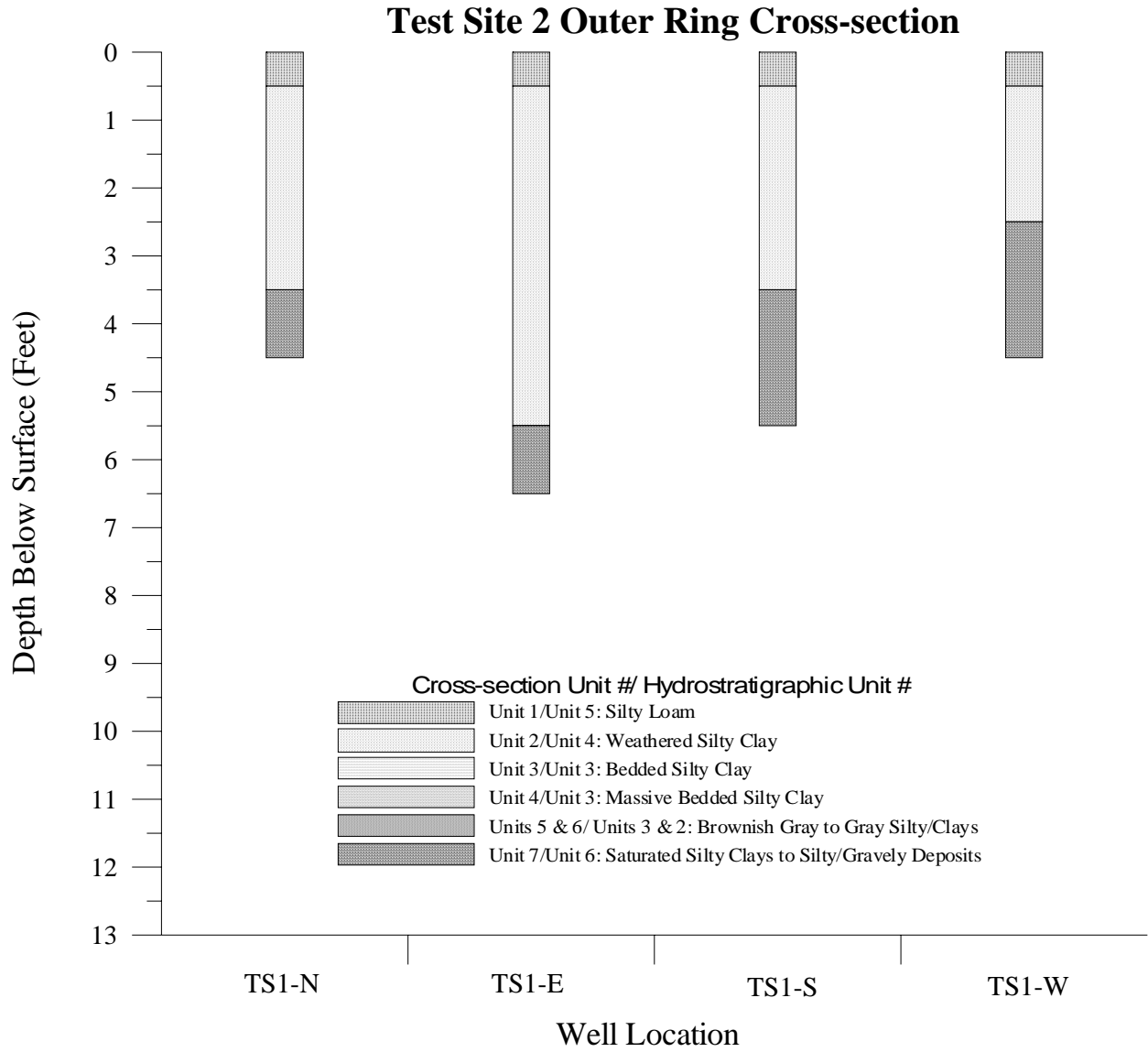


Figure A-22. Test Site 2 Outer Ring Cross-section.

Preliminary Test Holes

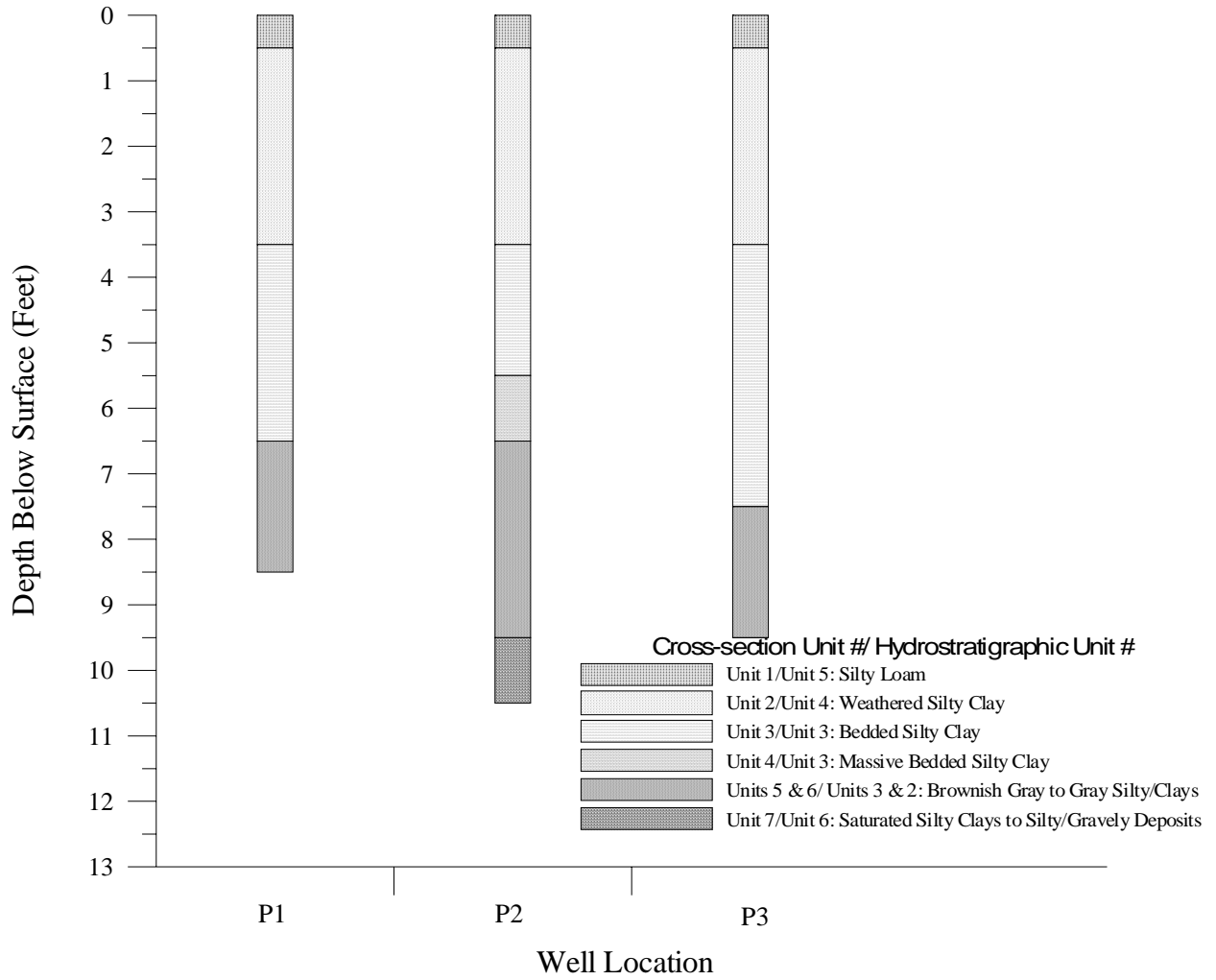


Figure A-23. Preliminary Test Holes.

Appendix B. Infiltration

<u>Section</u>	<u>Page</u>
B.1 Infiltrimeters and Water Supply	78
B.2 Infiltration Initiation and Maintenance	79
B.3 Infiltration Monitoring and Calculation of Infiltration Rate	79
B.4 Results	79

B.1 Infiltrometers and Water Supply

Both of the infiltration sites utilized a 2.2 m diameter single ring infiltrometer (Figure B-1) to infiltrate ponded water onto a non-disturbed surface. The ponded depth was kept at a constant 5 cm level by a manifold of four float valves supplied by two 500-gallon infiltrometer supply tanks (See Appendix G, Plates 1,2,10, 11, 12). The infiltrometer supply tanks were refilled as needed from two 2500-gallon main supply tanks. Water was delivered by truck to fill the main supply tanks. Ametec brand model PSCL-SI, 20 micron filters were used to filter particulates from the water supply as water was fed from the main tanks to the infiltrometer tanks (Plate 3).

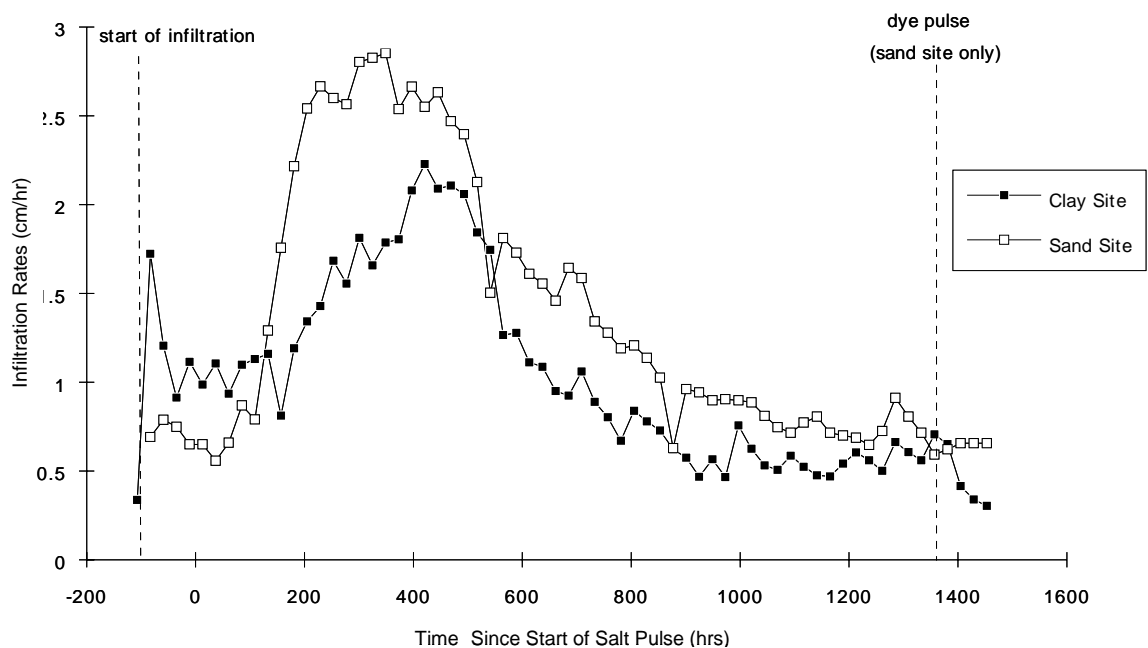


Figure B-1. Infiltration rates at the Clay and Sand Site.

The infiltrometers were constructed of three sheets of polyethylene fastened end to end to form a ring 2.2 m in diameter and 40.3 cm high. Gaskets and silicone sealer prevented leakage at joints. To form a seal between the infiltrometer ring and the soil, a circular trench approximately 10 cm deep and 5 cm wide was filled with granular bentonite. The infiltrometer ring was set into the bentonite seal. The bentonite around the inside edge of the infiltrometer was covered with sand to prevent contamination of the soil surface inside the infiltrometer by expanding bentonite. Four Ryan Herco rinse tank float valves plumbed to the site supply tanks maintained a constant ponded height of 5 cm above the infiltration surface (Plates 11, 12) observed across this seal at any time during infiltration.

B.2 Infiltration Initiation and Maintenance

Infiltration was initiated June 15, 1994 at 1415 hours by pouring four 133-liter containers of water into the infiltrometers and simultaneously opening the water supply valves, yielding an initial and essentially instantaneous ponded head of 5 cm. The undisturbed soil surface was protected from scouring by placing splash deflectors under the flow valves and the areas where the large containers were emptied into the infiltrometer. These deflectors were removed after initial filling of the infiltrometer. Infiltration was not interrupted until the terminated at both tests on August 20 1994 at 1130 hrs.

B.3 Infiltration Monitoring and Calculation of Infiltration Rate

Two pressure transducers in the bottom of the infiltrometer supply tanks provided mV readings every 15 minutes for the duration of infiltration. The mV readings were converted to height of water above the transducer and provided the means to track infiltration rates. See Appendix E for a discussion of transducer calibration procedures. Cumulative flow over time was calculated by multiplying the drop in water height by the cross-sectional area of the tanks and summing the results. To simplify flow calculations, the tanks were never filled beyond the height of the constant rectangular horizontal cross-sectional area of the tanks (approximately 385 gallons). Volume changes over known time intervals were used to calculate the flux through the infiltrometer in centimeters of water.

B.4 Results

Infiltration rates are plotted versus time for both the Clay and Sand Sites Figure B-1. The two sites produced similar trends in the infiltration rates in that an initial rise was followed by a drop which was then followed by a very significant rise and asymptotic decline to steady flow. The Sand Site initially experienced a lower infiltration rate than the Clay Site, but after introduction of the Cl^- tracer pulse, the rate at the Sand Site exceeded that at the Clay Site and maintained a slightly higher level until after almost 1300 hours of infiltration when a long time steady state had been reached.

The maximum daily average infiltration rate at Clay Site was 2.2 cm/hr which occurred approximately 570 hours after the start of infiltration (430 hours after the start of the Cl^- tracer pulse) followed by the drop approaching a steady flow of 0.7 cm/hr. During the dye pulse, the infiltration rate at Clay Site again experienced a significant decline to approximately 0.5 cm/hr (Figure B-1). The maximum daily average infiltration rate for the Sand Site was 2.8 cm/hr which was reached approximately 514 hours after the beginning of infiltration (350 hours after initiation of the Cl^- tracer pulse). The steady flux at the Sand Site also approached 0.7 cm/hr. Both the initial rise and subsequent decline occurred sooner at the Sand Site than at Clay Site.

This pattern of rapid initial rise followed by a sharp decline, renewed rise and final steady decline may be controlled by several mechanisms including impacts of water quality, clay swelling and shrinking, or growth and decay of algae. Other researchers have observed similar patterns (See Muckel, 1959, Figure 18). Muckel (1959) attributed the second rise in infiltration rate to the displacement of entrained air followed by a steady decline in rate due to biological and chemical activity constricting pores. Such mechanisms probably occurred in these

infiltration experiments as well, however there is only evidence suggesting that algae die-off and re-growth caused the major rise and drop in infiltration rates. This evidence is based on observations of significant algae growth that occurred in the water supply tanks (translucent HDPE) as well as in the infiltrimeters. Water temperatures measured as high as 95 F certainly enhanced algae growth and it is likely that growth of algae within the near surface macro pores resulted in decreasing infiltration rates after 400 hours (Figure B1), whereas the post salt pulse rise in infiltration rates (0 hrs to 400 hrs) may have resulted from dieing off of algae due to high salt concentrations.

A striking similarity in trends between the infiltration rates and total pressure head as measured with transducer equipped tensiometers indicates a cause and effect relationship between formation water pressures and infiltration rate. See Appendix E for a discussion of the measured subsurface water pressure.

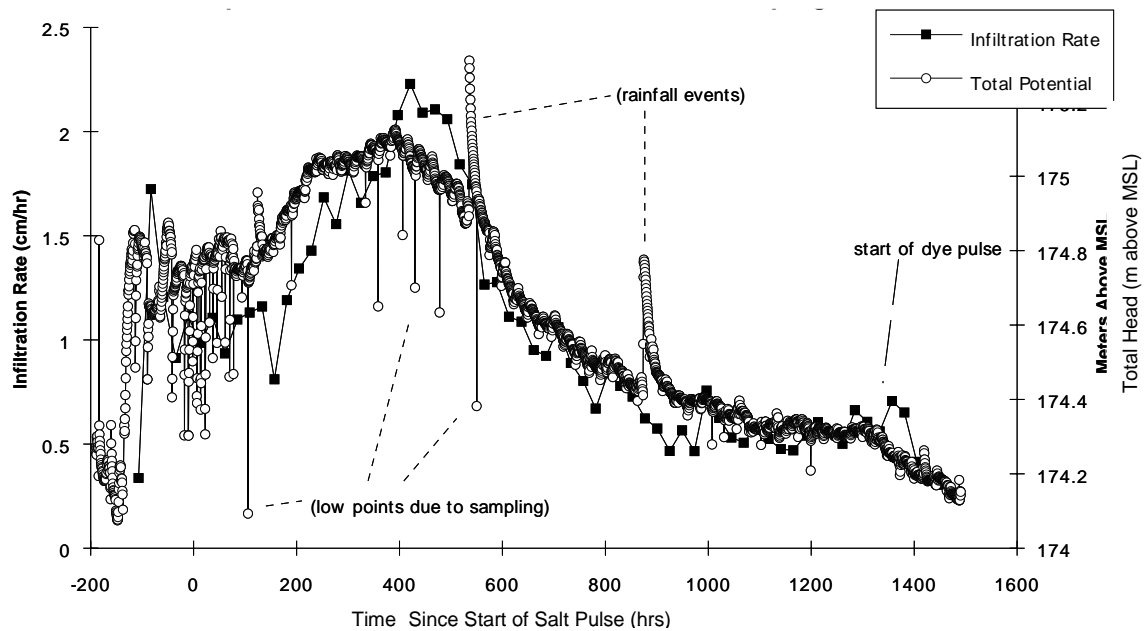


Figure B-2. Correspondence of trends between infiltration rate and changes in total head at the North Inner Upper sensor pack.

A sharp decline in the infiltration rate was also observed during the dye pulse at the Clay Site beginning about 1400 hours after the salt pulse (Figure B-1). The dye pulse was implemented by introducing a 4 liter container of a thick slurry of dissolved dye powder into the infiltrimeter supply tanks and it is very likely that the resulting high concentration of dye clogged near surface pores (Plate 19) causing a reduction in infiltration rates.

The worst-case scenario for flow and transport at the FEMP is that it occurs under saturated conditions. Saturated conditions apparently occur during the early spring months. Observations that support this statement includes seeps in Paddys Run during the spring months that disappear

as the summer progresses and standing water in wells augered for instrumentation at both the Sand and Clay Sites. Because the steady state infiltration rate gives a rough estimate of saturated hydraulic conductivity for very near surface deposits, comparing infiltration rates to published hydraulic values can yield some useful information.

According to Freeze and Cherry (1979) the range of saturated hydraulic conductivity commonly accepted for sands is 10^{-4} to 1 cm/s, for silty sand 10^{-5} to 10^{-3} cm/s, for silt and loess 10^{-7} to 10^{-5} cm/s, for glacial till 10^{-12} to 10^{-5} cm/s, and for unweathered clay 10^{-13} to 10^{-9} cm/s. The maximum infiltration rates experienced at the Sand Site exceed the conductivities of these published values by two to four orders of magnitude while at the Clay Site infiltration rates exceed the expected conductivity by two to eight orders of magnitude. Based on this information alone, it is apparent that water flow in the near surface deposits is through macropores and fractures rather than through the matrix.

This page intentionally left blank.

Appendix C. Sensor Design and Array

<u>Section</u>	<u>Page</u>
C.1 Sensor Array Design	84
C.2 Sensor Construction	85
C.3 Sensor Installation	85

C.1 Sensor Array Design

The preliminary study during the summer of 1993 (Brainard et al., 2005) and the results of exploratory investigations during 1994 demonstrated that the oxidized tills at the FEMP are capable of significant groundwater flow through macropores such as fractures, worm borings, and root casts. In designing the sensor packs, a primary concern was choosing a measurement scale that would maximize the likelihood of obtaining meaningful data given the size and spatial distribution of the macropores. That is, if the scale of the measurement volume is large relative to the spatial distribution of the macropores, then the measurement may be an integration of impacts from several intersecting macropores. On the other hand, if the measurement volume is small relative to the spatial distribution of macro pores, then intersections with single macropores might be missed and the measurement would not, again, capture potentially important information. In designing the sensor packs, we decided to increase the likelihood of intersecting macropores by the sensor packs by combining all sensors into one sensor pack. This increased the sensor pack size significantly which certainly reduced the sensitivity of the sensors to small scale features that may impact the flow field, but yet maximize the probability of intersecting larger, yet important features. Additionally, a large number of sensor packs (44 at the Clay Site, 32 at the Sand Site) within a fairly limited volume (10 m diameter by 3 m deep), once again increased the likelihood of intersecting macropores with the sensor packs. Several angled wells placed sensor directly under the infiltrometer increasing the likelihood of having water and tracers infiltrated through the infiltrometer reach at least some of the sensor packs. Another reason for installing multiple sensors in a single pack includes the ability to compare data from different sensor types exposed to the same sampling environment. Comparison between TDR measured Cl^- concentrations with those from suction samplers were important due to this somewhat unique and promising application of TDR technology.

Each sensor pack contained a tensiometer (Figure C-1), a Time Domain Reflectometry (TDR) probe (Figure C-1), and solution and colloid water samplers (Figure C-2). All sensors were situated in close proximity to each other, -within a 50 cm in the vertical dimension of the 10 cm diameter well (Figure C-3). To provide a permeable media for tracer transport from the formation to the sensors, the sensor packs were backfilled with equal volumes of #8 fine sand and #4 filter pack sand. Where two sensor packs were installed in the same well, a plug of bentonite was placed between the packs to prevent intra-well flow between the two sensor packs. In all cases the wells were backfilled to the ground surface with bentonite. Figure C-4 is a schematic cross-section through the center of the Clay Site depicting both vertical and angled installation of sensor packs. Plan-view maps with location identifiers for each of the sensor packs at the Clay and Sand Site are presented in Figure C-5.

The colloid and suction samplers allowed collection of soil water samples for laboratory analysis of tracer concentration while the TDR probes allowed in situ measurement of tracer concentrations. Tensiometers are typically used to measure negative water pressures (pressures lower than atmospheric pressure or the air pressure within the porous media) under unsaturated conditions. Here we were able to measure positive pressures resulting from saturated conditions at the sensor packs.

C.2 Sensor Construction

Colloid and suction sampler samplers were constructed at Sandia National Laboratory personnel from PVC pipe, acrylic and PVC tubing, polyethylene filters, and solute resistant 1 bar 653X02-B1M3 Soil Moisture Equipment ceramic cups (Figure C-2).

Tensiometers were constructed of 1/2" Schedule 80 PVC pipe, 1/2" polycarbonate sight glass and Soil Measurement Systems rubber septums, Soil Moisture Equipment 655X01B1M1 ceramic porous cups, and Micro Switch PC126 differential transducers incased in epoxy. The site tubes, auxiliary valves and pressure transducers were glued into schedule 40 PVC pipe "tees" (Figure C-1)

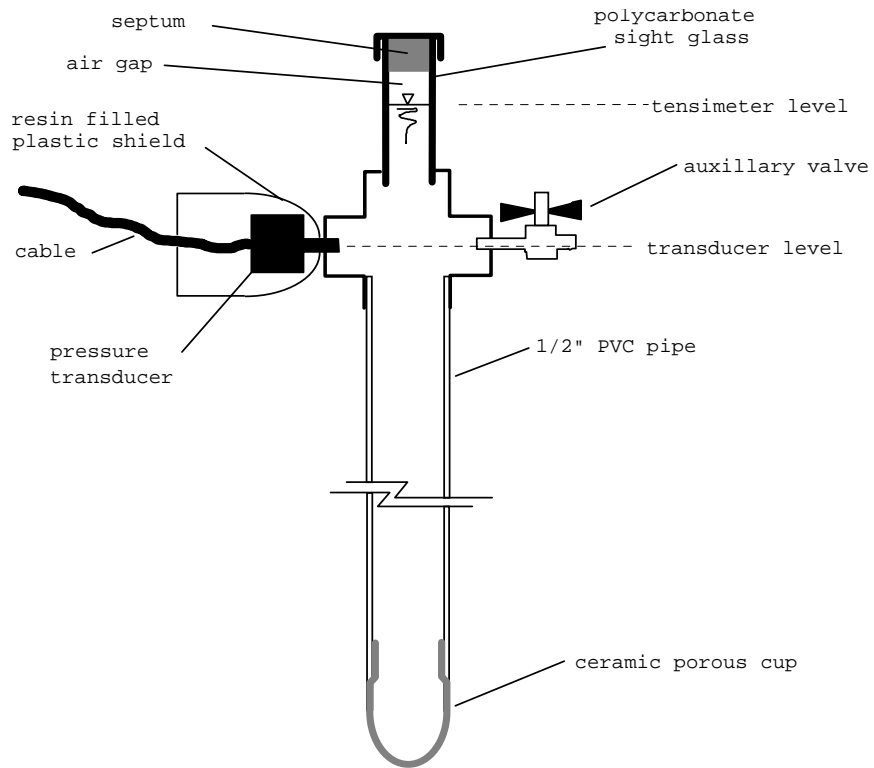
The tensiometer sight glass allowed for checking water levels in the tensiometers and to check for malfunctioning tensiometers. Tensiometers were filled by removing the sight glass septum. The tensiometers experienced a high rate of failure due to air leaks. A simpler design with fewer connections would have decreased the likelihood for leaks.

The TDR probes used were three prong models with 5/16"× 6" stainless steel prongs (waveguides) in 2"× 3"×4" polycarbonate blocks (Figure C-1). Signal transmission between the TDR unit data acquisition system and the TDR probe was over Alpha brand RG58-A low noise coaxial cable. The relatively short and thick prongs were chosen to minimize reflective signal loss due to the electrical conductivity of the clays and saline tracer.

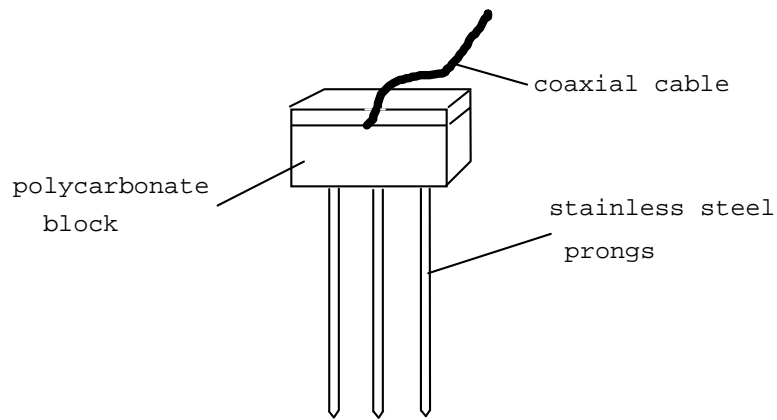
C.3 Sensor Installation

Sampling station locations for each site were located and flagged on the surface. Initial borings were made with 2" hand augers to provide samples for geologic interpretation and analysis. Wells were then enlarged to 4" with either a "Little Beaver" gasoline engine powered hydraulic continuous flight auger, or 4" bucket hand augers. The "Little Beaver" auger caused a significant layer of cuttings (skin) to adhere to the well walls, especially where standing water or saturated materials were encountered. This skin was removed by scraping with wire brushes and re-boring with four inch hand augers.

After completion of the sensor wells, approximately six inches of a mixture of equal parts of #8 fine and #4 filter pack sand was deposited in the bottom. The TDR probe was then inserted in the sand. The suction sampler was taped to the tensiometer and lowered until just above the TDR probe. A spacer was inserted between the tensiometer and suction sampler to prevent voids and ensure proper operation of both sensors. The colloid sampler was taped to the 3/8" PVC pipe protecting the TDR probe's coaxial cable, and lowered into the well until it also was just above the TDR probe. The sampling point was then filled with sand and the well sealed with granular bentonite (Figures C-3 and C-4). In wells with bi-level sensor packs e.g. two sensor packs per well, the bentonite was backfilled to the lower elevation of the upper pack and then instrumentation of the upper pack followed the same procedures as the lower pack. Upon completion of the upper pack, the well was backfilled to the surface with bentonite (Figure C-4).



Tensiometer



TDR Probe

Figure C-1. Tensiometer and TDR probe construction.

Suction Lysimeter Sampler

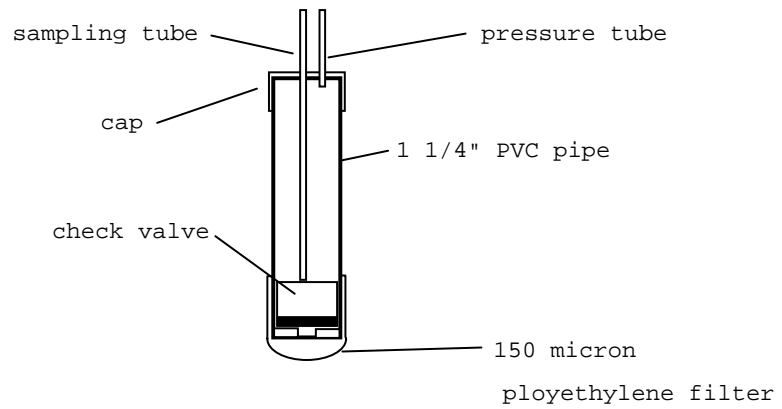
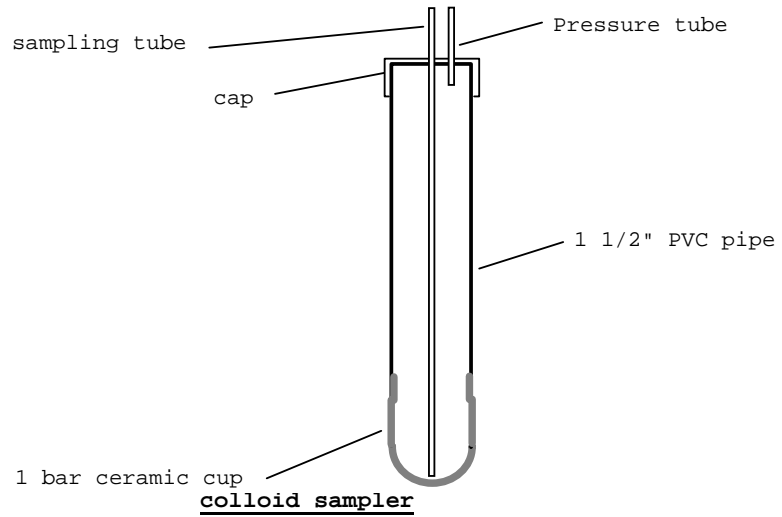


Figure C-2. Solution and colloid water samplers.

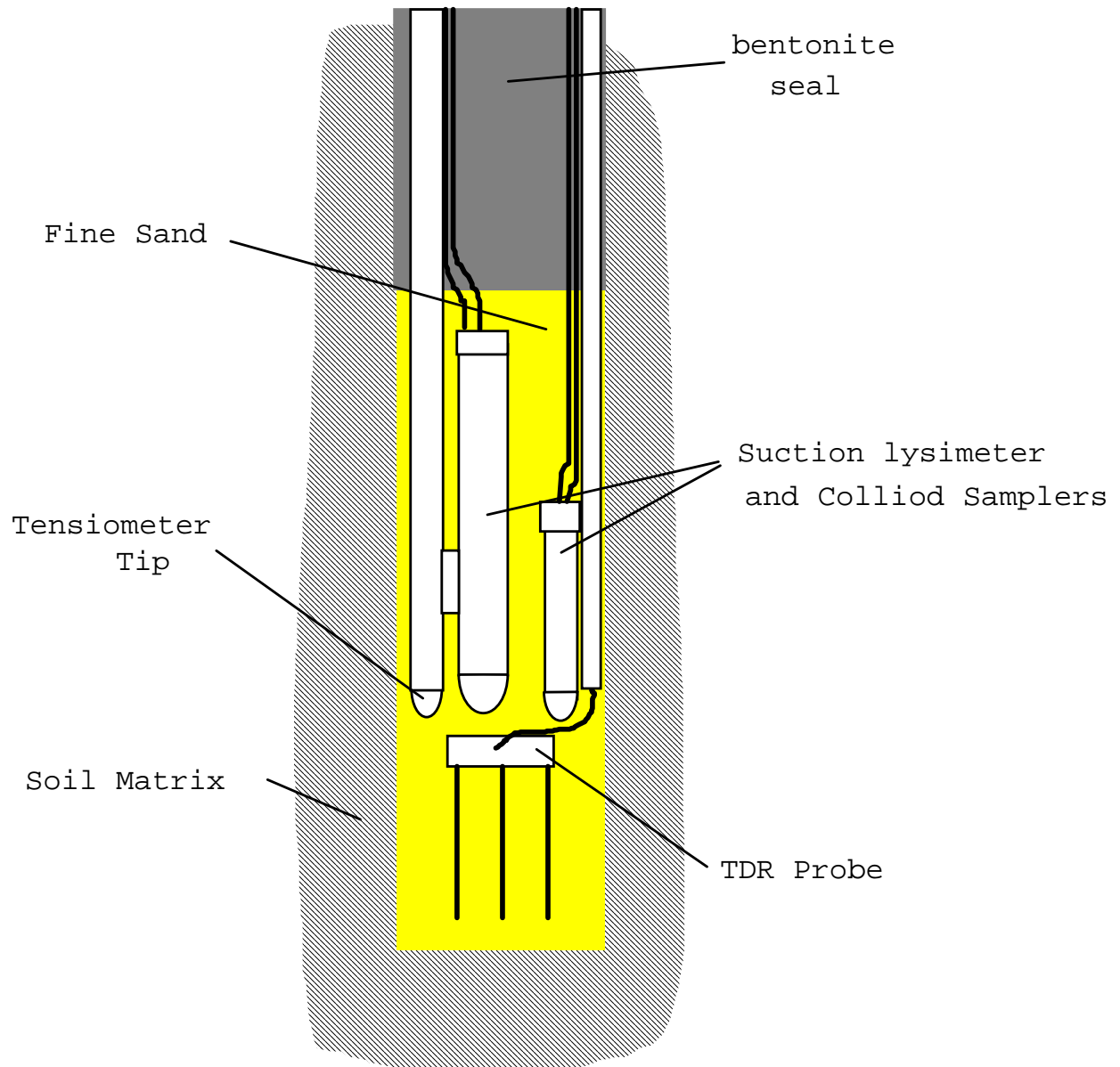


Figure C-3. Sensor Packs.

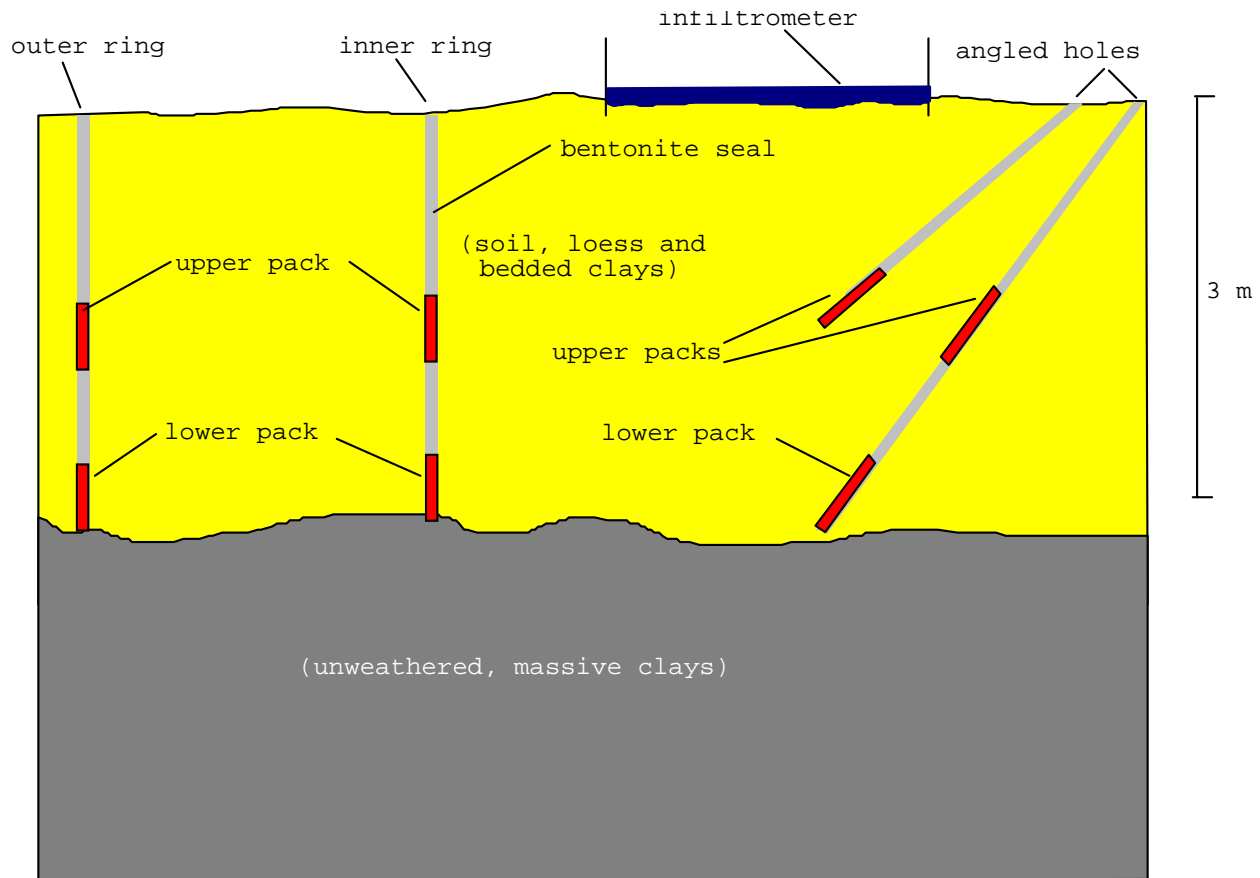


Figure C-4. Cross-section of ponded infiltrometer and sensor array at the Clay Site. The sensor array at the Sand Site is identical, but the geology is different.

The bentonite was backfilled to the lower elevation of the upper pack and then instrumentation of the upper pack followed the same procedures as the lower pack. Upon completion of the upper pack, the well was backfilled to the surface with bentonite. (Figure C-4).

The TDR probes were installed in backfilled sand rather than the glacial tills for several reasons:

First, with the TDR probe installed in the same manner as the suction sampler, comparisons between data from the two sensors could be made in a meaningful way and thus provide some insight on the influence of the measurement technique on the breakthrough data as well as provide additional information on the flow field. Second, installing the TDR probes directly in the clays would have resulted in greater signal attenuation leading to a decreased range and perhaps sensitivity of the electrical conductivity measurement. Third a robust measurement would probably result if the entire length of the waveguide was exposed to the tracer solution, rather than the very short sections of the waveguides that intersect fractures or burrows. Fourth, installing the waveguides in the clay deposits could result in smearing of the clays along the waveguides during insertion. This smearing could have blocked tracer solution from the waveguides in all but the largest macropores. Finally, we were not interested in measuring soil moisture because we seriously doubted that it would be important due to a lack of matrix flow.

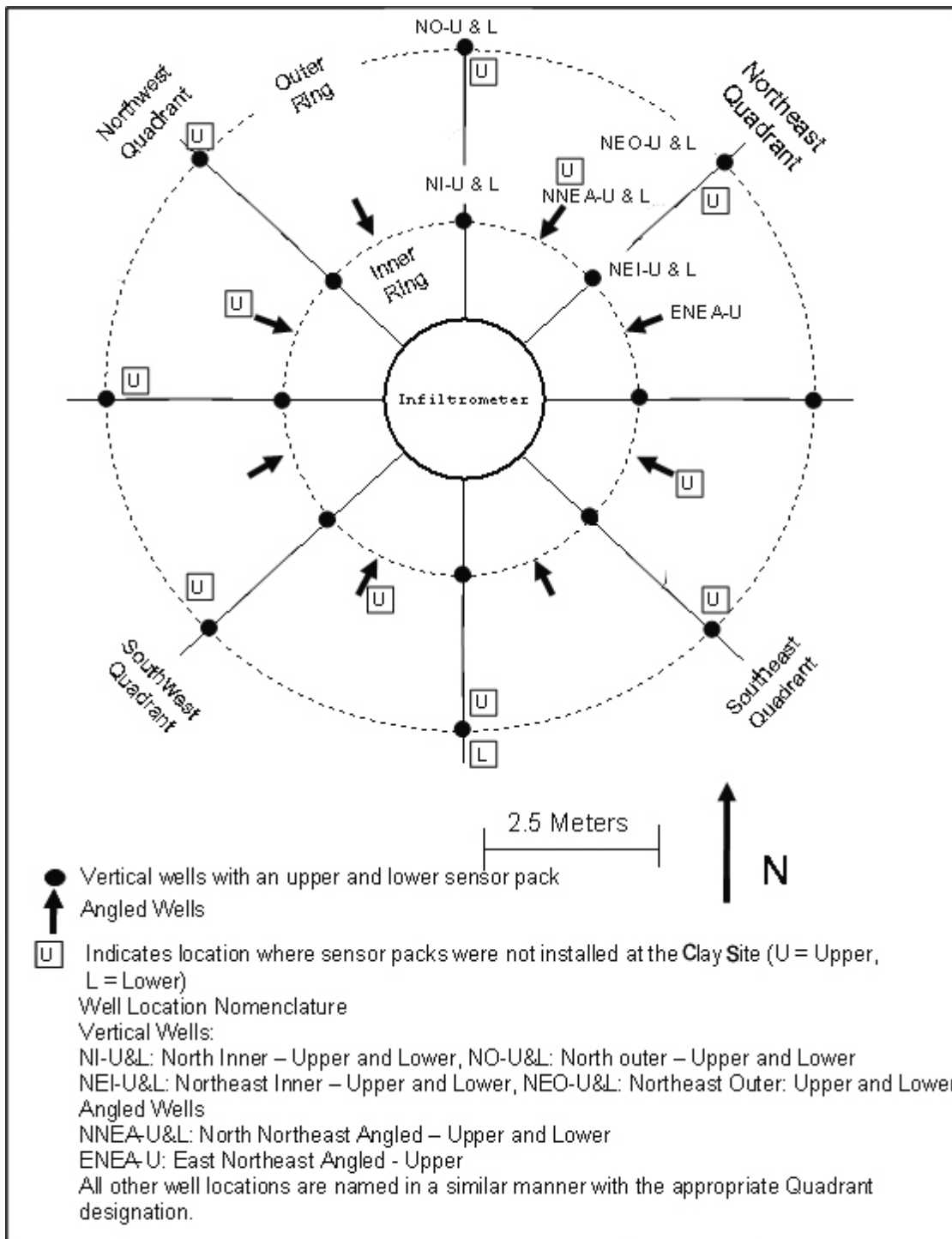


Figure C-5. Plan-view and nomenclature of Clay and Sand Site sensor arrays. Note that some of the sensor packs were not installed at the Sand site as indicated in the figure.

Appendix D. Colloid and Chloride Tracers

<u>Section</u>	<u>Page</u>
D.1 Analog Colloid Tracer	92
D.2 Cl ⁻ Tracer Application	92
D.3 Soil Water Sampling Cl ⁻ Tracer Concentrations	93
D.4 Time Domain Reflectometry Measurement of Cl ⁻ Tracer Concentrations	96
D.5 Results	171

Identical tracer pulses were implemented at both the Clay and Sand Sites. The pulses consisted of an analog colloid and a salt tracer. At both sites the colloid tracer was monitored through sample collection from the colloid samplers while the salt tracer was monitored with both Time Domain Reflectometry and samples collected from soil suction samplers. These sensors were installed in the same sensor pack and arranged in an axi-symmetric array at two elevations in close proximity of the infiltrometer. See Appendix C for more details on instrumentation.

D.1 Analog Colloid Tracer

An analog colloid tracer pulse composed of 260 ml (2% solids) of 1 mm blue fluorescent and 25 ml (2% solids) of .2 mm yellow *Interfacial Dynamics Corporation's* latex fluorescent microspheres was introduced into the Clay Site infiltrometer at June 20 at 1030 hours. The water supply to the infiltrometer was shut off upon introduction of the analog colloids and resumed after the water level dropped to the ground surface (approximately five hours later). A 25 ml pulse of *Interfacial Dynamics Corporation's* .2 mm yellow fluorescent microspheres was introduced in the same manner into the Sand Site infiltrometer at June 21 at 1030 hours.

Soil water samples were captured in 15 ml glass sampling bottles to prevent possible adhesion of the microspheres to the polyethylene sample bottles being used for Cl^- tracer sampling. The samples were transported to Los Alamos National Laboratory in New Mexico for testing. By the time testing was performed, the fluorescent materials had either degraded to the extent that no definable measurement of concentrations could be made or no micro spheres were transported to the samplers.

D.2 Cl^- Tracer Application

A calcium chloride pulse lasting two days was introduced through the infiltrometers at the Clay and Sand Site. Subsurface salinity was monitored by TDR and samples were collected from suction samplers at the sensor packs (Figure C-5). The concentrations were plotted in time for each sampling location. Details concerning the salt pulse infiltration are given below and the complete set of breakthrough plots are presented in the last two sections of this appendix.

The same procedure was used for initiating the salt pulse at the Sand and Clay Site. A 12.6 Kg of commercial grade calcium chloride was dissolved in a 50-gallon drum of fresh water. This solution was then pumped to the infiltrometer supply tank. Fresh water was pumped into the infiltrometer supply tank to obtain 300 gallons of a 0.1 M CaCl_2 solution. Prior to the introduction of the tracer to the infiltrometer, the infiltrometer water supply was turned off and the water level in the infiltrometer was allowed to drop as near as possible to ground level. The tracer pulse was then initiated by pouring three 133-liter containers filled with 0.1 M CaCl_2 into the infiltrometer and simultaneously opening the valve to the infiltrometer supply tank. This procedure resulted in an essentially instantaneous 5 cm ponded level in the infiltrometer. Splash deflectors were placed on the ground surface to prevent scouring of the infiltrated surface. The float valves in the infiltrometer maintained a constant 5 cm deep pond of the Cl^- solution in the infiltrometer duplicating infiltration conditions prior to the introduction of the tracer pulse.

The salt tracer was initiated on June 21, 1030 hours at the Clay Site and on June 22 at 1030 hours at the Sand Site. Samples were taken from the infiltrometers as part of the normal sampling

routine. The first samples taken from the infiltrometers were used to determine the initial Cl⁻ concentration, C_o. The C_o for the Clay and Sand Site was 5558 mg/L and 6572 mg/L respectively. The disparity between the C_o at the two sites and the target concentration of 7090 mg/L is probably due to inadvertently mixing fresh water remaining in the drained infiltrometer with the tracer solution. The tracer pulses were terminated approximately 48 hours after the start of application. The total salt pulse at the Clay Site was 1534 Liters, and the total salt pulse at the Sand Site was 1209 liters.

D.3 Soil Water Sampler Measurement of Tracer Concentrations

Base line soil-water samples were collected from the suction samplers before introduction of the salt tracer. These samplers are also known as suction lysimeters and pressure-vacuum lysimeters. The samples were analyzed in the laboratory for Cl⁻ concentration using an ion specific probe. The discussion in this section concerns sampling procedures, analysis techniques, and the method employed to compensate for certain laboratory measurement errors.

Collection of Cl⁻ Samples by Soil Water Samplers

Soil water samples for solute and analog colloid concentration analysis were collected from either the colloid or suction samplers. Because of the ease of operation and the lesser suction which needed to be applied, samples for both the analog colloid and Cl⁻ tracers were obtained from the colloid samplers where possible.

Identical procedures for obtaining samples from the colloid and suction samplers were followed. First, the sampling and pressure tubes (see Figures C- 2) were opened and a positive air pressure was applied to the sampler via the “pressure tube” with a vacuum/pressure pump (model 2006G, manufactured by *SoilMoisture Equipment Corporation*). This action forced most of the water out the “sampling tube” leaving the sampler nearly empty. The “sampling tube” was then clamped closed and a vacuum applied to the “pressure tube”, after which the “pressure tube” was clamped closed. To allow adequate time for water to be drawn into the samplers, these steps were repeated on all of the samplers at one of the sites before continuing. This process required about one hour. To collect the sample from the sampler, both the sampling and pressure tubes were opened and a positive pressure was again applied to the pressure tube, forcing out the water sample through the sample tube into the sample bottle. For Cl⁻ tracer analysis, samples were collected in 25 ml Nalgene® polyethylene bottles. During the week prior to the introduction of the Cl⁻ tracer, daily sampling provided baseline concentrations.

Analysis of Cl⁻ Concentrations in Soil Water Samples

Chloride concentrations, measured in mg/L, were obtained with an Orion Benchtop® pH/ISE Meter model 920A and a model 94-17B chloride combination electrode. The two probes of the combination electrode were inserted into the un-agitated sample bottle and held just above the bottle bottom until the reading stabilized. The readings were manually entered into a spreadsheet along with date, time and sensor pack location into a spreadsheet. The probes were then rinsed with deionized water and immersed into two 5-liter Nalgene® bottles of deionized water. Excess water was shaken from the probes and the sides of the probes wiped with a Kim-Wipe® before the probes were inserted into the next sample.

Analysis of Cl⁻ tracer concentrations from soil water samplers was performed in three batches, (runs). The majority of the 2341 samples were analyzed in Sample Run 1 where, in contrast to Sample Run 2, an ISA buffering solution was not used due to an oversight. The ISA solution is a 5 M sodium nitrate solution which lowers the pH to an optimal level to complex out interfering ions. Procedures for measuring Cl⁻ concentrations and for compensating for lack of the ISA in the Sample Run 1 are discussed next.

Sample Run 1

Samples in this run were analyzed without buffering with an Ion Strength Adjuster (ISA) solution (See Sample Run 2 below). Calibration standards were prepared by diluting the Orion chloride standard solution number 941706 with deionized water. Orion meter calibration was accomplished following the manufacturer's recommendations on page 8 of the Orion *Chloride Electrode Instruction Manual*. On page 6 of the *Orion Chloride Electrode Instruction Manual*, it is recommended that recalibration of the Orion meter be performed every two hours during normal operation.

Sample Run 2

In Sample Run 2 a test was performed to test the impact of the Ion Strength Adjuster (ISA) measurement results. The ISA solution was added as 2 ml per 100 ml of sample, or 0.30 ml for the 15 ml samples used in this test. To check the efficacy of the ISA solution, samples from four sensor packs at the Sand Site were re-measured using the ISA solution. The comparison of ISA versus non-ISA analyses are shown for the four sets of samples in Figures D-1 to D-3. As seen in three out of the four plots, the un-buffered measurements produced slightly lower or higher measures of Cl⁻ concentrations except in the peak where the un-buffered solution measurements were significantly lower.

Chloride concentration measurement error was determined during Sample Run 2 by including nine solutions of each calibration concentration into the sample stream. These test solutions were made from reagent grade sodium chloride and distilled water. The results and statistics from this test are presented in Table D-2. The percent error relative to the actual concentration was obtained by dividing the standard deviation of the difference between measured and actual concentrations by the actual concentration and multiplying the result by 100. This percent error ranges between 8.66 and 3.8 of the actual concentration which ranges between 3.45 and 3545 mg per liter.

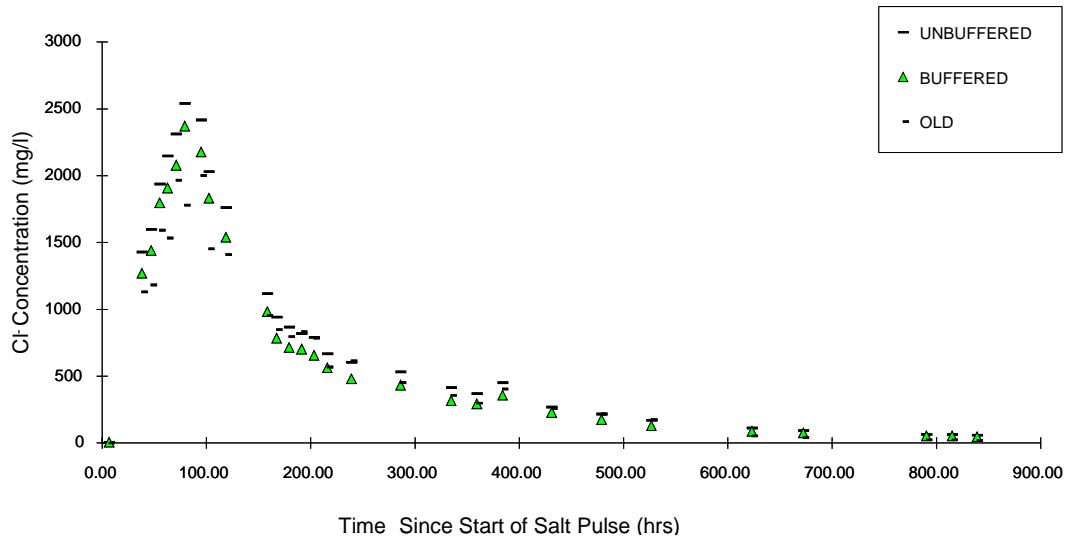


Figure D-1. Graphical Results of Sample Run 2 showing the difference between Cl⁻ concentrations using a buffered versus an unbuffered solution. Sample are from a Clay Site Sensor: North-Northeast Angled Lower (3 m beneath the infiltrrometer).

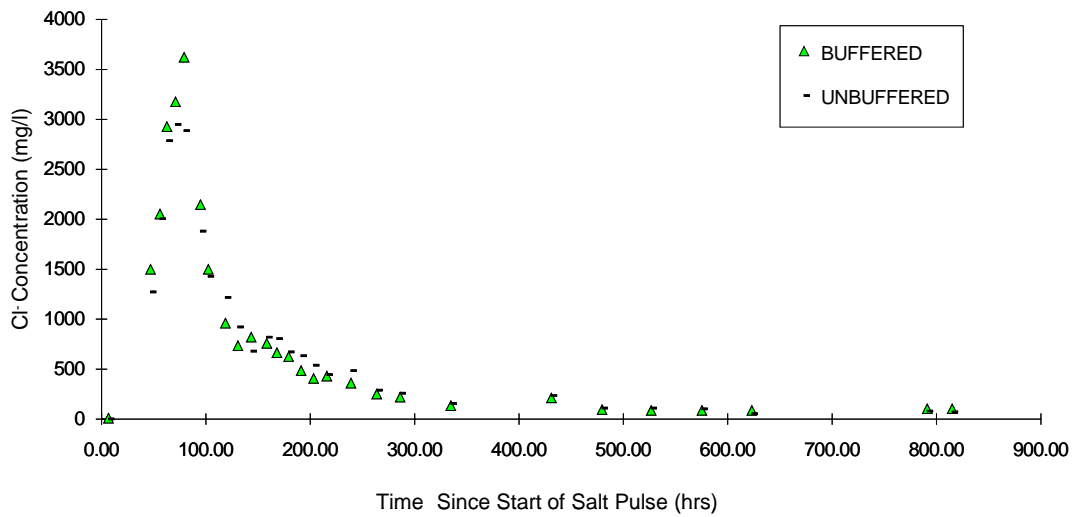


Figure D-2. Graphical Results of Sample Run 2 showing the difference between Cl⁻ concentrations using a buffered versus an unbuffered solution. Samples are from a Clay Site Sensor: South-Southwest Angled Lower (3 m beneath the infiltrrometer).

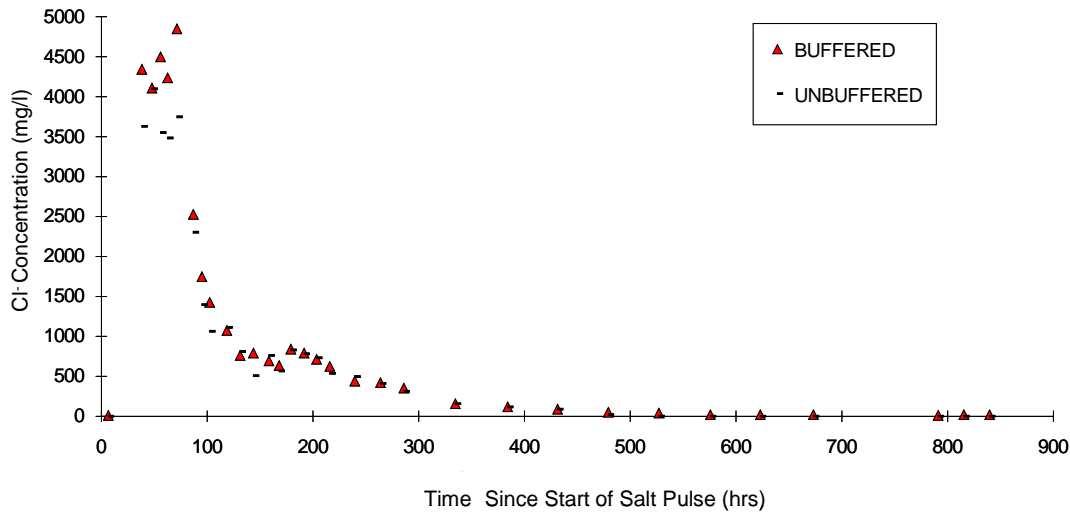


Figure D-3. Graphical Results of Sample Run 2 showing the difference between Cl⁻ concentrations using a buffered versus an unbuffered solution. Samples are from a Clay Site Sensor: North-Northwest Angled Lower (3 m beneath the infiltrometer).

Sample Run 3

The results from Sample Run 2 prompted reanalysis samples from 24 hours before and after the peaks. Additional reanalysis was performed on samples that produced questionable data. Four hundred and fifty-seven samples were selected for re analysis. Of the 457 samples in Run 3, 289 comparisons were possible between the un-buffered analyses of Run 1 and the buffered analyses of Run 3. Additional results from Sample Run 2 were incorporated into the data set yielding a final total of 371 buffered/un-buffered pairs. A scatter plot of this data set is presented in Figure C-4. A linear regression analysis of this data set yielded the following equation for converting the un-buffered measurements to an approximation of a buffered measurement: "Buffered approximation = 1.055*Un-buffered Measure + 7.978". The R² value for the regression equation was 0.975.

D.4 Time Domain Reflectometry Measurement of Cl⁻Tracer Concentration

Time Domain Reflectometry (TDR) is a relatively new method for monitoring both soil moisture and soil water salinity. Utilizing a signal generator and multiplexed switches, all controlled by a laptop computer, TDR provides an efficient and not destructive method of monitoring these essential hydraulic variables in both time and space. Building on the scoping study conducted the previous year (Brainard et al., 2005), where fully automated data acquisition systems were constructed and installed, a more robust and adaptable system was implemented.

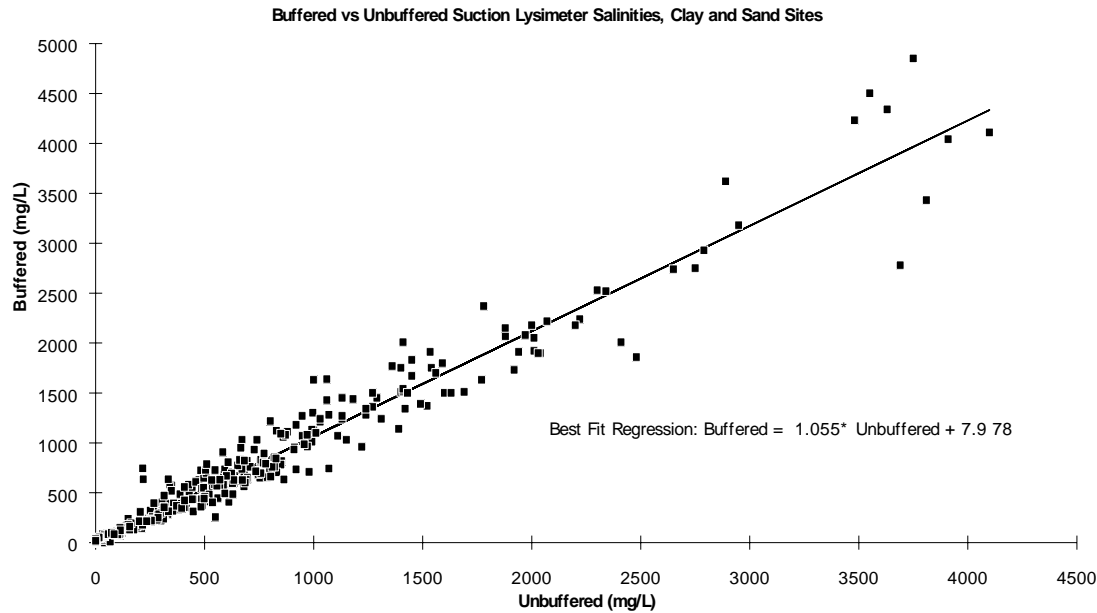


Figure D-9. Regression of un-buffered (non-ISA) versus buffered (ISA) salinity analyses.

The system used at the Sand Site consisted of a Tektronics® 1502B signal generator and receiver, a JFW 32 port automated coaxial cable switch, an array of 32 three-prong probes (Figure D-10), and a Compaq Contura 486-25X laptop computer for system control and data acquisition. TDR data at the Clay Site was collected with two separate systems, each with a Tektronics 1502B signal generator and receiver, a single automated 24 port JFW coaxial cable switch, an array of 22, three-prong probes, and a Compaq Contura® 486-25X laptop computer for system control and data acquisition. The TDR systems used in the TPC tests were controlled by a Sandia National Labs written program configured to collect data for both moisture content and salinity concentrations. All systems were battery powered with two deep-cycle 120 amp-hour marine batteries. The batteries were replaced with fully charged batteries every two days.

Soil Moisture Analysis

Sand pack moisture calculations were accomplished using the algorithm developed by Topp et al. (1980). Details of the required TDR data analysis for obtaining moisture content is not discussed here. The moisture content measurements were shown to have a repeatability of ± 0.015. Soil moisture measurements reflect soil moistures within the sensor sand packs and were used only to determine that conditions were saturated or nearly saturated. Sensor pack moisture content data and with corresponding soil water sampler concentrations are presented for both the Clay Site and the Sand Site in the last section of this appendix.

TDR Soil Water Salinity Analysis

Analysis of the reflected TDR wave form may be used to calculate soil water salinity concentrations (See Dasberg and Dalton, 1985; Kachanoski et al., 1992, and Wraith et al., 1993). Salinity analysis was initially attempted utilizing the method of Wraith et al. (1993):

Table D-2. Blind Test Measurements

Blind Test

Bottle Number	standard (mg/l)	measured (mg/l)
9	3.545	3.12
5	3.545	3.24
30	3.545	3.29
26	3.545	3.41
7	3.545	3.43
28	3.545	3.43
1	3.545	3.51
24	3.545	3.88
3	3.545	4.08
6	35.45	31.5
10	35.45	32.5
27	35.45	32.9
2	35.45	33.2
29	35.45	34
25	35.45	34
4	35.45	34.8
8	35.45	35.1
23	35.45	35.7

Bottle Number	standard (mg/l)	measured (mg/l)
13	354.5	303
11	354.5	334
17	354.5	334
15	354.5	348
32	354.5	350
38	354.5	352
34	354.5	356
19	354.5	357
36	354.5	361
40	354.5	371
20	3545	3390
37	3545	3410
12	3545	3550
35	3545	3550
14	3545	3560
33	3545	3580
18	3545	3630
16	3545	3670
39	3545	3750
31	3545	3840

Blind Test Statistics

Standard (mg/l)	Maximum (mg/l)	Minimum (mg/l)	Average (mg/l)	Standard Deviation (mg/l)	Standard Deviation as % of Standard
3.55	4.08	3.12	3.49	0.31	8.66
35.45	35.70	31.50	33.74	1.35	3.80
354.50	371.00	303.00	346.60	19.03	5.37
3545.00	3840.00	3390.00	3593.00	138.49	3.91

σ = bulk soil electrical conductivity

$$\sigma = \frac{f_t}{Z_1} K, \text{ with}$$

Z_1 = the resistive impedance

K = probe geometric constant

f_t = a temperature correction factor

The resistive or load impedance, Z_L , is computed using:

$$Z_L = Z_o \frac{(V_i + V_f)}{(V_i - V_f)} \text{ where } \begin{array}{l} Z_o = \text{transmission line nominal impedance} \\ V_i = \text{the incident voltage} \\ V_f = \text{the final voltage} \end{array}$$

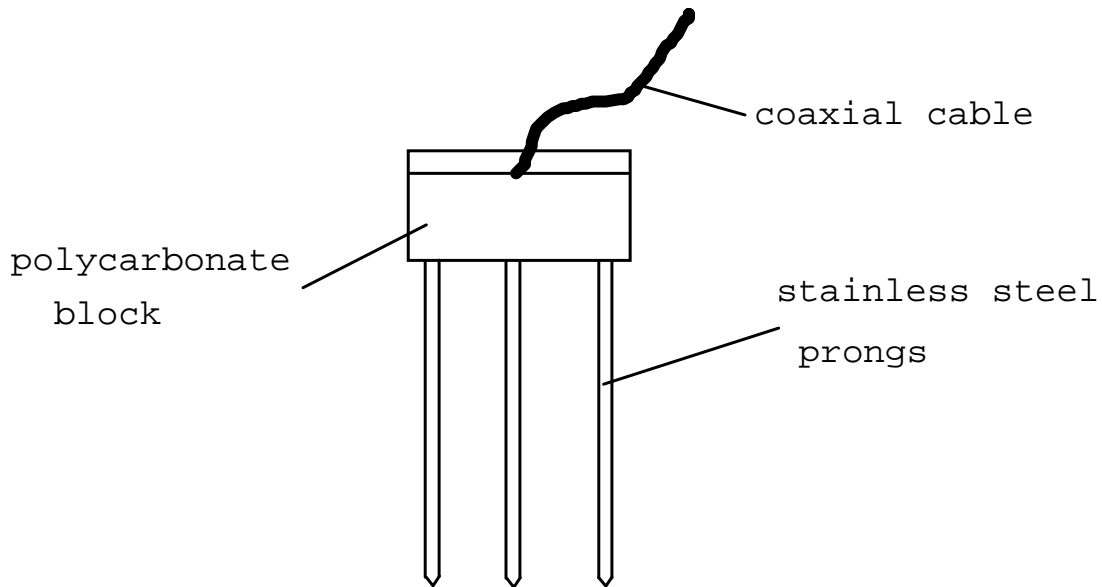


Figure D-10. Time Domain Reflectometry probe.

V_i and V_f are measured as illustrated in Figure D-11.

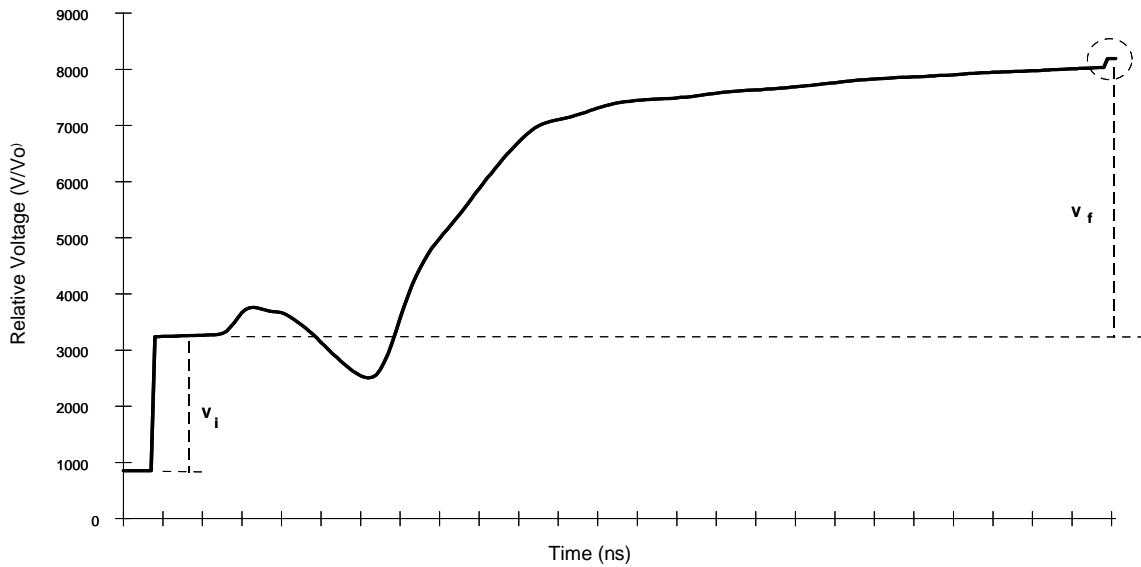


Figure D-11. An example of TDR trace data used to obtain solute concentrations.

It is apparent from the relative magnitudes of V_i and V_f , above, that the quantity $(V_i - V_f)$ will be negative, rendering both resistive impedance, Z_1 , and the bulk soil conductivity, σ , also negative. Correspondence with Jon Wraith disclosed no apparent reason for this seeming impossibility. A study of Wraith et al. (1993), Nadler et al. (1991), Dalton et al. (1984), and Kachanoski et al.

(1992) found that the potential existed in all methods for the calculation of negative soil conductivities. Thus, an alternative approach was needed. Since the change in soil water conductivity is indirectly proportional to the change in V_f , we adopted an empirical relationship:

$$\frac{C}{C_o} = \frac{1}{R} \frac{(V_{f_o} - V_{i_o}) - (V_{f_i} - V_{i_i})}{(V_{f_o} - V_{i_o})} = \frac{1}{R} \frac{(V_{f_o} - V_{f_i}) - (V_{i_o} - V_{i_i})}{(V_{f_o} - V_{i_o})}$$

where:

C = concentration at the probe some time during the tracer pulse

C_o = initial concentration of tracer the start of the pulse

V_{f_i} = final reflected voltage at some time during the tracer pulse

V_{f_o} = final reflected voltage at the start of the tracer pulse

V_{i_i} = initial reflected voltage at some time during the tracer pulse

V_{i_o} = initial reflected voltage at the start of the tracer pulse

R = an empirical correction factor

In the above equation, the quantity $(V_{f_o} - V_{f_i})$ represents the drop in the final reflected voltage due to the increase in soil water salinity, the quantity $(V_{i_o} - V_{i_i})$ normalizes the changes due to effects on the system other than changes in soil water salinity, and the quantity $(V_{f_o} - V_{i_o})$ represents the difference between incident and final reflected voltages at a baseline concentration. The baseline concentration chosen was the average of $(V_f - V_i)$ for the 24 hours immediately prior to the introduction of the salt pulse.

Comparison of TDR and Soil Water Sampler Concentrations

The plots in Figure D-12 show that the TDR solution concentration measurements compare favorably with that of the soil water sampler results, especially while concentrations are rising and during the peaks. This was especially true where for the sensor packs where significant breakthrough occurred.

One of the factors that may be responsible for the discrepancy seen at later times is the increased in temperature over the duration of the infiltration test. As summer proceeded, infiltration water temperatures reached 95°F. Soil water temperatures were not taken during the test, but temperatures during early sampling events were low enough to cause the normally reliable Sharpie brand markers to fail in labeling polyethylene sample bottles when filled with *in situ* soil water samples. All authors working on the problem of obtaining solute concentration from TDR recognized the effect of temperature (Dasberg and Dalton, 1985; Kachanoski et al., 1992; and Wraith et al., 1993).

Another reason for the deviation may be measurement by TDR of ion concentrations other than Cl^- . It is reasonable to assume that the infiltrated Cl^- ions would exchange with other ions present in the soil matrix. This would yield soil water with a total ion concentration greater than just the Cl^- concentration. Because the TDR measurement is a reflection of the bulk soil water

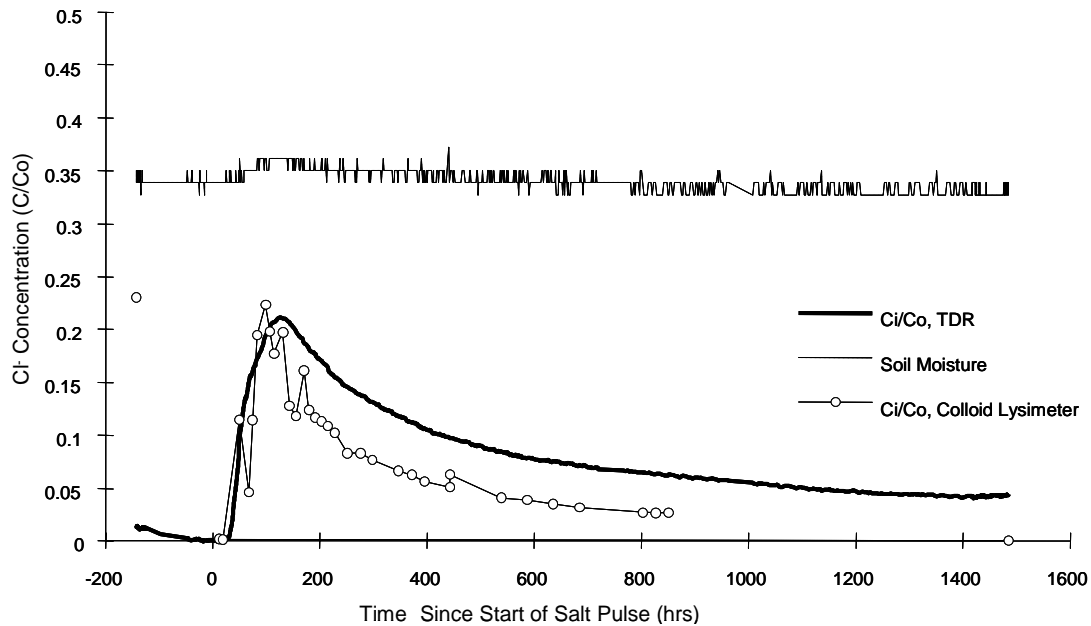


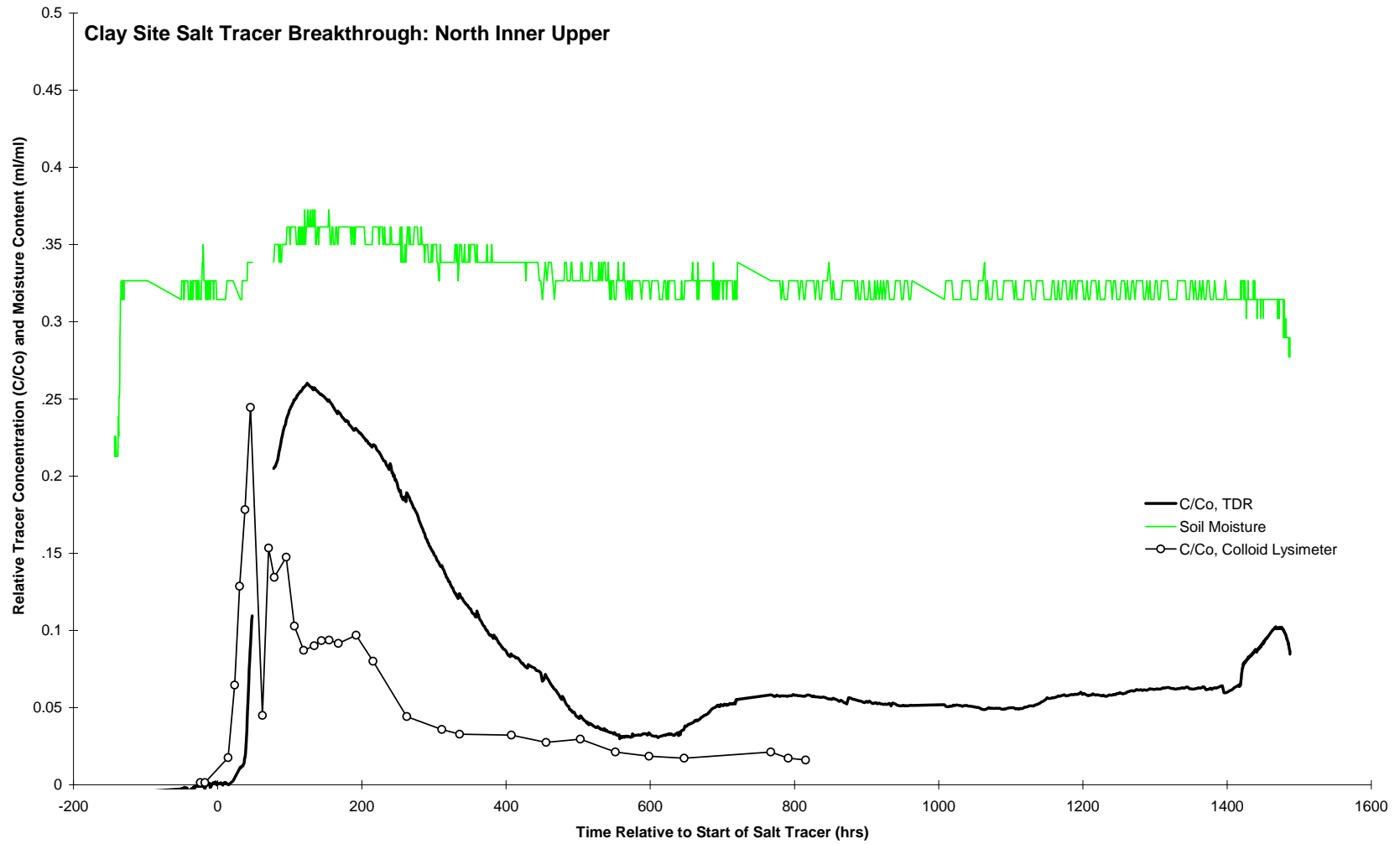
Figure D-12. Salinity breakthrough curves from TDR and suction sampler at the East Southeast Lower Angled sensor pack.

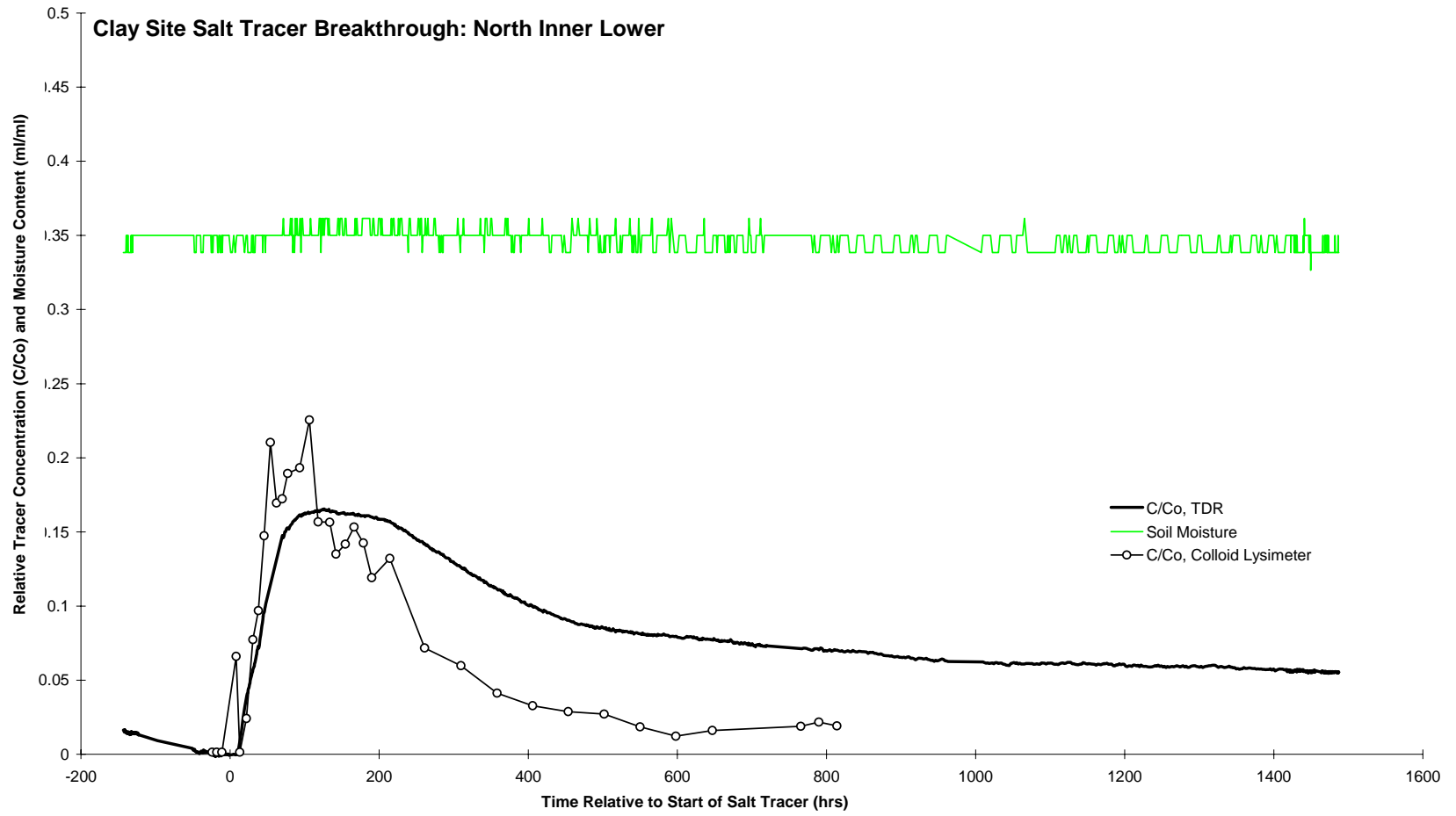
conductivity, this additional ion concentration would be reflected in the TDR measurements but not in the ion specific Cl^- analysis of soil water samples.

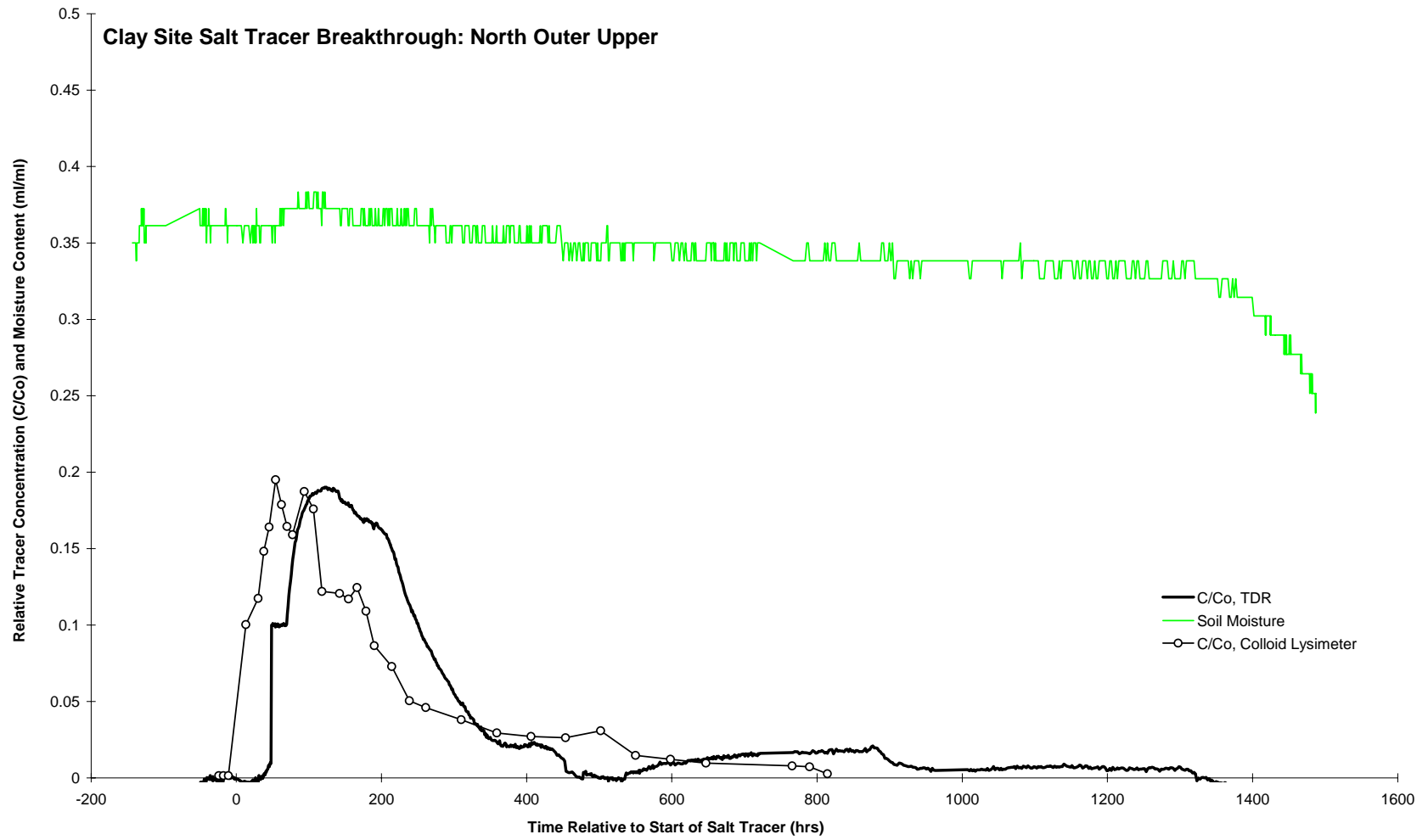
Colloidal influences may also play a part. During boring of the sampling points, disruption of the soil matrix is inevitable. The argillaceous nature of the soil resulted in high concentrations of suspended clay particles in many sample points. It is possible that clay colloids may have been flushed from the matrix and transport pathways by the infiltration itself. Because the baseline C/C_0 ratio was taken as the 24 hours immediately preceding the salt pulse when the colloid suspension would still be relatively high, a changing colloid density may also influence TDR measurements as fresh water from infiltration flushed sampling points.

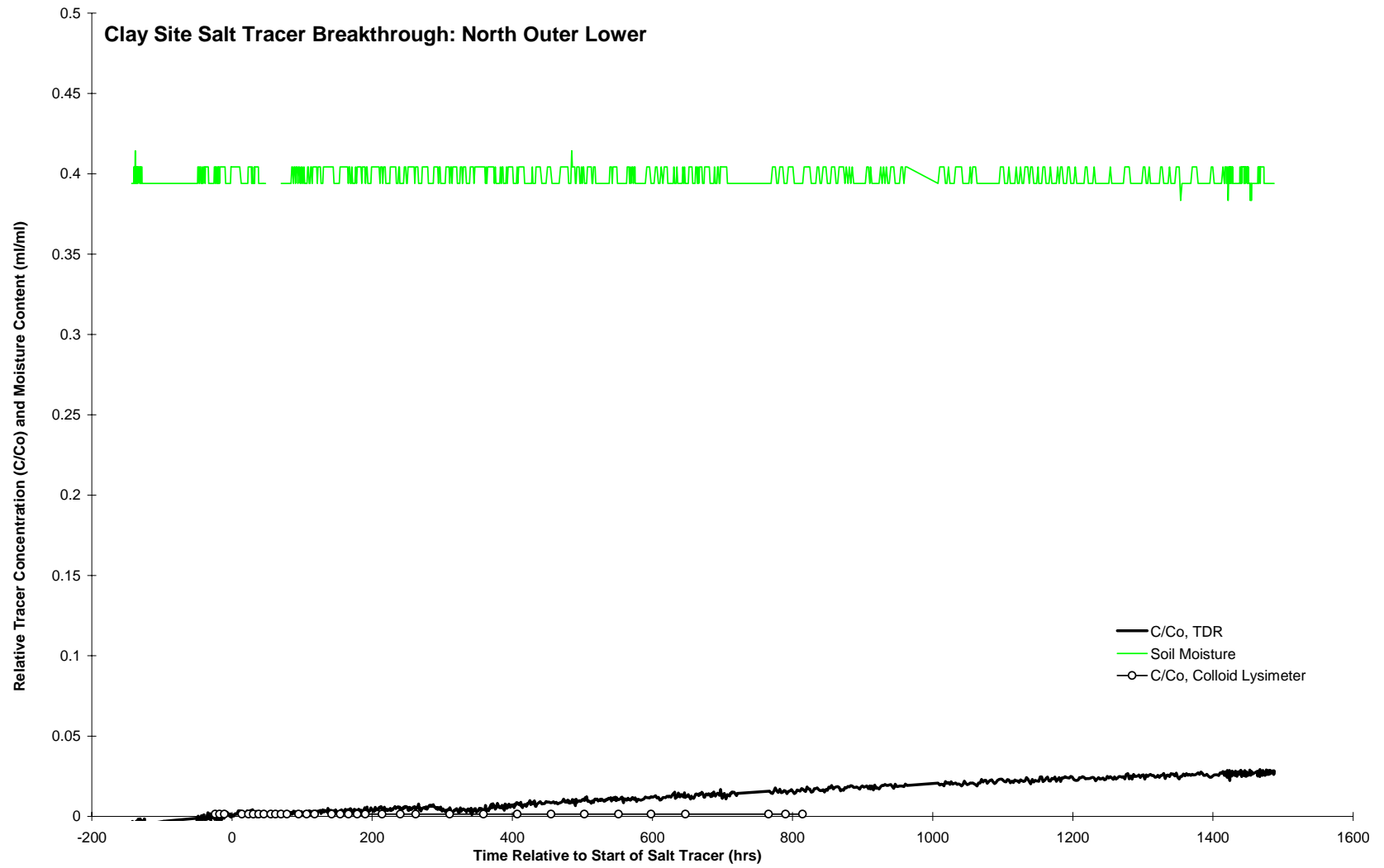
Lack of Data in Unsaturated Conditions

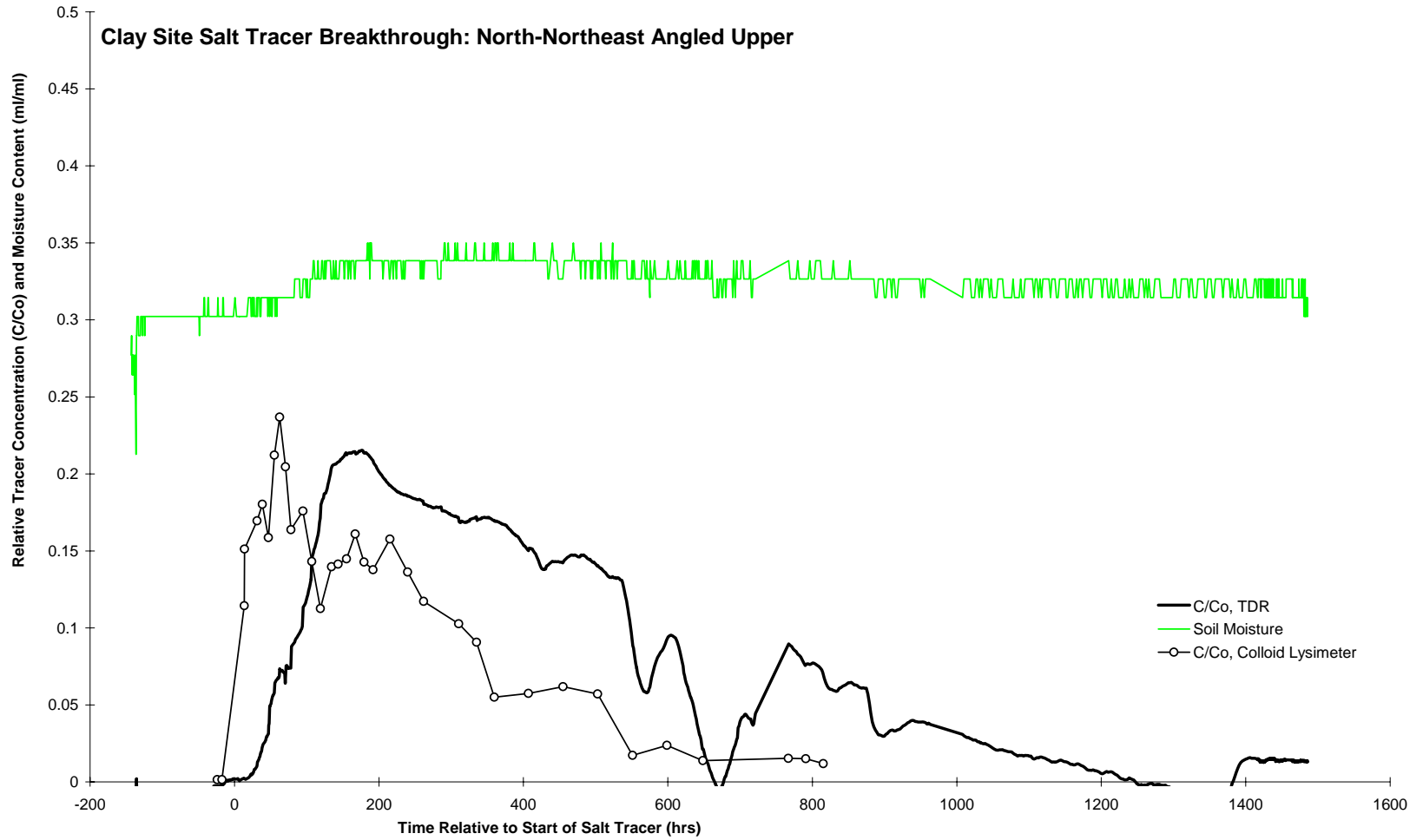
The TDR systems were optimized for saturated or near saturated media. This provided greater resolution of both relative salinity concentrations and soil moistures. In instances where the sensor packs did not approach saturation, primarily the upper outer ring sampling points and some of the upper inner ring sampling points at the Sand Site, the TDR settings resulted in off scale readings (noted as "bad data" in plots).

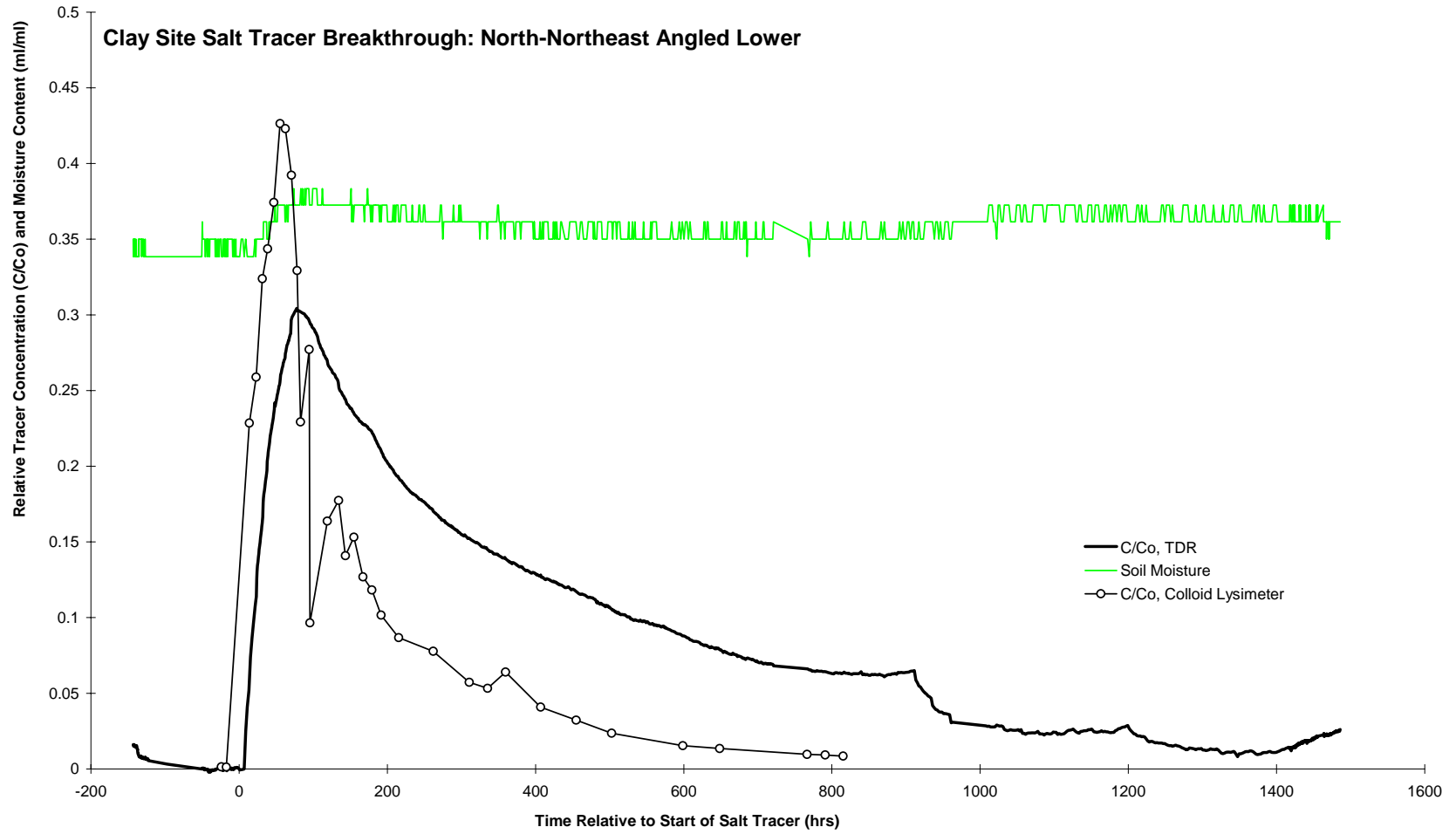


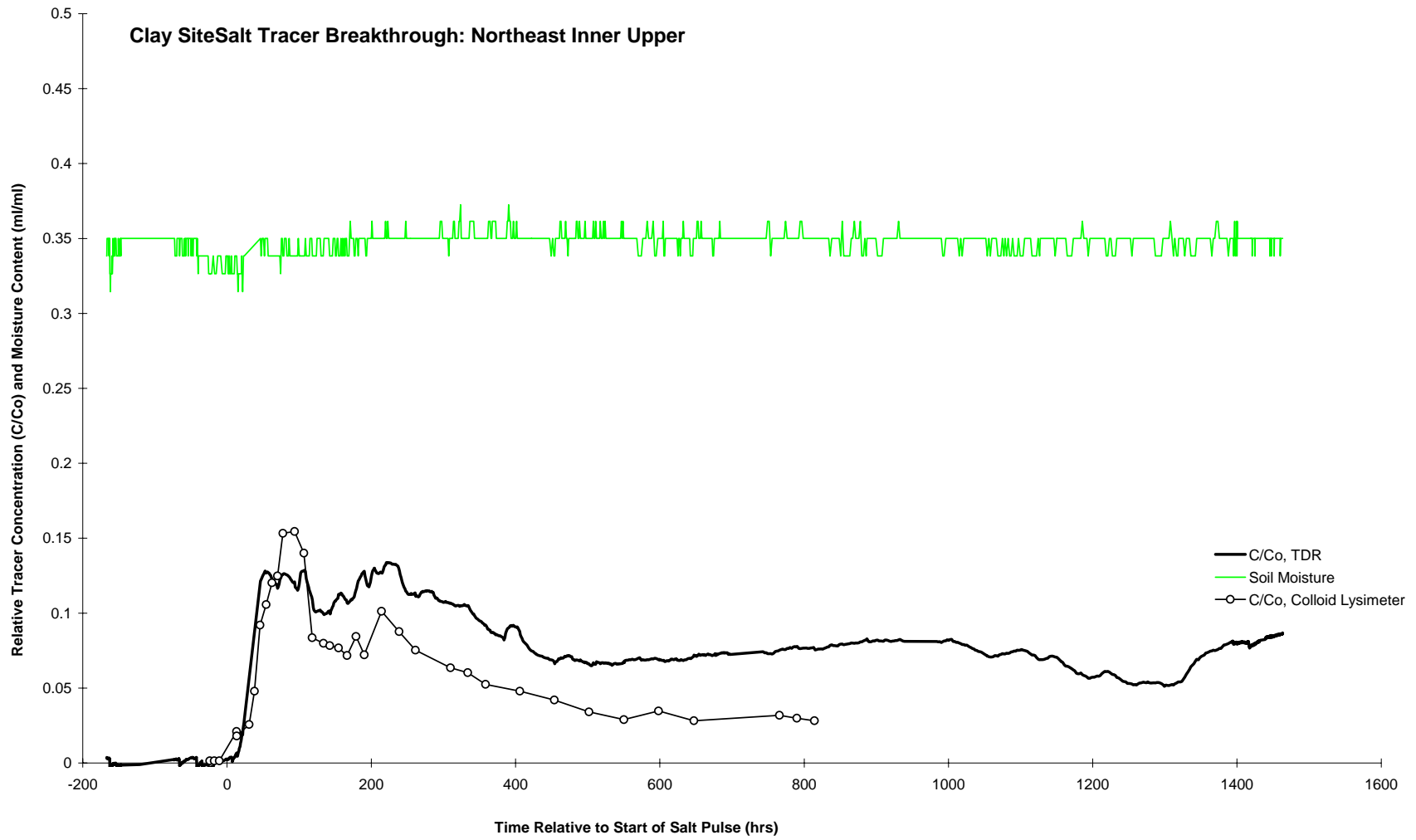


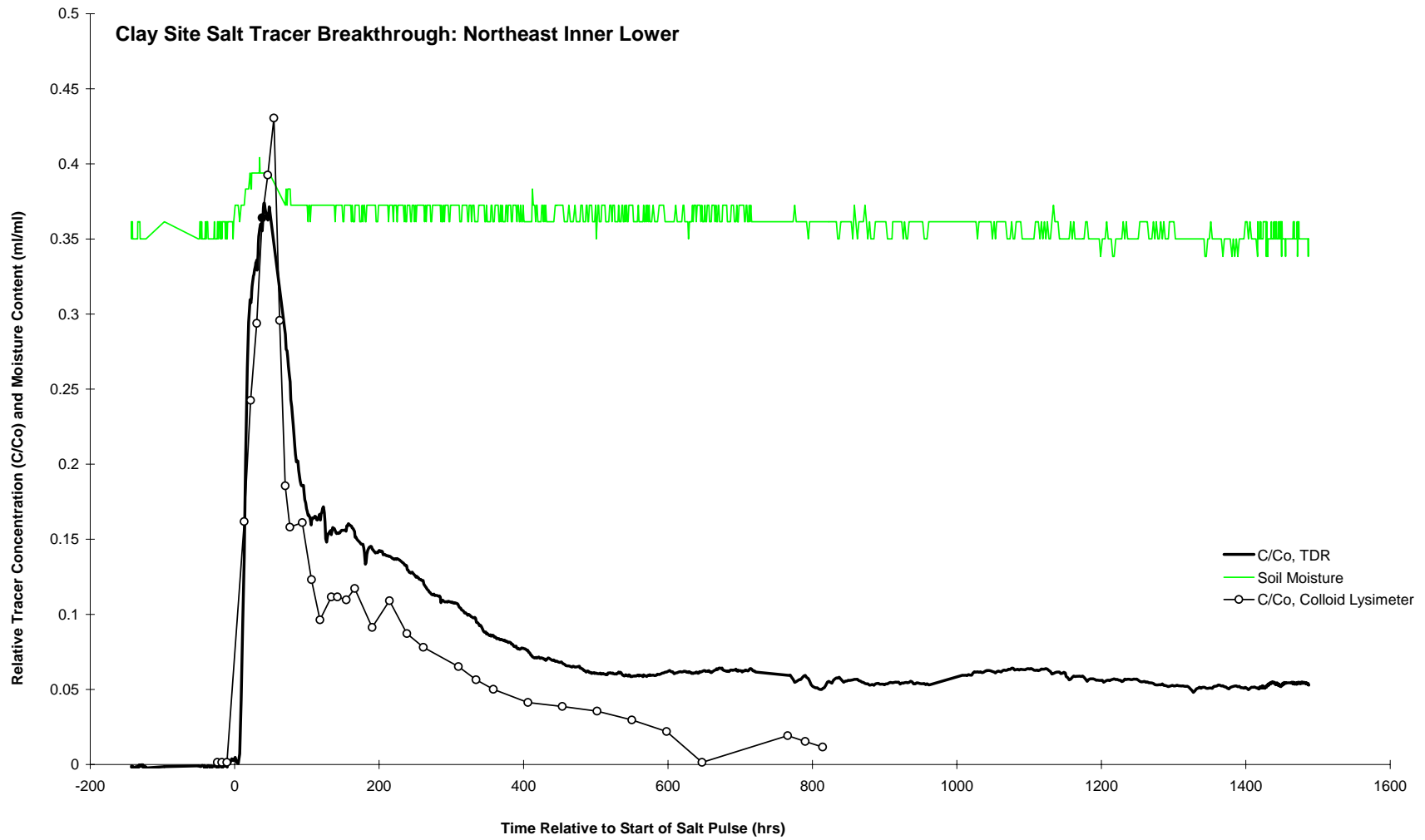


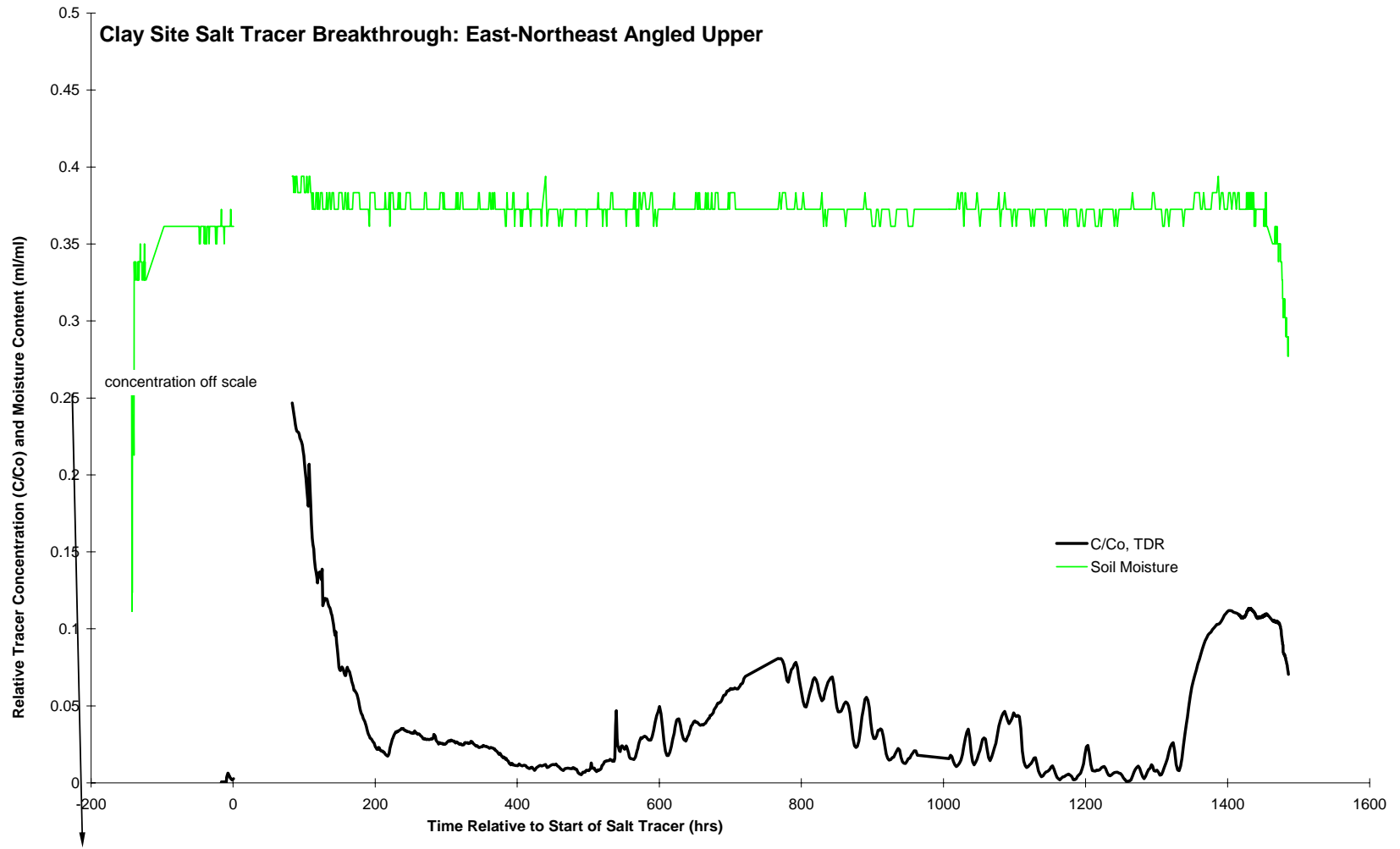


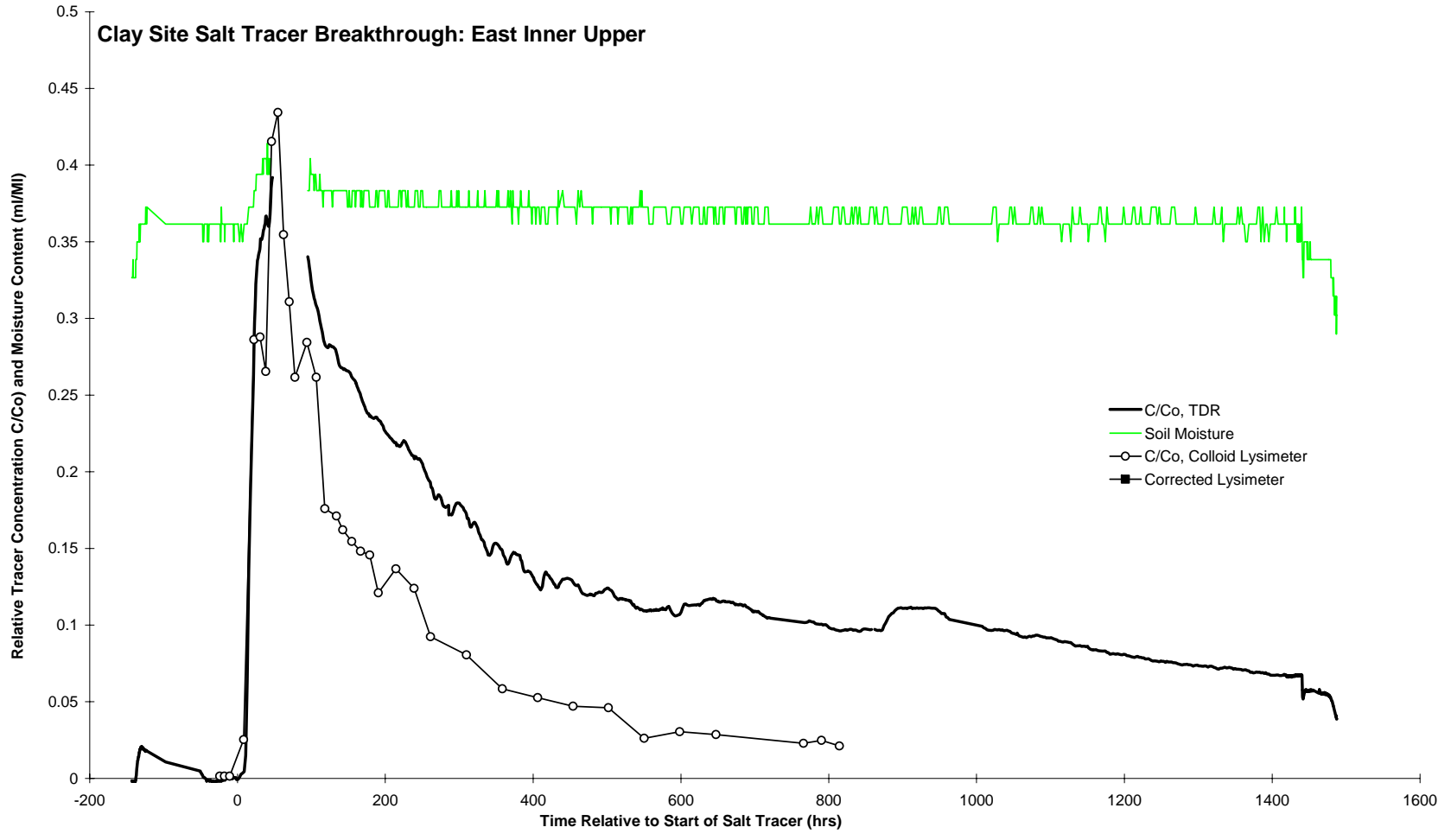


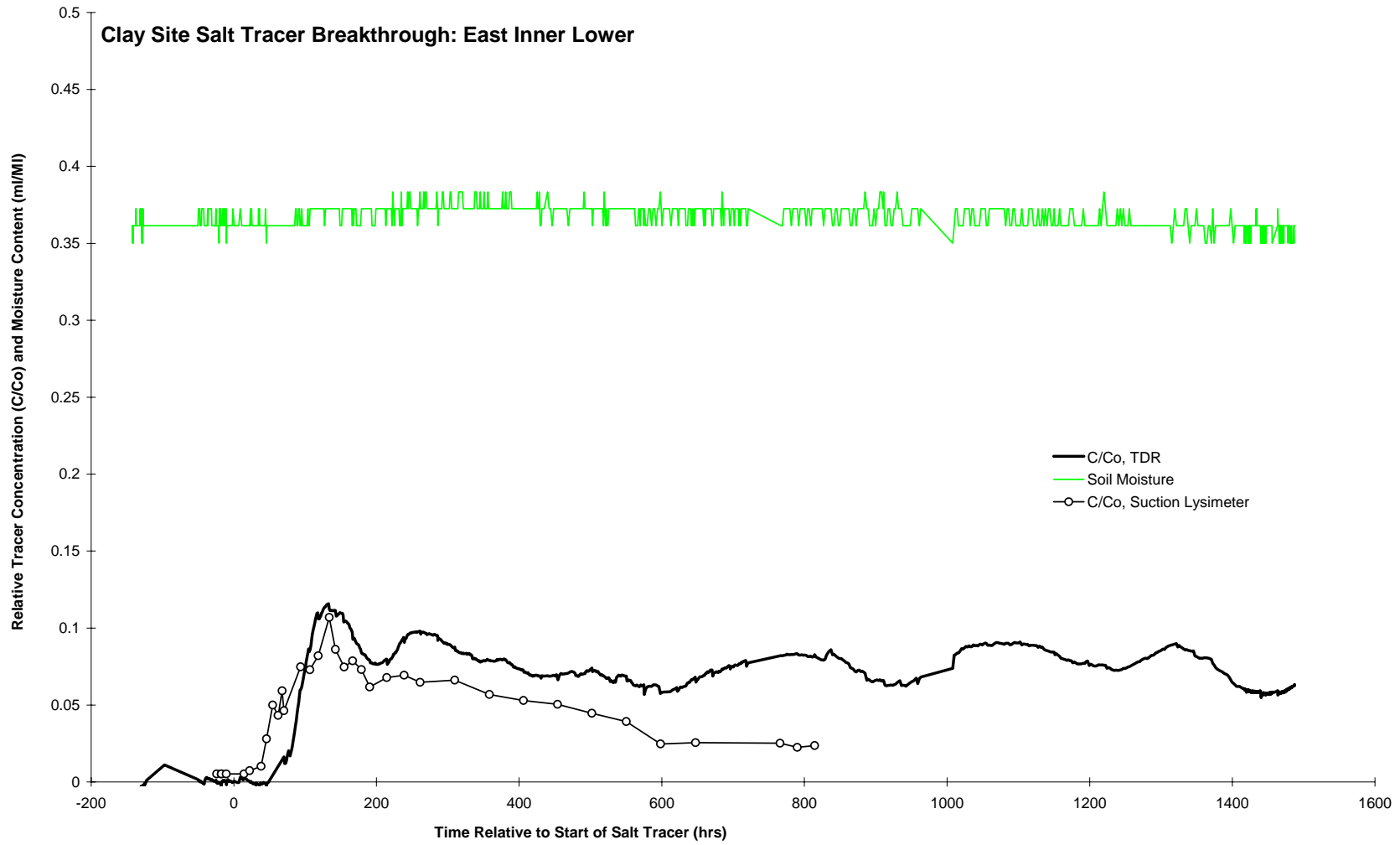


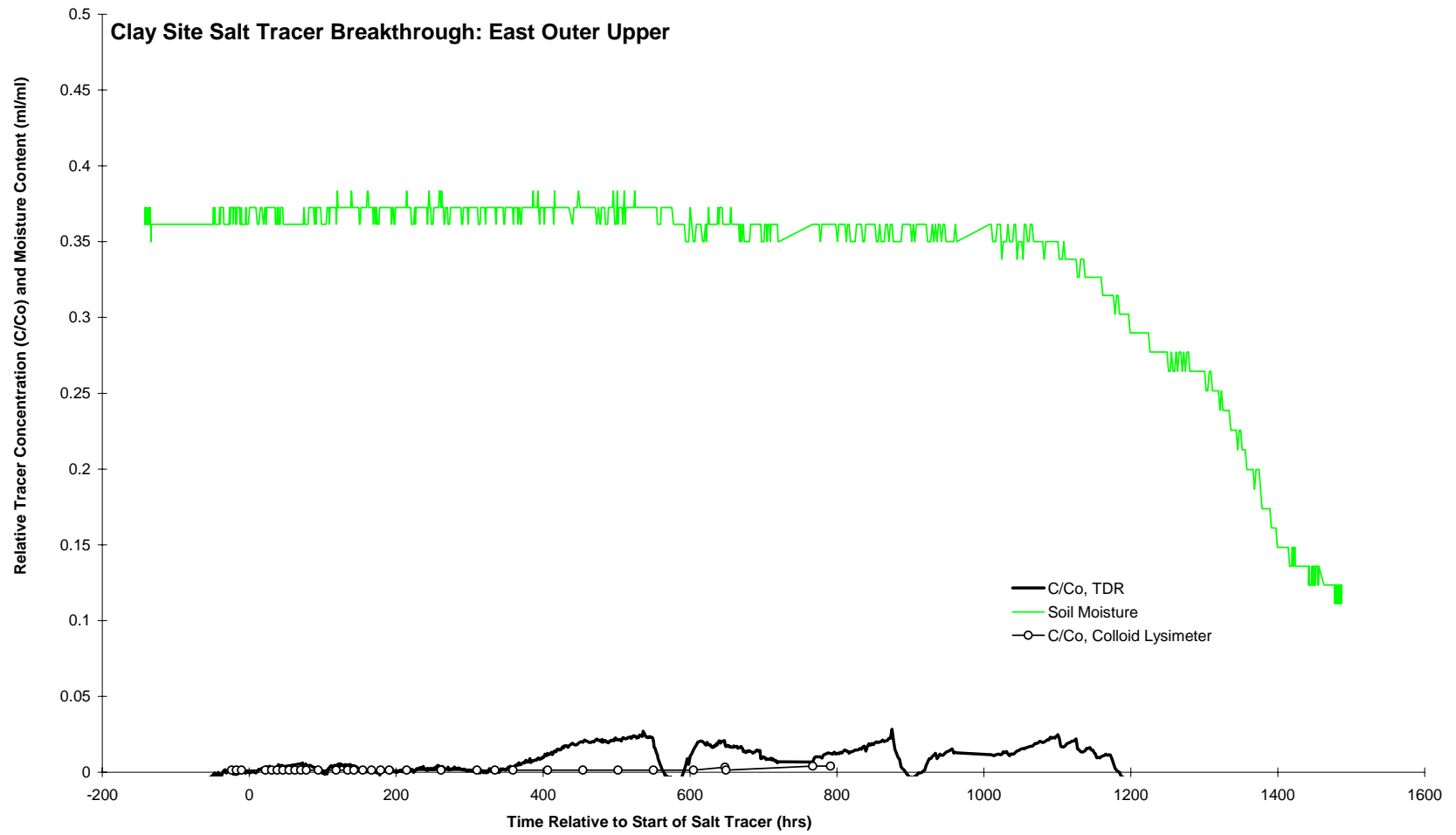


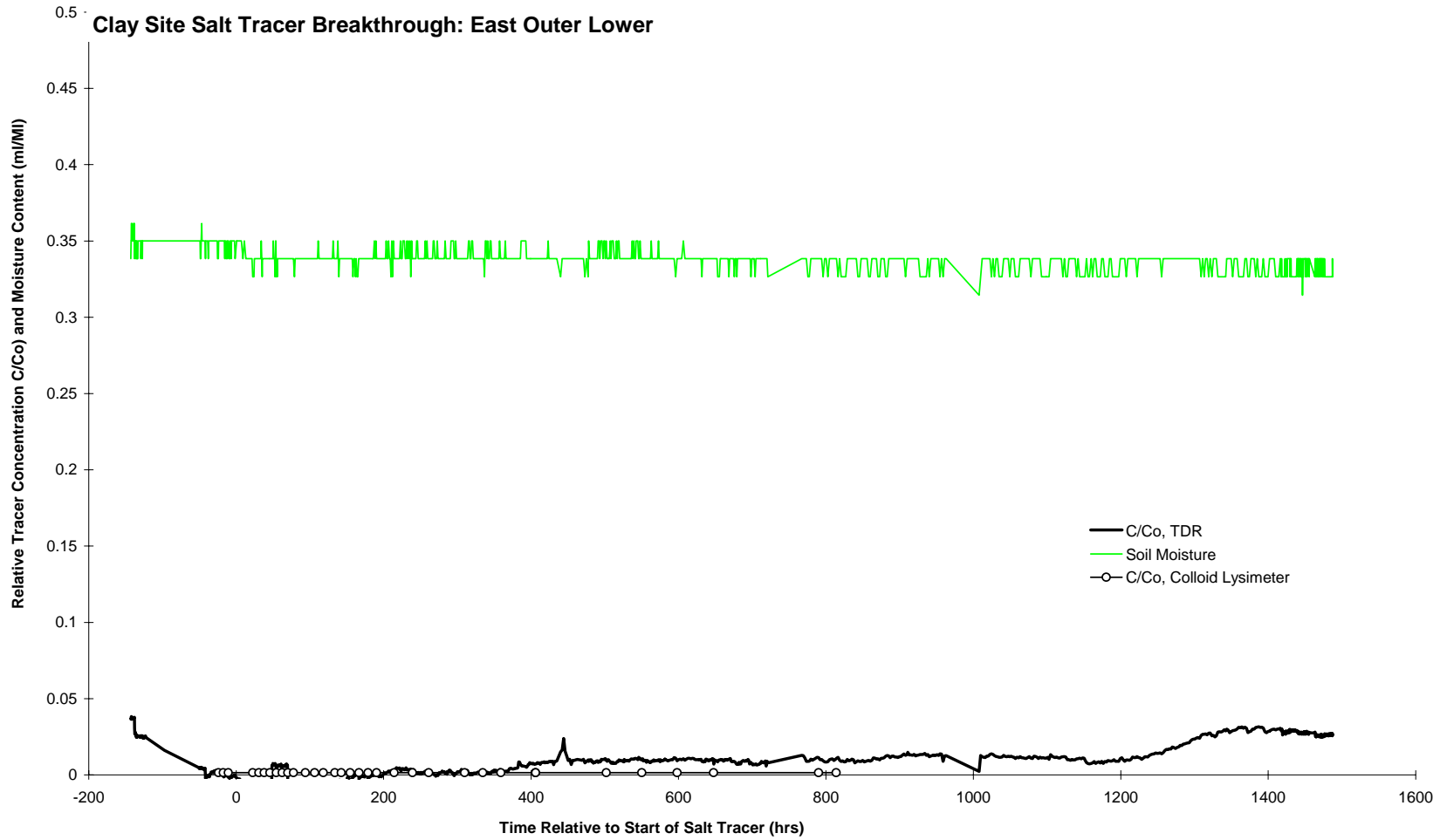


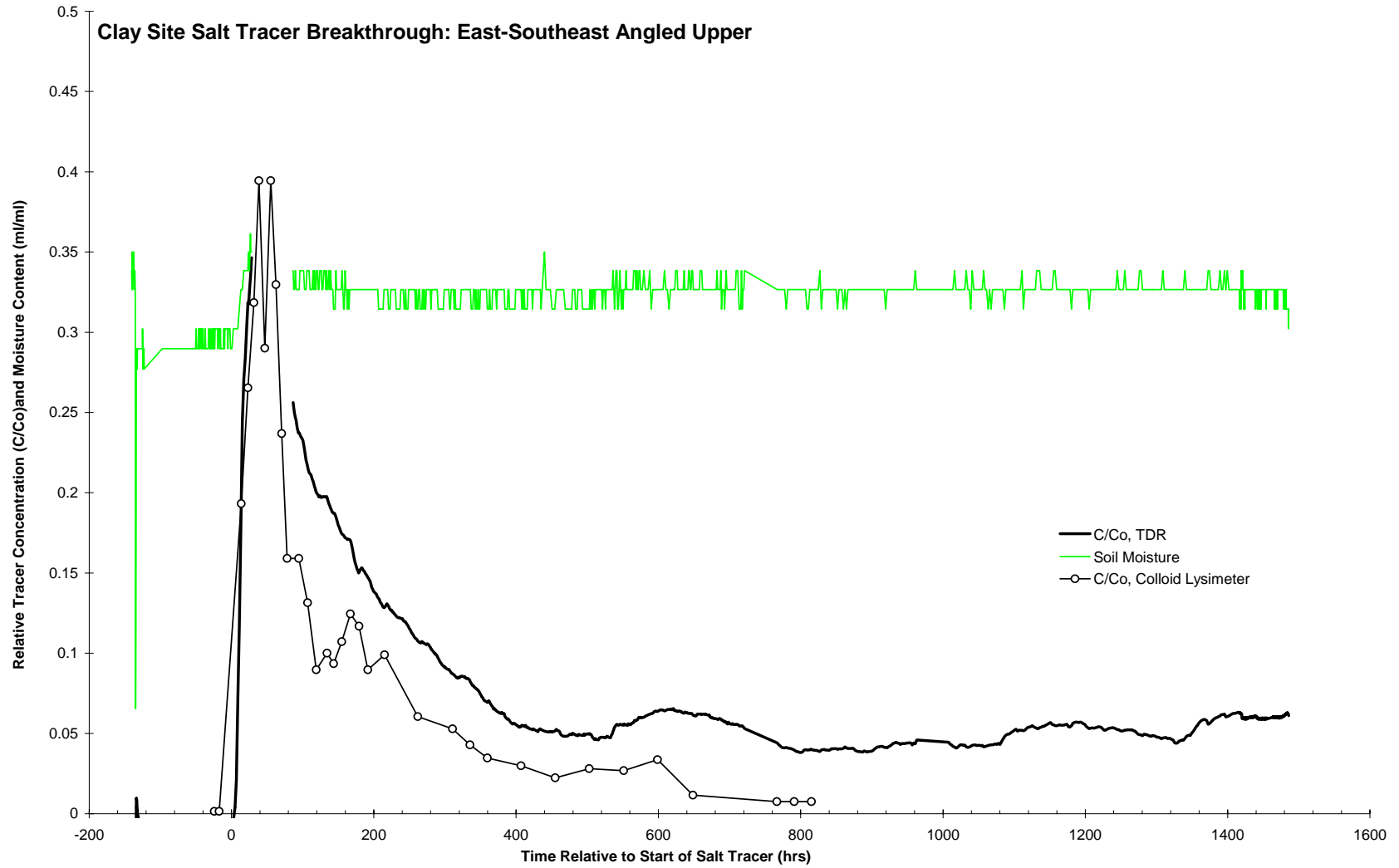


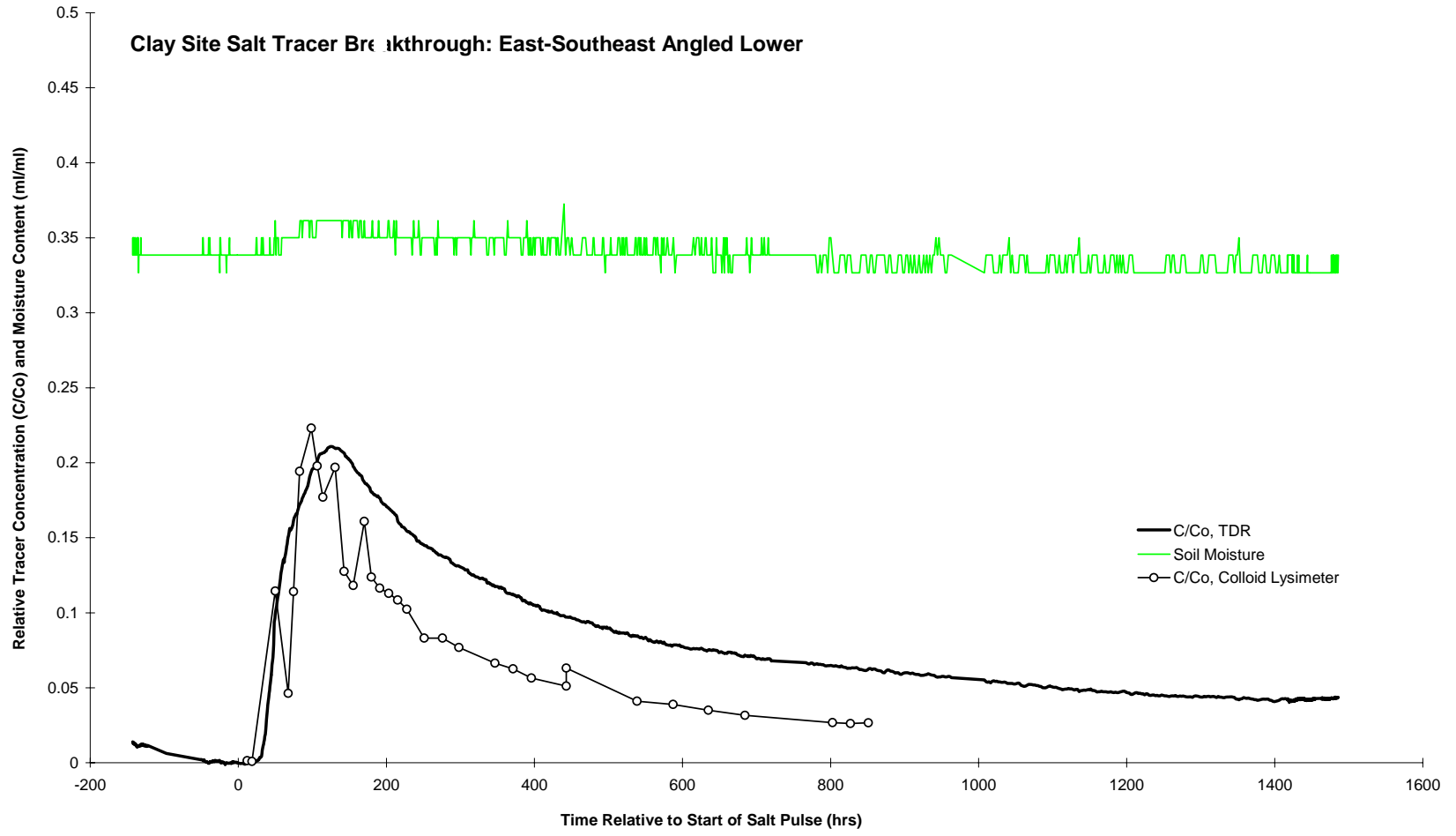


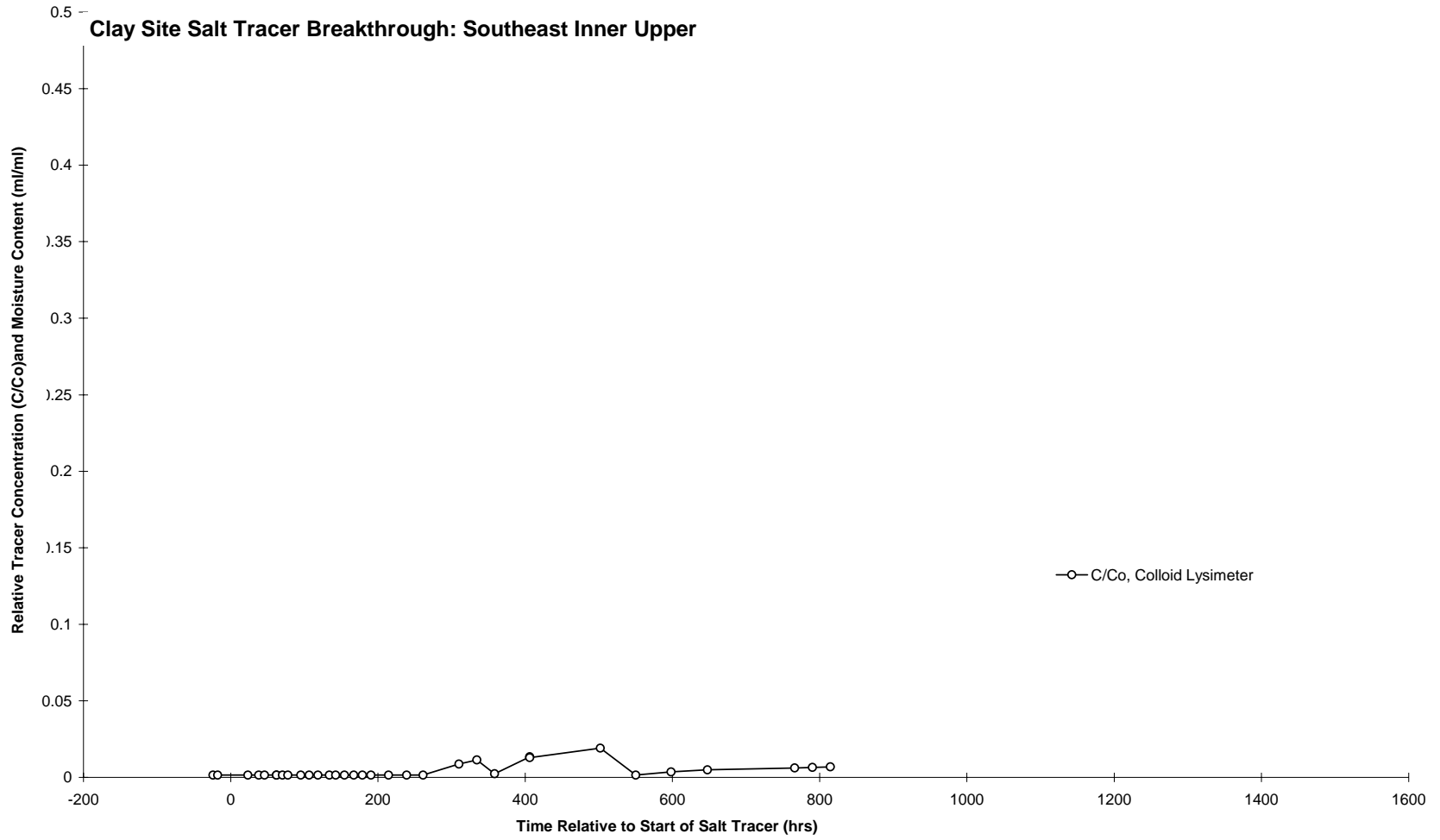


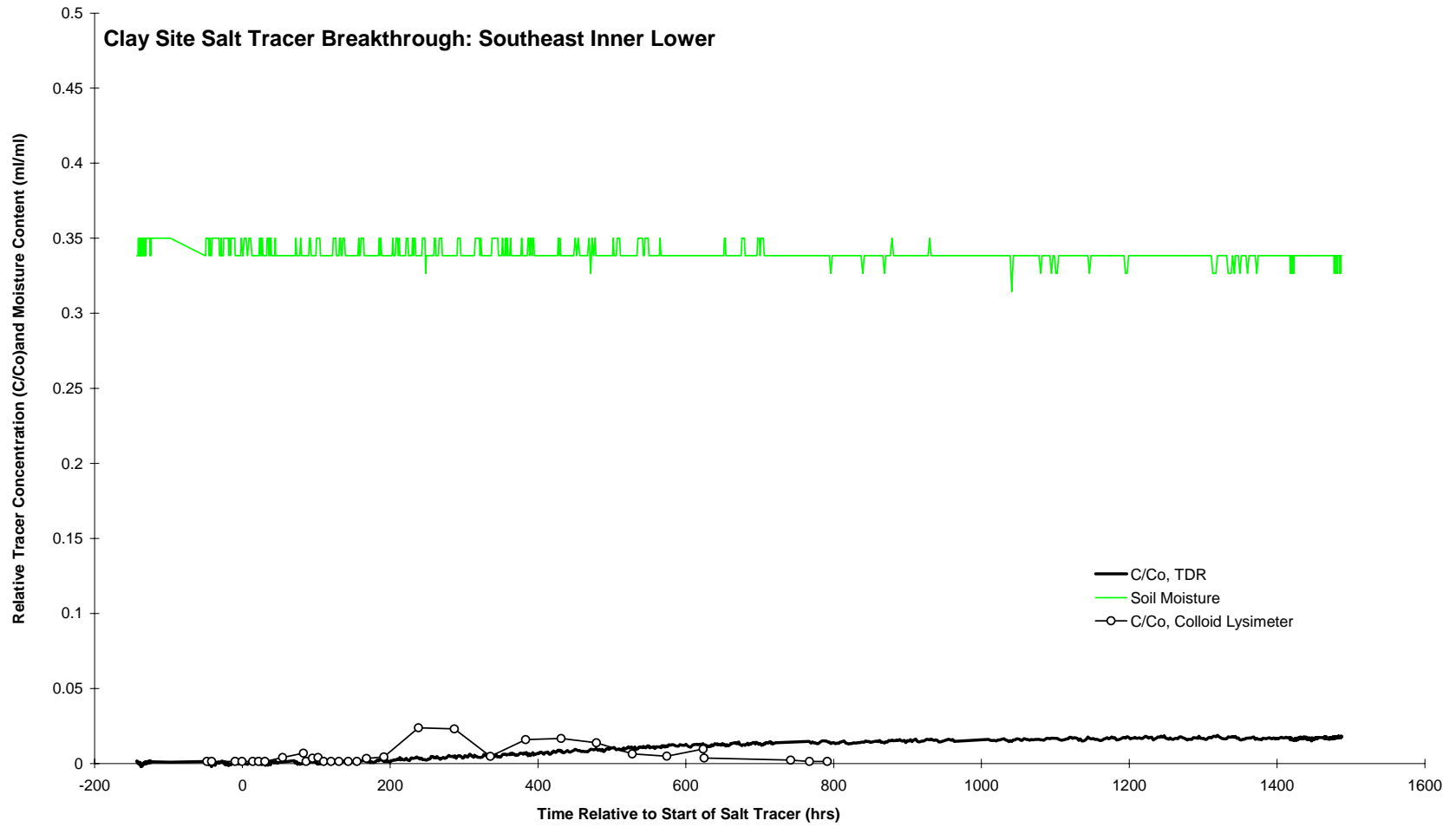


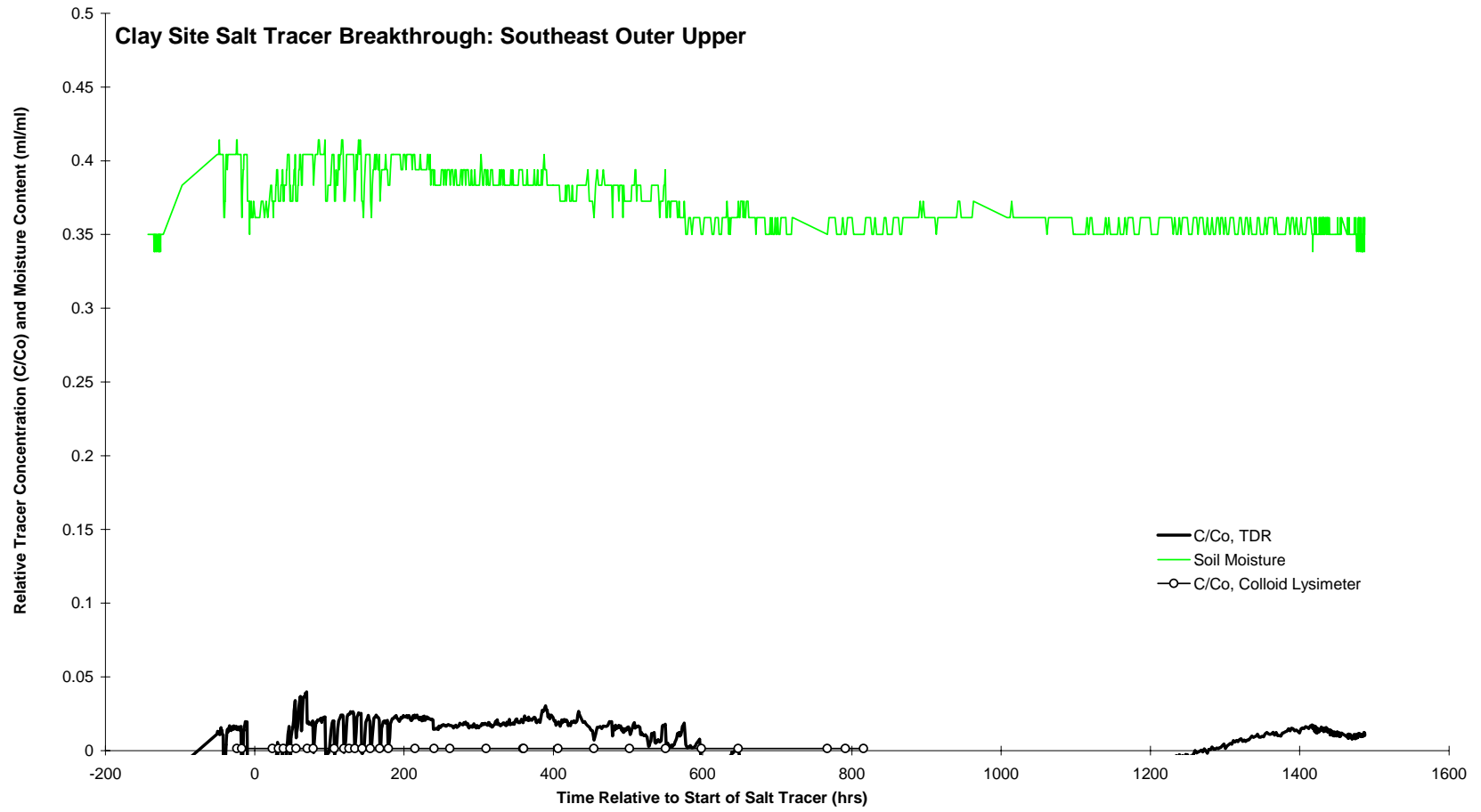


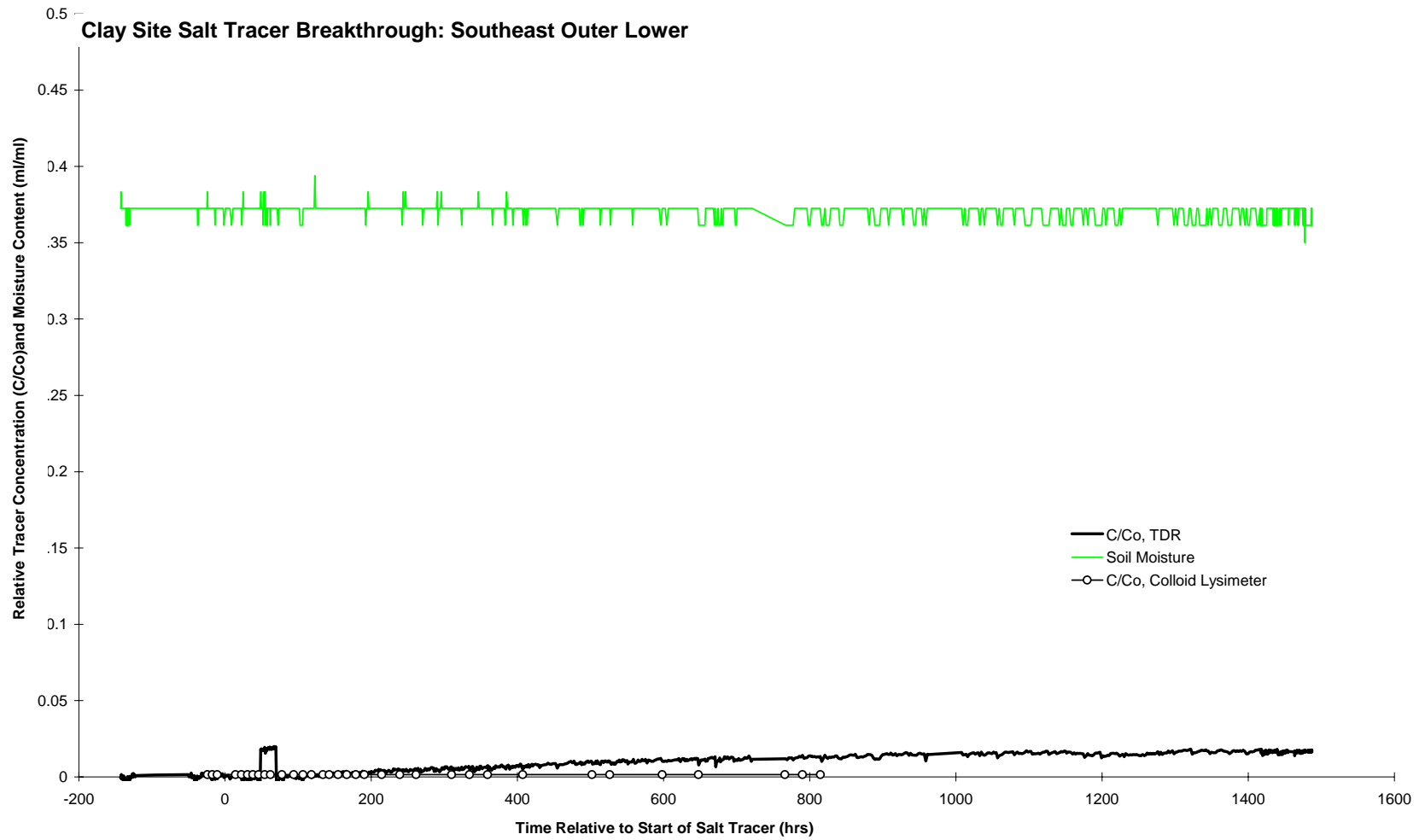


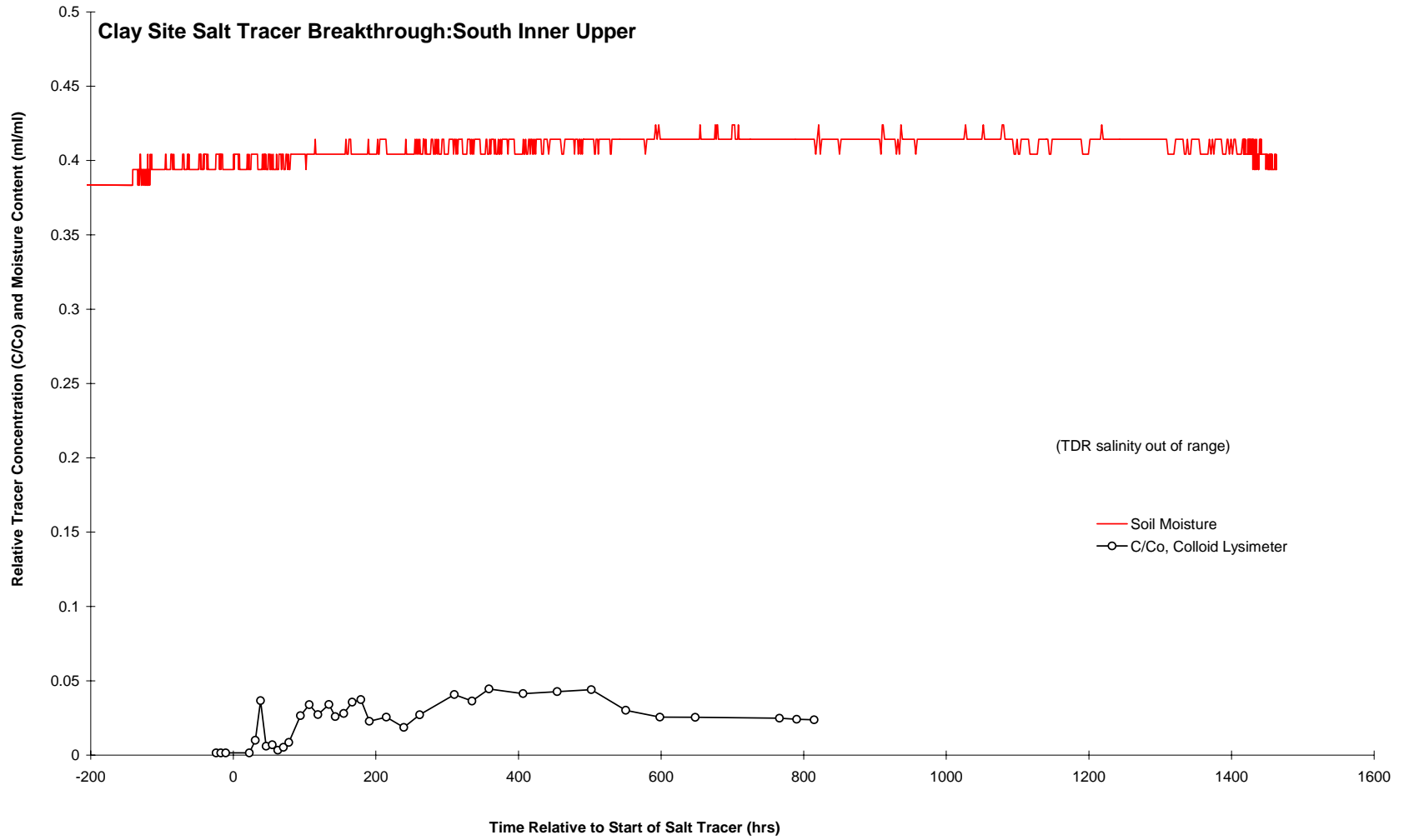


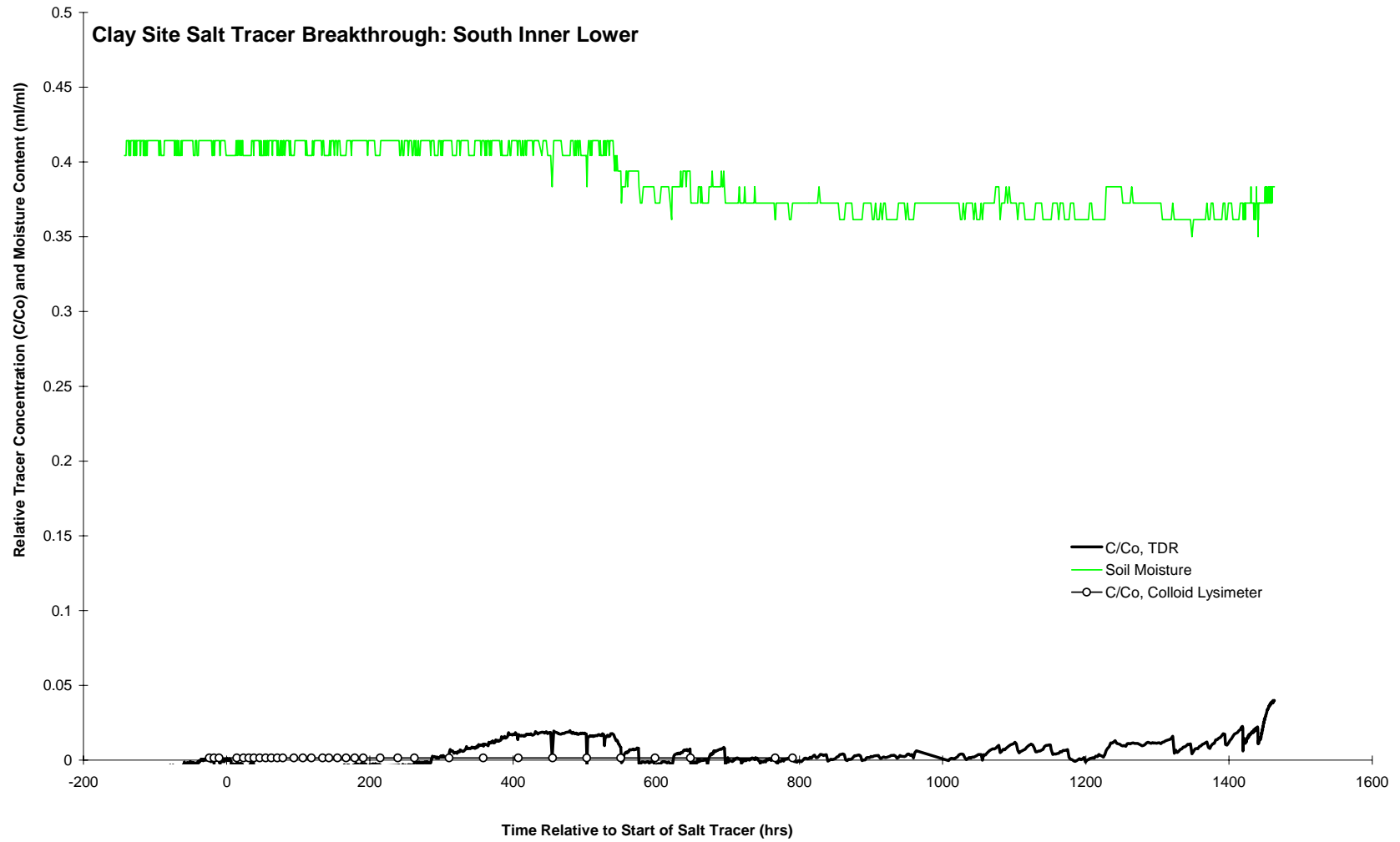


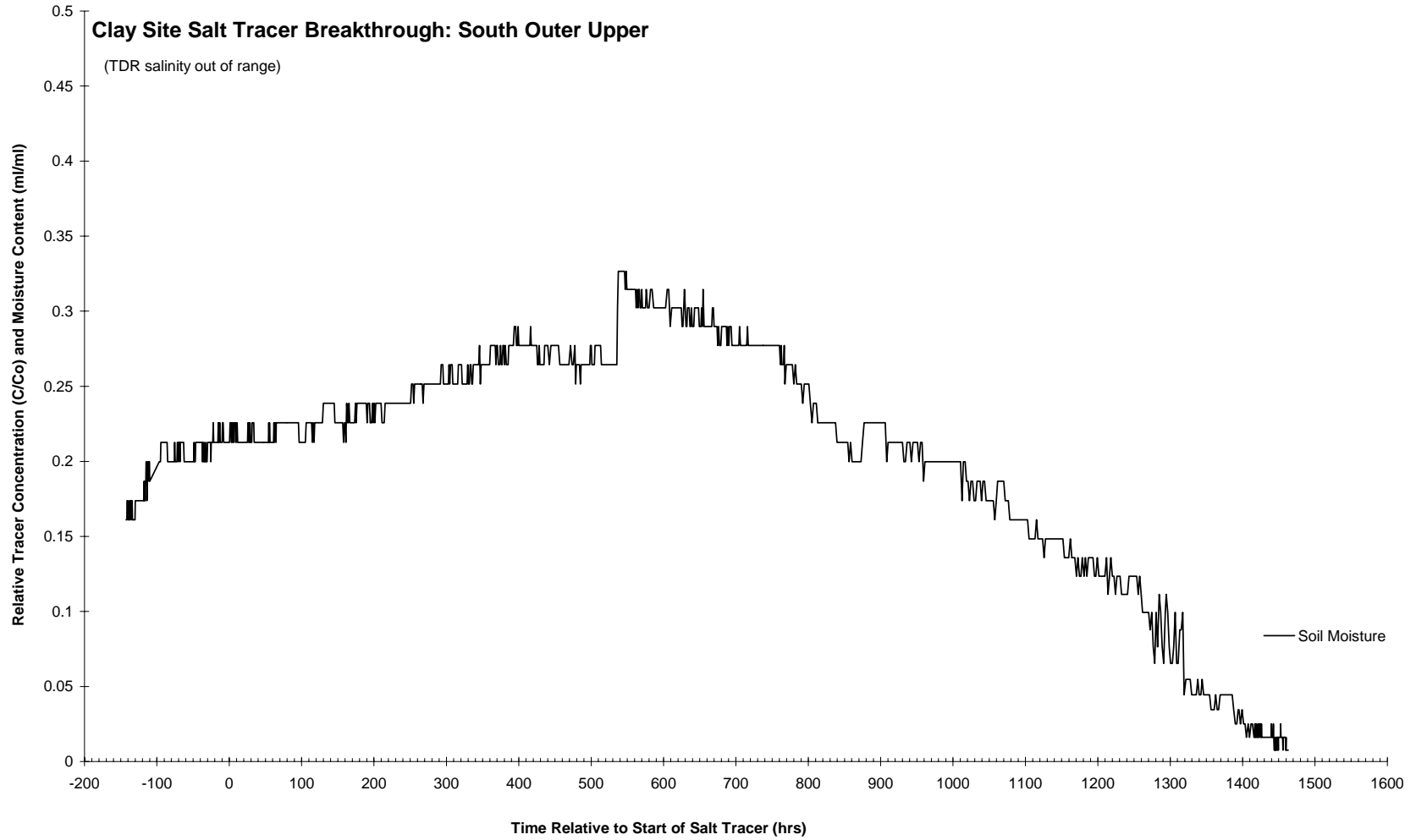


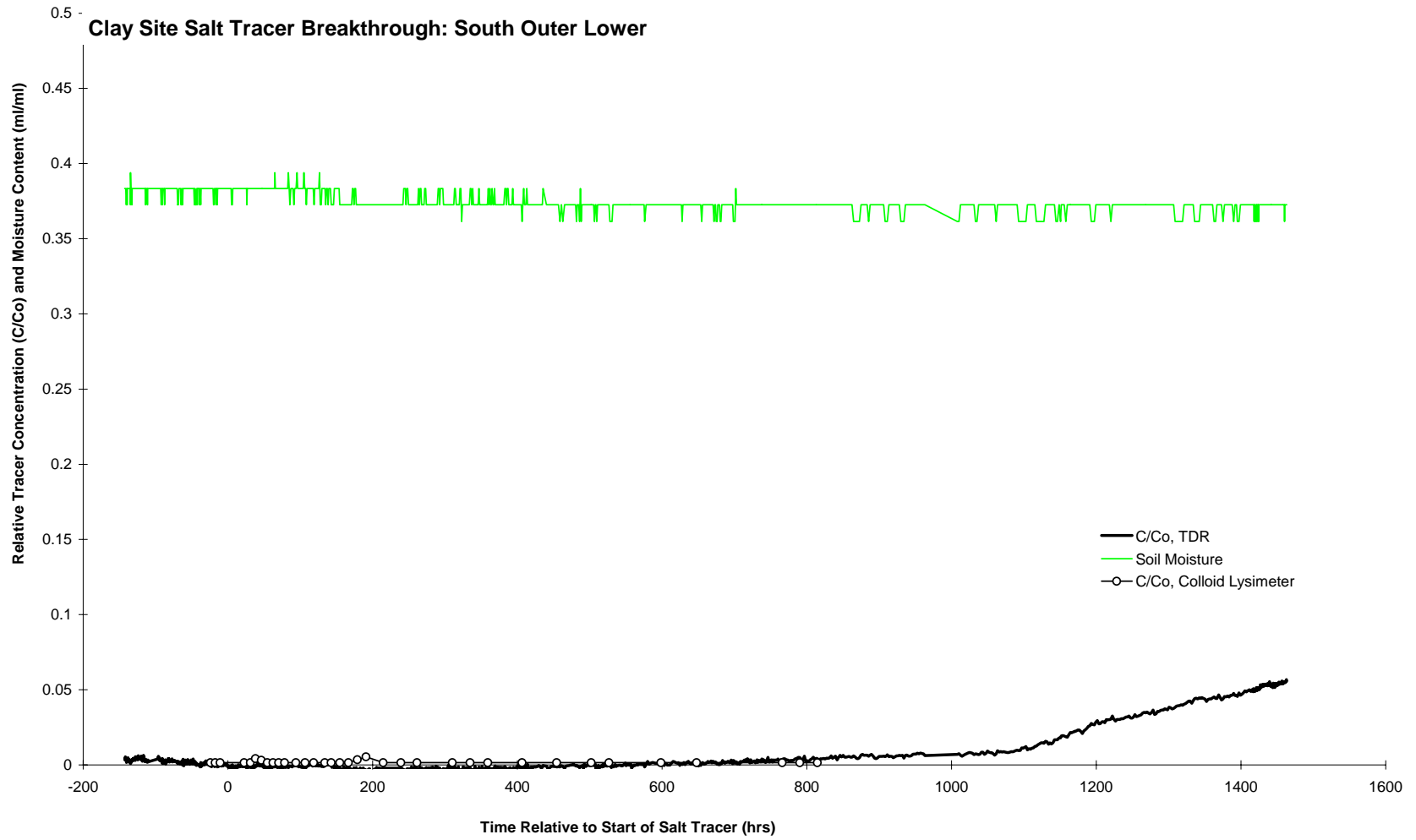


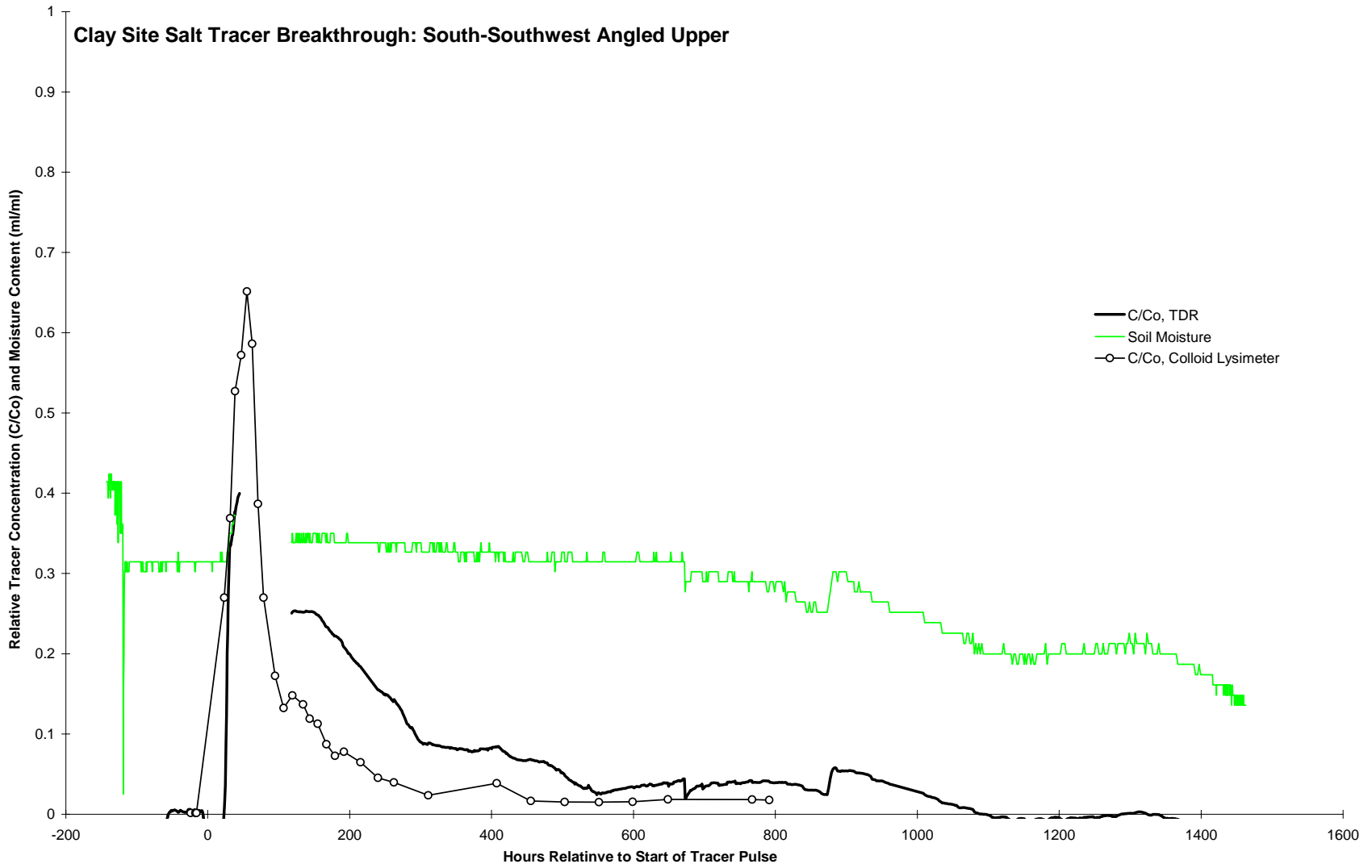


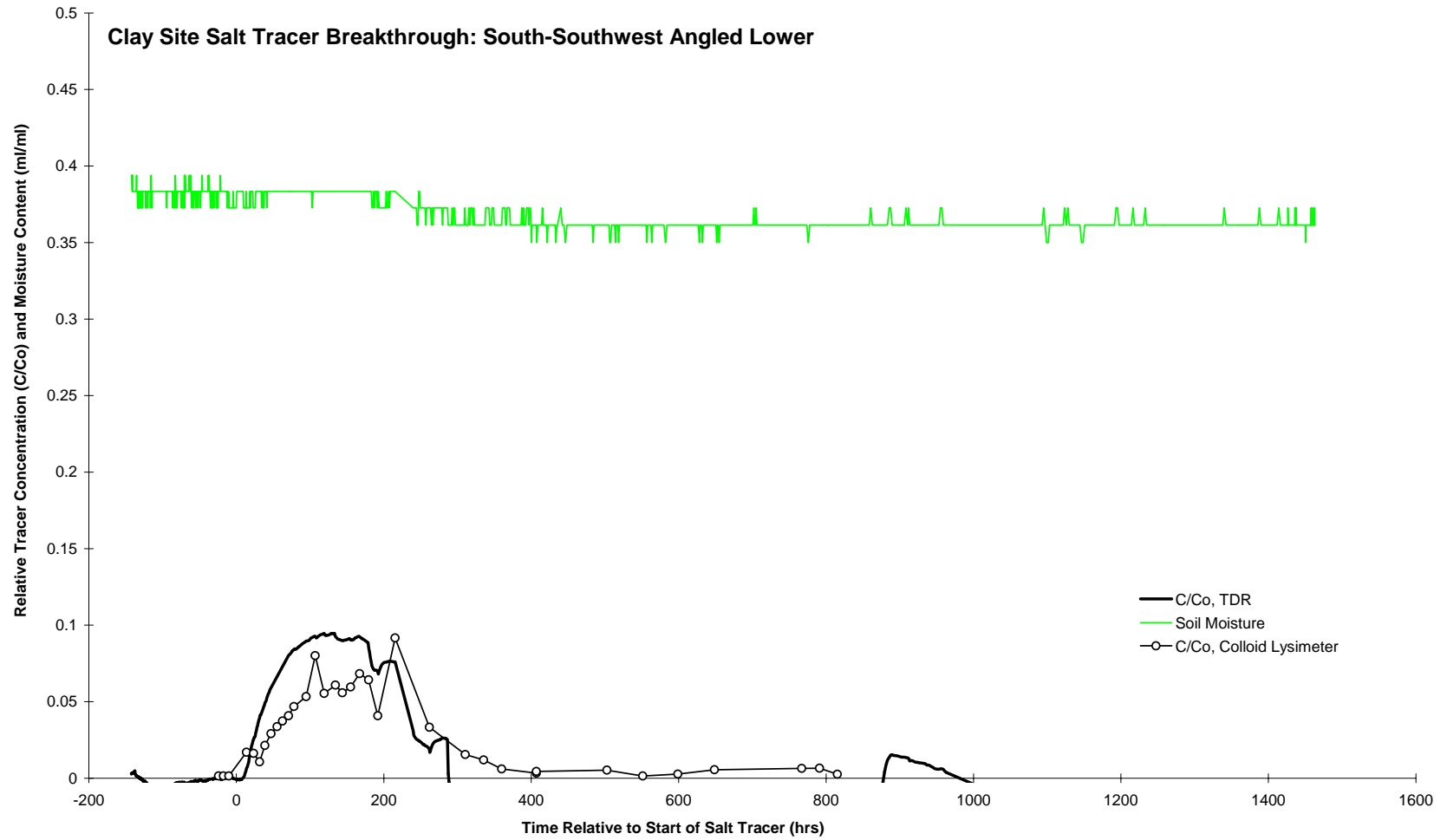


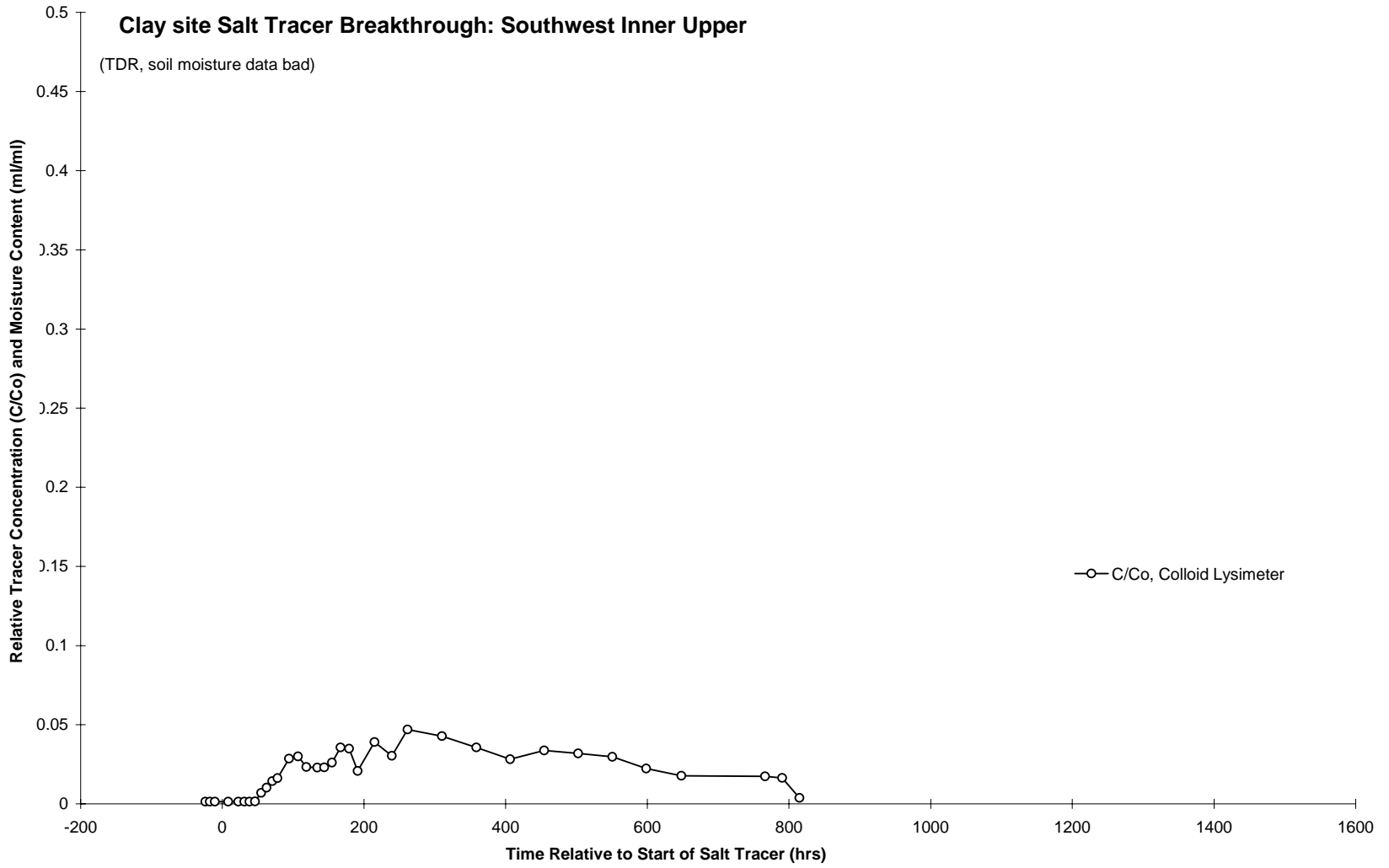


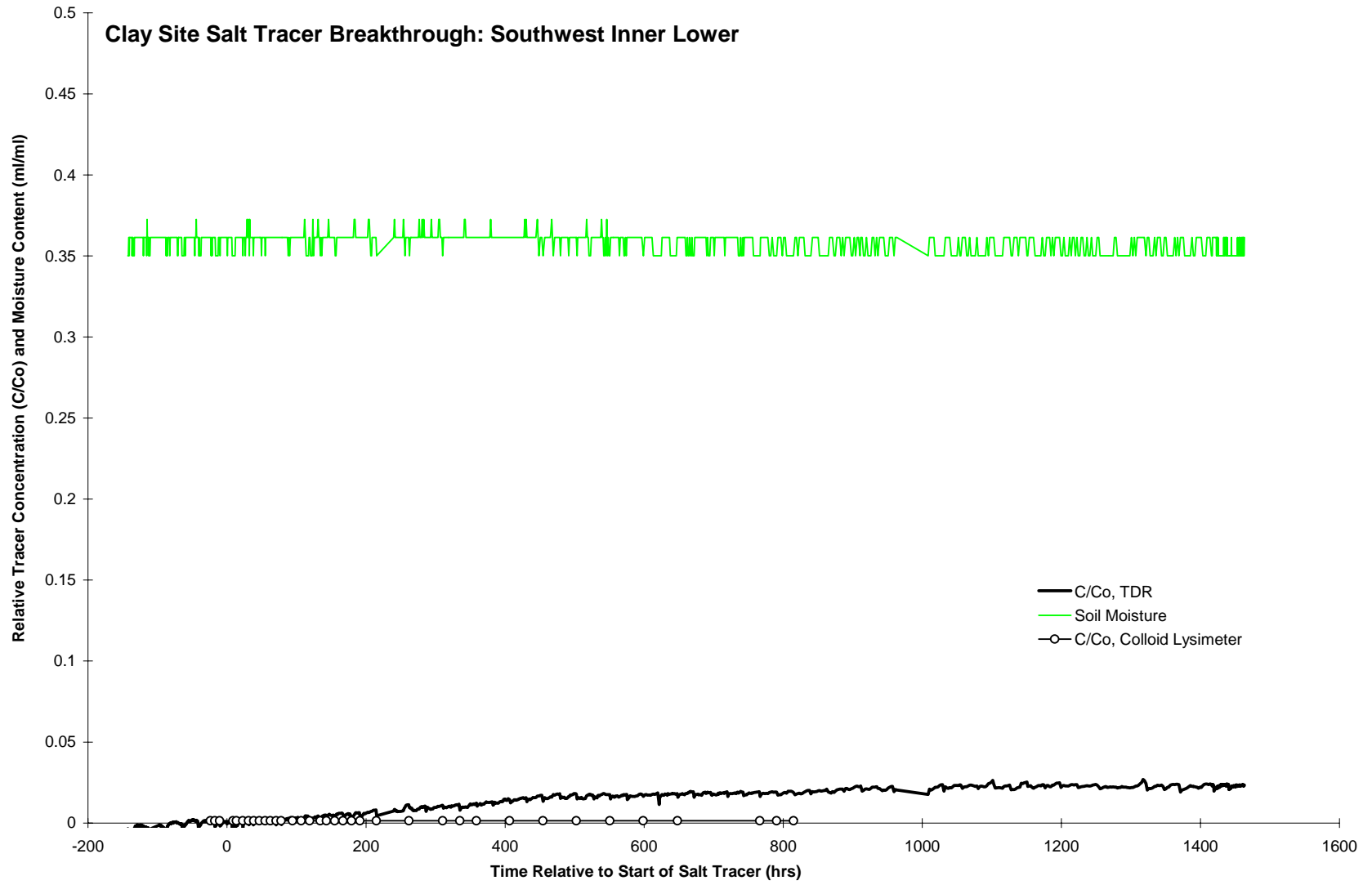


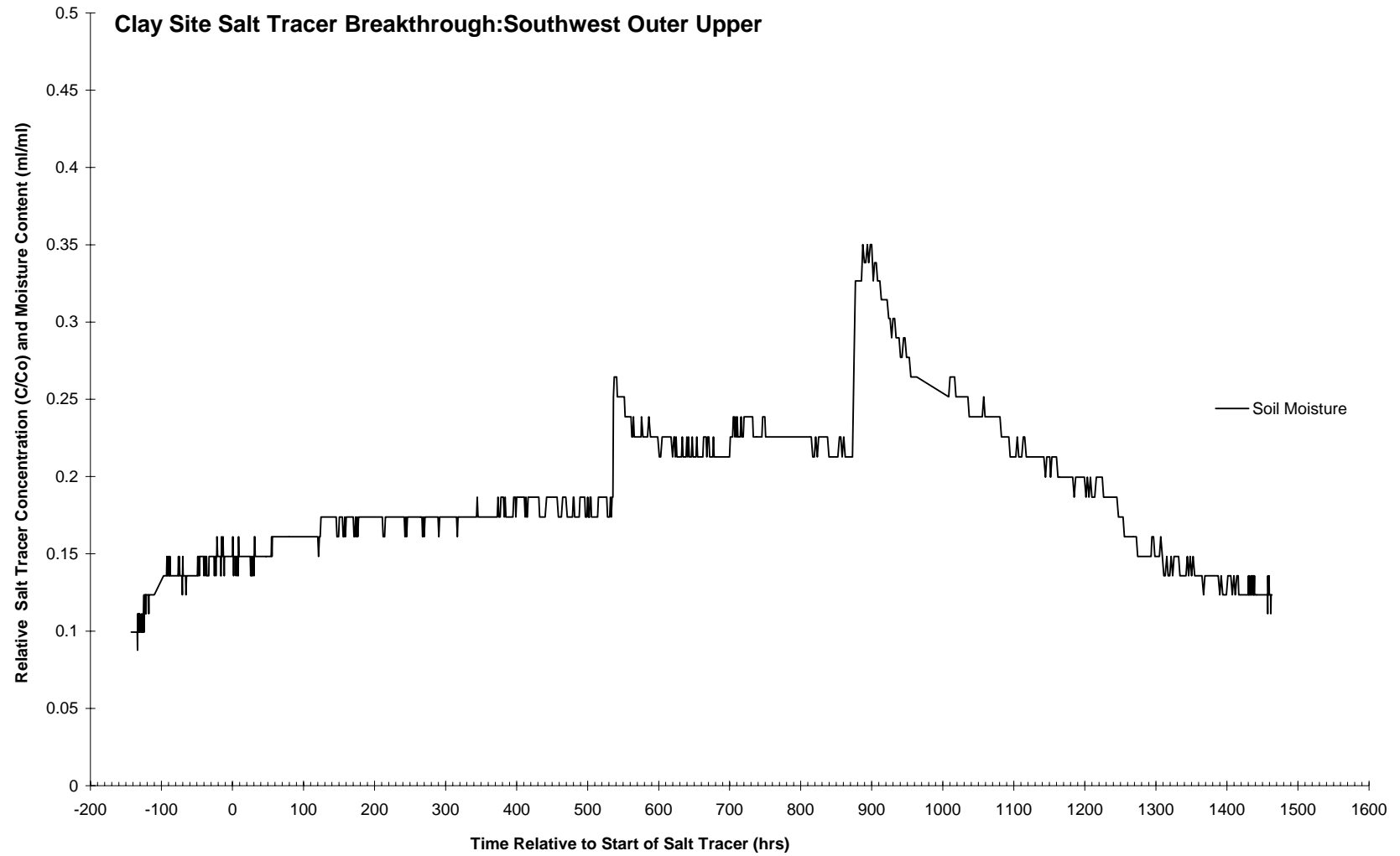


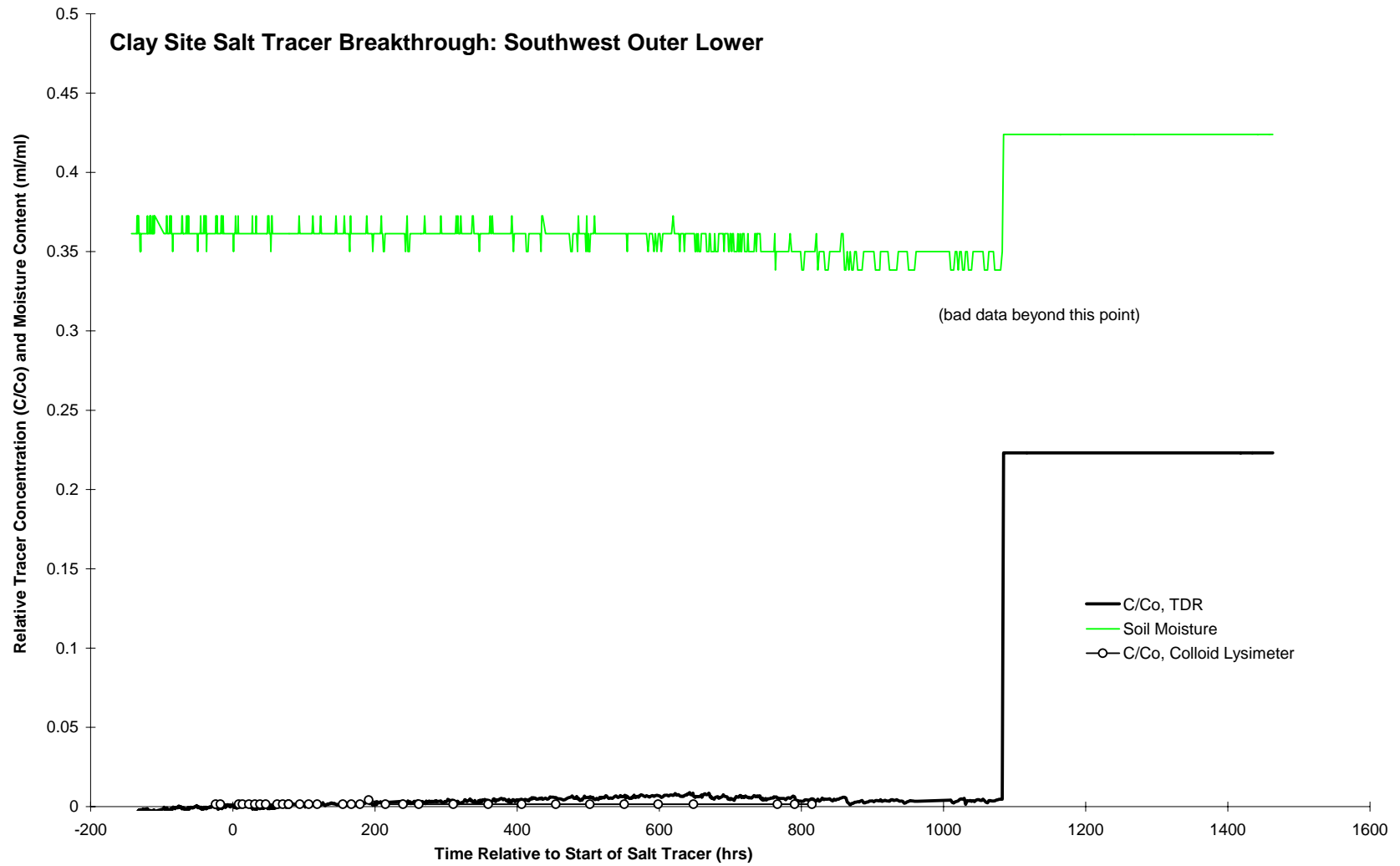


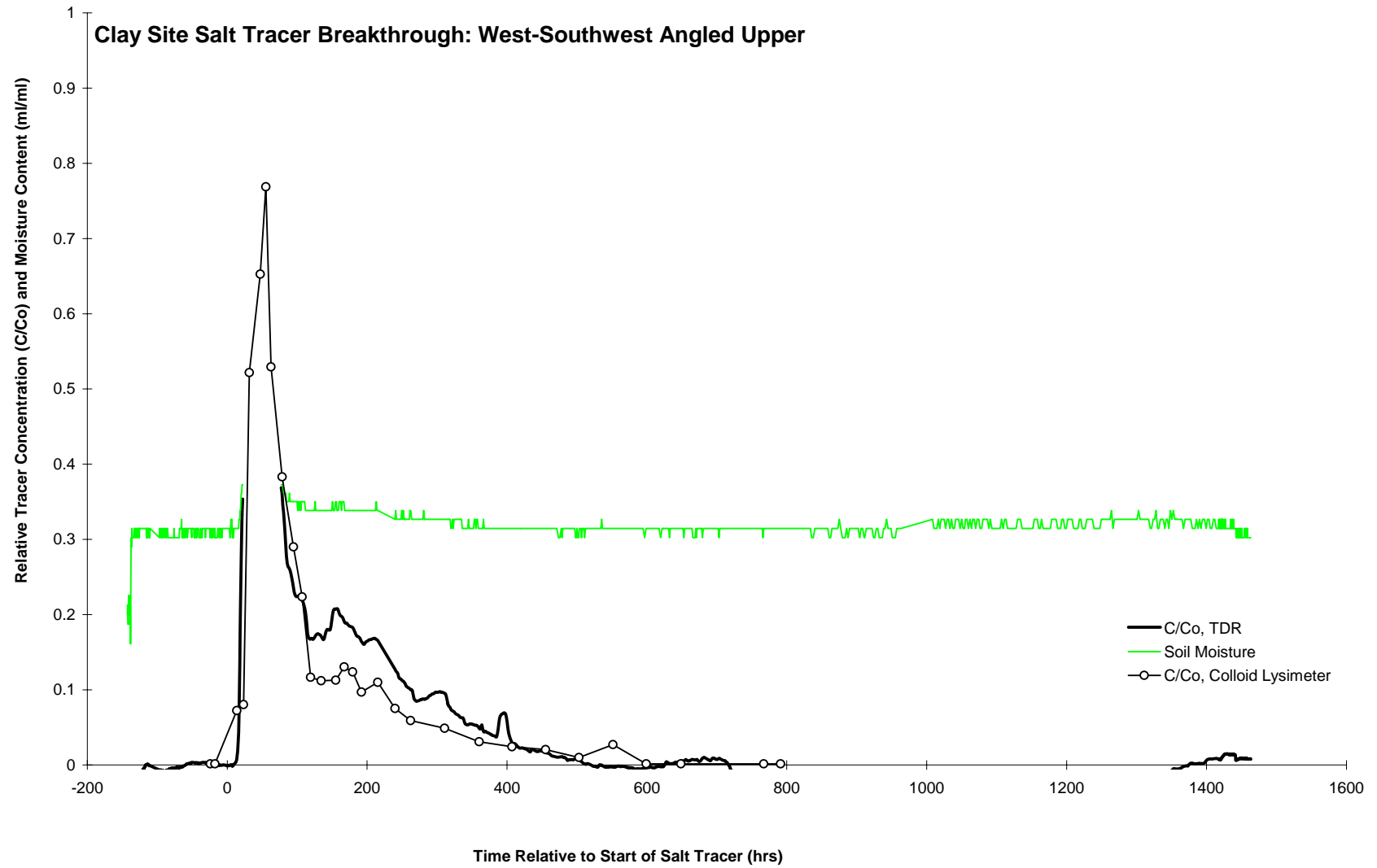


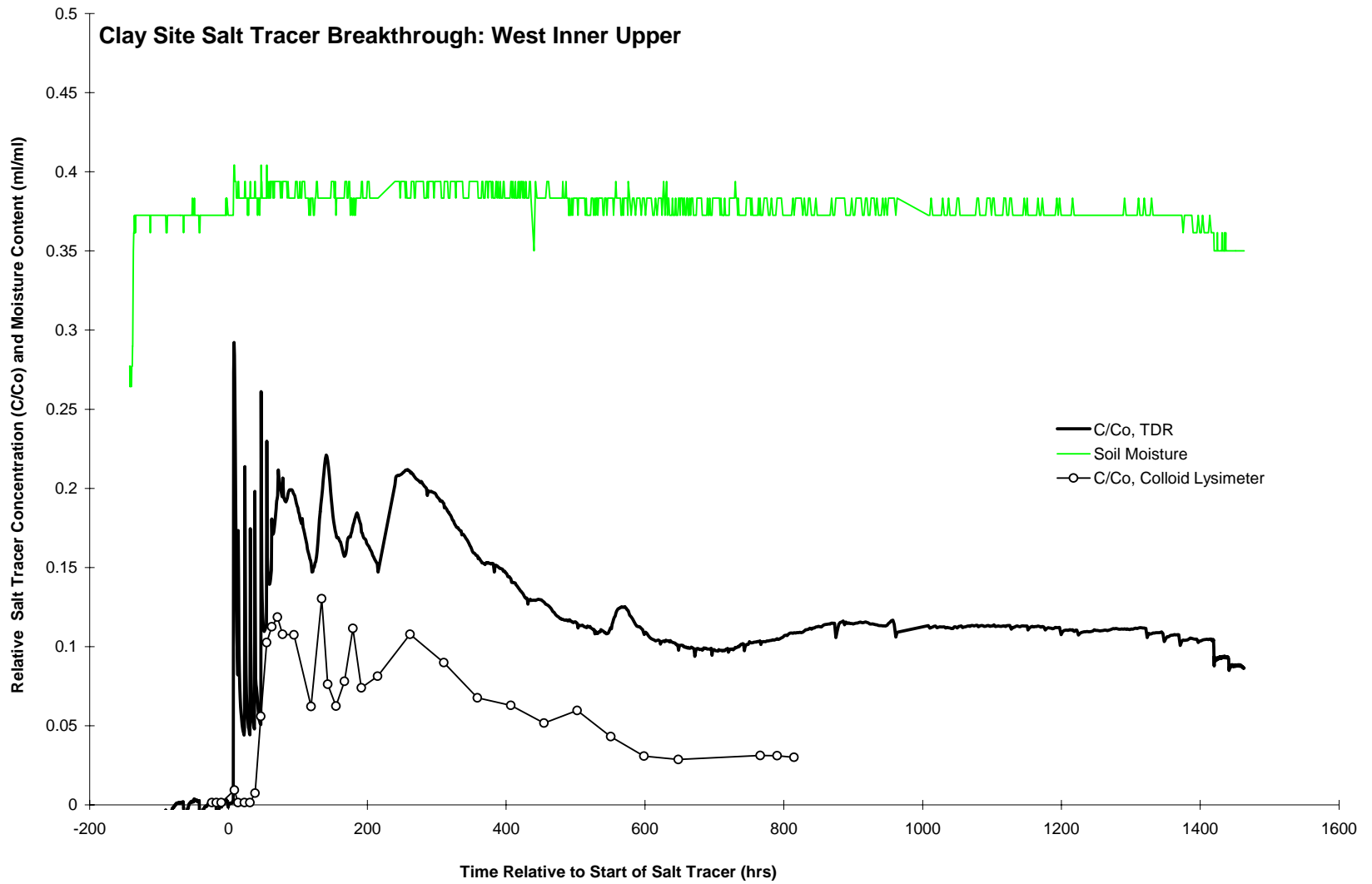


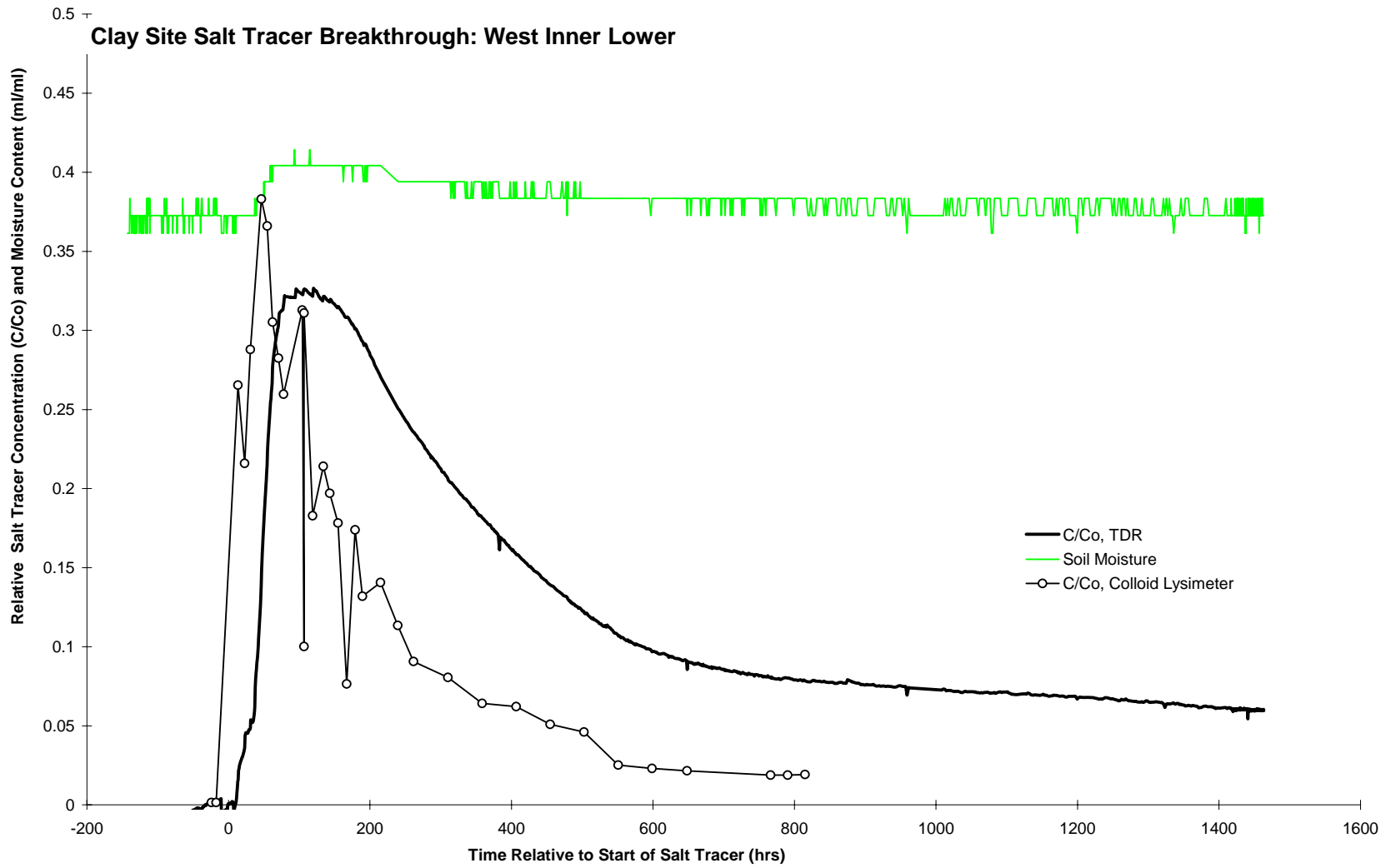


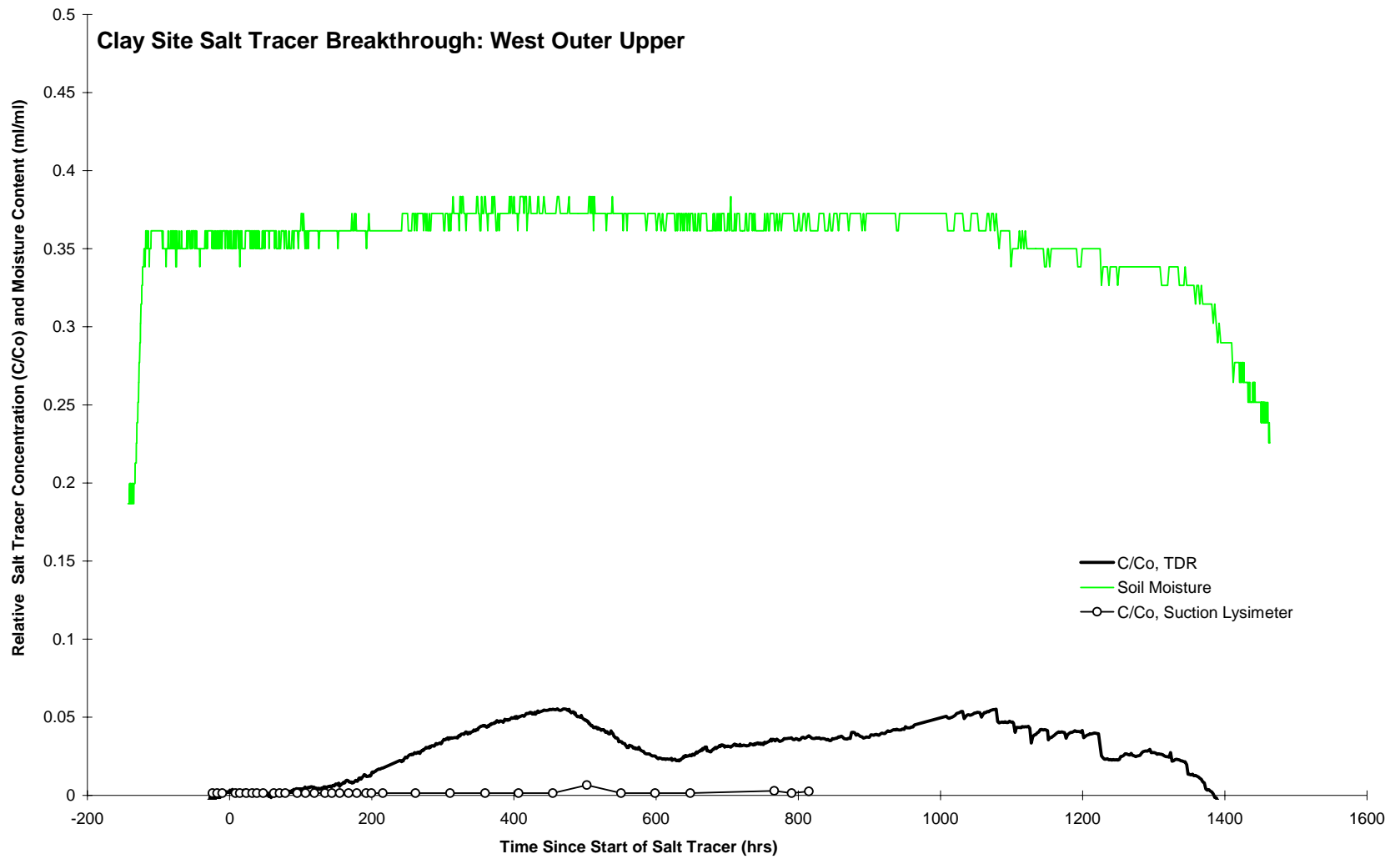


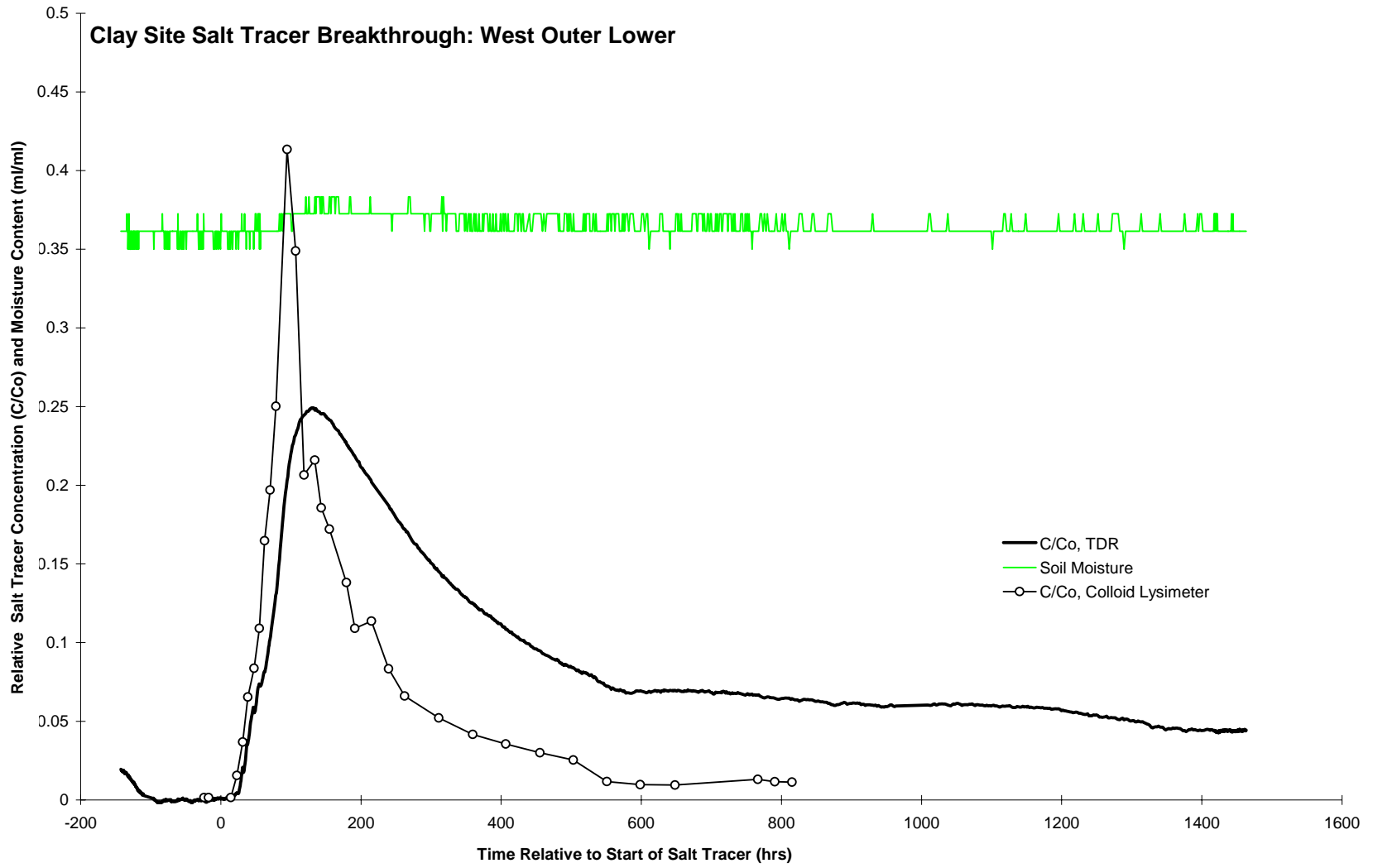


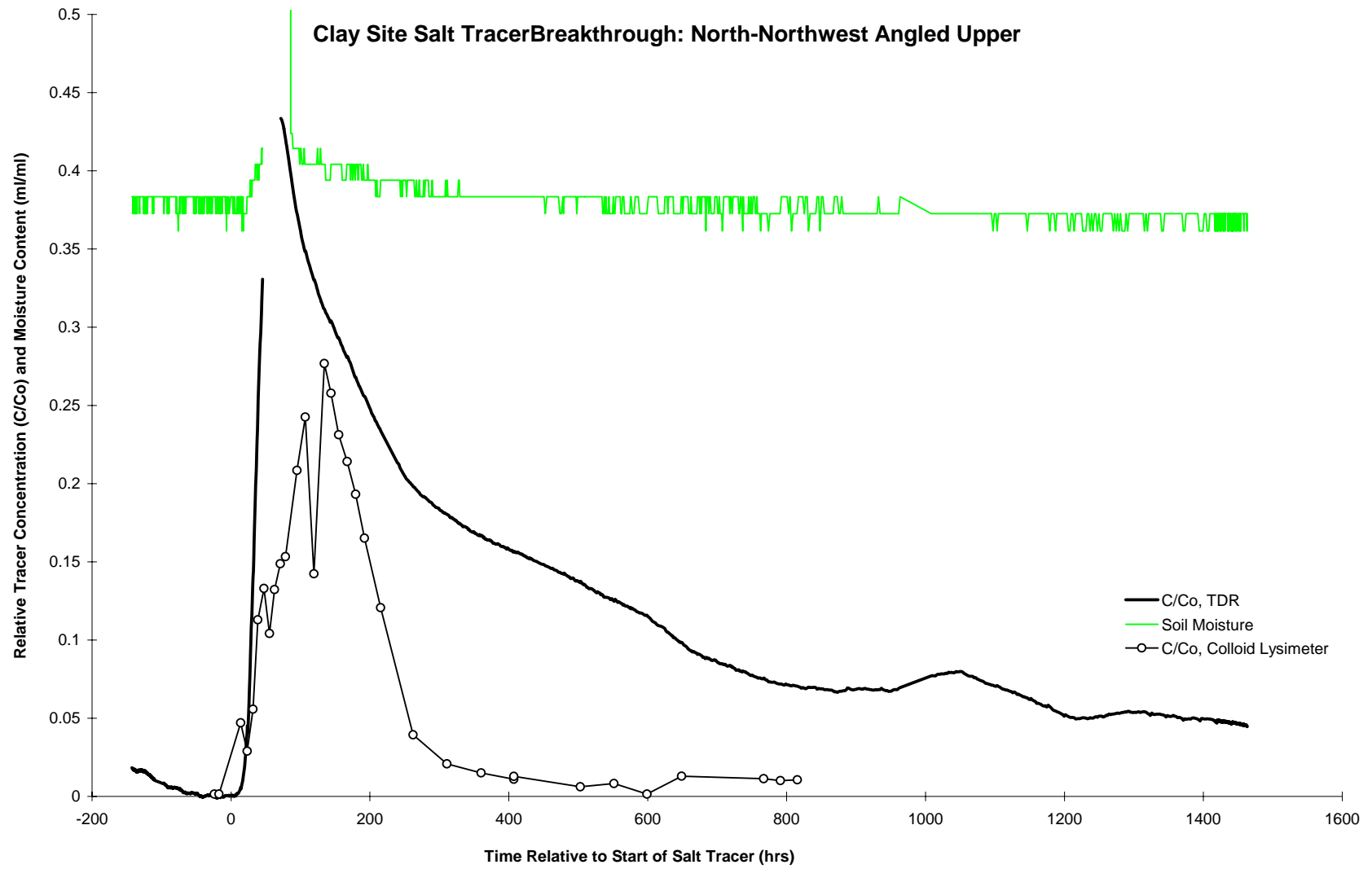


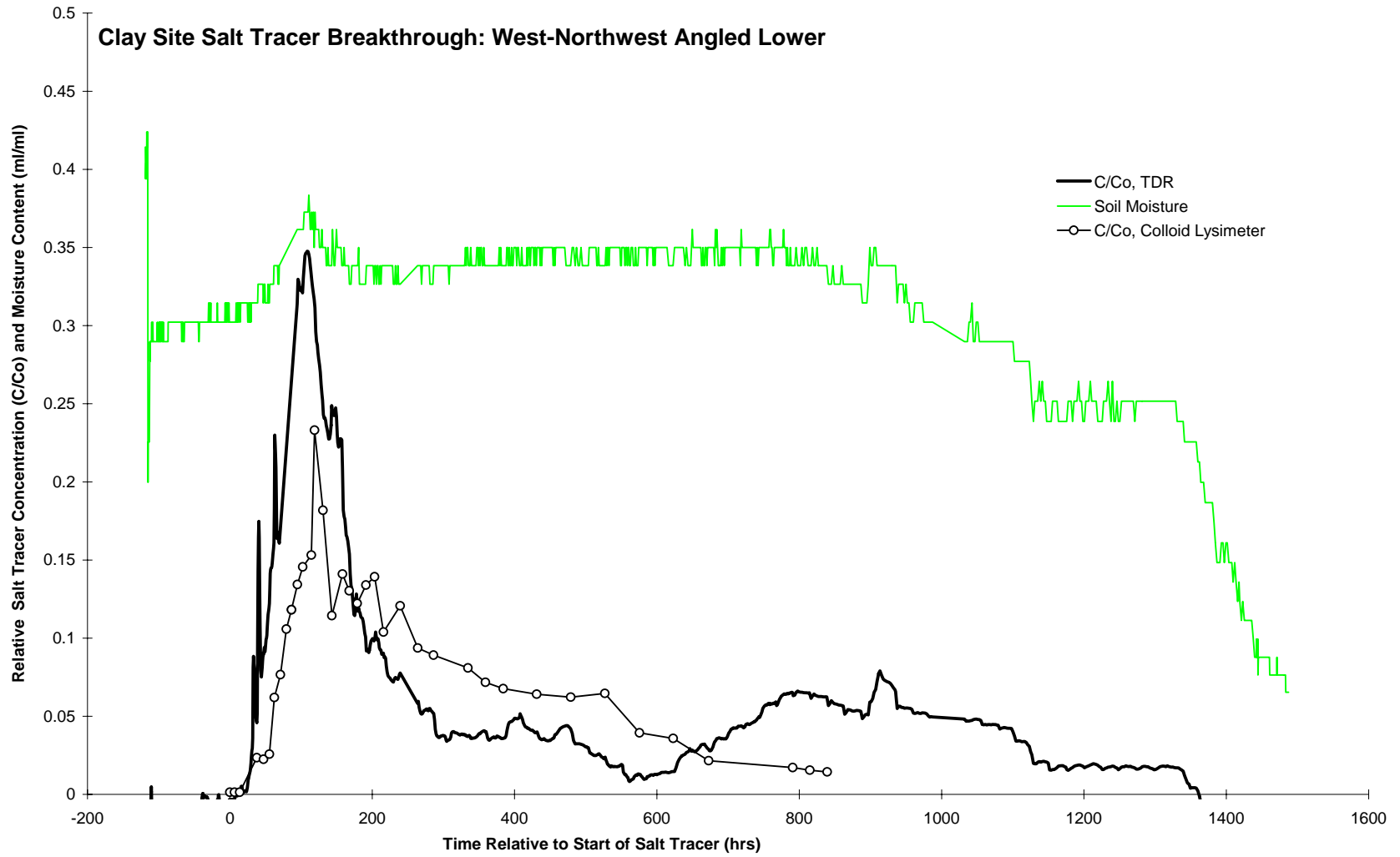


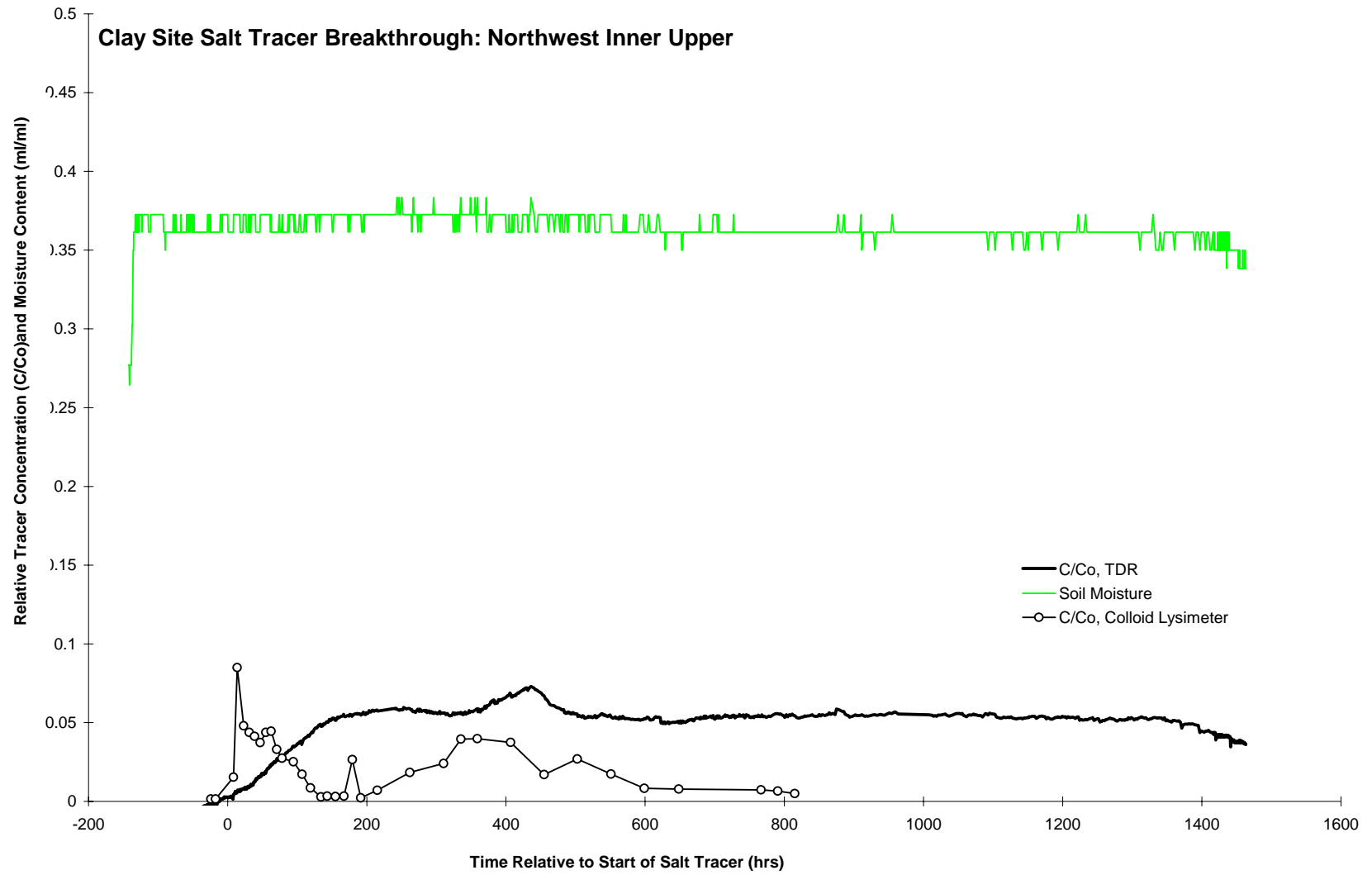


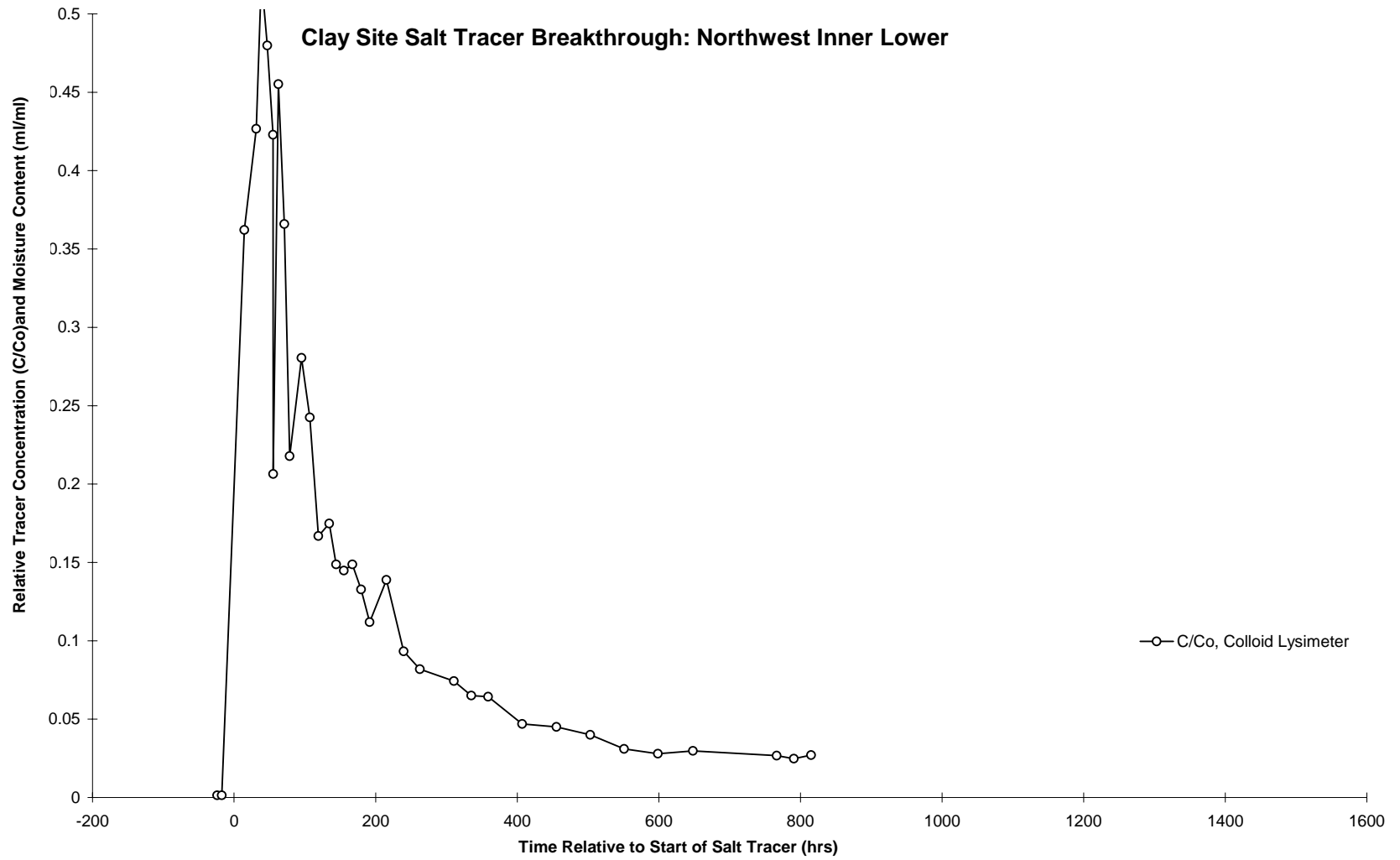


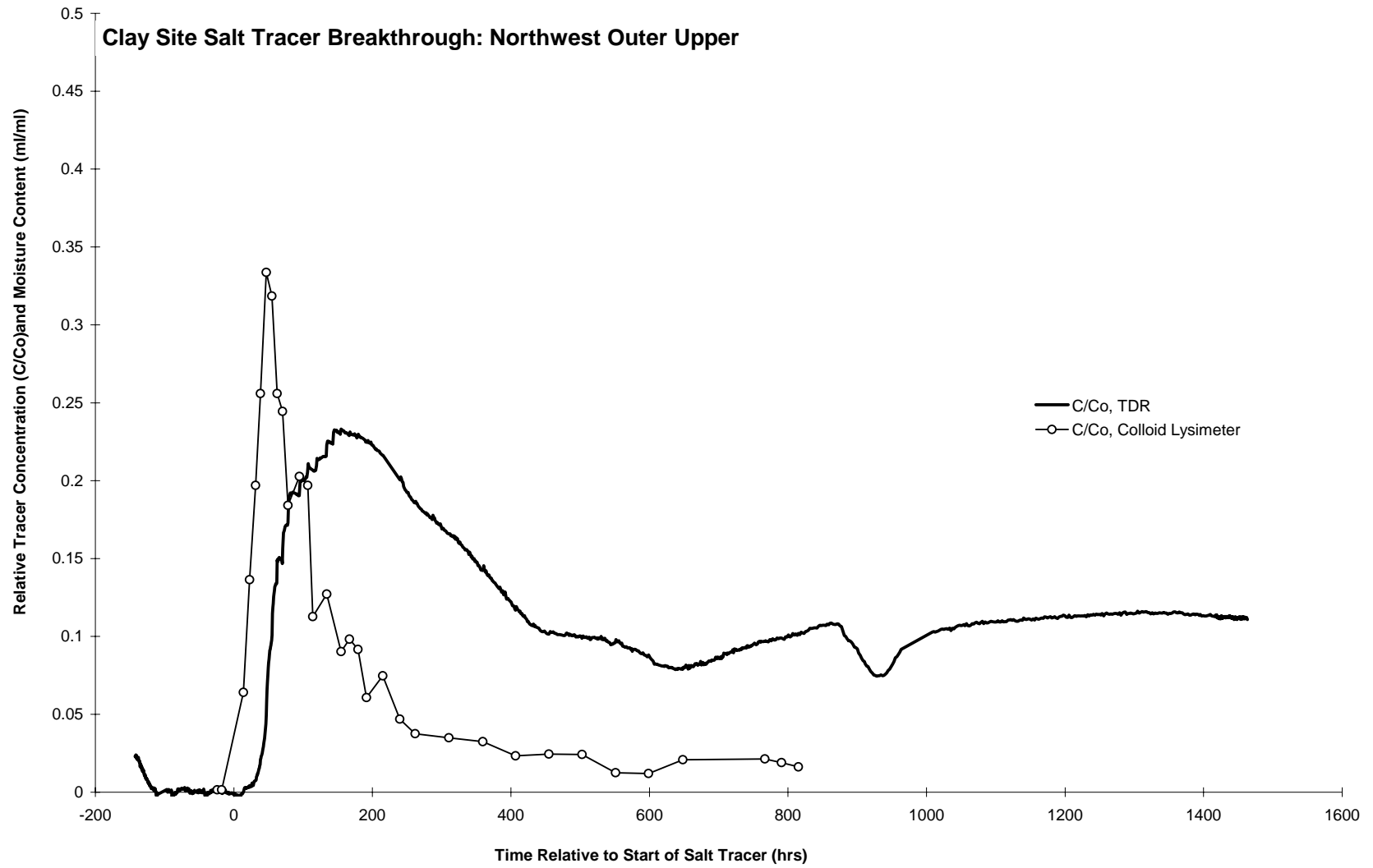


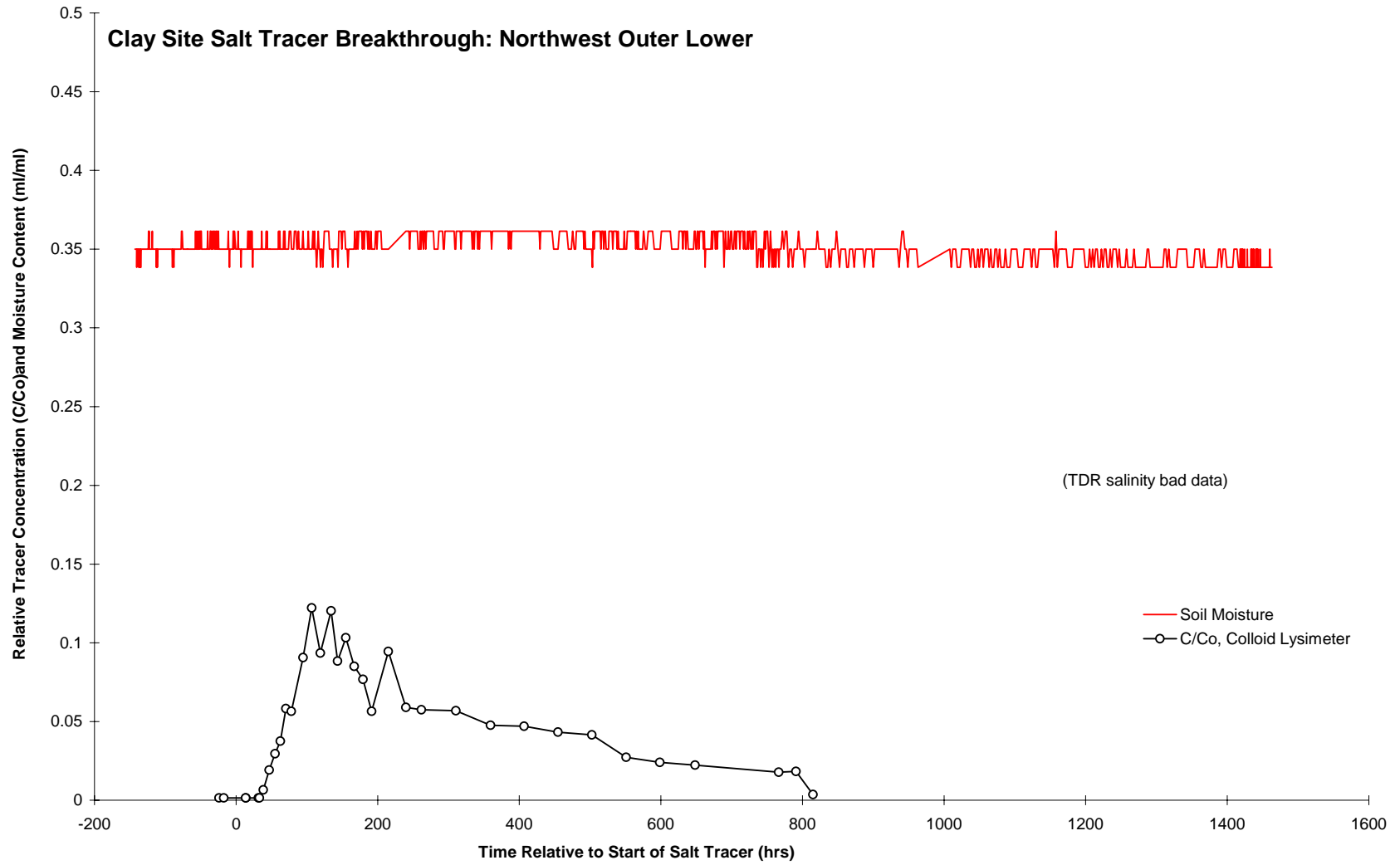


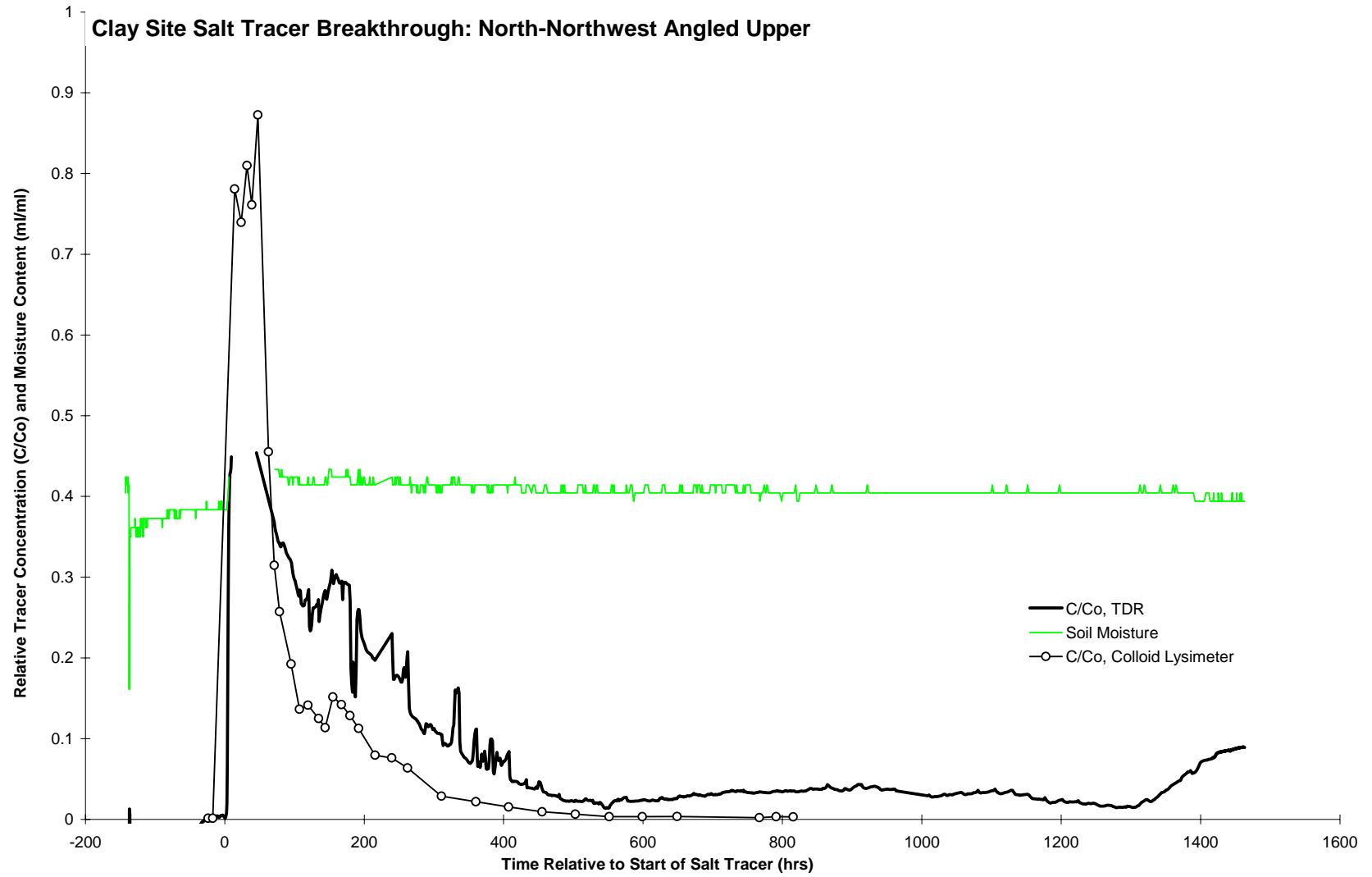


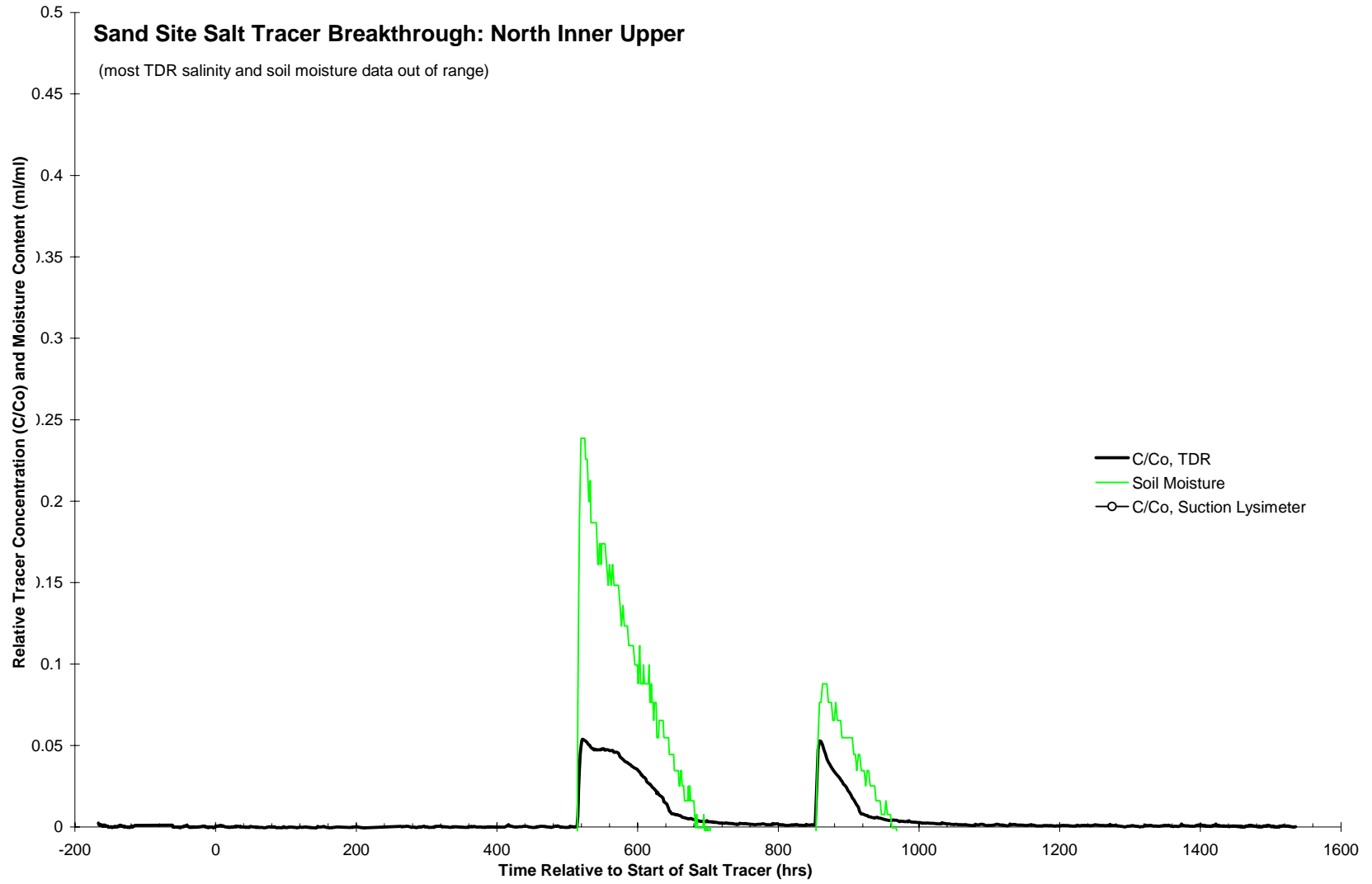


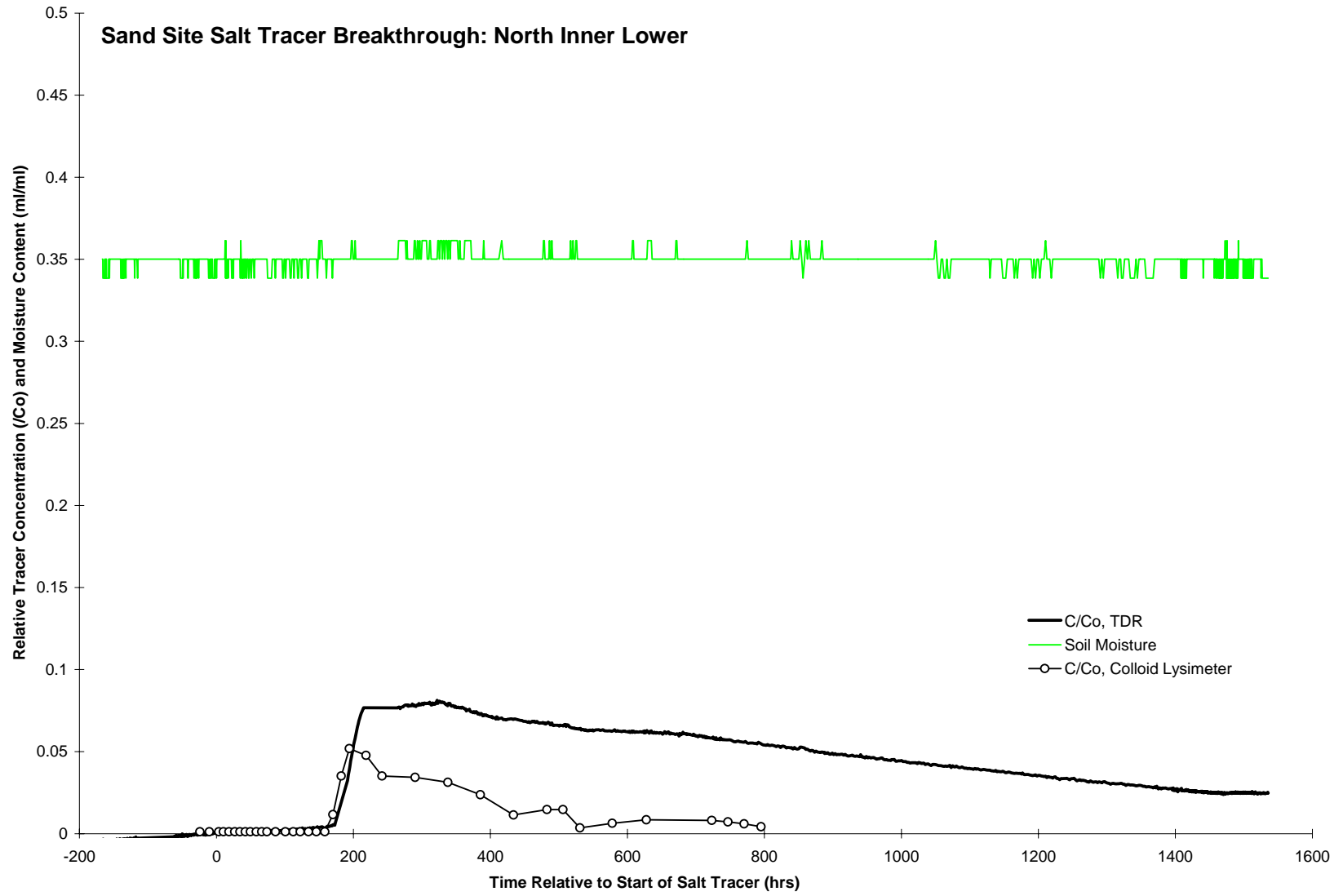


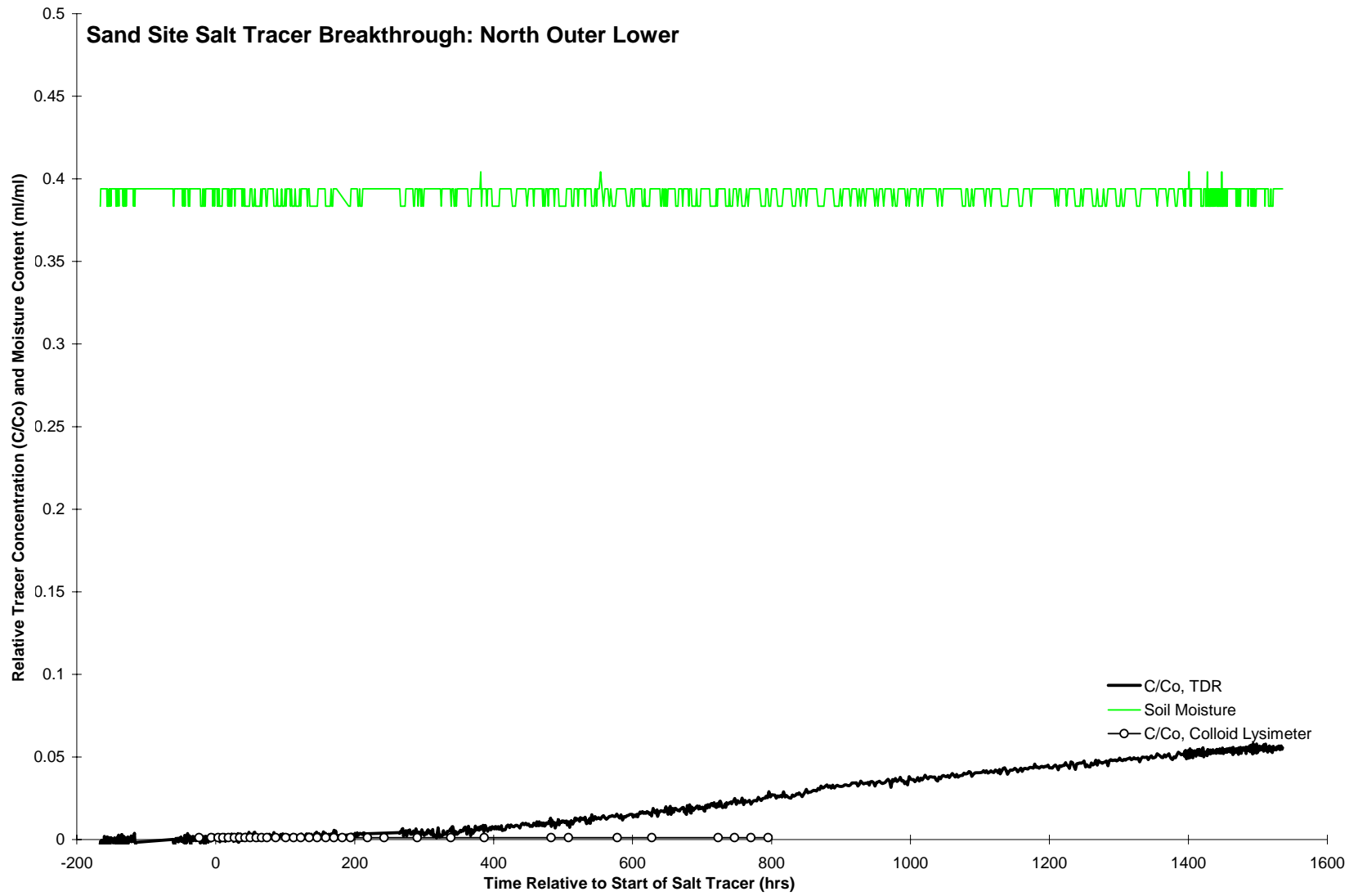






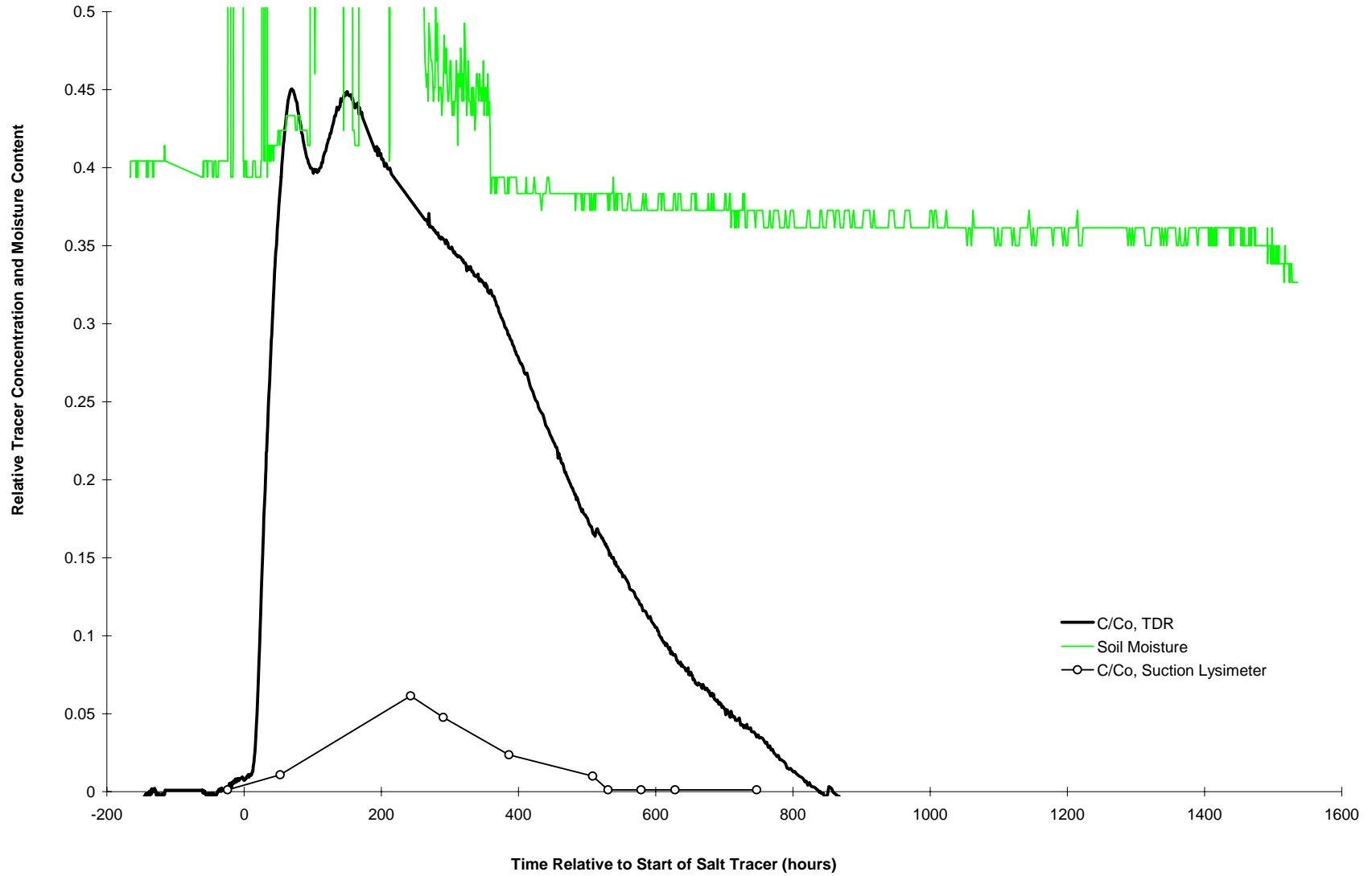


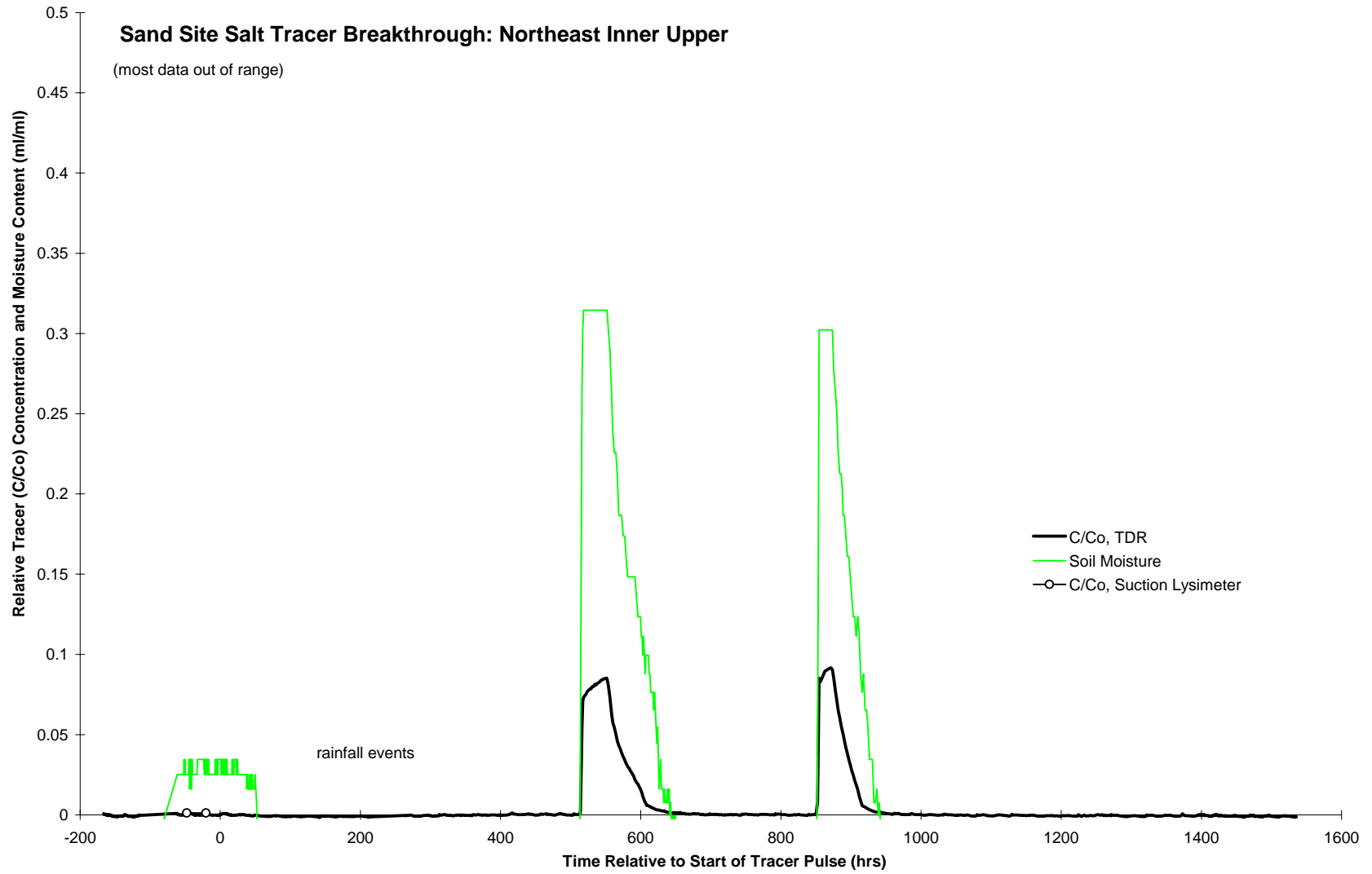


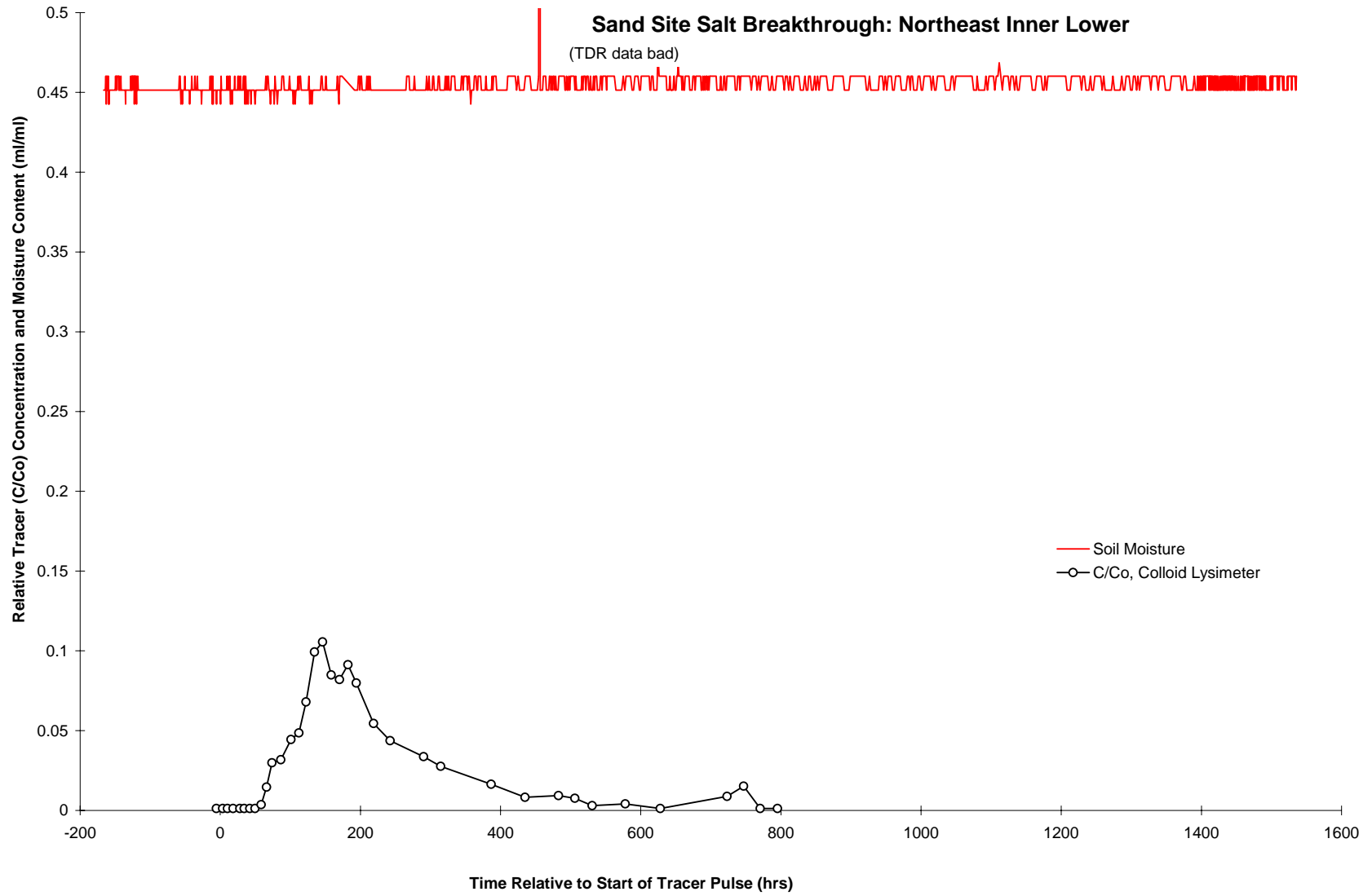


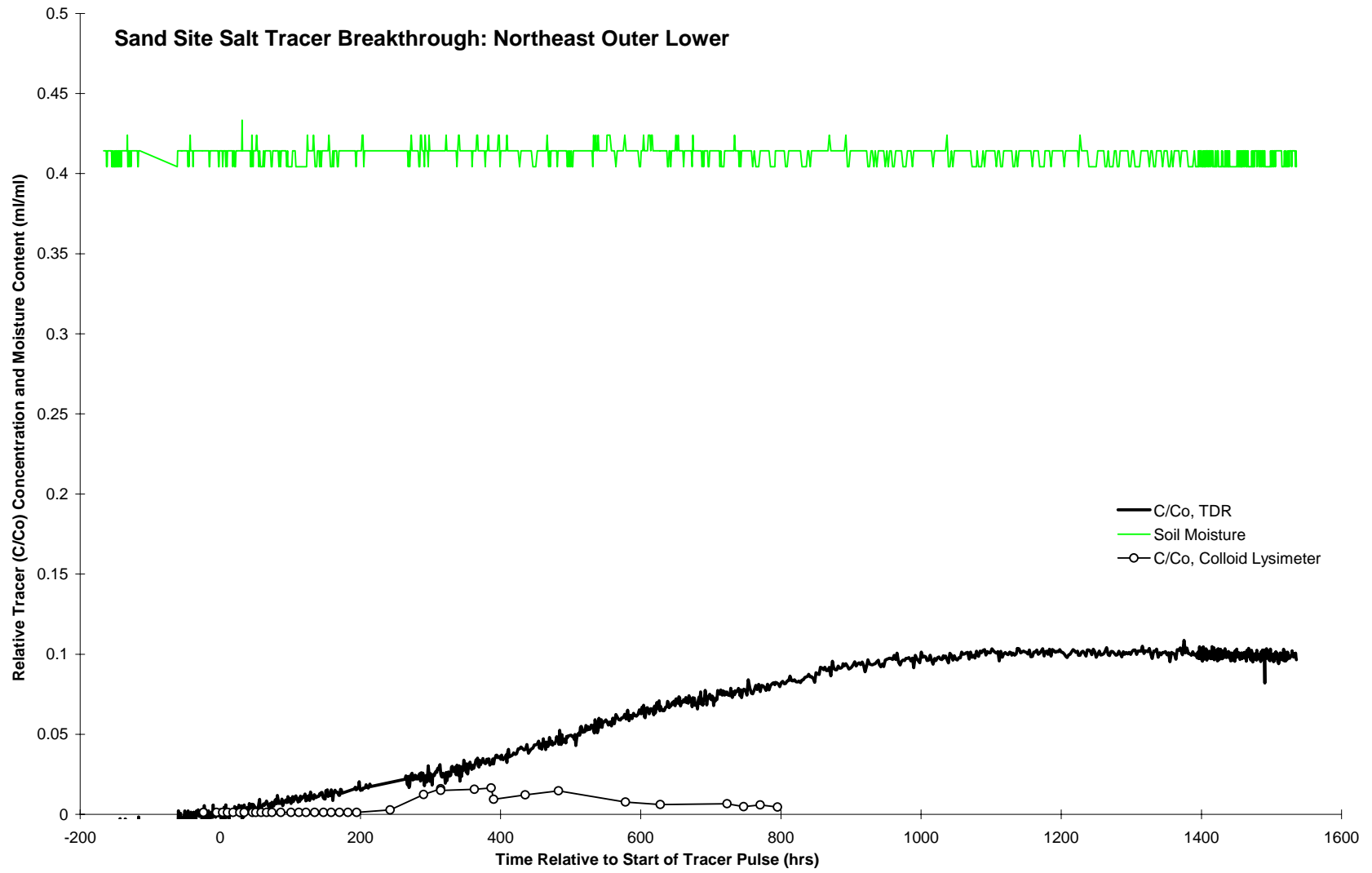
Sand Site Salt Tracer Breakthrough: North-Northeast Angled Lower

146

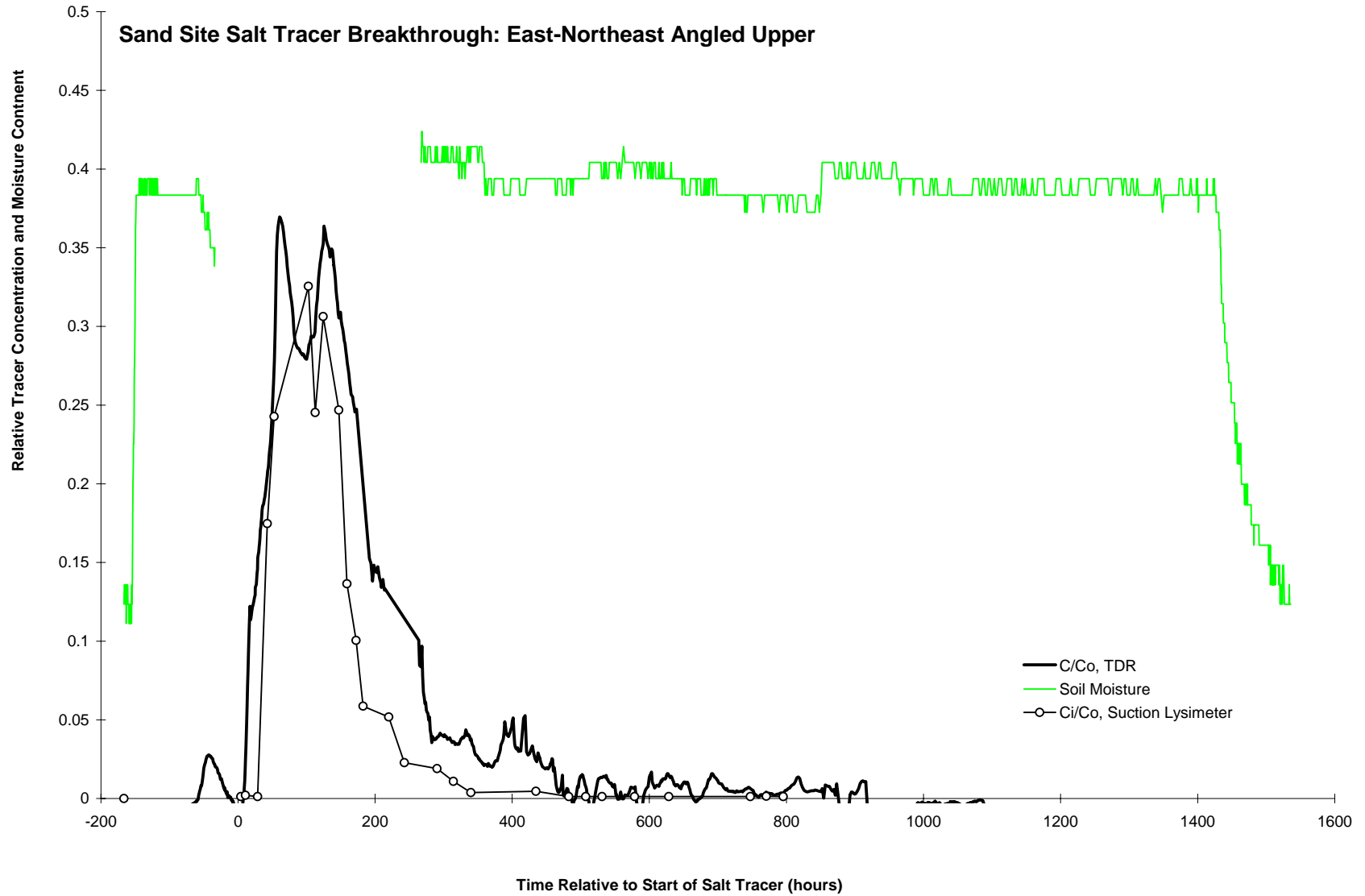


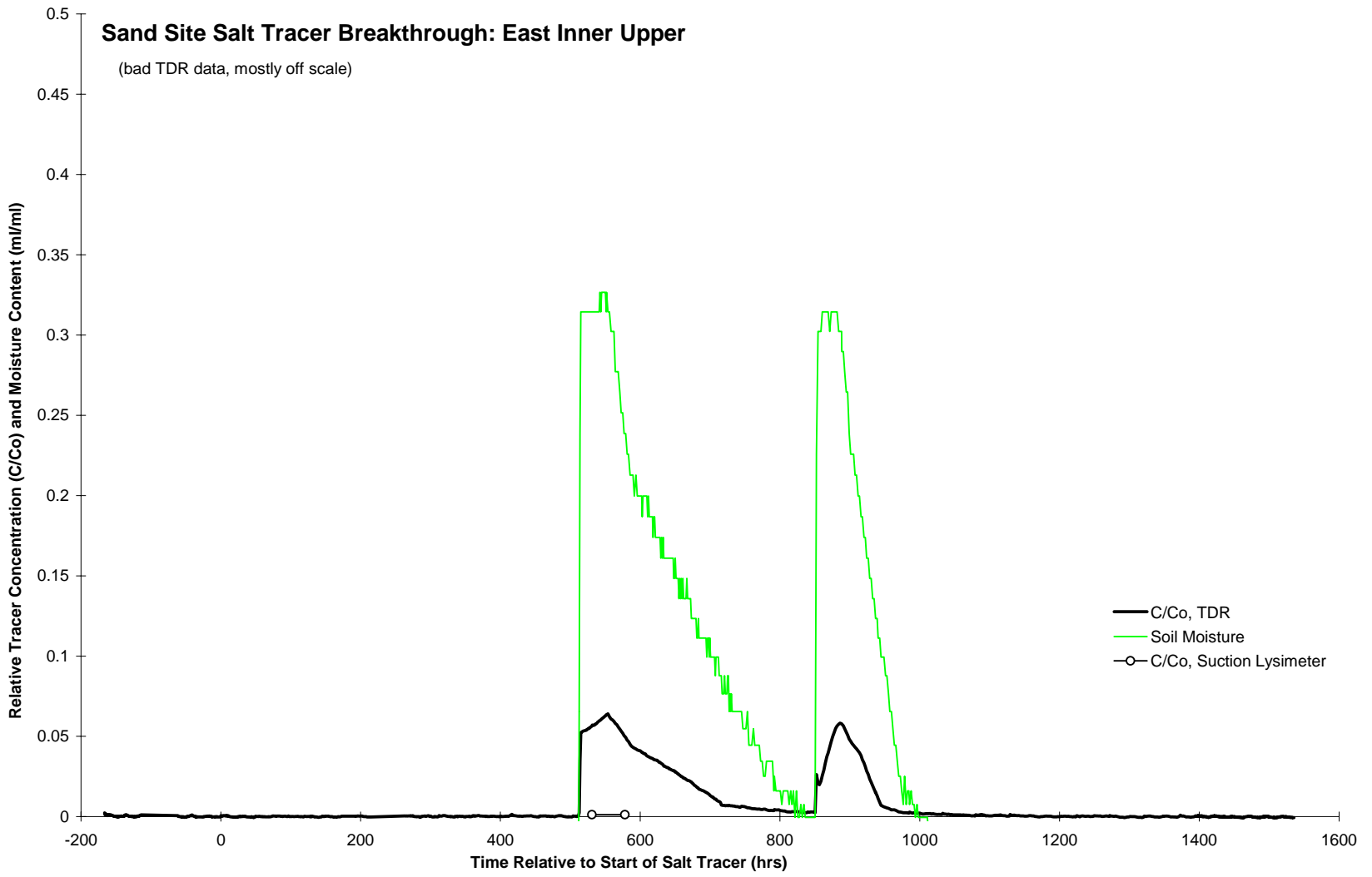


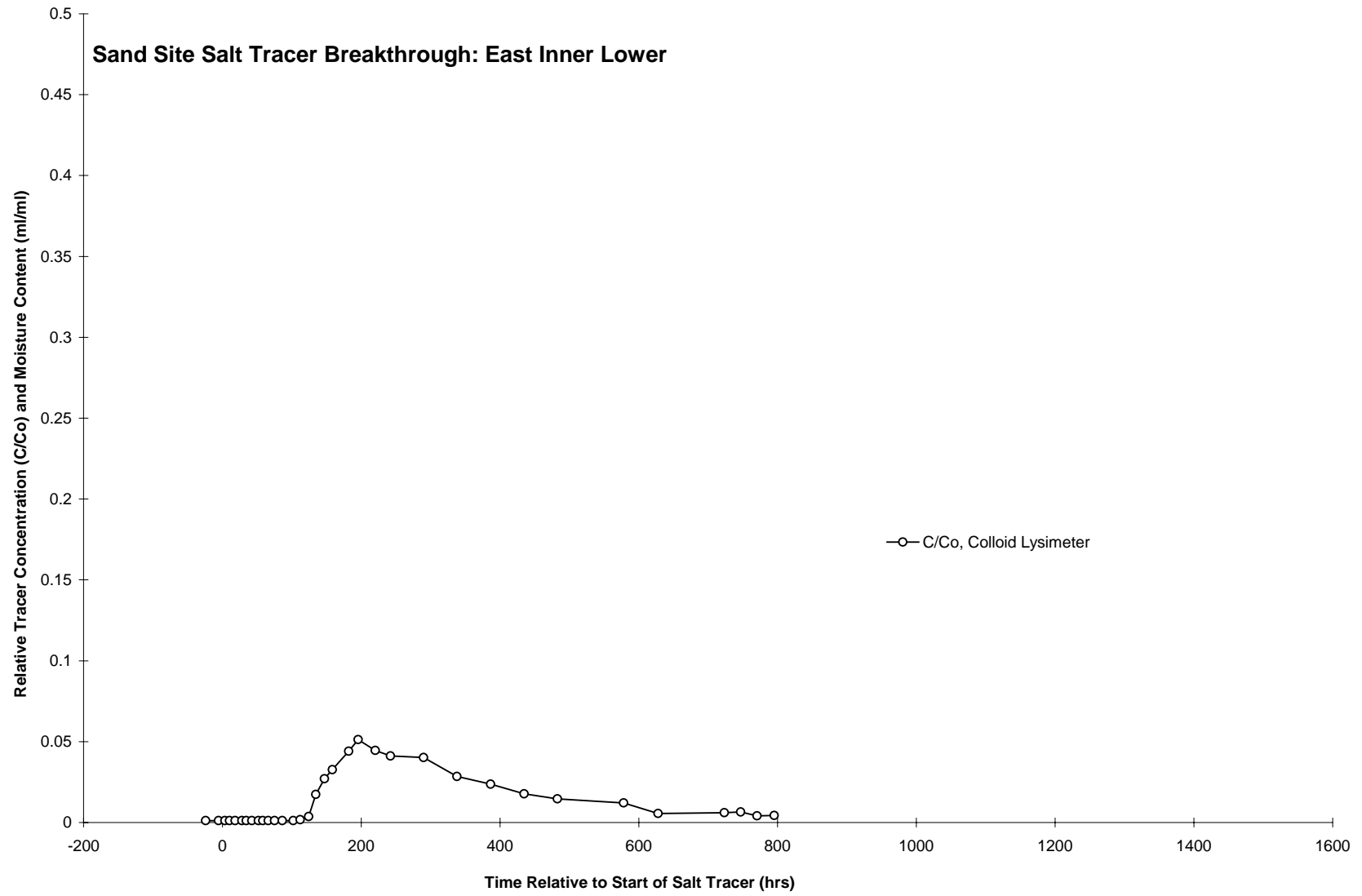


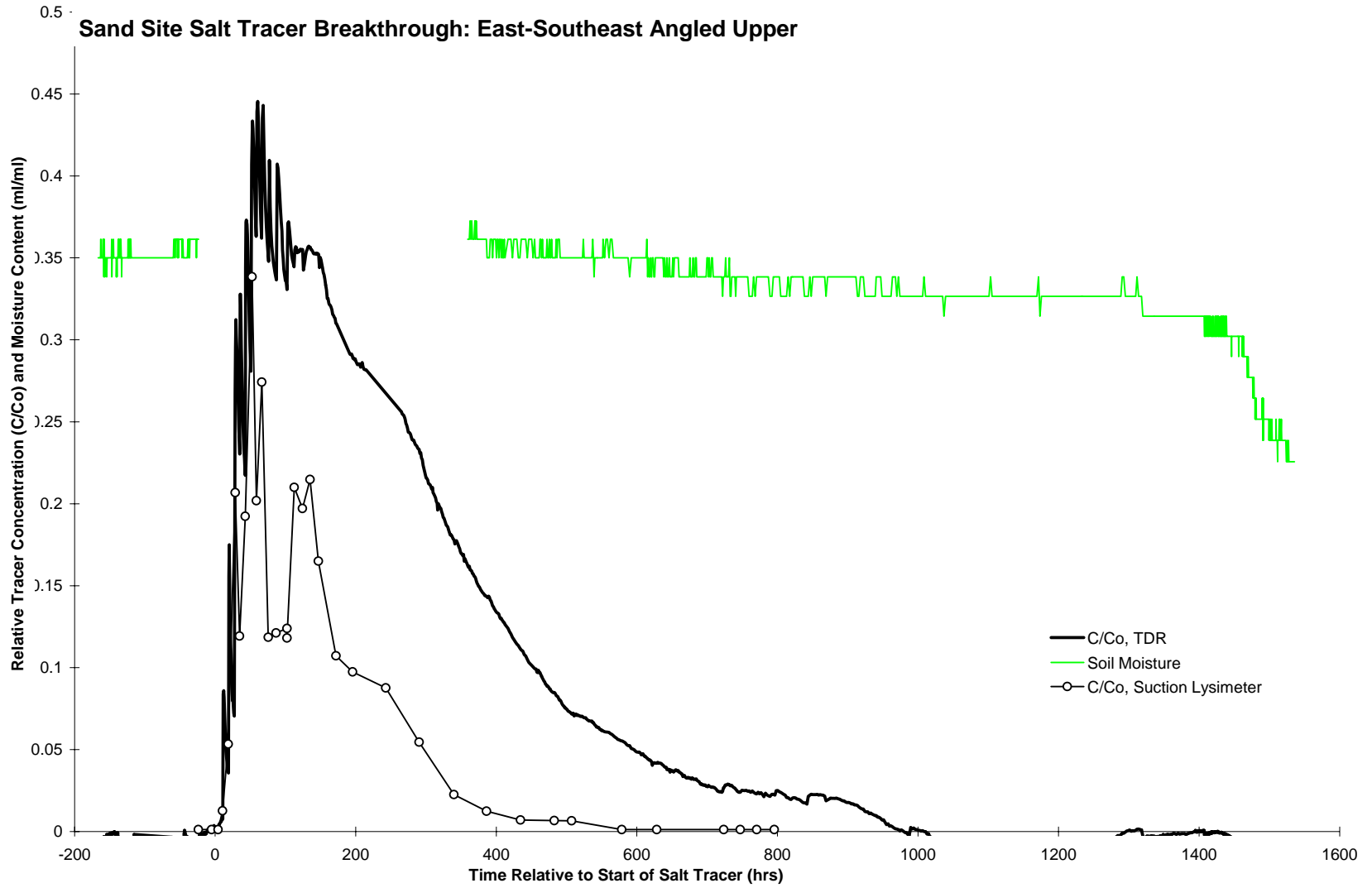


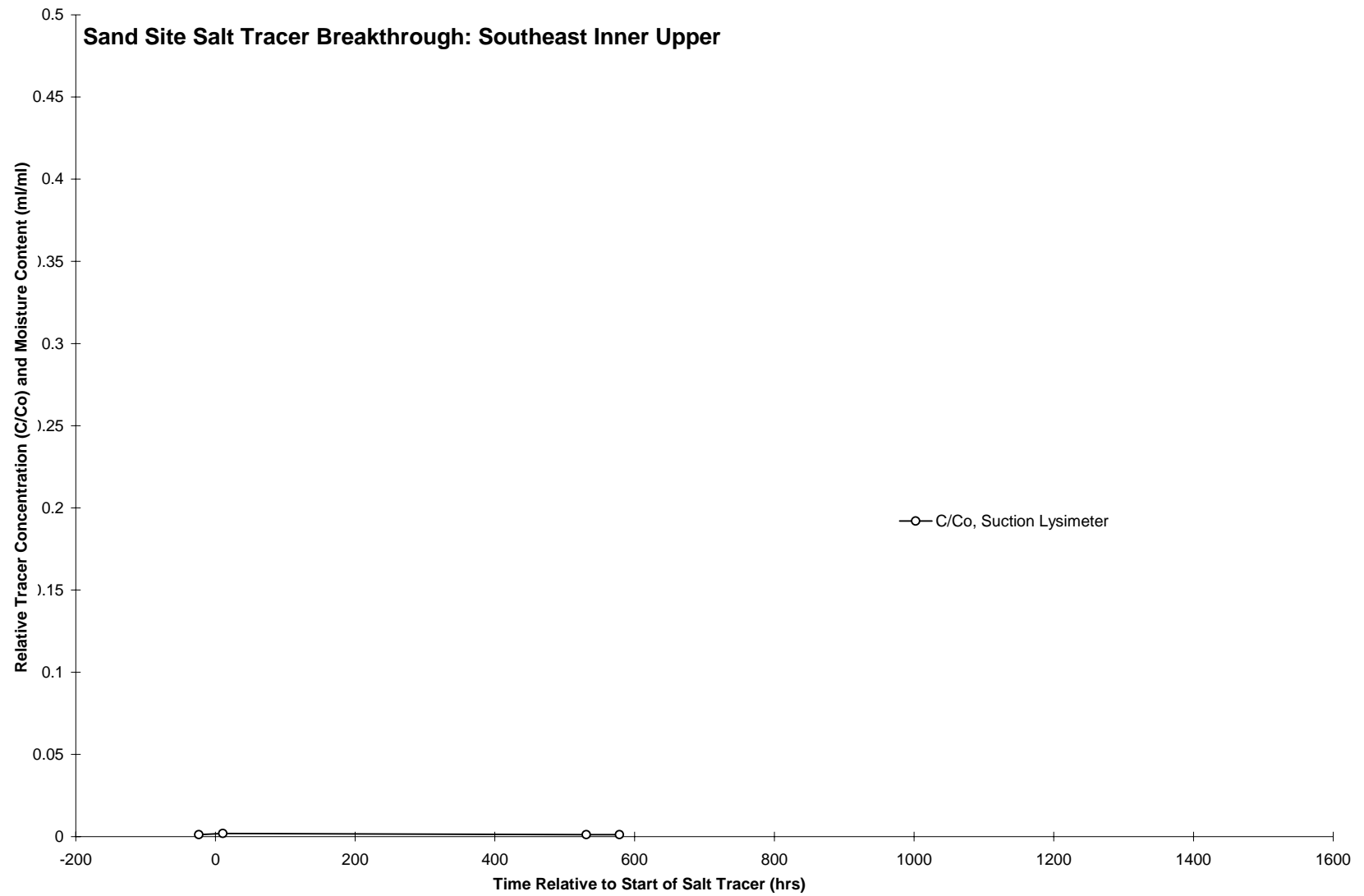
150

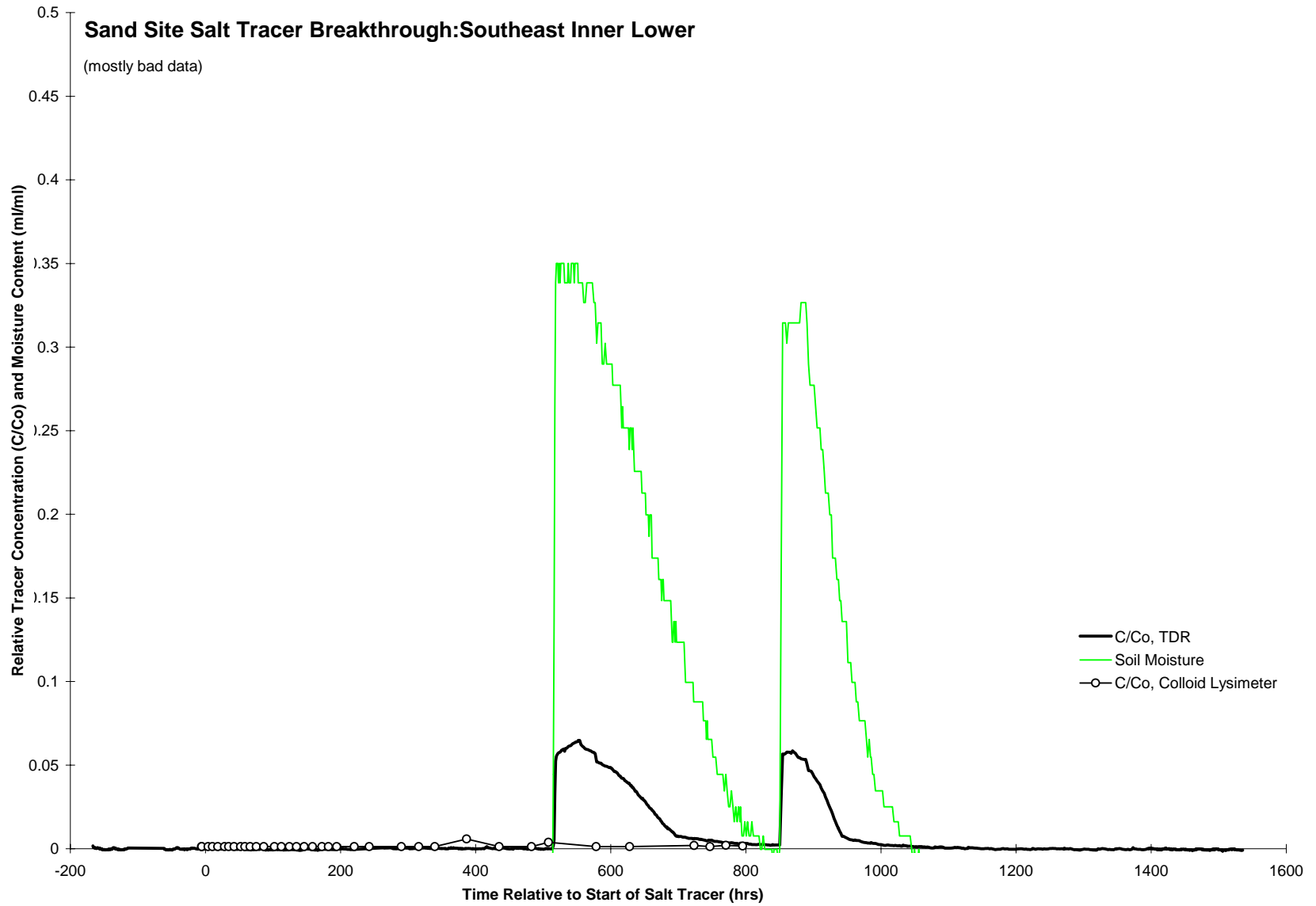


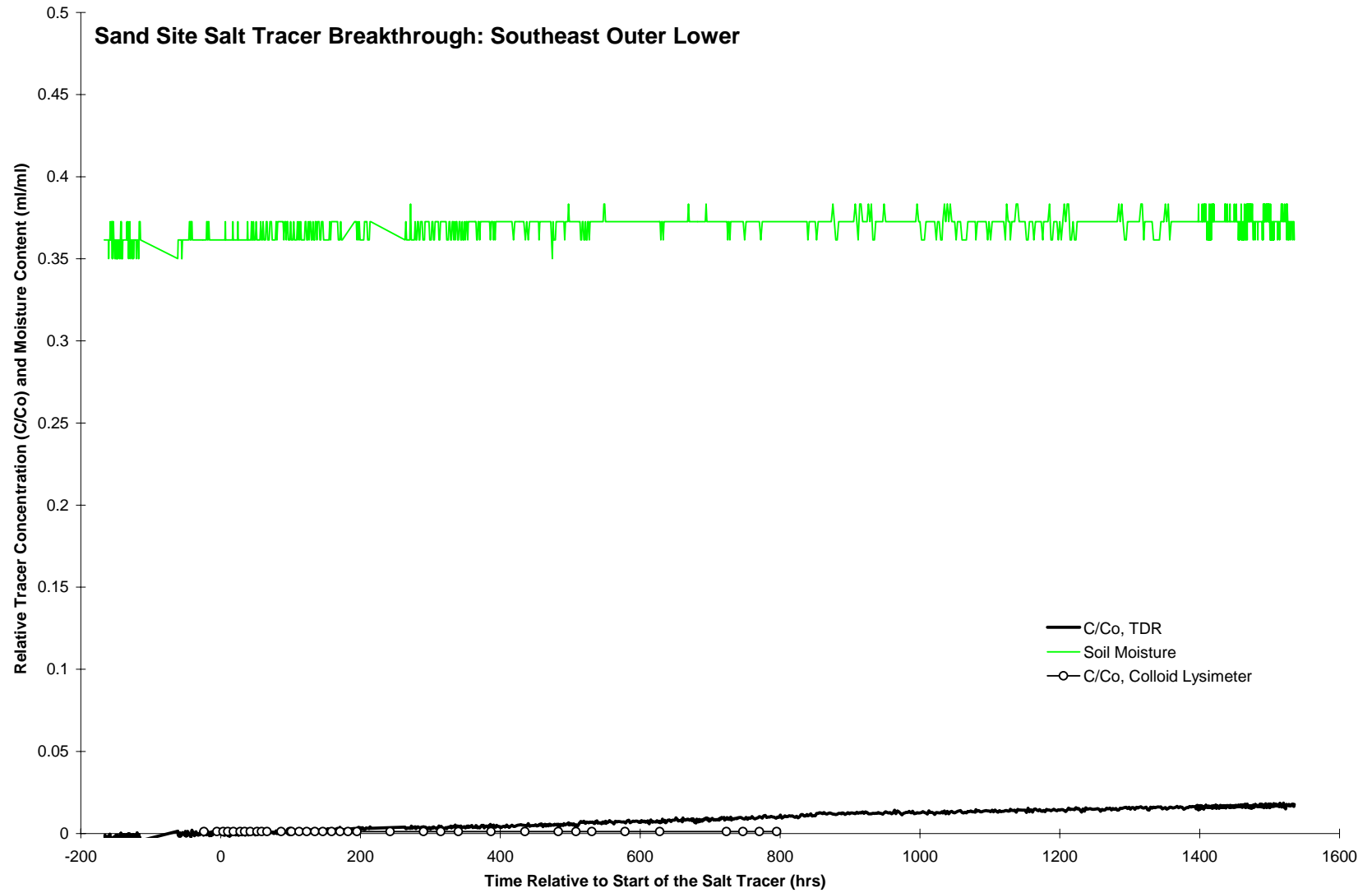


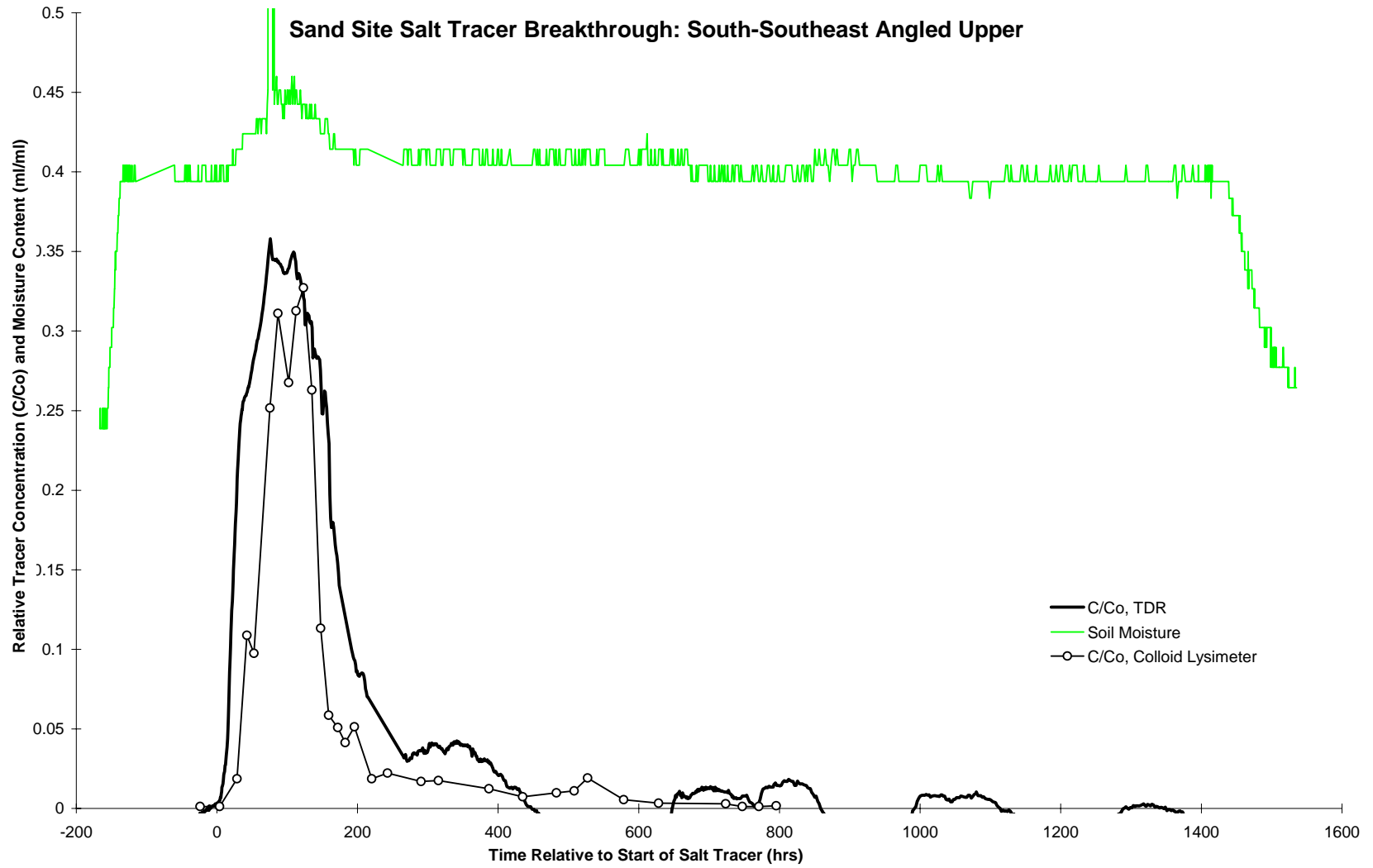


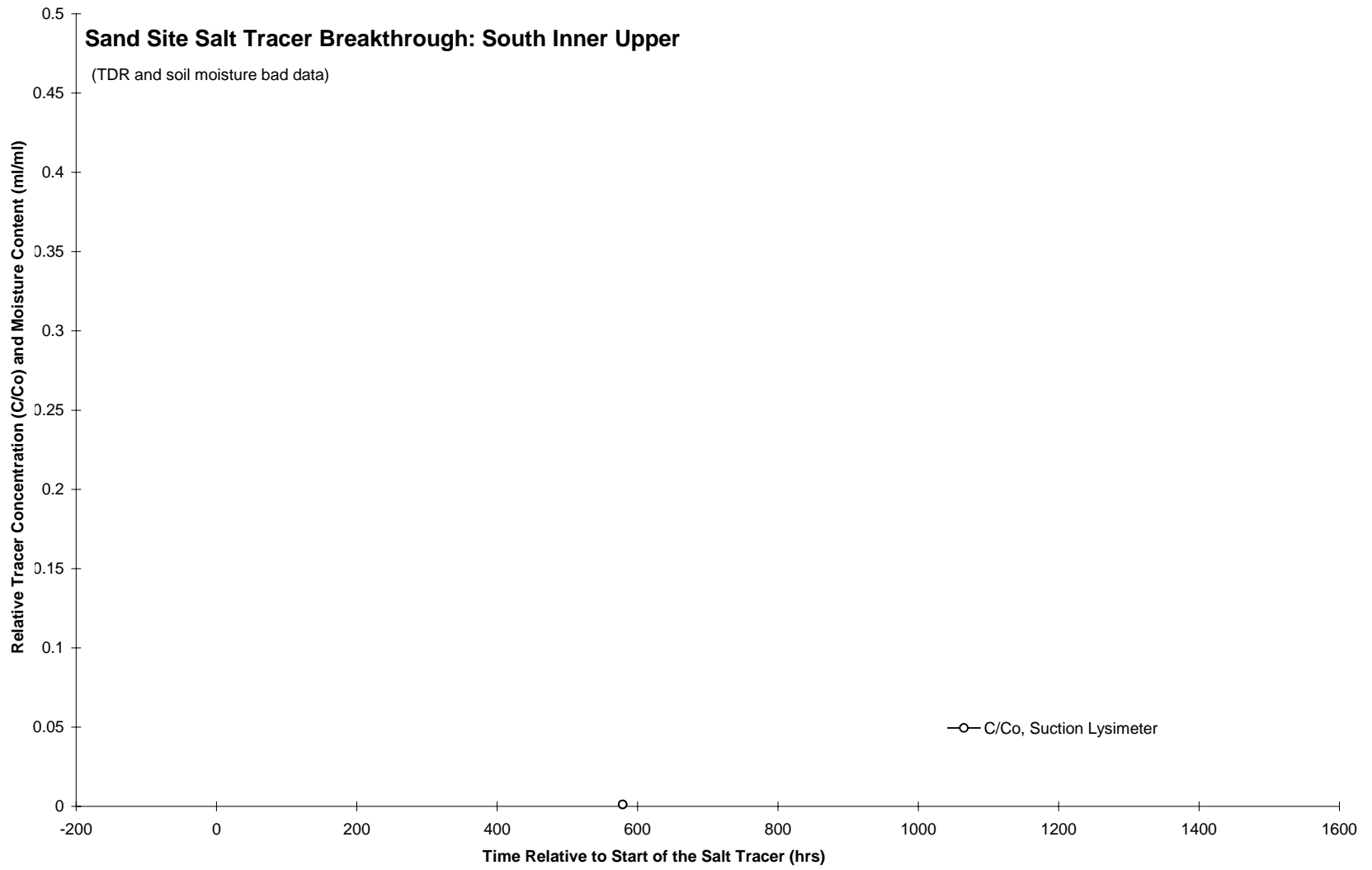


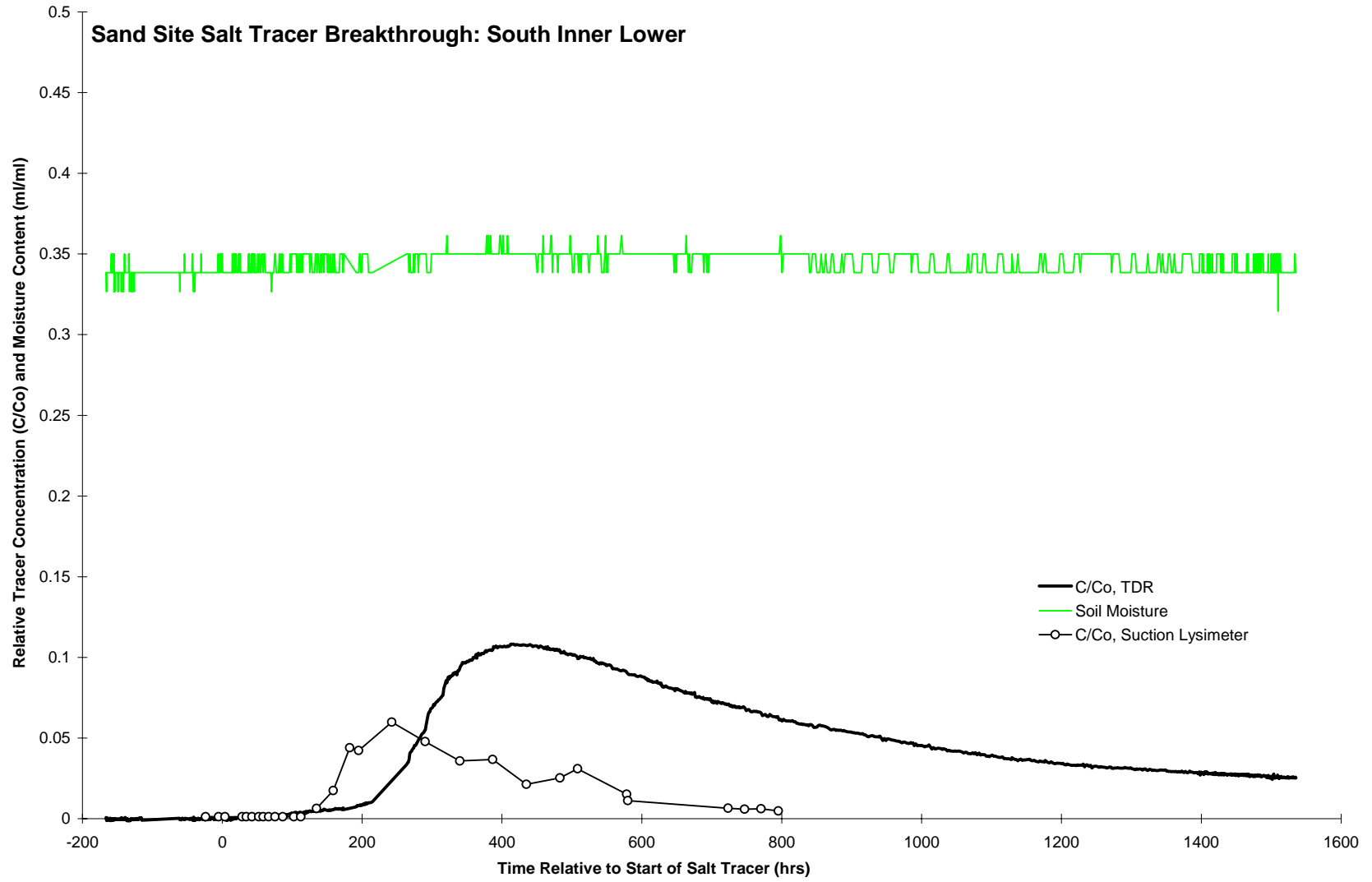


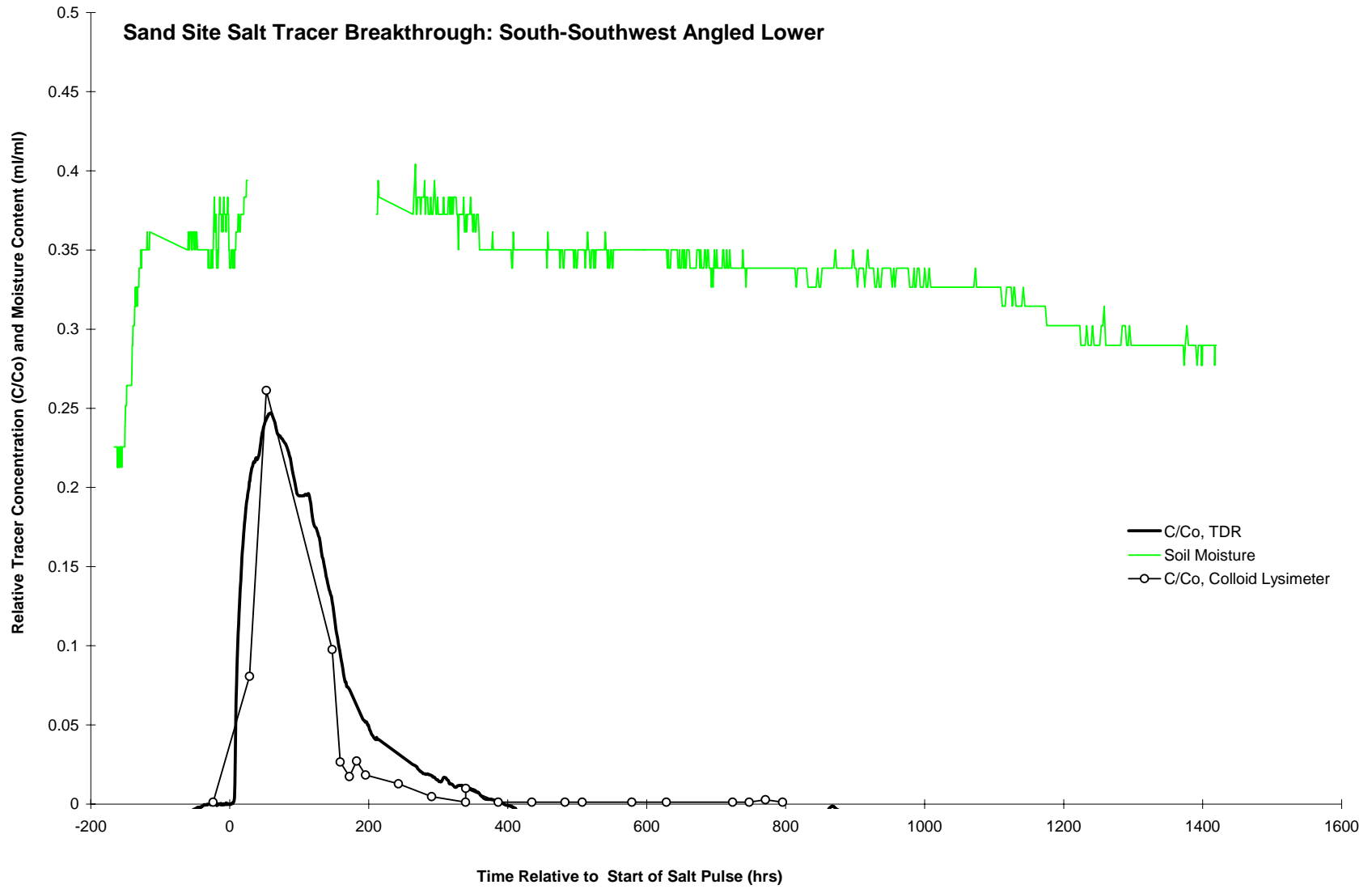


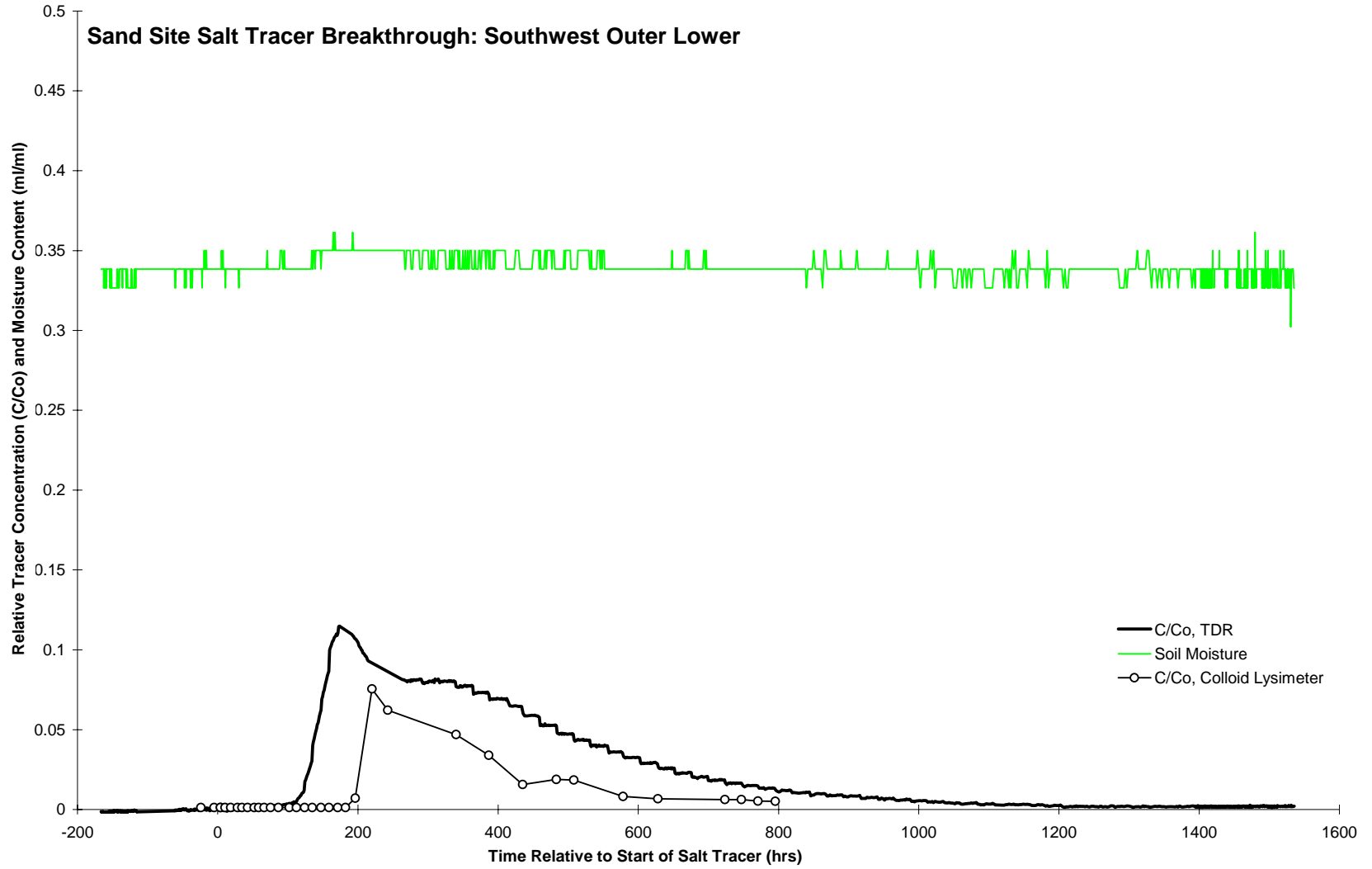


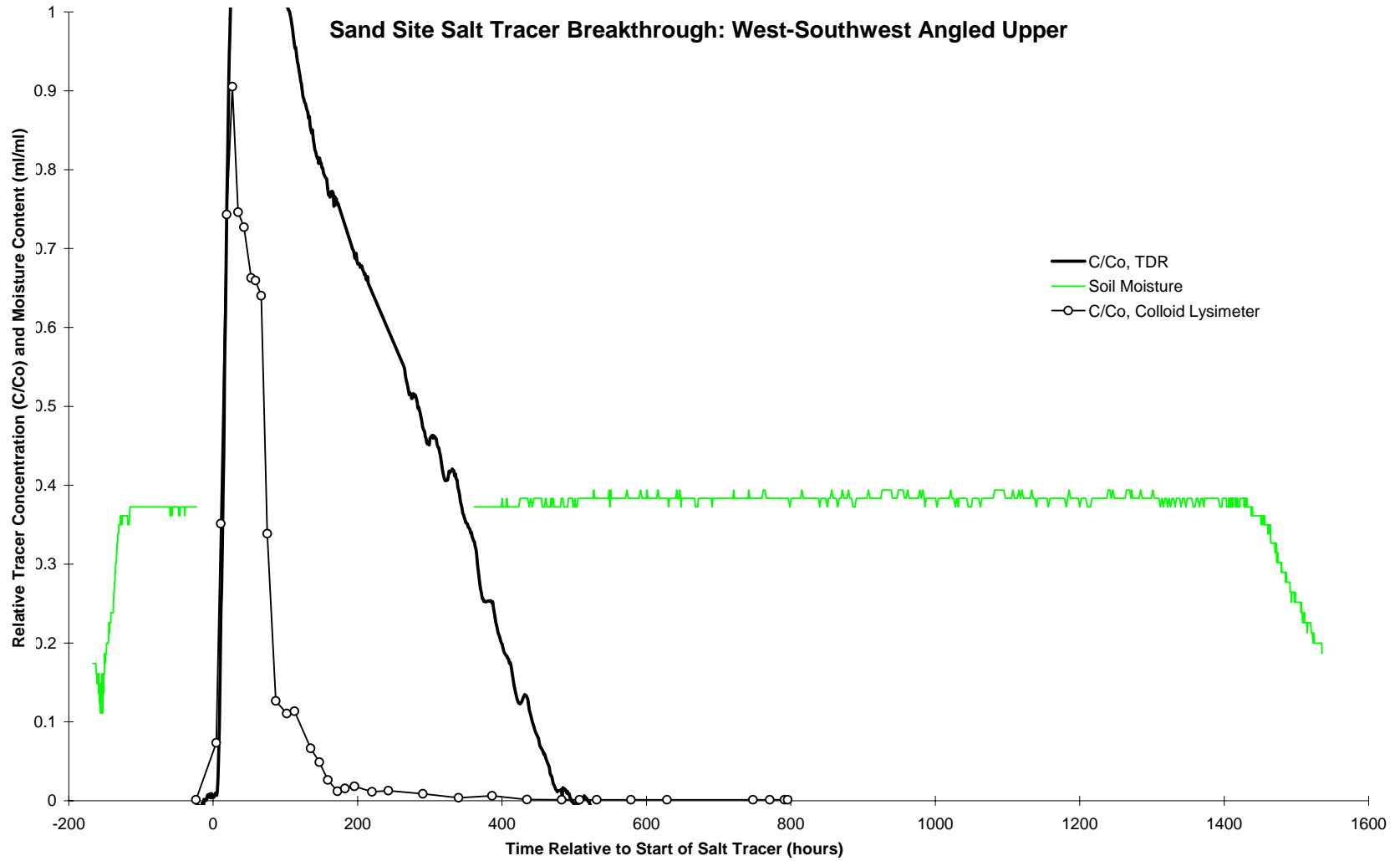


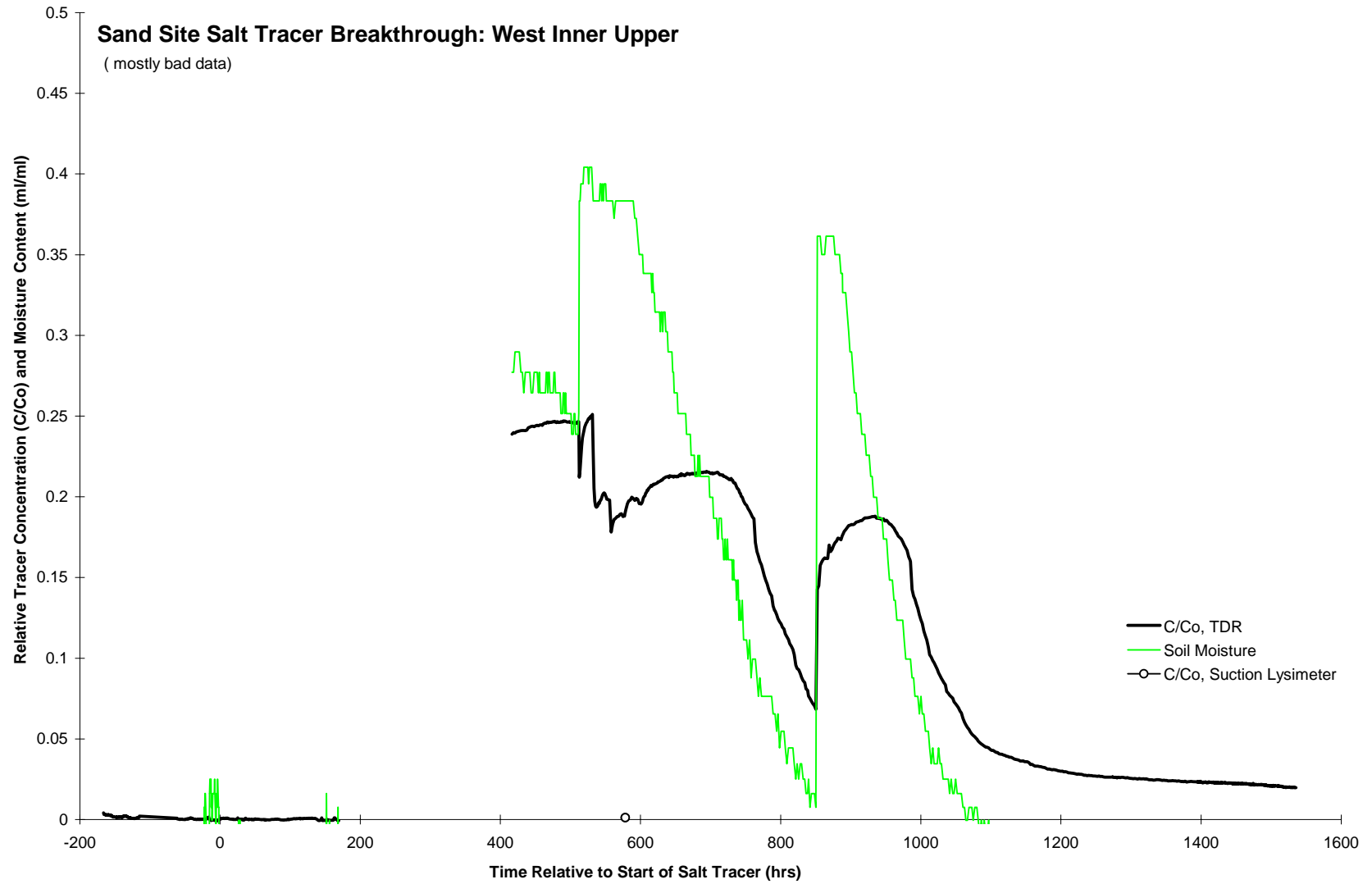


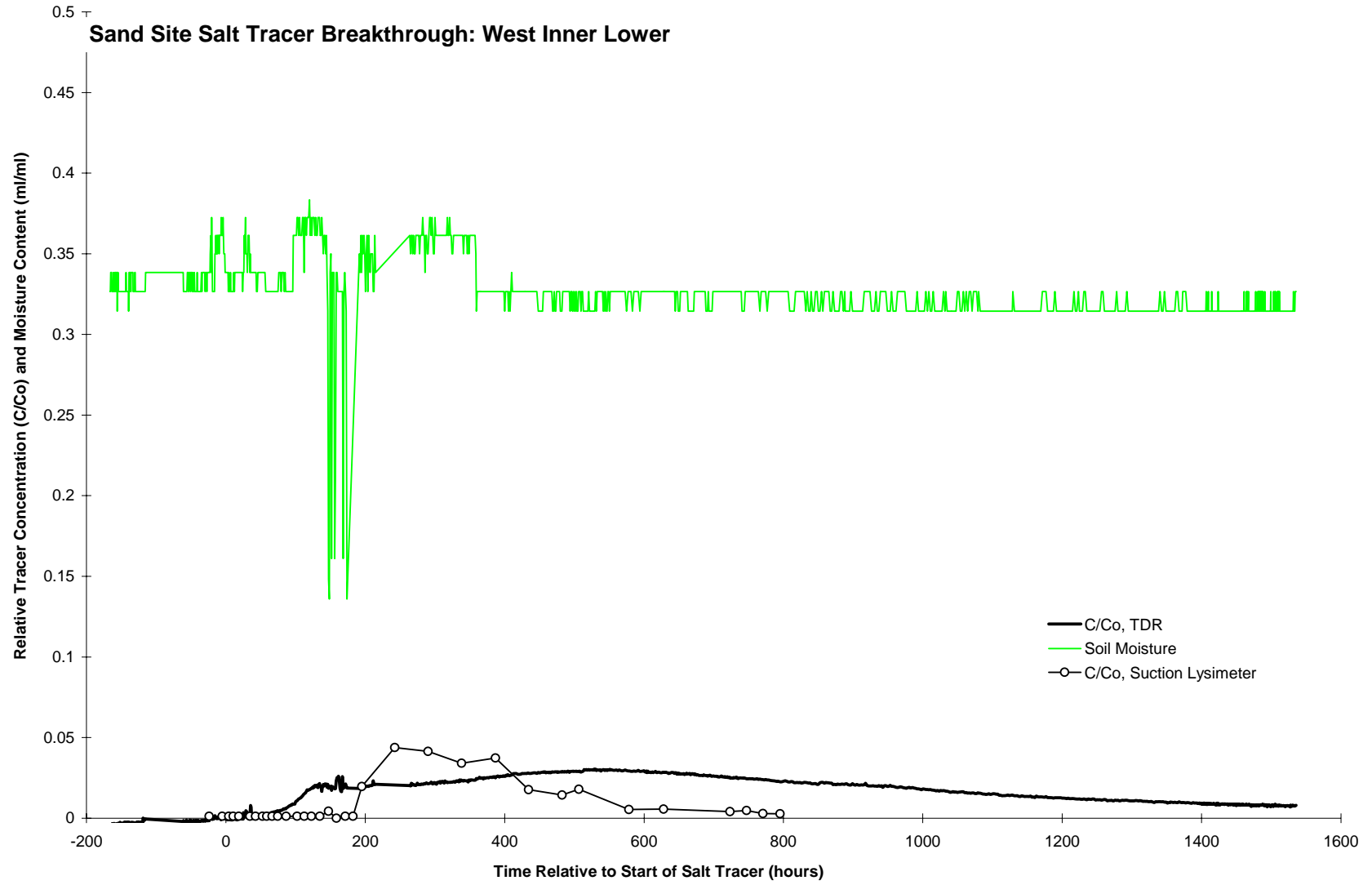


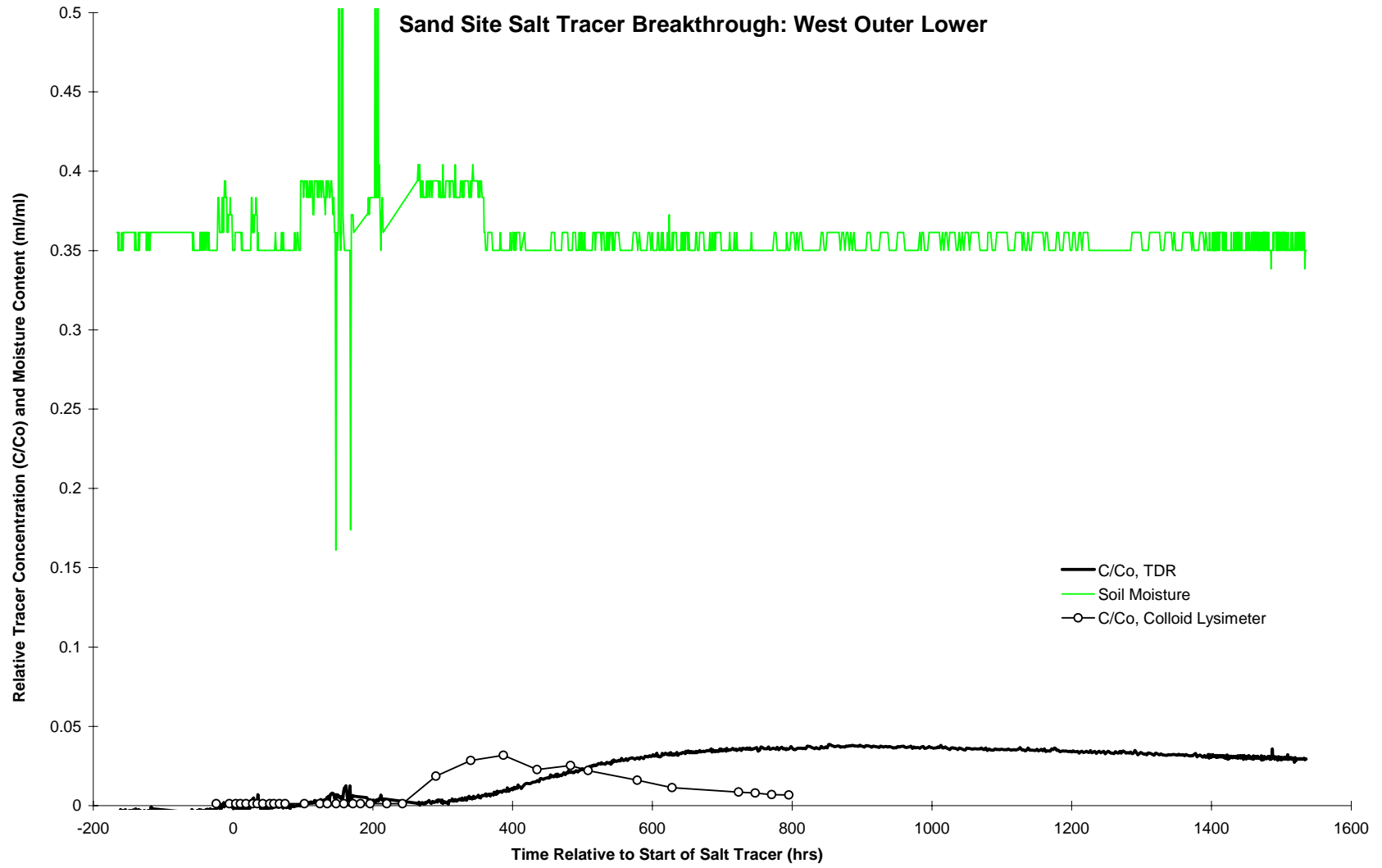


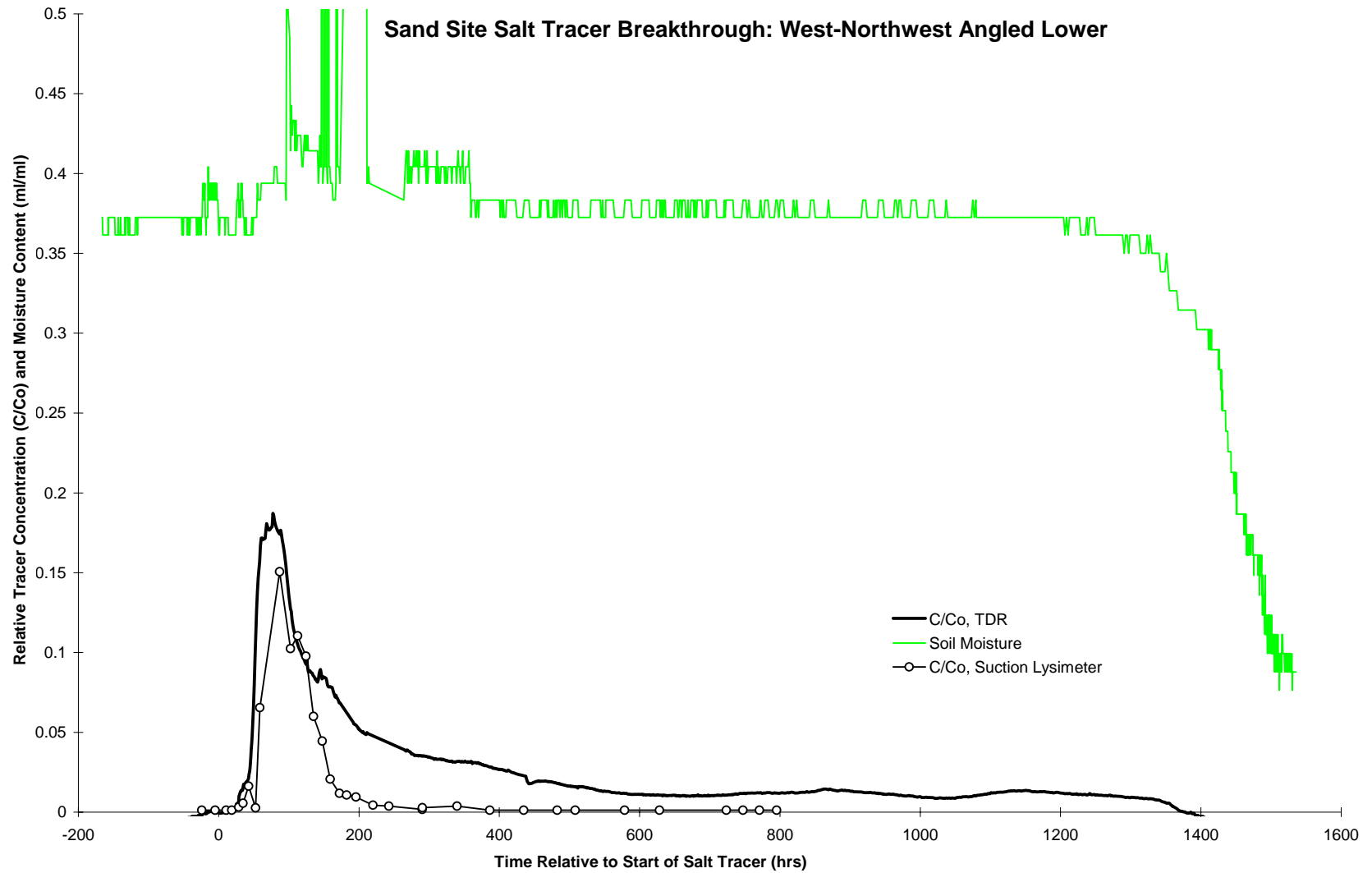


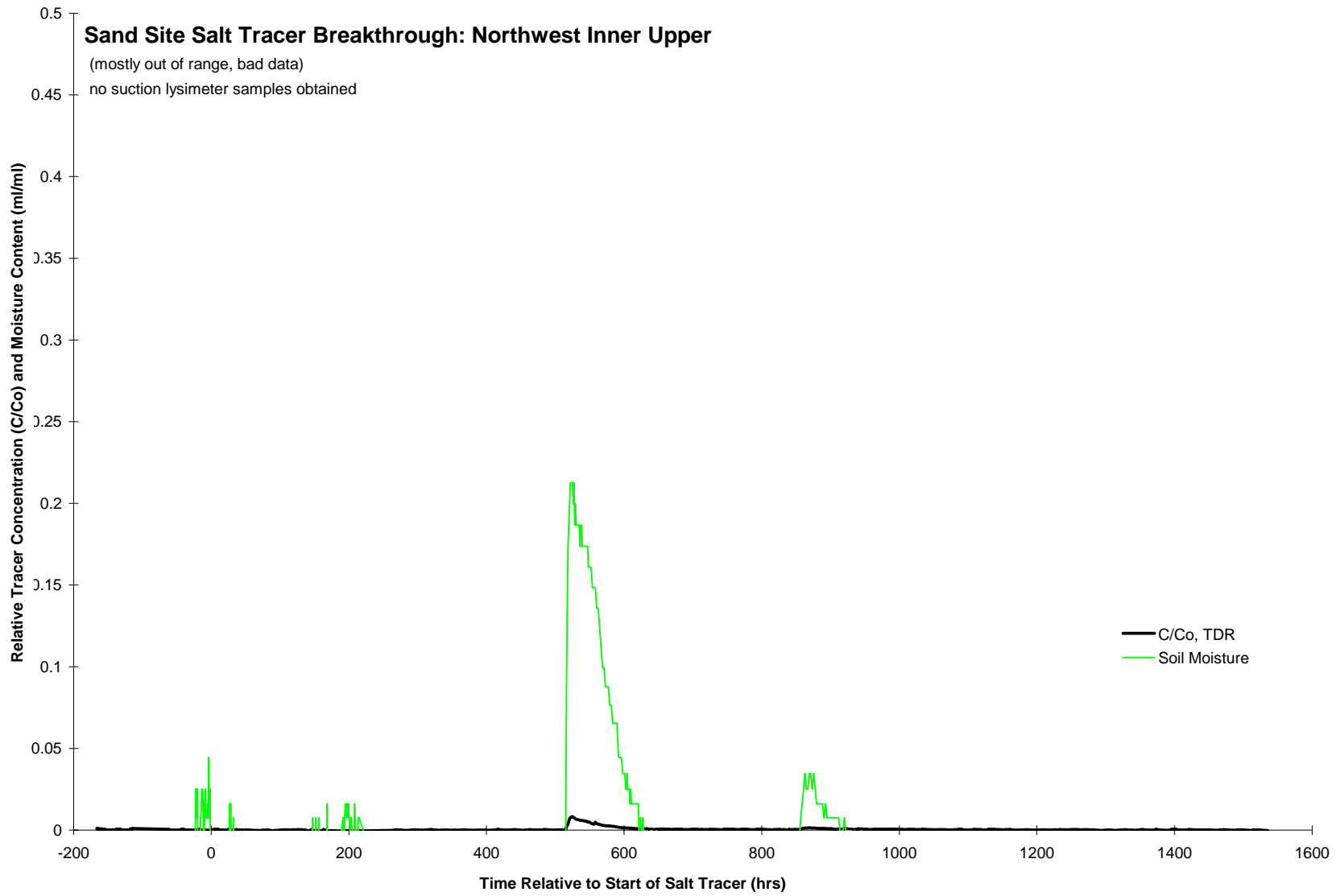


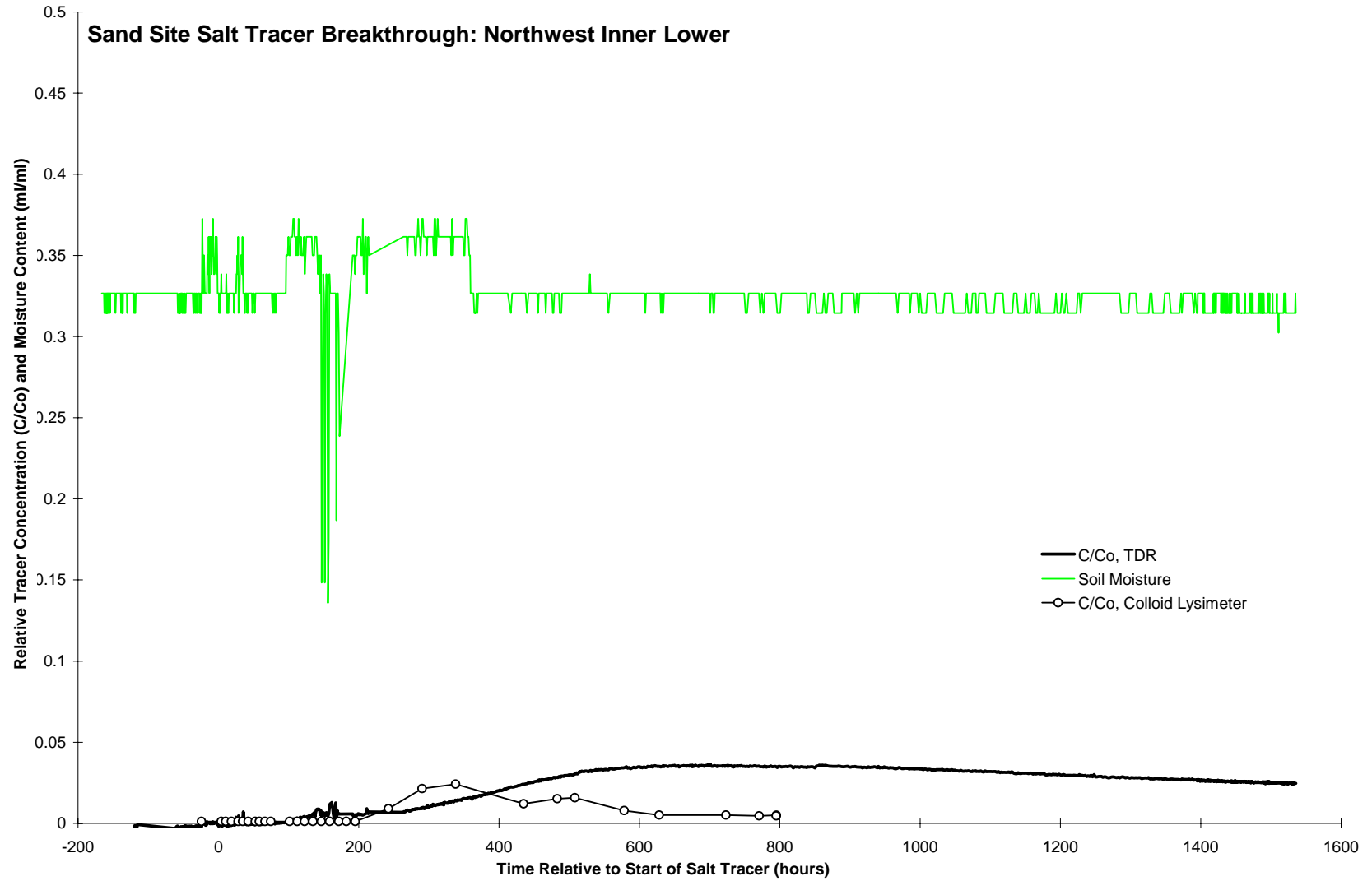


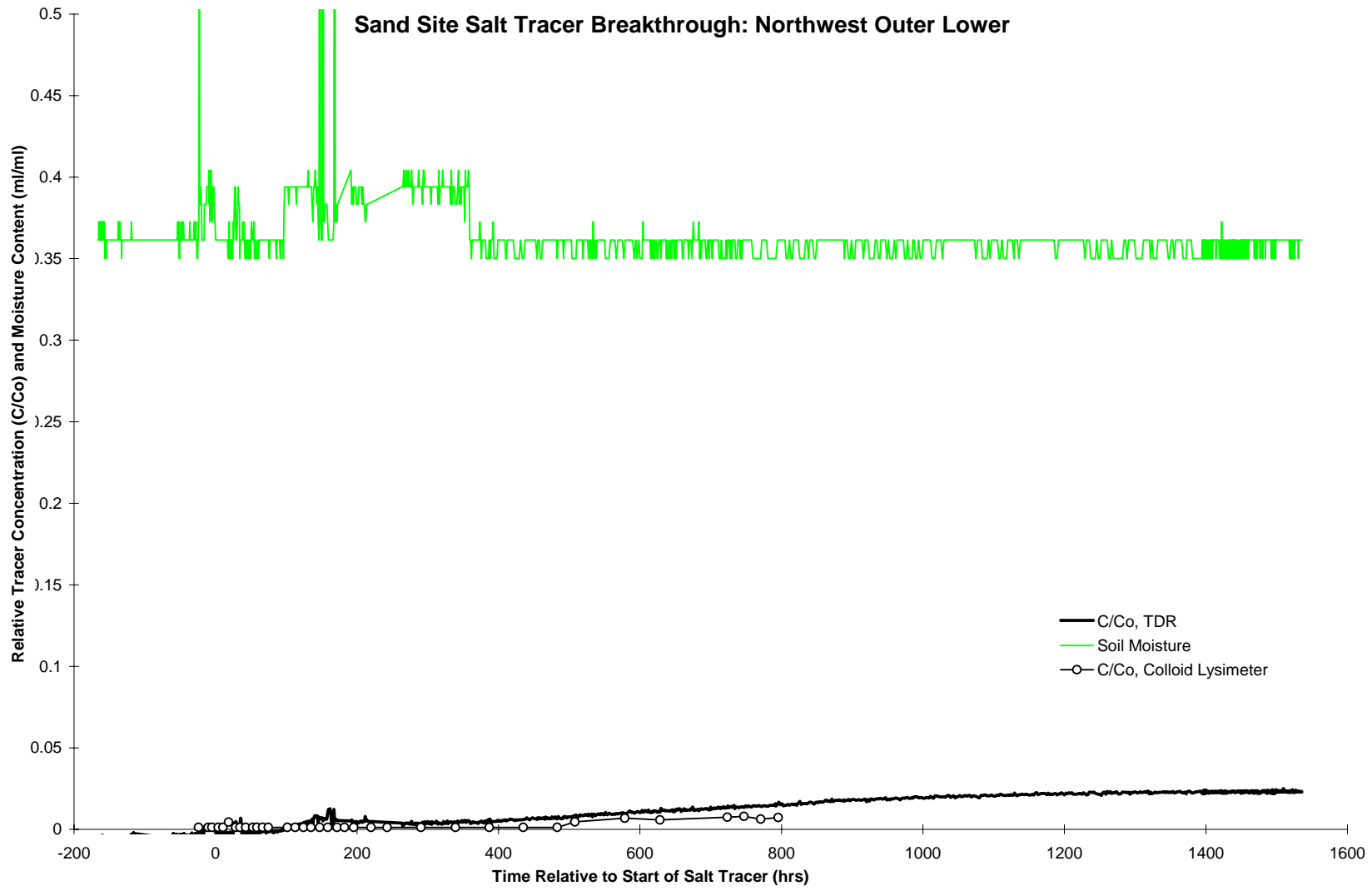




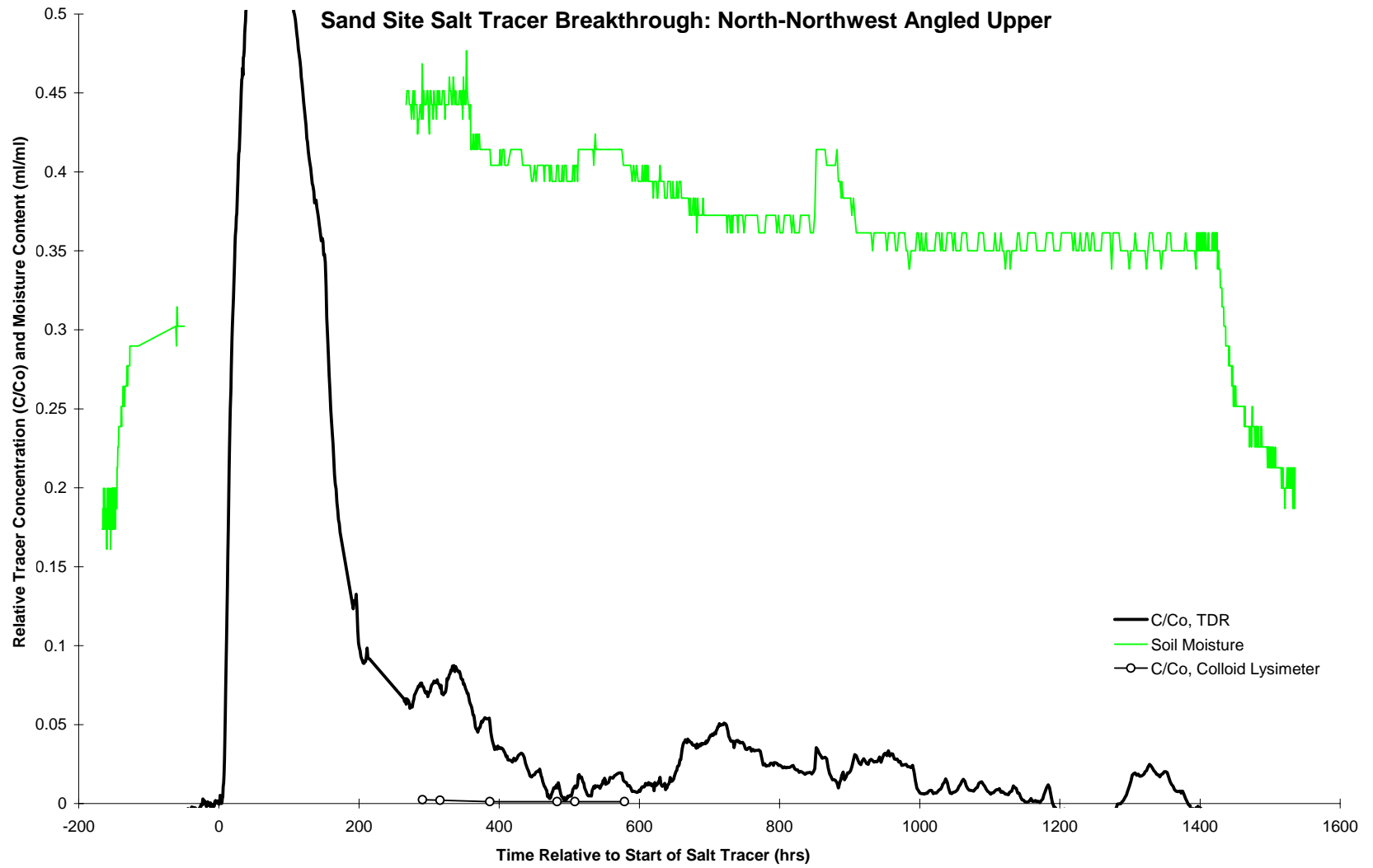








170



D.5 TPC Test Results

Cl⁻ Tracer Movement

Tracer movement in time at the Clay Site shows a definite westerly radial trend. Solute concentrations appear to initially increase in the upper level sensor packs located in the silty sand body in the northwest quadrant of the site. Peak concentrations then occur in the lower level sensor packs in the northeast (Northeast Inner Lower sampling point), See Figure D-1 for sensor pack array layout and nomenclature) and then quickly decrease. This initial northeast movement was followed by concentration increases in the West Inner Lower and West Outer Lower sensor packs, where concentrations peak and then decline to almost zero after approximately 500 hours.

The higher Cl⁻ tracer concentrations at the 2 m level in the Clay Site generally occur in the silty sand body located in the northwest quadrant of the site (Refer to Appendix A, TPC test Site Geology Section and Appendix F - Dye Pulse and Excavation). The peak tracer concentration observed in Northwest Outer Upper (2 m depth) sampling pack of the outer ring, (peak C/Co = .35) was greater than the peak concentration observed in the sampling pack immediately (Northwest Outer Lower) at the 3 m depth (peak C/Co = .12) and almost equivalent to the concentrations derived from the West Outer Lower and West Inner Lower sensor packs indicating that the Cl⁻ tracer may have moved preferentially through the silty sand body in the northwest quadrant of the site at the upper level, then down to the lower level in the west, bypassing the lower northwest level almost entirely. The site excavation (See Appendix F) revealed that sand stringers from this silty sand body penetrated the bedded clays of HS Units 2 and 3 and that one intersected the West Outer Lower sensor pack. Pink dyed water (Plates 77 and 78) was observed seeping from the sand stringer at this location and the salinity concentrations at this sampling point were both higher and arrived sooner than at any adjacent sampling sites at the three meter depth, or at the sampling site directly overhead at the two meter depth (Refer to the graphs of tracer concentration in time at the end of this appendix).

The lack of any significant tracer concentration sensed by the sampling points in the south and southeast portion of the site may be a true reflection of the flow direction or a result of transport through un-intercepted flow paths such as fractures and crayfish holes which were frequently encountered in that region during excavation (See Plates 56, 81, 82, and 83 in Appendix F).

Movement of tracers at the Sand Site was less complex. Peak concentrations are observed almost directly beneath the infiltrometer until approximately 120 hours, followed. Concentrations then increase at other sensors away from the infiltrometer, with slightly higher concentrations in northeast and southwest sampling locations. Concentrations do not decline to negligible levels until over 800 hours after the beginning of the tracer pulse. Other than directly under the infiltrometer, the peak concentrations at the Sand Site never reach the same levels as at the Clay Site. The Cl⁻ tracer also took longer to disperse at the Sand Site.

In both sites the Cl⁻ tracer movement can be discerned moving at first vertically through the top soils and blocky structured silty clays of HS Units 5 and 4 and then spreading laterally at depth. As the tracer pulse at the Clay Site encountered the planar structures of the bedded clays of HS Units 3 and 2 (refer to Figure D-5, Main Report), it began moving horizontally, notwithstanding the initial lateral flow through the silty sand body in the northwest upper levels of the site.

TDR Indications of Preferential Flow

Forty-five minutes after the start of the Cl^- tracer measurements from the TDR sensor in East-Northeast Upper sensor pack went off scale almost instantaneously ($C/C_0 > 0.45$, Figure D-12), indicating the presence of a fast transport pathway at that location. During excavation (see Appendix F) we discovered that a dye stained worm hole intersected this sensor pack which explains the rapid arrival time as well as the sudden increase in concentrations. Apparently the Cl^- tracer was not diluted by preexisting water in the worm hole resulting in off scale readings.

Repeated peaks in breakthrough curves, such as those in Figure D-13, are also strong evidence for the existence of preferential flow paths in the form of secondary transport pathways.

The presence of preferential flow paths in the form of biologically produced conduits that intersect sensor packs may be inferred from comparisons between the TDR and suction sampler derived concentration measurements. The 70 to 80 PSI suction placed on soil water samplers during the sampling process impacts the ambient flow field by drawing water to the suction sampler. If the conduit contains a concentration different than that of the water in the sensor

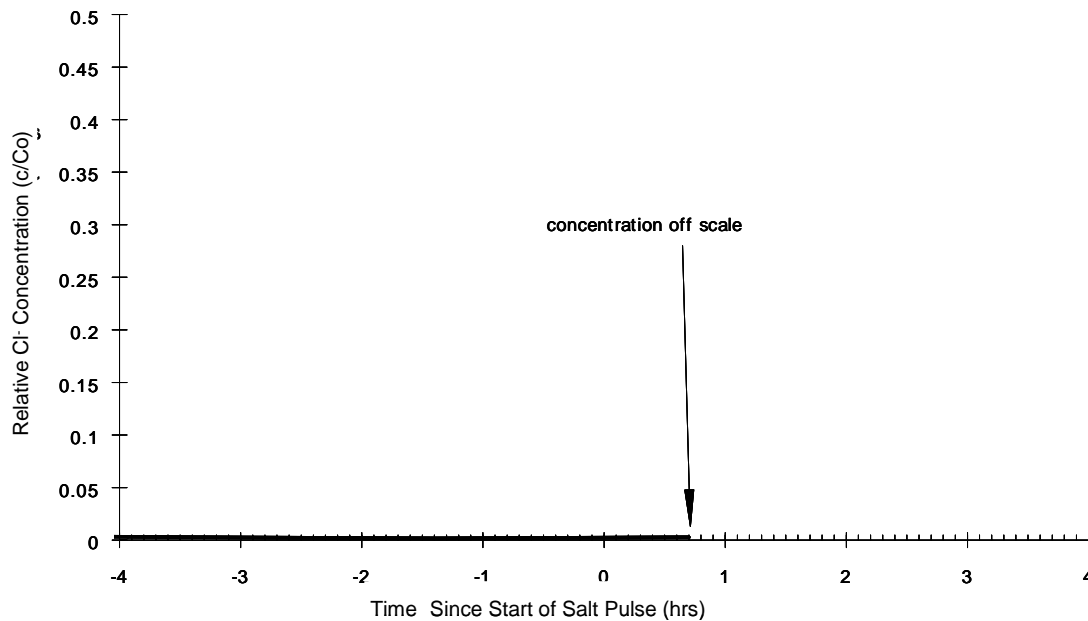


Figure D-12. TDR trace showing arrival of Cl^- pulse at the North-Northeast sensor pack via macropore forty-two minutes after Cl^- introduction in the infiltrometer.

pack sand, then there is a potential for the conduit water to flow into sensor pack and to the suction sampler during sampling. The conduit water that flows into the sensor pack and is not drawn into the suction sampler is left to be diluted by, or to dilute the sensor pack water. The location of the conduit entry has an impact on the arrival of the conduit solution to the TDR probe relative to the suction sampler. Where the suction sampler is between the conduit and the TDR probe the tracer will be drawn preferentially to the soil water sampler while at the same time ambient water will be pulled past the TDR probe. Assuming that the conduit has a higher

concentration of tracer than the sand pack, a lag in initial and peak arrival times would be expected in the TDR data relative to the suction sampler data. This scenario is illustrated in Figure D-14a and data from the Northeast Outer Upper sensor pack corroborates this reasoning.

The opposite may also result if the conduit intersects the sensor pack below the TDR probe as illustrated in Figure D-15a. In this configuration and once again assuming a higher concentration of tracer in the conduit versus the sensor pack, the suction applied to the soil water sampler would cause solutes to arrive first and in greater concentrations at the TDR probe. This apparently was the case at the West Inner Upper (Figure D-15b) where the breakthrough and the peak occurred almost instantaneously during a solution sampling round. The abrupt and repeated peaks seen in Figure D-15b correspond to soil water sampling times and can be attributed to the flushing in of Cl^- from a conduit.

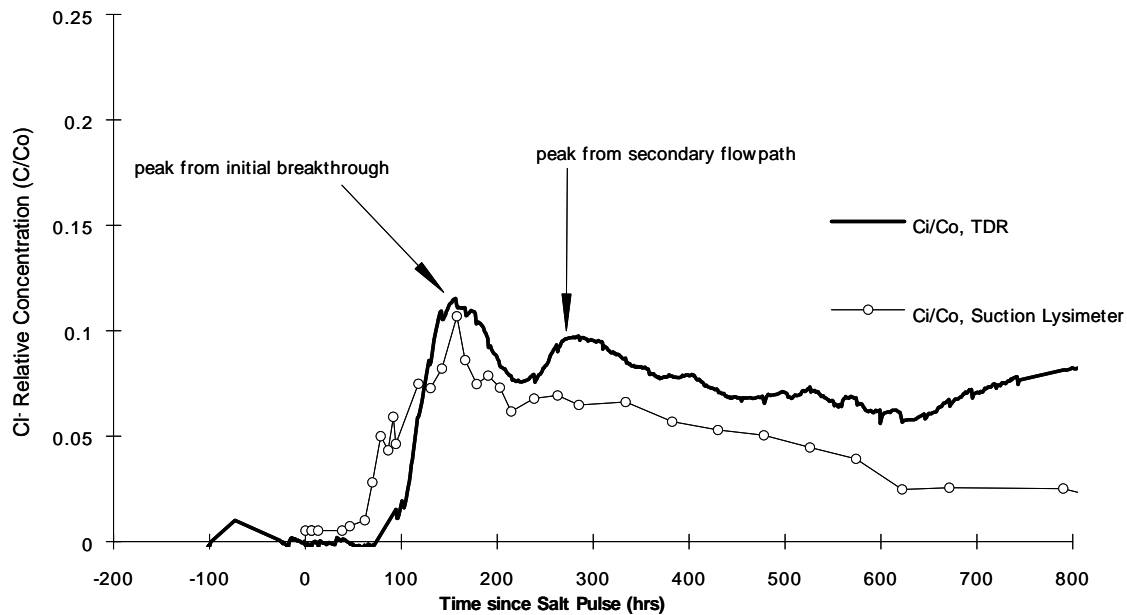


Figure D-13. Repeated peaks in the solute concentration breakthrough curve from primary and secondary flow paths in the East Inner Lower sensor pack.

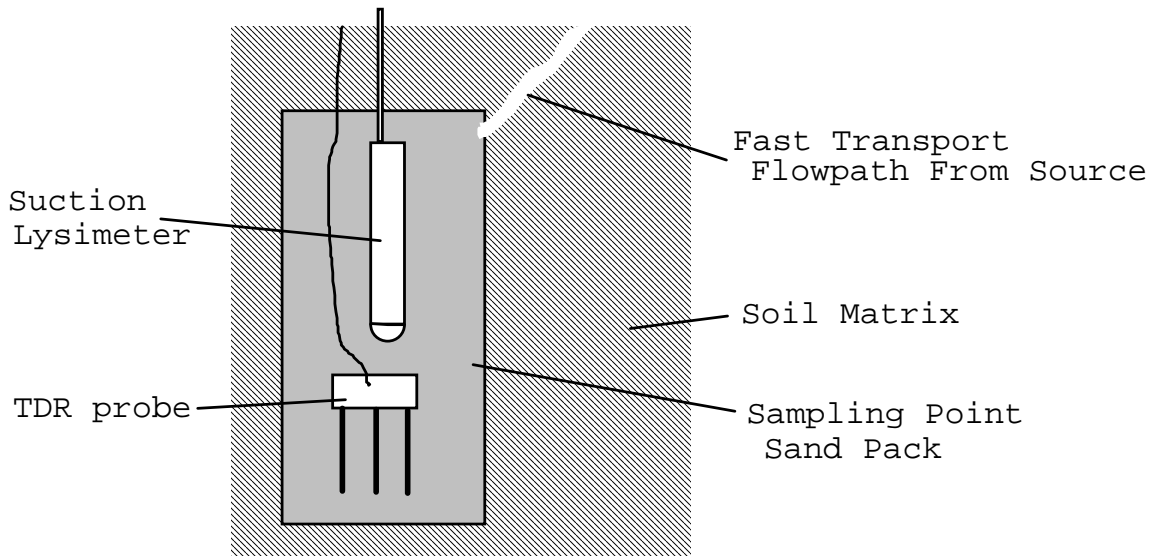


Figure D-14a. Soil water sampler between transport pathway and probe.

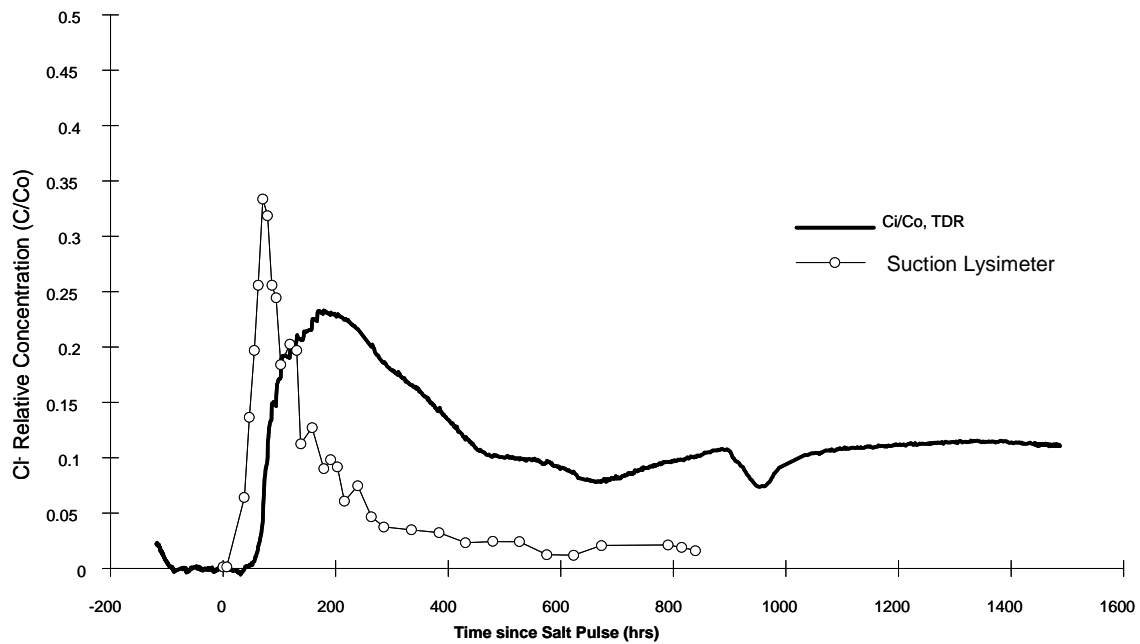


Figure D-14b. Differences in arrival times and peaks due to TDR probe, suction sampler, and fast transport flow path geometry which favor suction sampler (Northwest Outer Upper sensor pack).

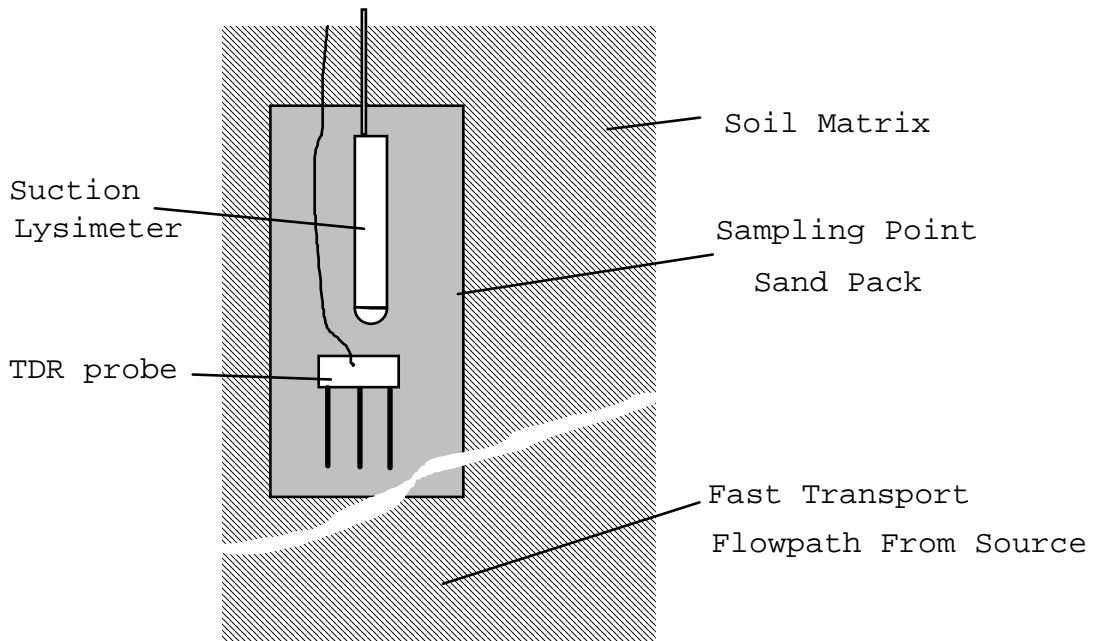


Figure D-15a. TDR probe between transport pathway and soil water sampler.

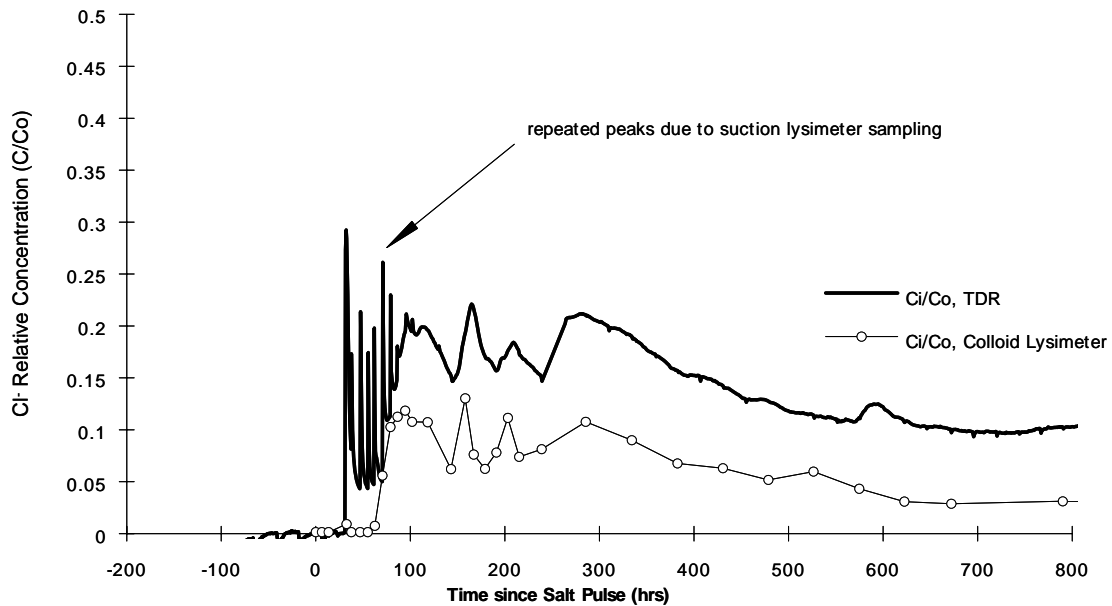


Figure D-15b. Faster arrival times at the TDR and higher peaks due to the favorable location of a fast transport pathway which favors solute transport past the TDR probe West Inner Upper sensor pack.

Comparisons between TDR and soil water sampler tracer concentrations where a significant breakthrough curve was observed -seven times at the Clay Site and three times in the Sand Site-revealed that soil water samplers yielded significantly earlier breakthrough times and higher peak concentrations than the TDR probe.

Tables D-3 and D-4 show the arrival and peak concentration times from the tracer test.

Table D-3. Clay Site Start, Peak, and End Time(t) and Concentration(C) of the Pulse

Location	t Start	C Start	t Peak	C Peak	t End	C End	t Total
A1	38.43	94.3	69.53	1263.41	622.05	111.49	583.62
A10	46.18	34.44	190.53	367.04	622.2	115.362	576.02
A11	Baseline Only						
A12	Baseline Only						
A13	333.95	61.15	430.1	85.35			
A14	216.08	34.04	286.23	138.6	815.2	24.37	599.12
A15	Baseline Only						
A16	Baseline Only						
A17	54.87	68.03	526.17	241.2			
A18	Baseline Only						
A2	45.87	140.53	78.2	1089.17	573.92	111.49	528.05
A20	Baseline Only						
A21	78.78	52.54	285.5	256.69	671.95	107.33	593.17
A22	Baseline Only						
A24	Baseline Only						
A25	62.38	55.25	94.55	620	622.53	174.41	560.15
A26	37.57	1369.89	78.92	1882.93	574.78	145.37	537.21
A27	Baseline Only						
A28	46.82	96	118.4	2124.93	574.85	76.64	528.03
A29	32.45	95.23	37.63	450.29			
A3	37.02	528.7	117.52	972.04	573.97	92.13	536.95
A30	38.4	2040	47.62	28.3	622.65	159.89	
A31	37.67	343.81	70.72	1540	430.85	135.69	393.18
A32	62.55	50.6	178.97	543.22	622.68	139.56	560.13
A33	37.5	600.33	86.52	1130	575.13	104.71	537.63
A34	37.33	1270	79.22	2370	790.63	53.8	753.3
A35	No Data						
A36	37.83	257	86.55	1240	790.68	149	752.85
A37	37.87	1002.05	79.22	1880	383.78	193.77	345.91
A38	37.88	194.74	79.25	1360	383.83	28.7	345.95
A39	47.33	1500	79.32	3620	334.9	131	287.57
A4	Baseline Only						
A40	37.92	103.75	131	425.12	384.03	47.89	346.11
A41	37.95	385.43	71.17	3810	622.97	24.37	585.02
A42	37.97	136.66	118.93	801	672.75	126.98	634.78
A43	38	235	167.9	1331.17	384.2	71.3	346.2
A44	38.02	4340	71.3	4850	479.22	52	441.2
A5	37.07	124.07	101.5	769	574.02	164.73	536.95
A6	37.1	842.33	78.35	2212.05	662.15	128.91	625.05
A7	62.08	34.63	285.13	182.15	622.17	46.92	560.09
A8	Baseline Only						
A9	32.23	146.34	86.23	2480	574.12	150.21	541.89

Table D-4. Sand Site Start, Peak, and End Time(t) and Concentration(C) of the Salt Pulse

Location	t Start	C Start	t Peak	C Peak	t End	C End	t Total
C10	136.22	27.76	219.67	326.39	651.92	50.51	515.7
C11	Baseline Only						
C12	97.9	39.86	170.08	322.51	651.93	138.95	554.03
C14	Baseline Only						
C16	Baseline Only						
C17	No Data						
C18	158.73	55.25	266.38	342	747.37	55.93	588.64
C19	No Data						
C2	194	71.5	218.08	329.29	554.75	38.31	360.75
C20	410.7	44.7	532.02	85.35			
C21	No Data						
C22	195.12	31.24	458.95	578	747.4	105.39	552.28
C23	No Data						
C24	220.28	50.5	244.13	433	602.38	66.28	382.1
C25	No Data						
C26	213.19	96.3	362.2	308	602.42	67.4	389.23
C27	No Data						
C28	314.28	128.91	506.92	169.57	747.48	68.51	433.2
C3	No Data						
C30	266.52	59	362.33	132			
C31	No Data						
C32	532.12	47.7	771.17	87			
C33	No Data						
C34	52.5	129.88	110.68	2020	458.83	61.44	406.33
C35	76.58	82.55	266.63	342	554.63	24.37	478.05
C36	34.52	101	76.6	2750	458.55	59.702	424.03
C37	No Data						
C38	52.62	1120	76.62	2150	363.67	44.7	311.05
C4	Baseline Only						
C40	52.62	503.53	76.63	1810	363.33	24.37	310.71
C41	28.17	459.97	76.65	4012.53	206.52	98.6	178.35
C42	52.68	35.99	110.82	924.61	410.43	24.37	357.75
C43	No Data						
C44	No Data						
C5	No Data						
C6	82.28	39.08	170.07	653.57	458.85	66.28	376.57
C7	No Data						
C8	266.37	34.05	338.65	107.42	770.82	46.05	504.45
C9	No Data						

This page intentionally left blank.

Appendix E: Pressure Field

<u>Section</u>	<u>Page</u>
E.1 Data Acquisition Systems	180
E.2 Pressure Transducer and Tensiometer Array	180
E.3 Pressure Transducer Calibration and Data Reduction	180
E.4 Results	186

The following sections discuss data acquisition systems used to monitor pressure transducers installed in the tensiometers and infiltrometer supply tanks as well as a rain gauge; construction and installation of the tensiometer array, data reduction, and results. Plots of total head in time at all sampling points is given at the end of this appendix.

E.1 Data Acquisition Systems

Three data acquisition systems for monitored transducers installed at both the Clay and the Sand Site). Each system included a Campbell Scientific® 21XL datalogger with SM416 16-channel multiplexers housed in a weatherproof fiberglass enclosure. MicroSwitch® PC126 series 0-5 PSI differential pressure transducers were used to monitor water height inside the 500-gallon infiltration supply tanks, and 44 tensiometers at each site. A Texas Electronics® TE525M tipping bucket rain gage. (Installed at the Clay Site only) was monitored with one systems. All sensors were wired to the data acquisition systems with 22-AWG two-pair shielded cable. All connections were sealed with Con-X-All® watertight connectors.

E.2 Pressure Transducer and Tensiometer Array

Tensiometers were arranged in a concentric ring sampling array surrounding the infiltrometer and with the porous cup approximately 5 cm above a TDR probe installed in the same well (Figures E-1 and E-2). The tensiometer tops were exposed at the surface allowing for refilling as necessary and access to the resin-encased pressure transducers (Figure E-3). A Texas Electronics® TE525M tipping bucket rain gage was installed at the Clay Site to collect rainfall measurements and connected to the datalogger, to monitor transducers.

A Compaq® LTE 486SX/25 laptop computer was used to download programs to the datalogger and upload data files from datalogger storage modules. Power to each system was provided by a Solarex® MSX10 15 volt, 8.9 amp regulated solar collector and a 12-volt deep cycle marine battery.

E.3 Pressure Transducer Calibration and Data Reduction

All pressure transducers were calibrated in groups of fifteen by connection to a common pressure chamber which was then connected to an inverted manometer Figure. All pressure transducers were calibrated under a vacuum, which was provided by the inverted 7 m manometer depicted in Figure F- 10. To duplicate the field installation, the data acquisition system (datalogger and multiplexer) to be used for monitoring the tensiometers in the field were used in calibrating the pressure transducers. Included in this system were 12.2 m long transducer extension wires. A data acquisition program was written using the same core program as the field program (both programs took and average of 10 readings), but incorporating starting, stopping, and data insert flags. These flags provided the ability to input observed column heights into the calibration data file in the same row as the correlated millivolt reading. The use of the field data acquisition system helped assure that resistive losses due to multiplexers and extension wires, if present, would be accounted for in the calibration process and provided the ability to calibrate numerous pressure transducers at a time. The calibration data for all the pressure transducers exists, but due to a lapse in record keeping there is no clear connection between the calibration coefficients and the tensiometers they belong to. Thus the coefficients are not documented here. However,

Figure E-4 shows a typical calibration curve as well as the coefficients and statistics obtained from the pressure transducers.

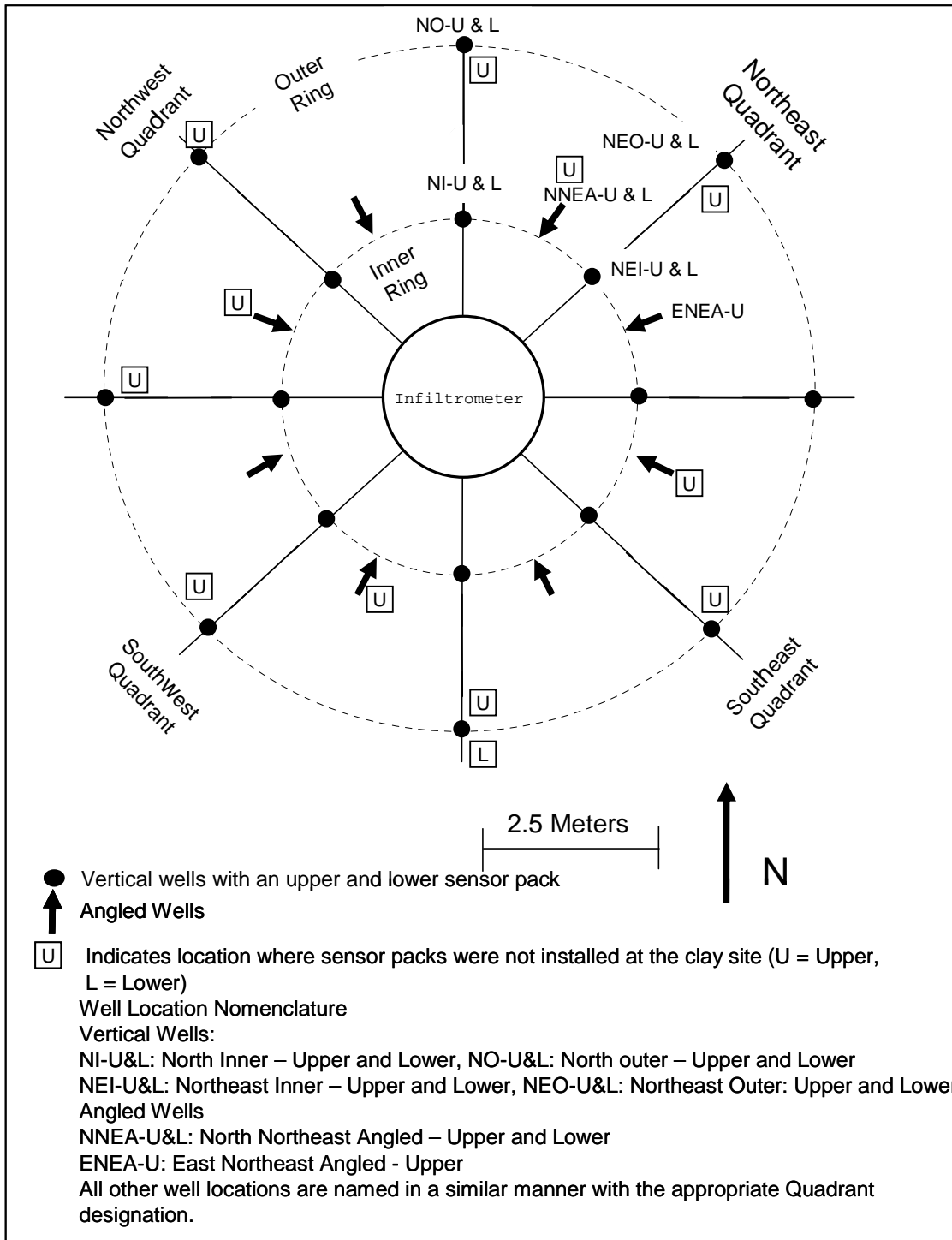


Figure E-1. Plan-view and nomenclature of Clay and Sand Site sensor arrays. Note that some of the sensor packs were not installed at the Clay site as indicated in the figure.

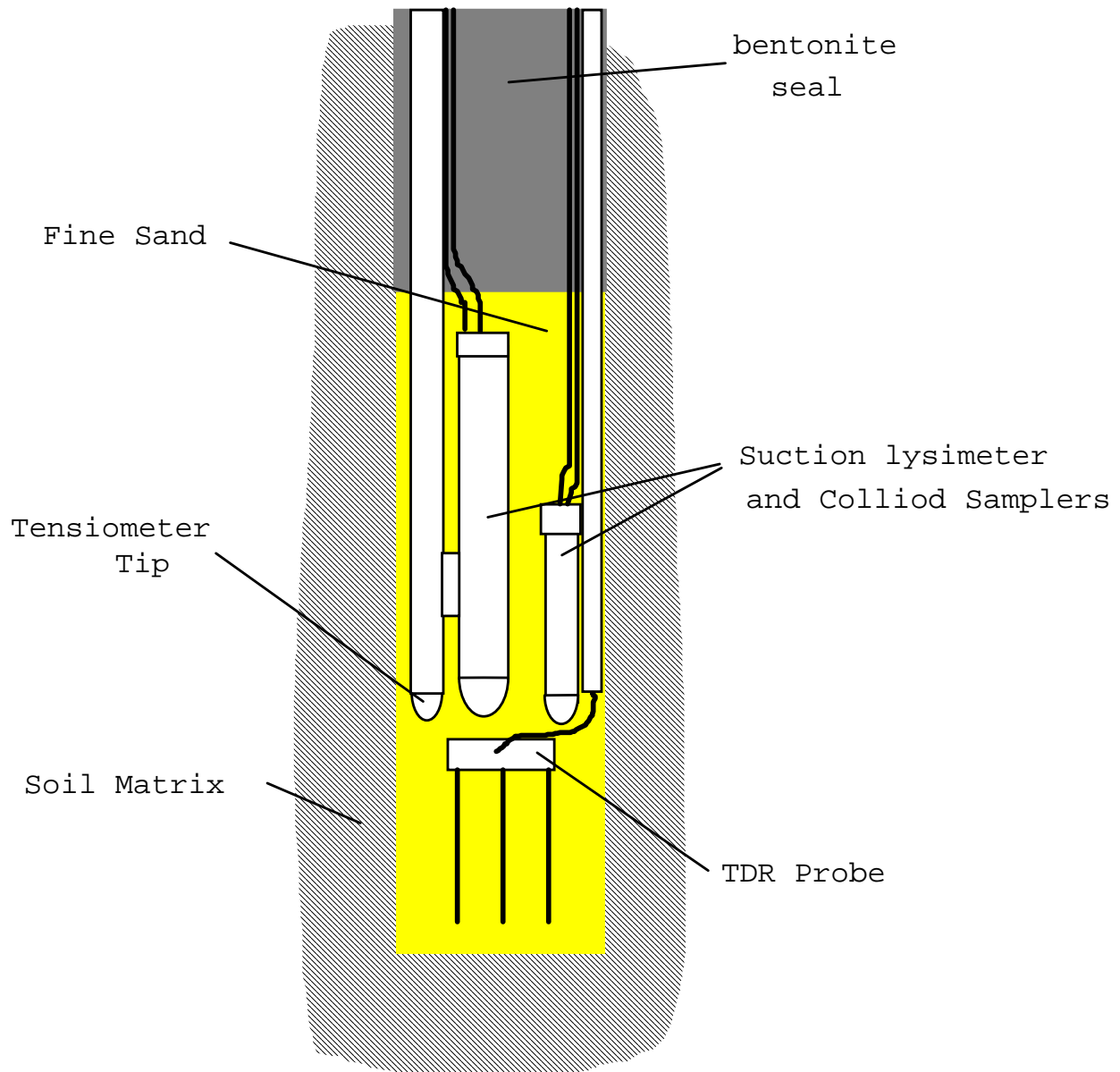


Figure E-2. Sampling point sensor pack.

Calculation of Pressure and Total Head

Calculation of pressure head in centimeters of water at the tensiometer transducer involved accounting for the hanging column of water between the porous cup and pressure transducer by adding this distance and adding the elevation of the porous cups (above mean sea level) to the pressure transducer reading: The total head was then used to plot changes in the pressure field with time and as a response to rainfall events (See last section of this appendix).

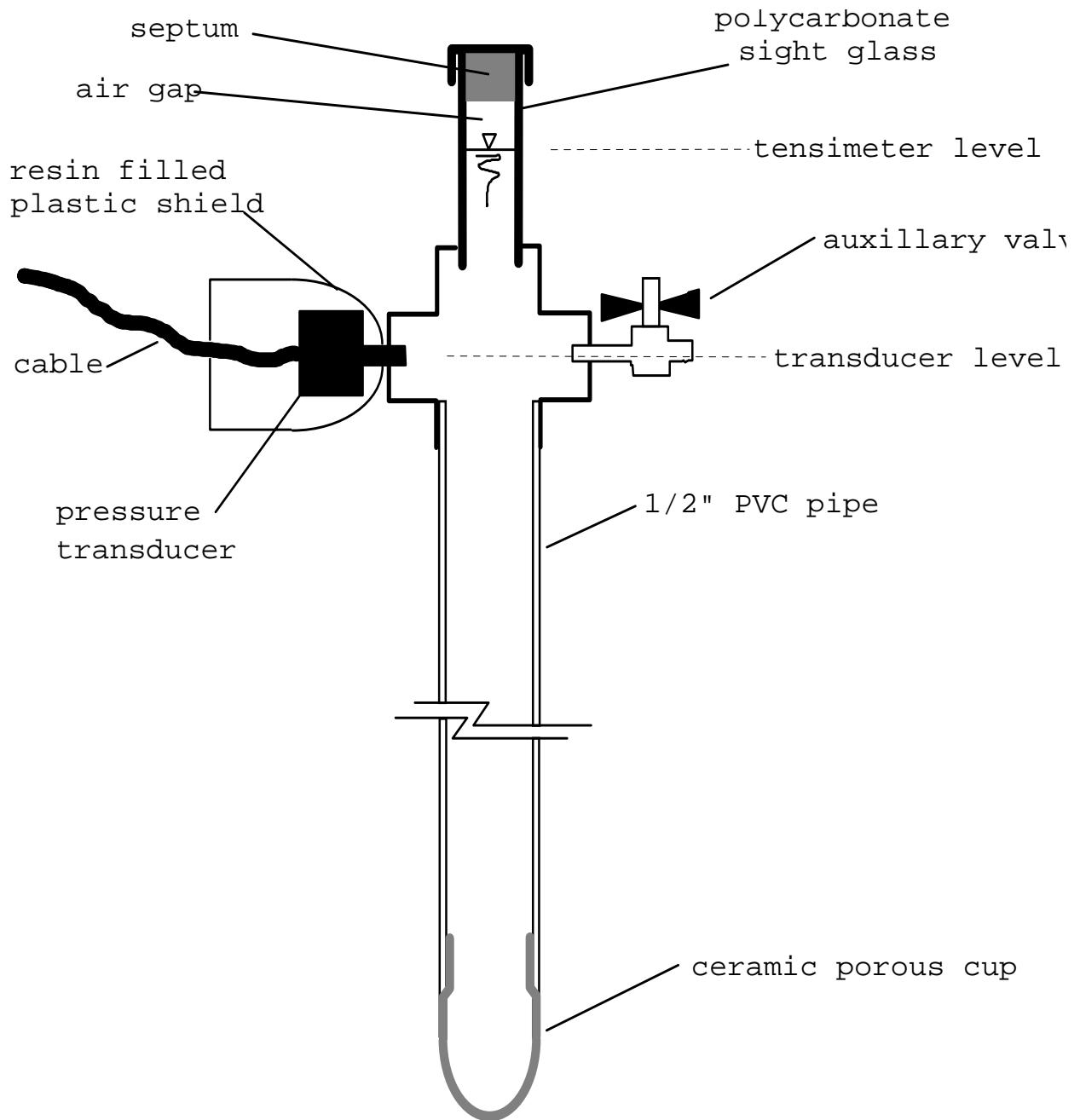


Figure E-3. Tensiometer construction.

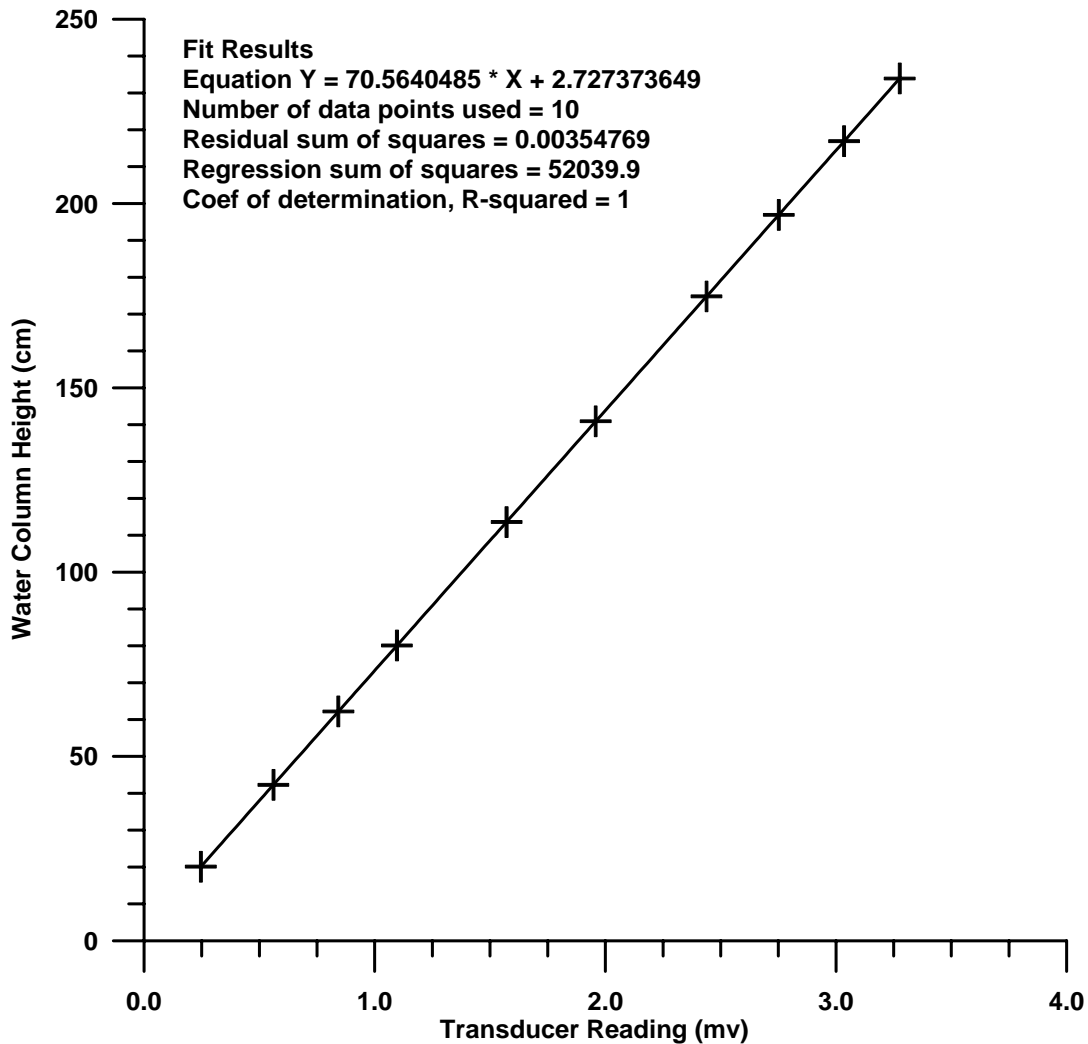


Figure E-4. An example of typical transducer calibration coefficients and statistics.

Transducer and Tensiometer Errors

Numerous problems were encountered with tensiometers. Of the 44 tensiometers installed at the Clay Site, 22 malfunctioned for all or a considerable portion of the infiltration test. Of the 22 malfunctioning tensiometers, 11 failed because of air leaks in the tensiometers, and five failed because of transducer malfunction. Six tensiometers showed major inconsistencies in pressure readings compared to manual tensiometer readings (see next paragraph).

Table E-1 lists tensiometers and probable causes for problems.

Tensiometer Accuracy

Transducer pressure readings were compared to the readings obtained from a Soil Moisture Systems tensiometer at five different times during the test. Tensiometer readings were taken by inserting a needle through the septum capping the top end of the polycarbonate sight glass (Figure E-4). A total of 175 comparisons were made. Eighty-six of those comparisons were discarded because they were taken when transducer readings were off scale due to soil water

Table E-1. Clay Site Tensiometer Malfunctions.

Sampling Location	Reason for Malfunction	Sampling Location	Reason for Malfunction
North Inner Upper (A1-1IU)		Southwest Outer Upper (A23-6OU)	
North Inner Lower (A2-1IL)		Southwest Outer Lower (A24-6OL)	Tensiometer/Transducer
North Outer Upper (A3-1OU)	Invalid data thru Hour 925	West Inner Upper (A25-7IU)	
North Outer Lower (A4-1OL)		West Inner Lower (A26-7IL)	
Northeast Inner Upper (A5-2IU)	Leakage	West Outer Upper (A27-7OU)	
Northeast Inner Lower (A6-2IL)	Leakage	West Outer Lower (A28-7OL)	Invalid Data from Hour 1275
Northeast Outer Upper (A7-2OU)		Northwest Inner Upper (A29-8IU)	
Northeast Outer Lower (A8-2OL)	Leakage	Northwest Inner Lower (A30-8IL)	*Leakage from Hour 1000
East Inner Upper (A9-3IU)		Northwest Outer Upper (A31-8OU)	Invalid Data
East Inner Lower (A10-3IL)	Leakage from Hour 825	Northwest Outer Lower (A32-8OL)	Invalid Data
East Outer Upper (A11-3OU)		North-Northeast Angled Upper (A33-A1U)	
East Outer Lower (A12-3OL)	Leakage	North-Northeast Angled Lower (A34-A1L)	Tensiometer/Transducer
Southeast Inner Upper (A13-4IU)	Leakage	East-Northeast Angled Lower (A35-A2L)	Invalid Data
Southeast Inner Lower (A14-4IL)		East-Southeast Angled Lower (A36-A3L)	
Southeast Outer Upper (A15-4OU)	Leakage from Hour 1450	East-Southeast Angled Upper (A37-A3U)	Tensiometer/Transducer
Southeast Outer Lower (A16-4OL)	Tensiometer/Transducer	South-Southeast Angled Upper (A38-A4L)	Leakage
South Inner Upper (A17-5IU)	Leakage	South-Southwest Angled Upper (A39-A5U)	
South Inner Lower (A18-5IL)	Invalid Data	South-Southwest Angled Lower (A40-A5L)	Invalid Data Hours 100-300
South Outer Upper (A19-5OU)	Leakage	West-Southwest Angled Lower (A41-A6L)	Leakage
South Outer Lower (A20-5OL)	Tensiometer/Transducer	West-Northwest Angled Lower (A42-A7L)	Invalid Data Hours 100-300
Southwest Inner Upper (A21-6IU)	Invalid Data from Hour 1400	West-Northwest Angled Upper (A43-A7U)	Tensiometer/Transducer
Southwest Inner Upper (A22-6IL)	Leakage	North-Northwest Angled Lower (A44-A8L)	

sampling, tensiometers were leaking or inoperable, or because transducers were malfunctioning. The remaining 89 transducer and tensimeter pressure readings were compared, compensating for the difference in water column height between the top of the water column (the tensimeter level) and the transducer level (Figure E-3). The results (in cm of H₂O) show an average tensimeter minus transducer difference of 6.49 cm, with a minimum difference of -44.65 cm, a maximum of 48.45 cm, and a standard deviation of 10.74 cm.

In the 24 cases where the water level in the tensiometer was below the transducer, both tensimeter and transducers read the pressure in the air gap between the top of the water column and the septum. Readings by the two measurement systems should be equal. In these cases, the average tensimeter minus transducer difference was 5.97 cm, with a minimum of -0.95 cm, a maximum of 16.15 cm, and a standard deviation of 5.24 cm. The difference in readings may be attributed primarily to the introduction of atmospheric air pressure into the tensiometer when the tensimeter needle was inserted through the sight glass septum, resulting in a higher (less

negative) reading. Increases of 2 to 20 cm of H₂O in consecutive readings were experienced during laboratory tests when the tensiometer needle was immediately reinserted into an operating tensiometer. The variance in magnitude of error was inversely proportional to the volume of air gap between the water surface and the sight glass septum (Figure E-3).

E.4 Results

Effects of Soil Water Sampling on Tensiometer Readings

During sampling, a vacuum was applied to the lysimeters and colloid samplers resulting in a pressure drop within the sensor pack as recorded by the tensiometers. As discussed above, the resulting drop in pressure often caused the 0 - 5 PSI pressure transducers to go off scale. After sampling, the pressure would return to the level that existed prior to sampling. This return rate varied between tensiometers indicating that the permeability of the formation surrounding the sensor packs is variable. For example, the slow return to pre-sampling pressures at the Southeast Outer Lower sampling point (Figure E-7) suggests that this sensor pack is isolated from an easily accessible water source as the pressures take up to 10 hours to return to pre-sampling levels. Compare the last case with the North Inner Upper sensor pack (Figure E-6) which returned to pre-sampling levels within 30 minutes.

Diurnal Fluctuations

Diurnal fluctuations such as those plotted in Figure E-7 were observed in all functioning tensiometers. Increases in tensiometer readings on most days started around noon and lasted until approximately 6 P.M. The fluctuations ranged from 2 cm to as much as 25 cm, with most ranging between 3 and 6 cm. The most likely cause of these fluctuations is the temperature dependent change in pressure within the air gap at the top of the tensiometers. This occurred despite shielding from direct sunlight with insulated aluminum shields placed over all 1 tensiometer tops (see Plate 9).

Long Time Patterns of Total Potential Change

Pressure head (or total head as plotted in Figure E-5) at both the Clay and Sand Site exhibit trends that mimic the infiltration rates. From the start of the CI pulse to 400 hours, both the pressure and infiltration rate increased whereas following 400 hours both measures gradually and consistently dropped with time. The fact that these measures duplicate each other so well indicates a strong link between the two. The observed changes in pressure head are likely due to a passive response to changes in infiltration rates. Infiltration rates were probably impacted by a tracer-induced die off of algae resulting in an unclogging of the near-surface macropores. This die off was possibly followed by a second algae bloom and a re-clogging after 400 hours, beyond which time the tracer was flushed from the system, resulting in lowered infiltration rates. See Appendix B for a further discussion of infiltration rate variability. Mounding of infiltrated water probably occurred within macropores below the infiltrometer and above the sensor pack. With changing infiltration rates, the pressure head passively responded to changes in the height of water mounding. Superimposed on this simple hypothesized mechanism are complicating factors including a decline of the perched water table during the summer months along with diurnal and seasonal changes in evapotranspiration rates.

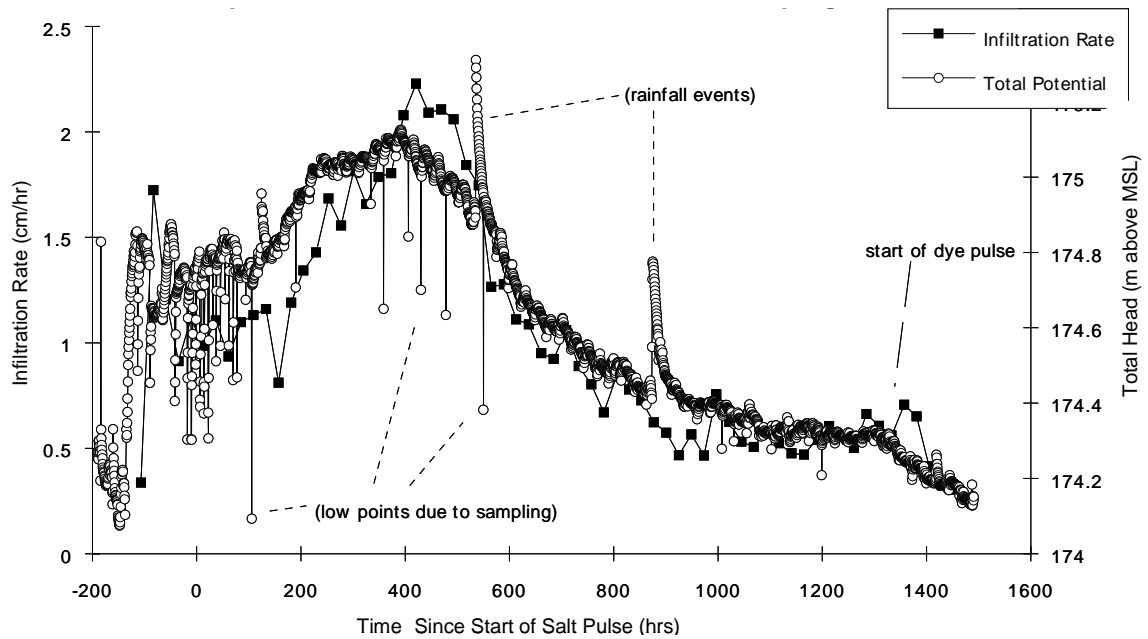


Figure E-5. Correspondence of trends between infiltration rate and changes in total head at the North Inner Upper sensor pack at the Clay site.

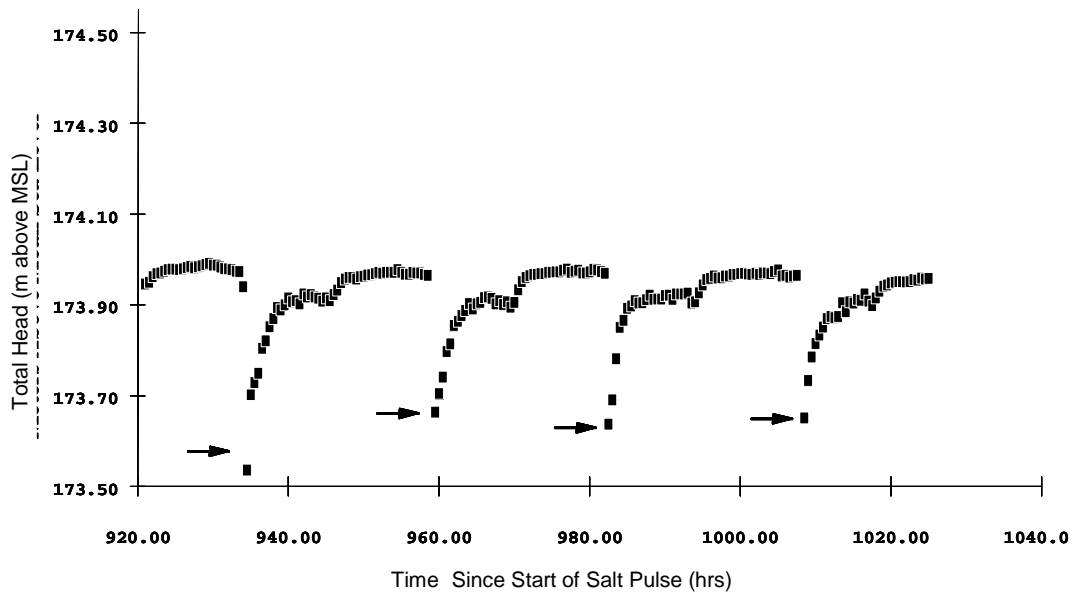


Figure E-6. Depression of pressure head during sampling and rapid return to pre-sampling pressure head after sampling in the North Inner Upper sensor pack.

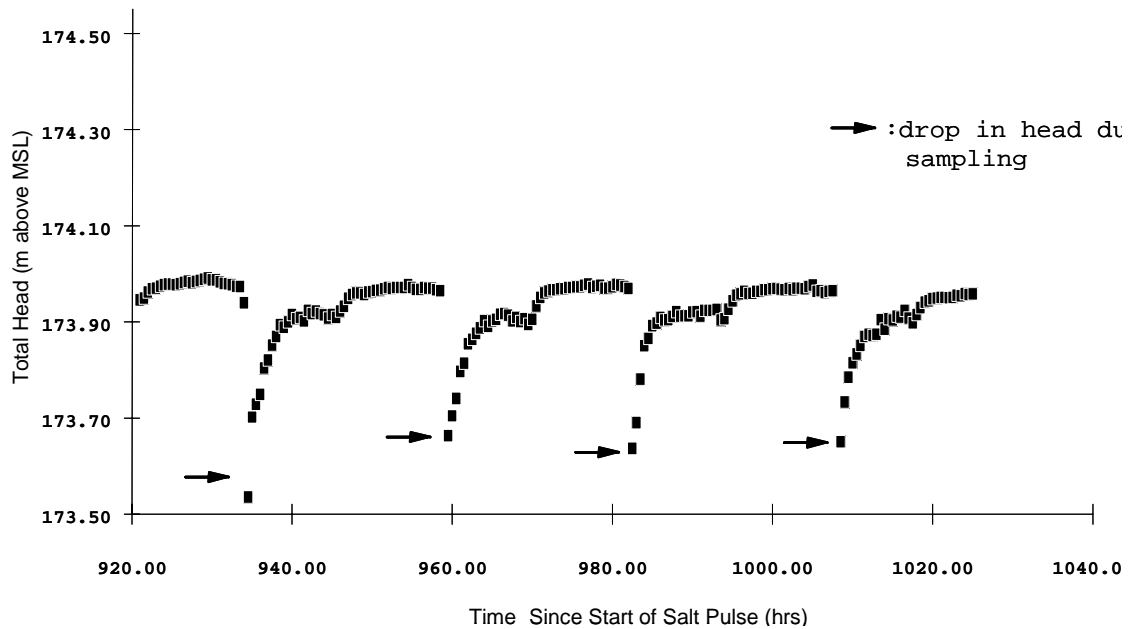


Figure E-7. Depression of head during sampling and slow return at sample point Southwest Outer Lower.

Response to Sampling

Impacts of the decreased pressures generated during soil water sampling were evident in the pressure head measurements (Figures E-6 and E-7). The magnitude and the duration of the impact were not consistent between sensor packs. A reasonable explanation for the difference in recovery time is that a fast return to pre-sampling pressures (Figure E-6) indicates that the sampling point is well connected by macropores to a larger source of water or the atmosphere, whereas those that show a significant lag are poorly connected. In such cases, the drop in pressure was significantly smaller in comparison to those with long re-equilibration times (Figure E-7), indicating that the sampling points were not well connected to either an air or water supply.

Rainfall Events

Recorded in the pressure head measurements are the impacts of three periods of heavy precipitation of 2.4, 5.5, and 3.3 cm over a span of a few hours. The response at the Clay Site was virtually instantaneous for all sensor packs for all three rainfall events whereas only the second and third rainfall events were recorded at the Sand Site. The 5.5 cm rainfall event raised the total pressure head by 30 to 40 cm on at most sensor packs at the Clay Site with the highest reading at 55 cm at the West Inner Lower sensor pack. The fact that the change in pressure head during the three rainfall events is much greater than the actual rainfall depth, even considering a hypothetical but unrealistic empty primary porosity of 50%, provides evidence for ponding of water above the sensor packs in macropores with subsequent attenuation of the mound once the precipitation event ends.

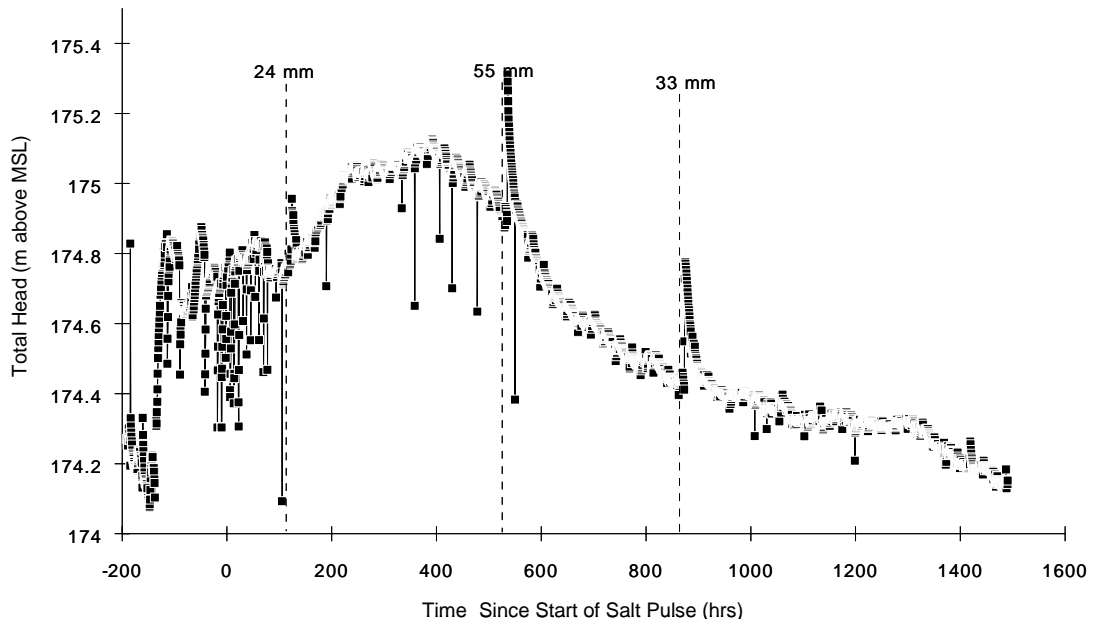


Figure E-8. Clay Site total head in time and rainfall events at the North Inner Upper sensor pack).

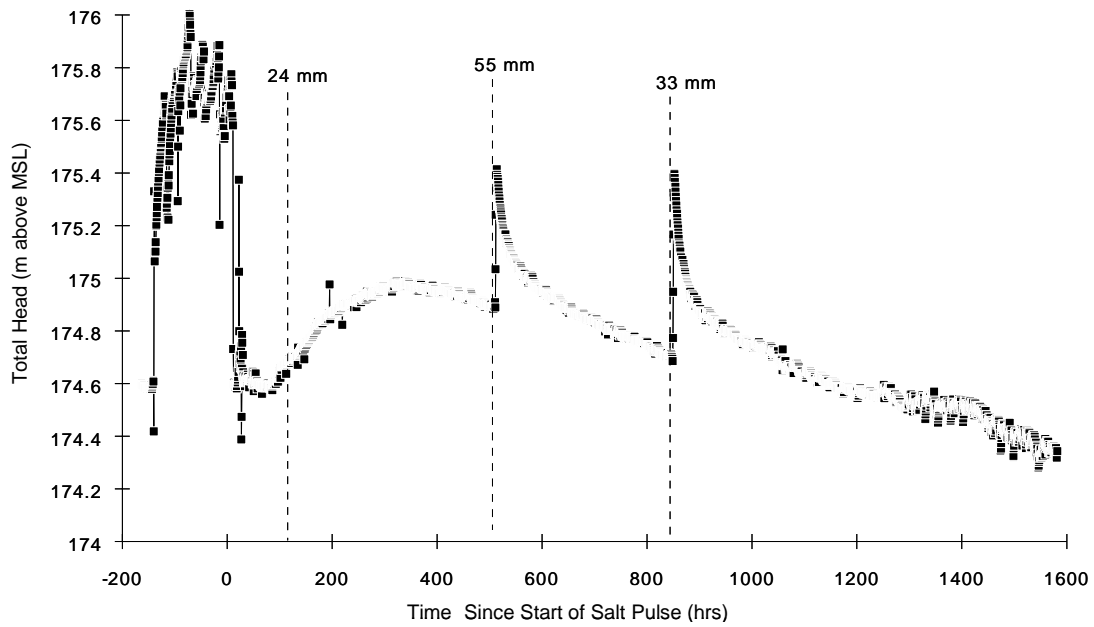
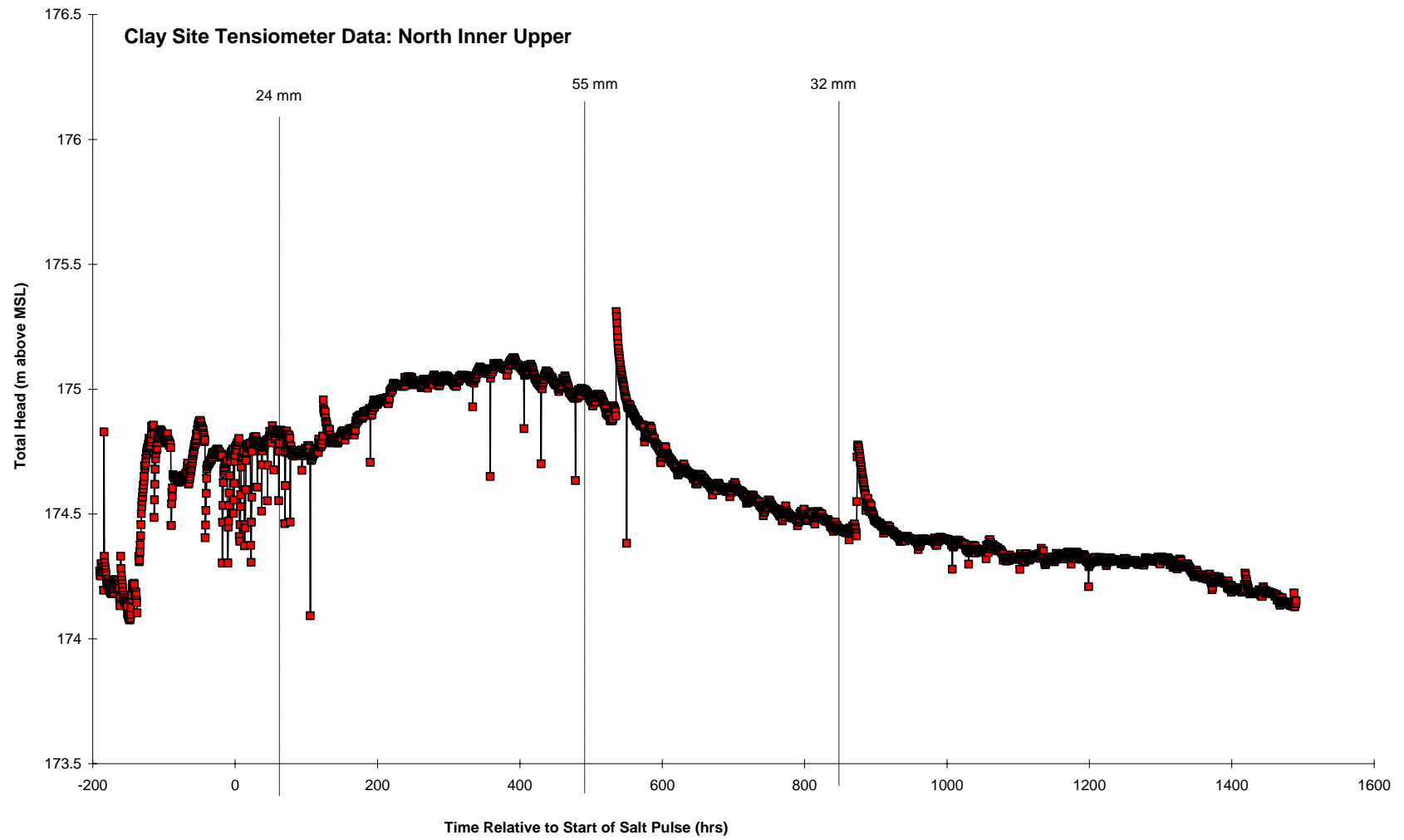
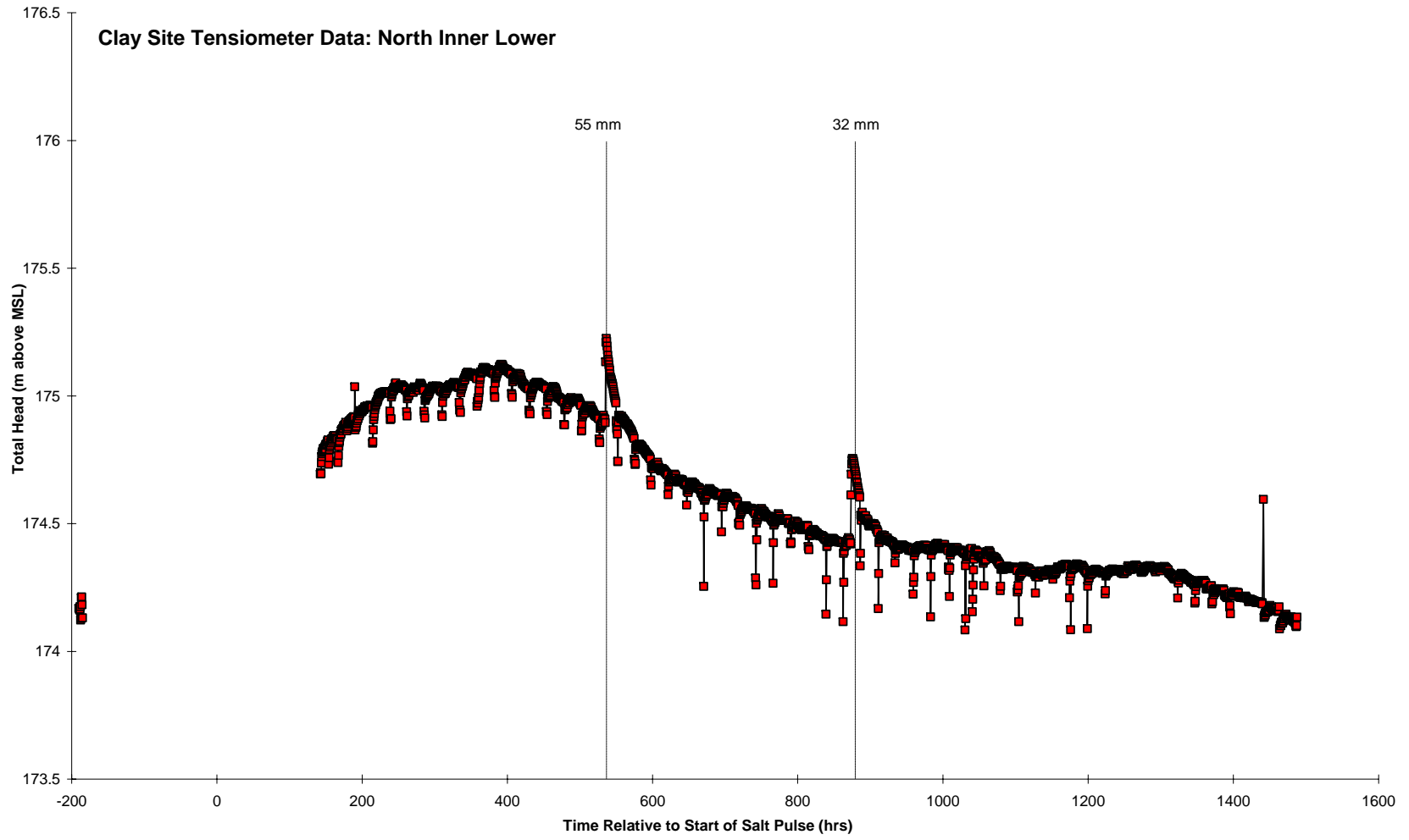
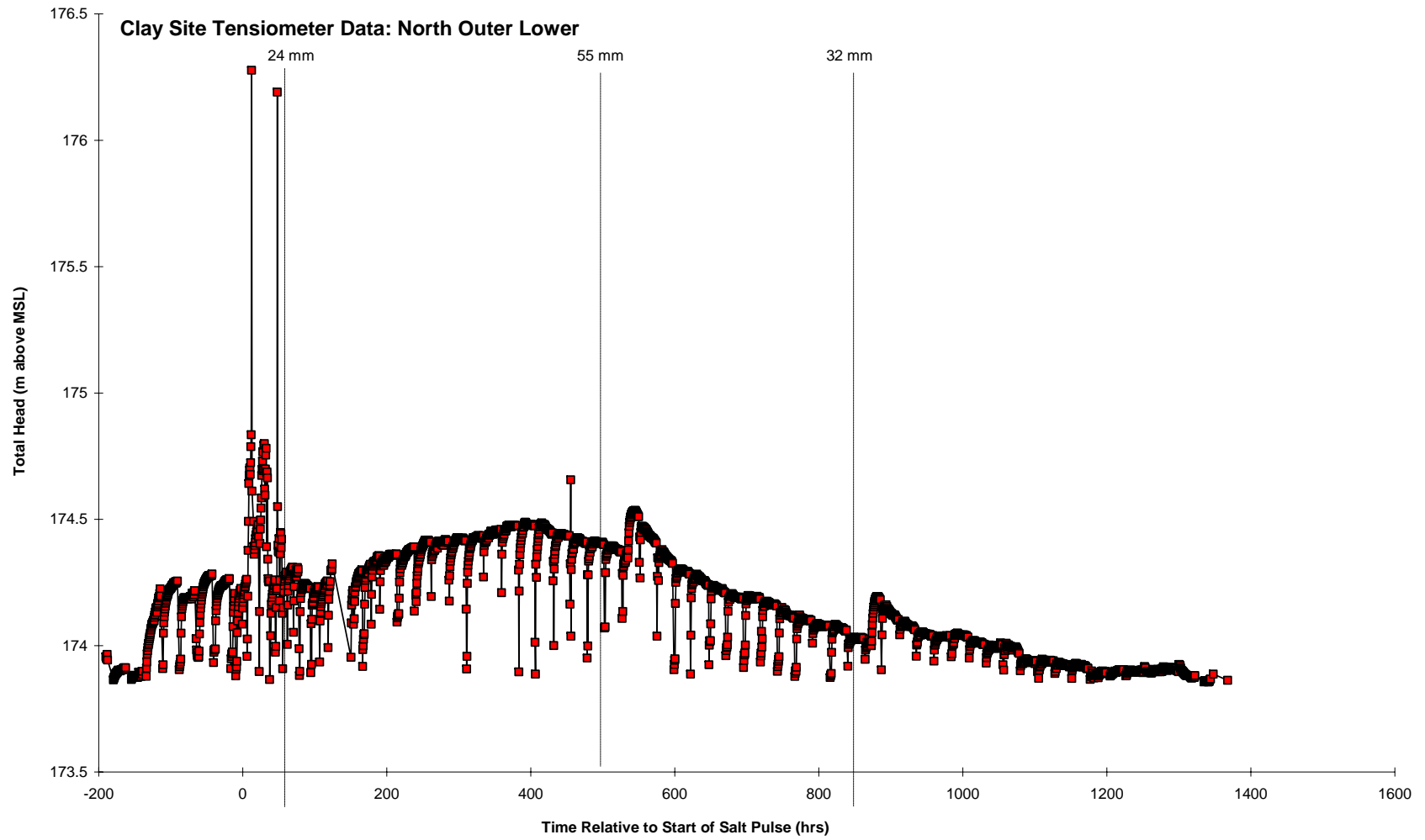


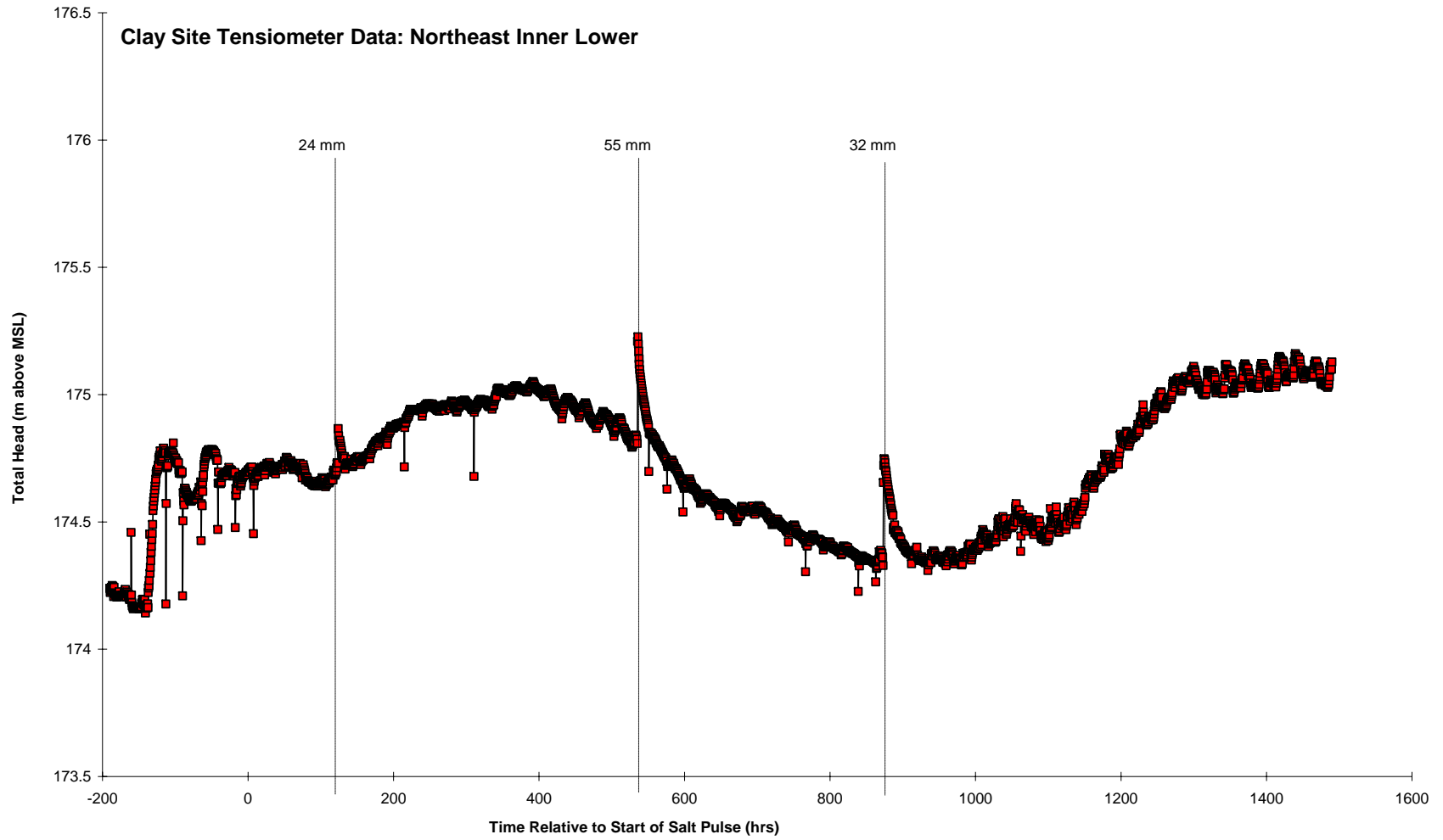
Figure E-9. Sand Site correlation of head rise and rainfall events at the West Inner Lower sensor pack.

190

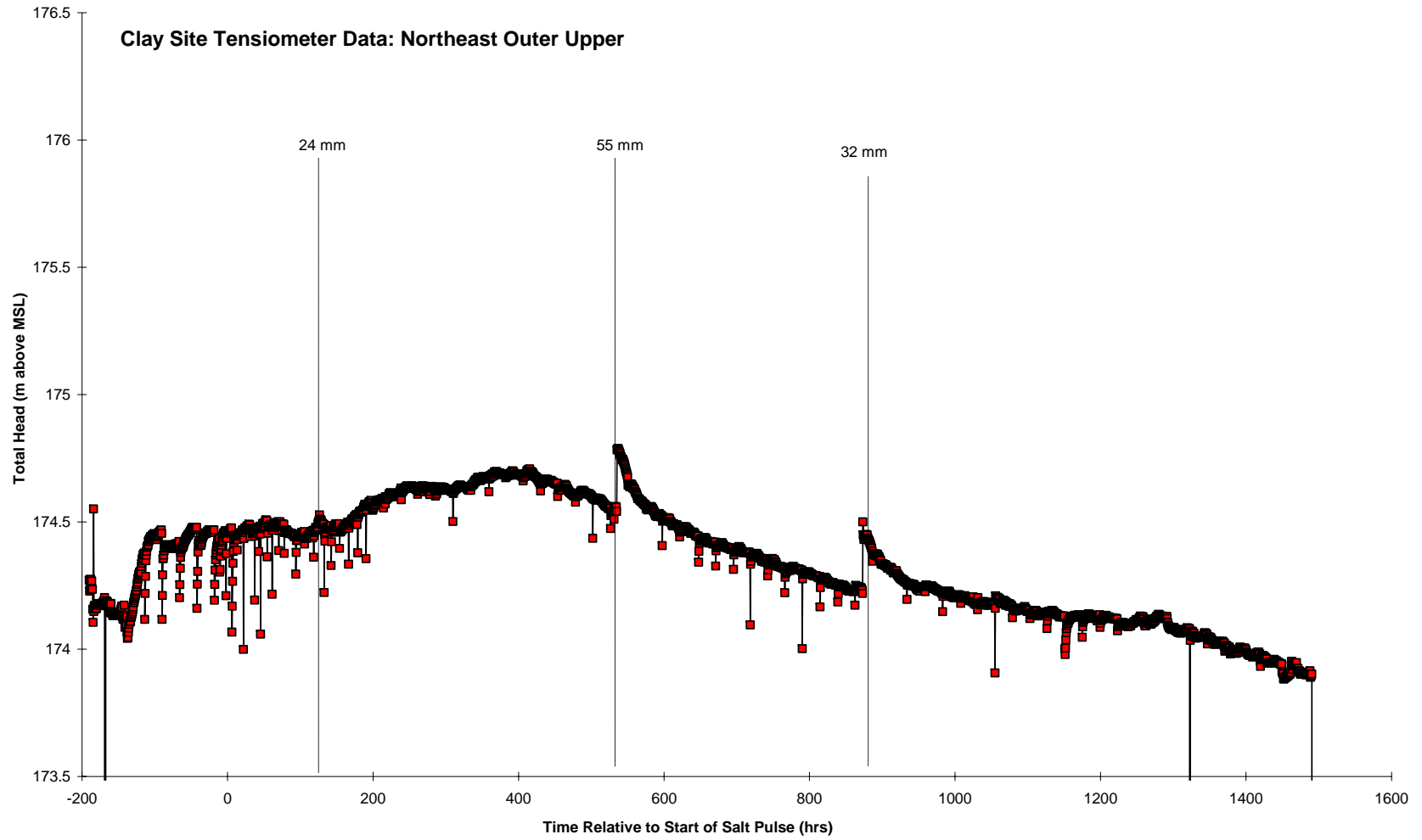


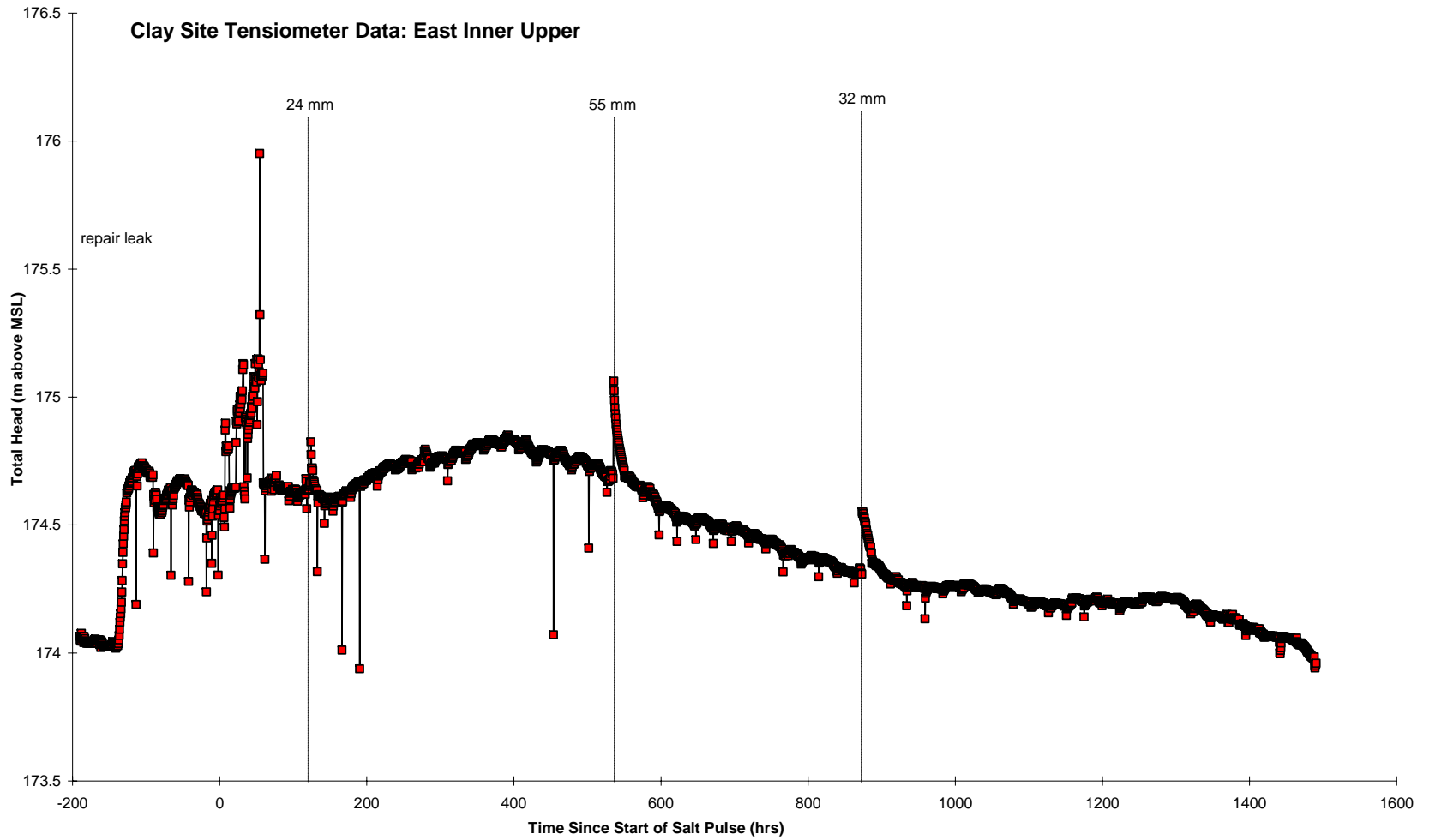


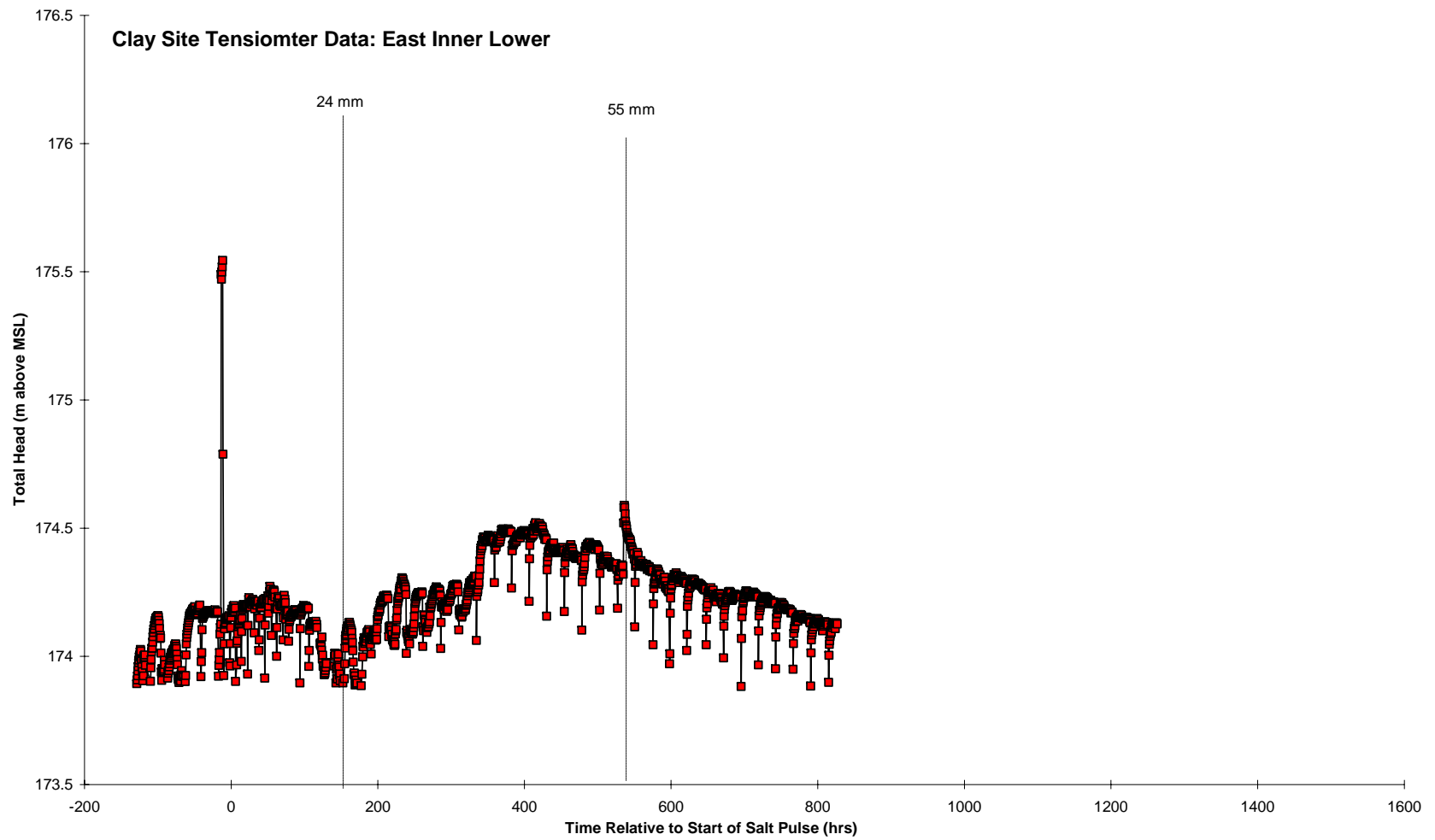


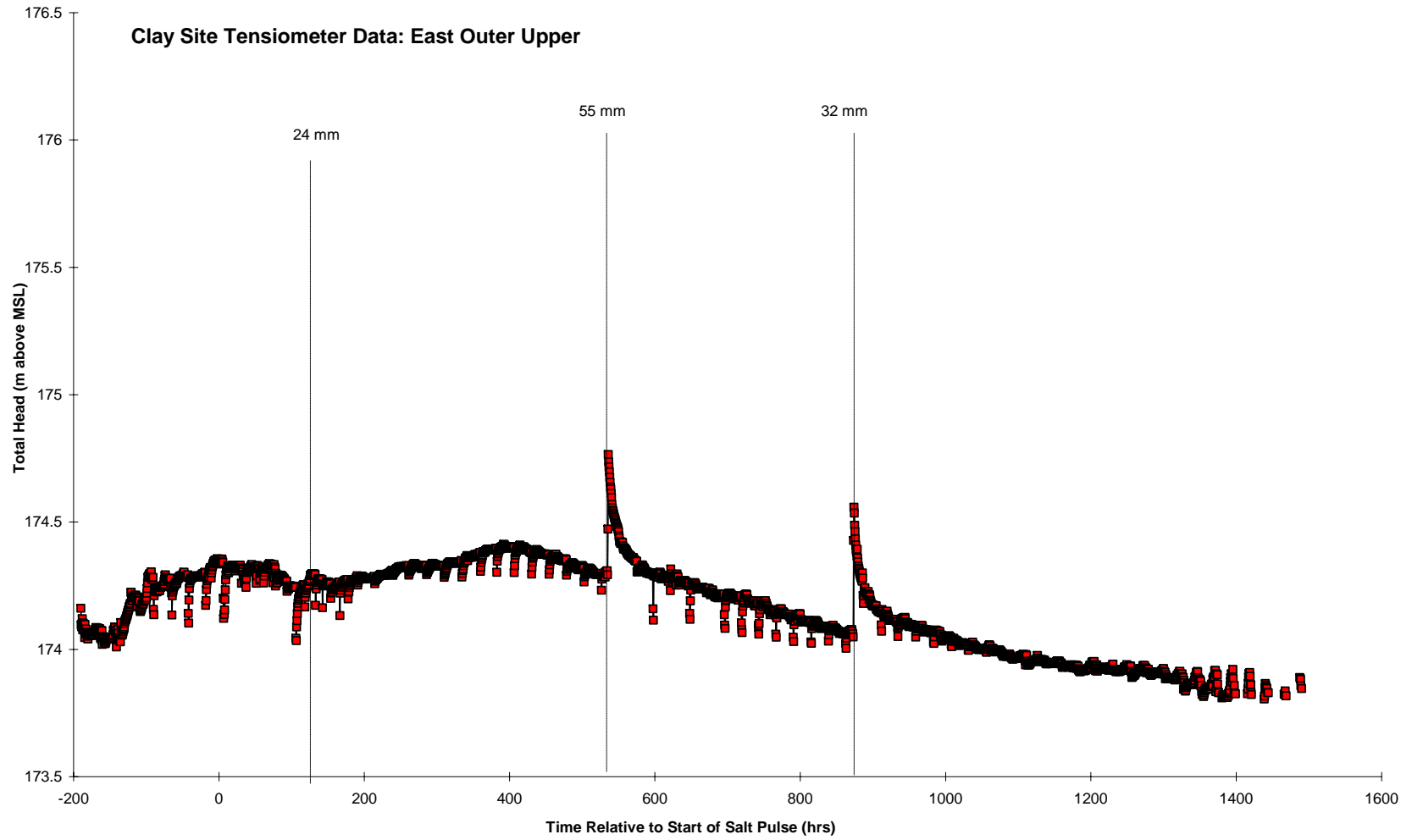


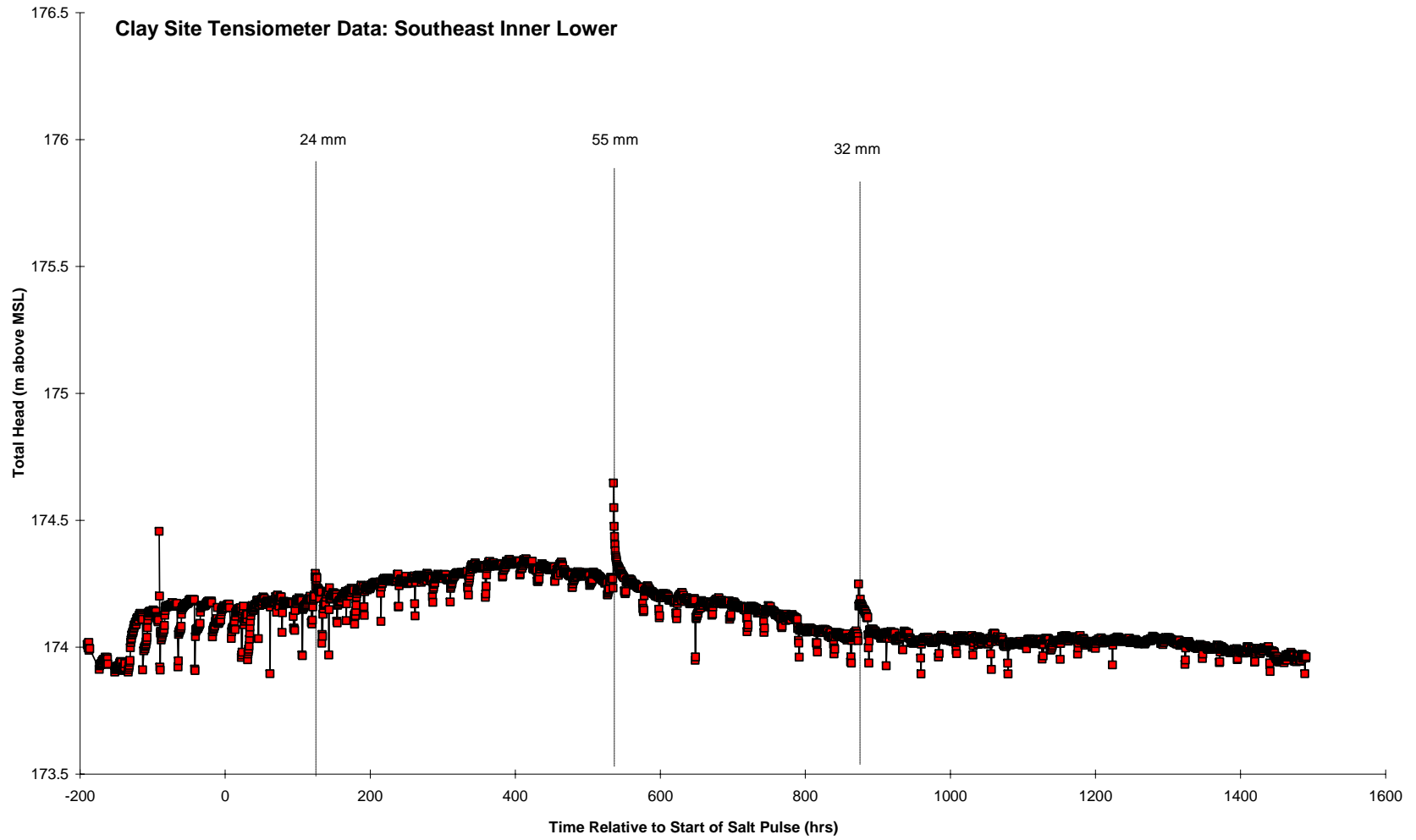
194

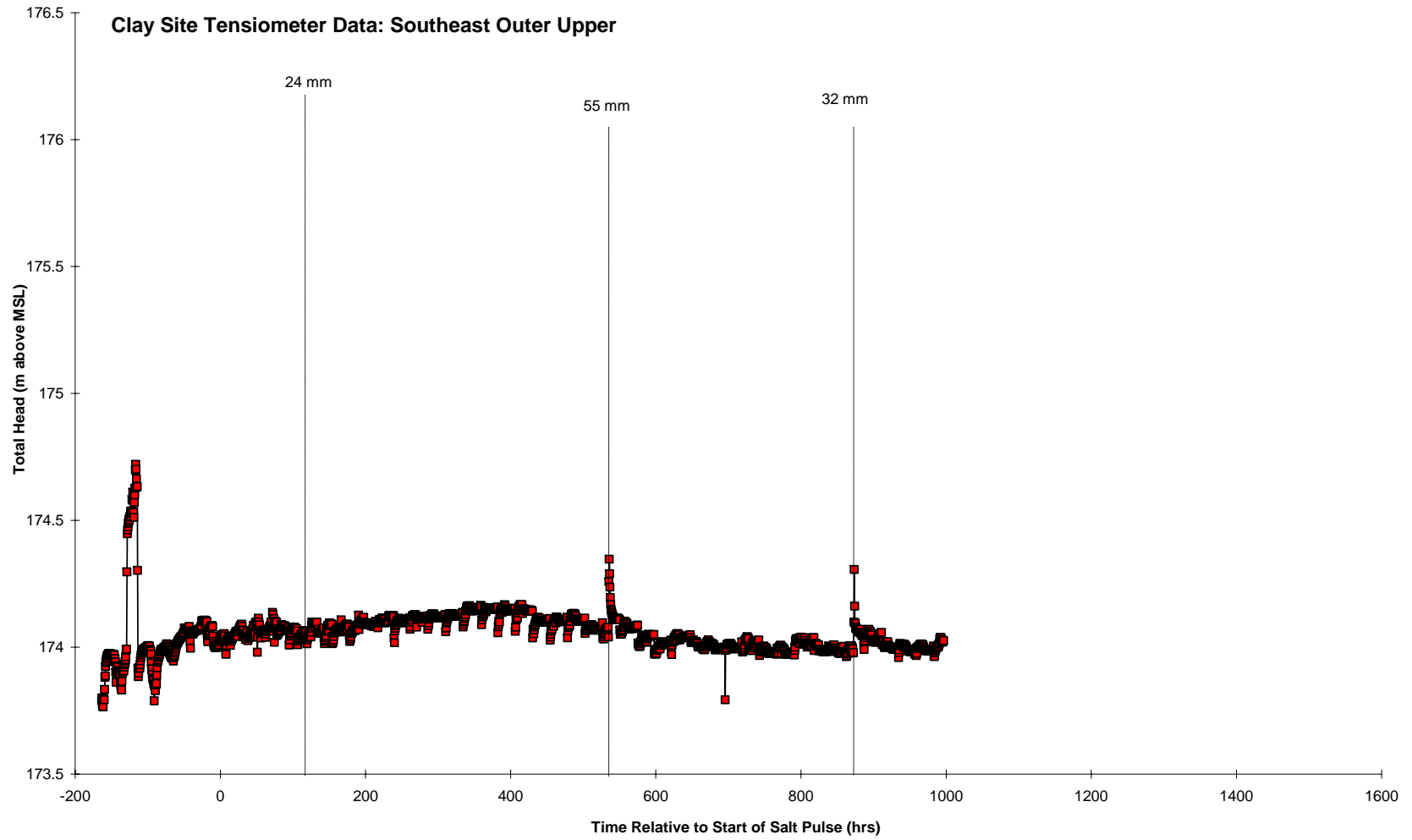




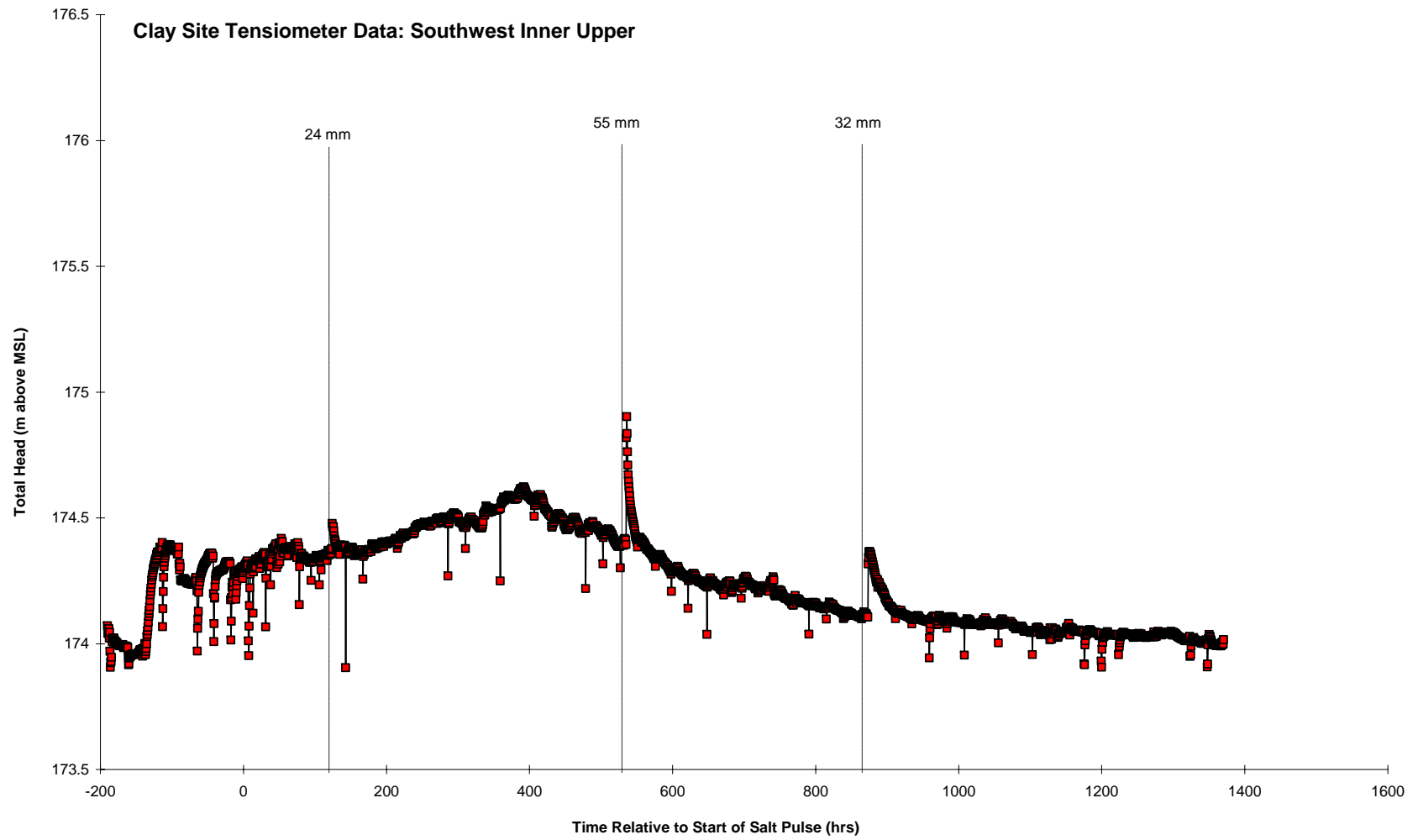


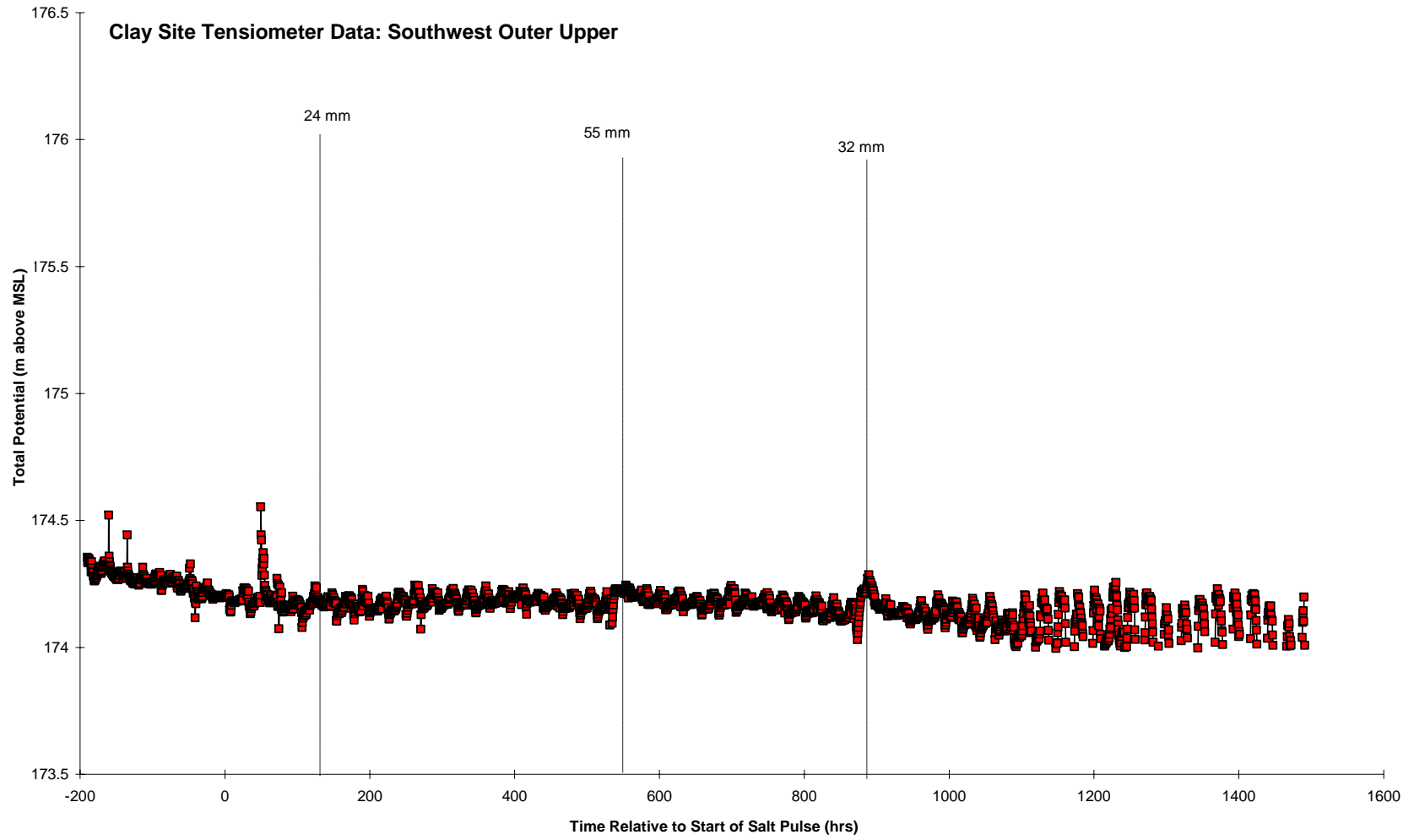




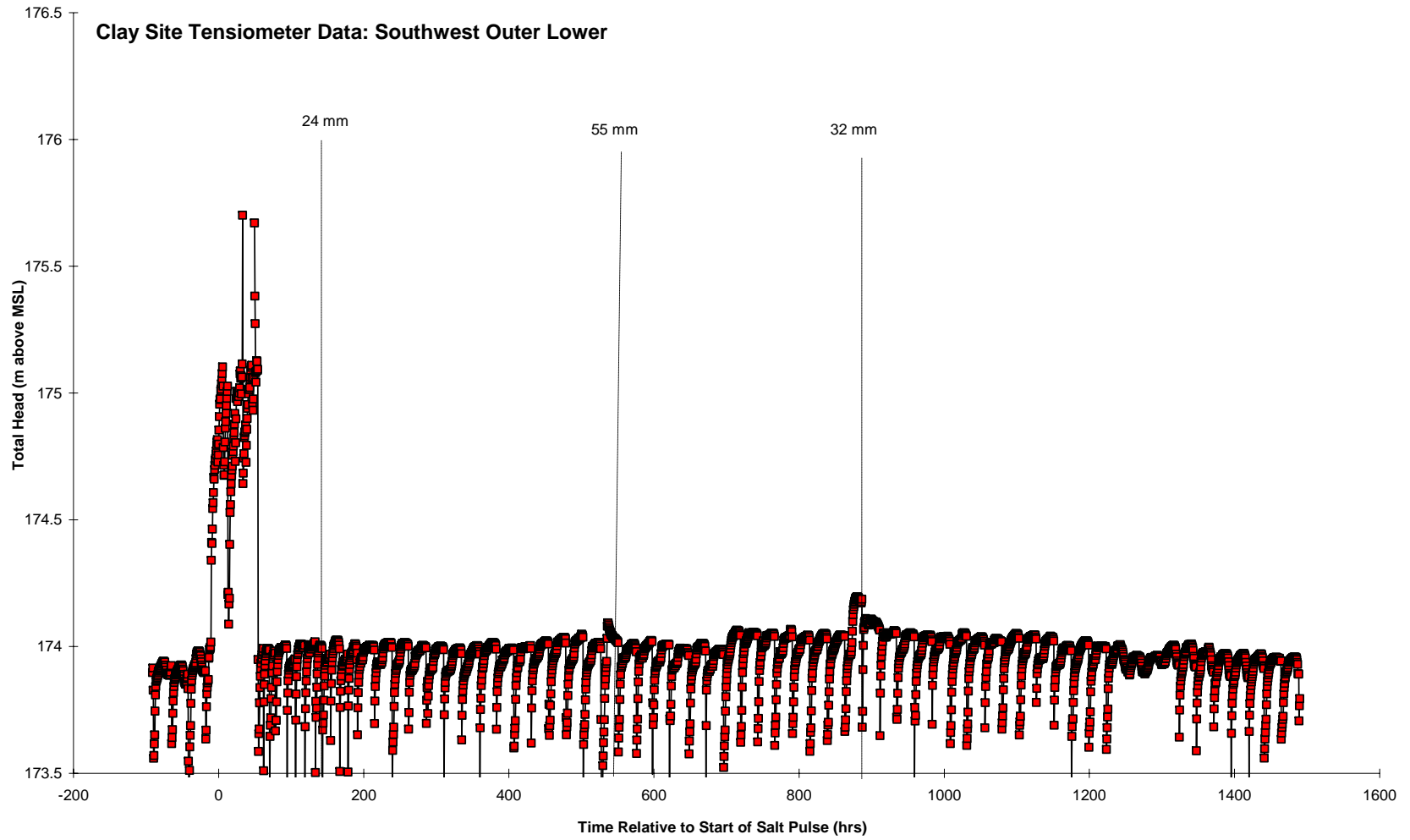


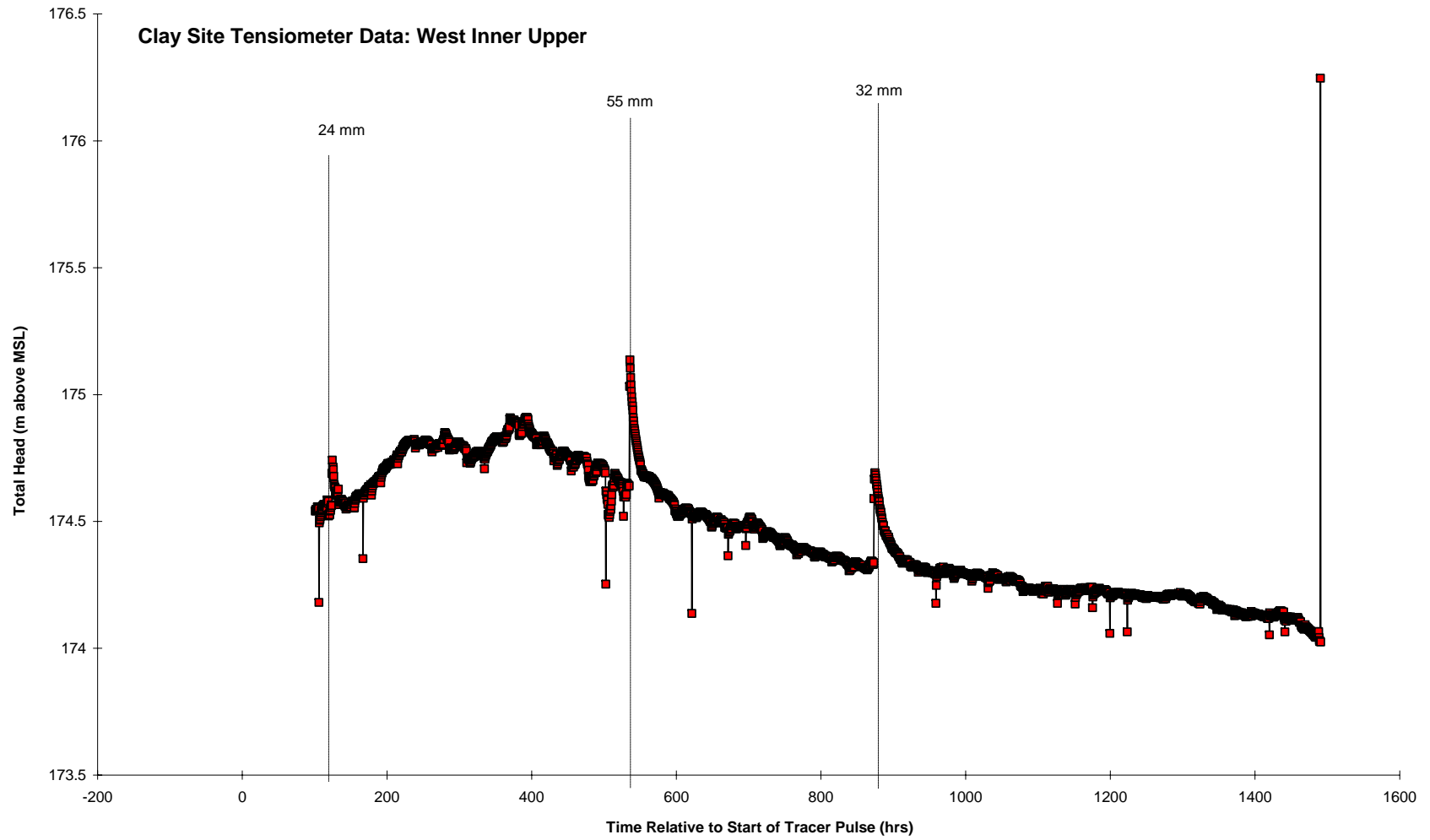
200



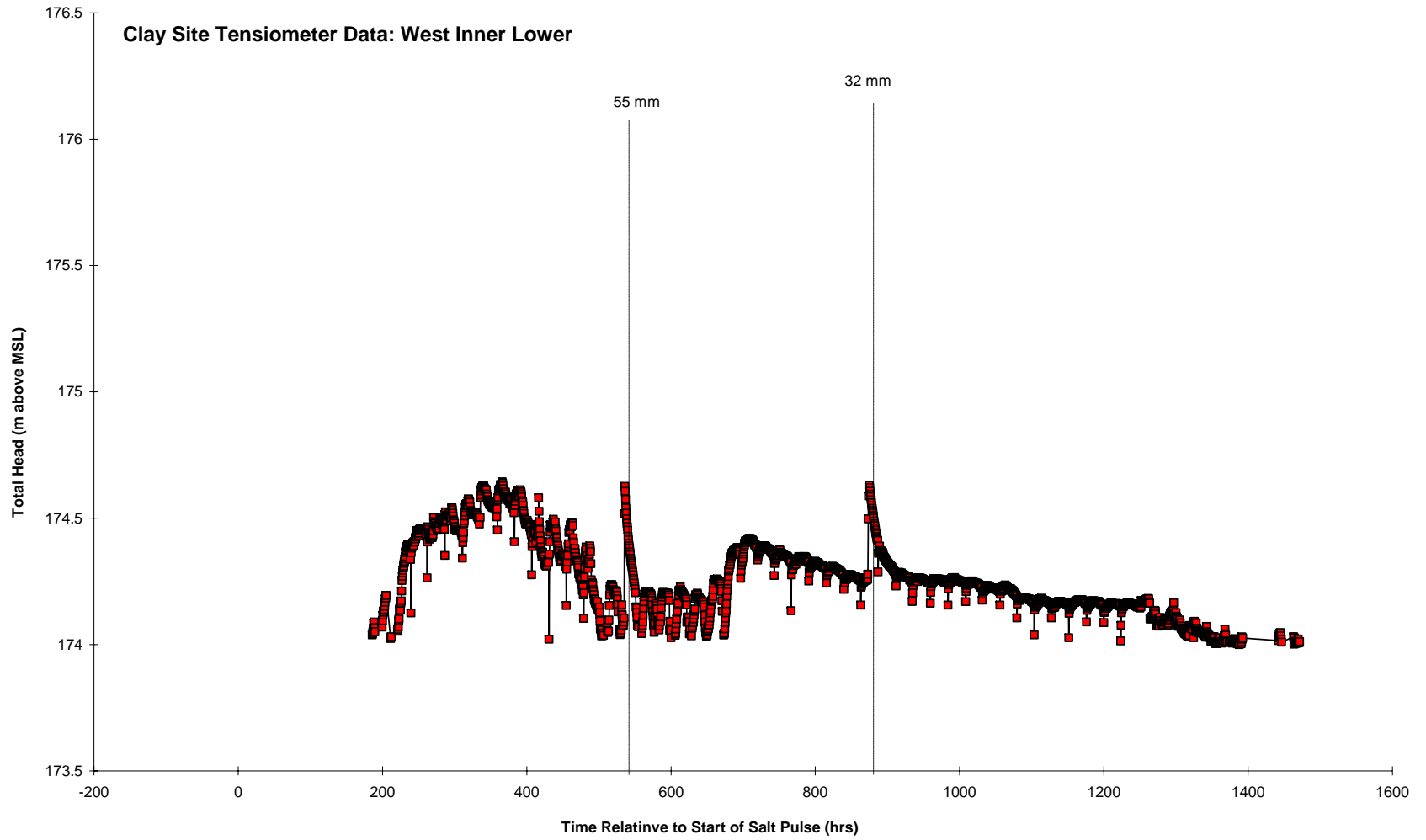


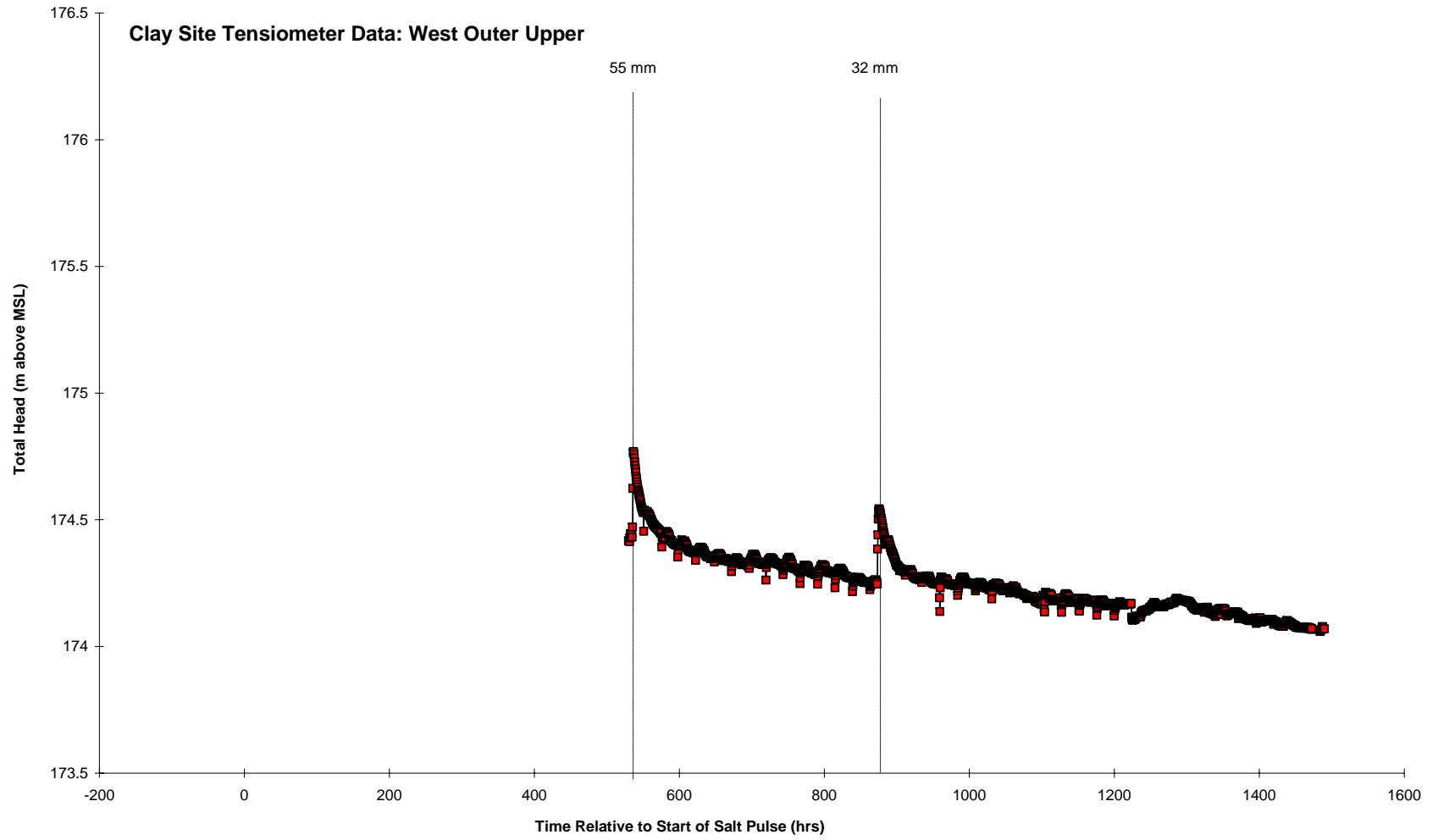
202

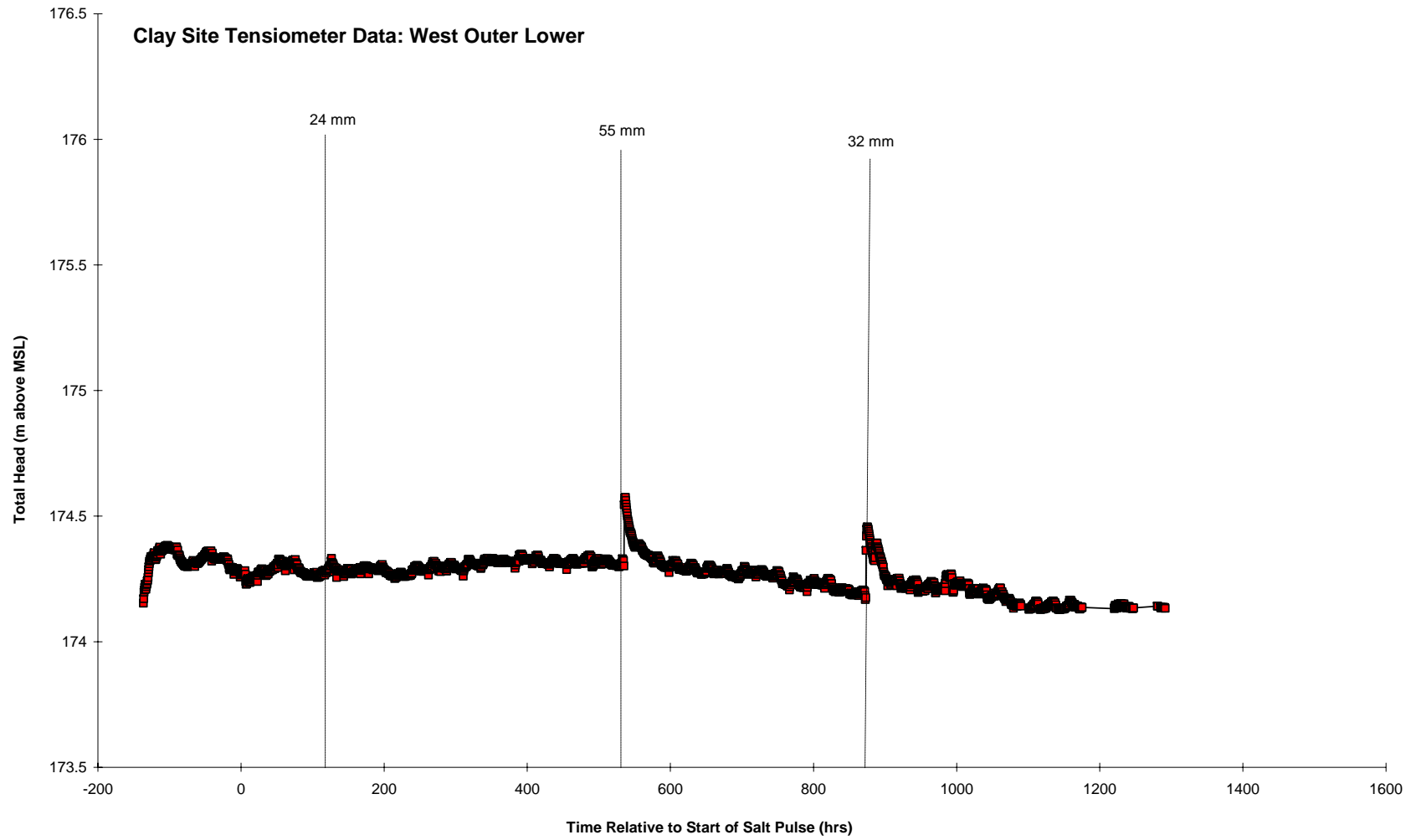




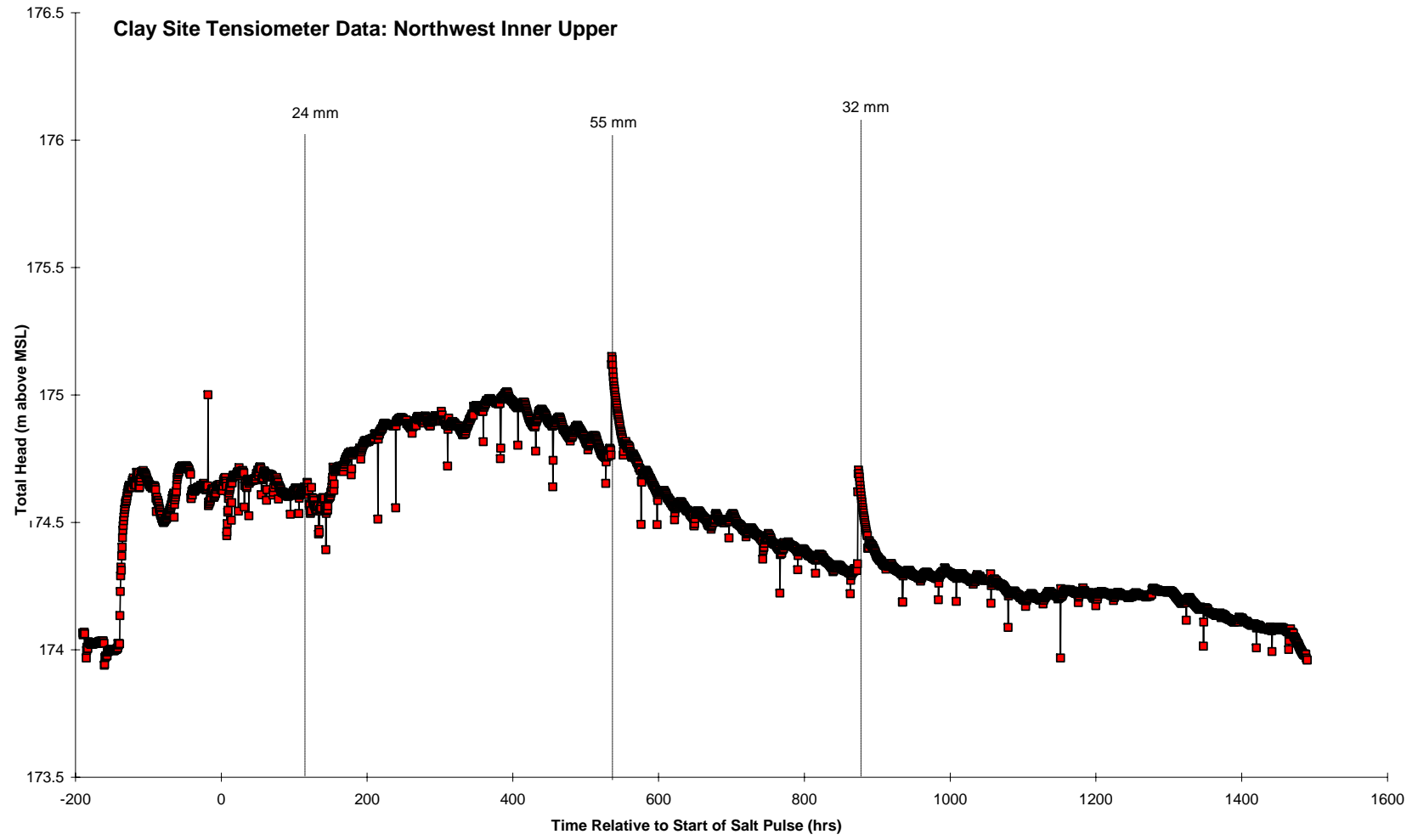
204

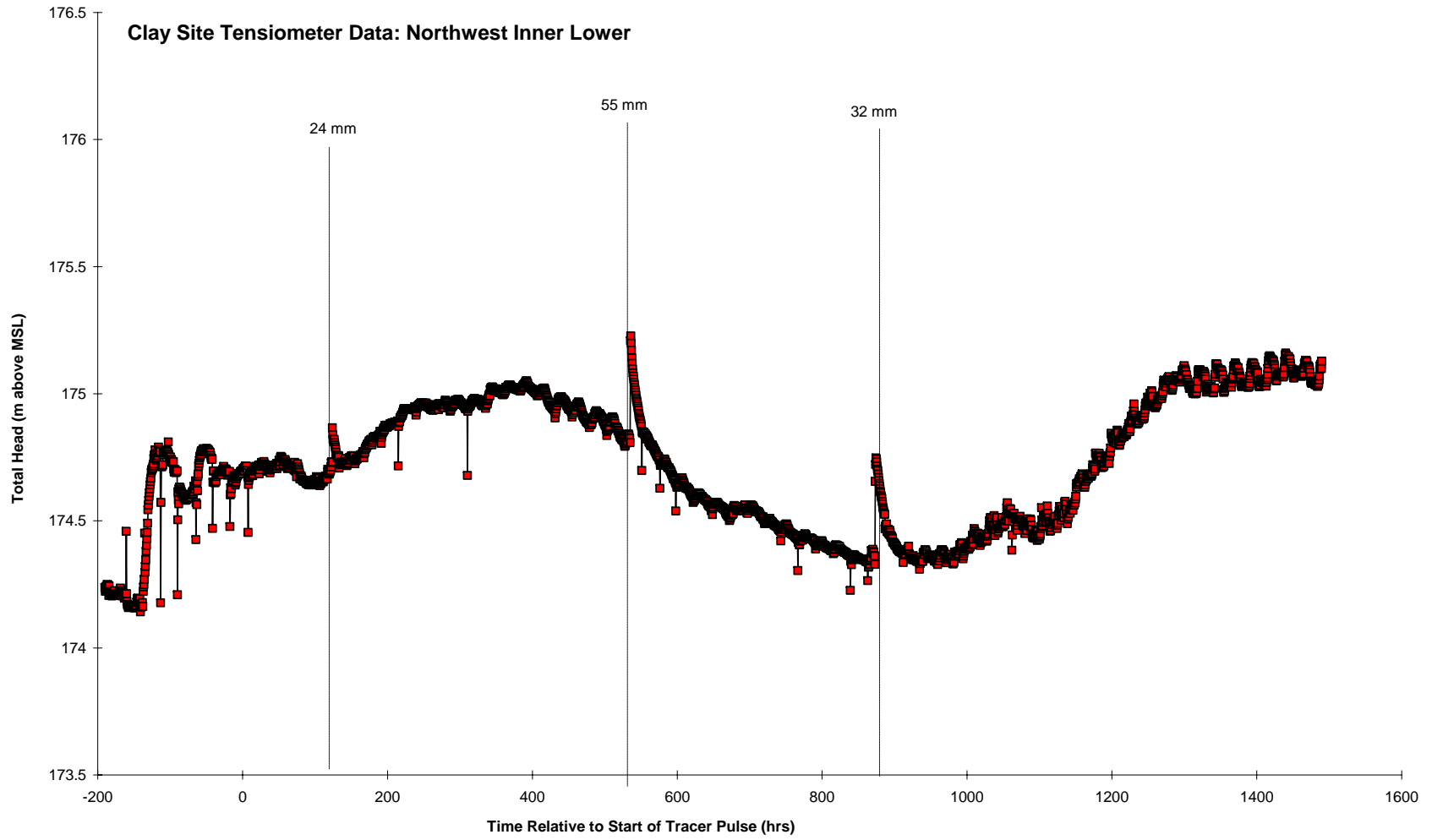


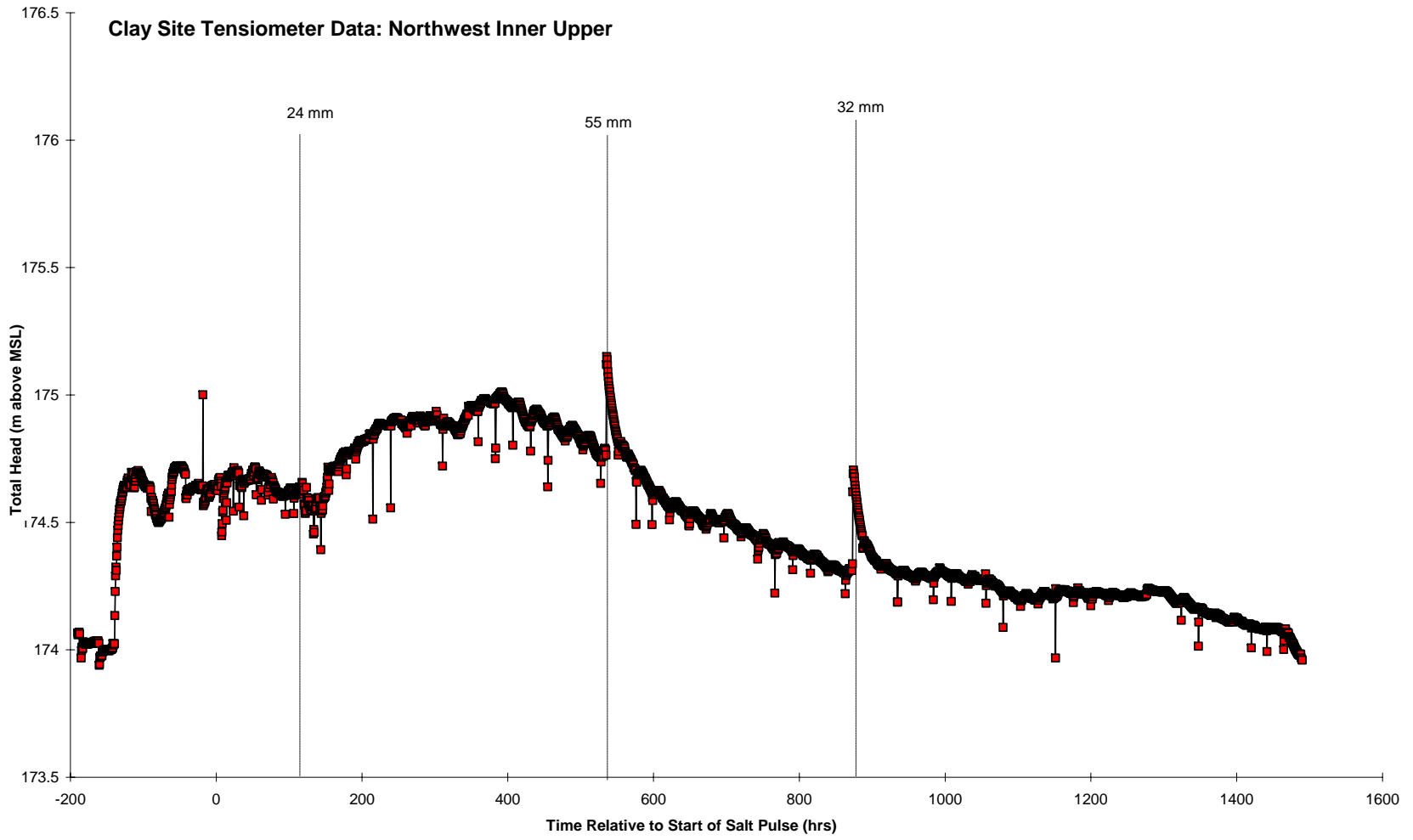


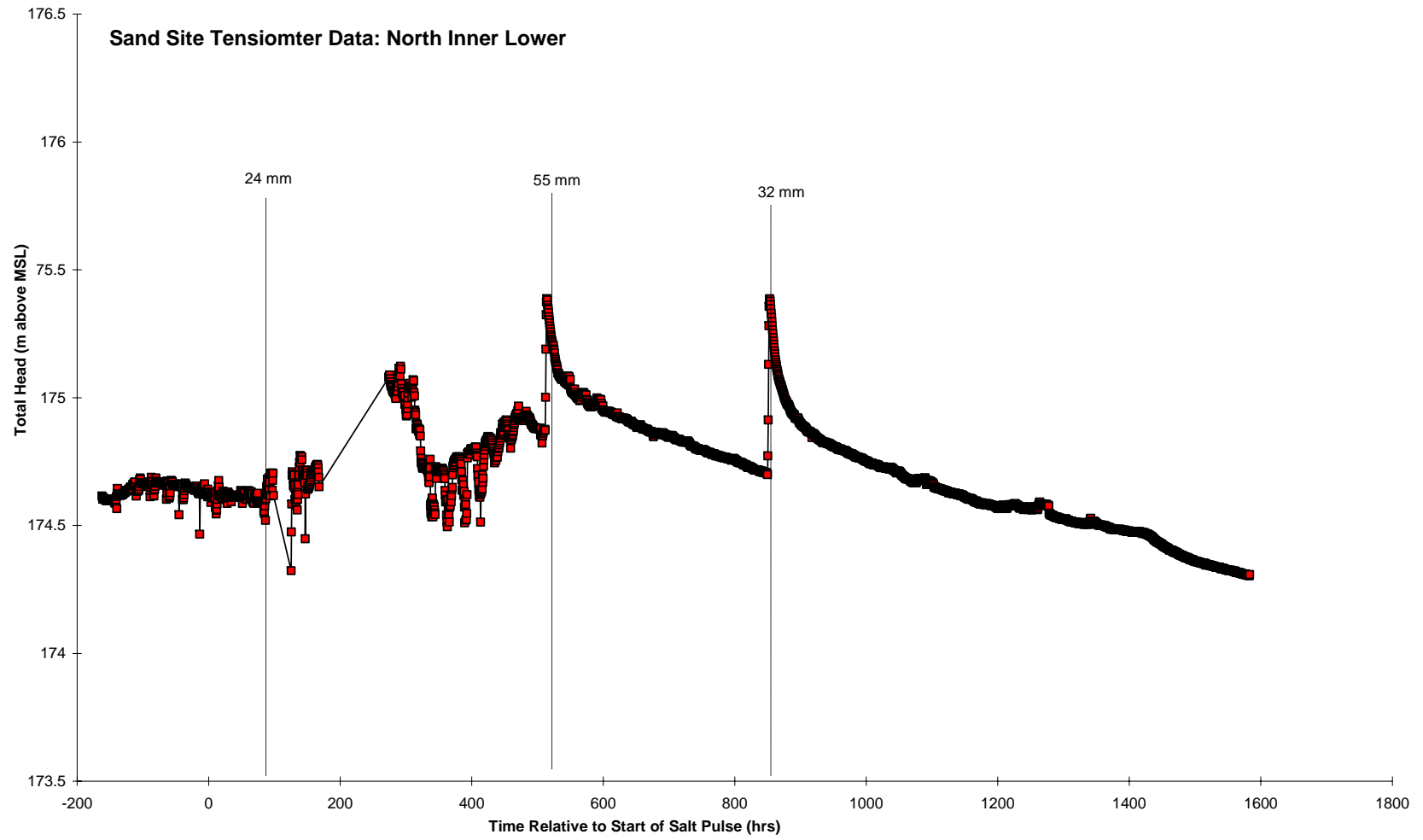


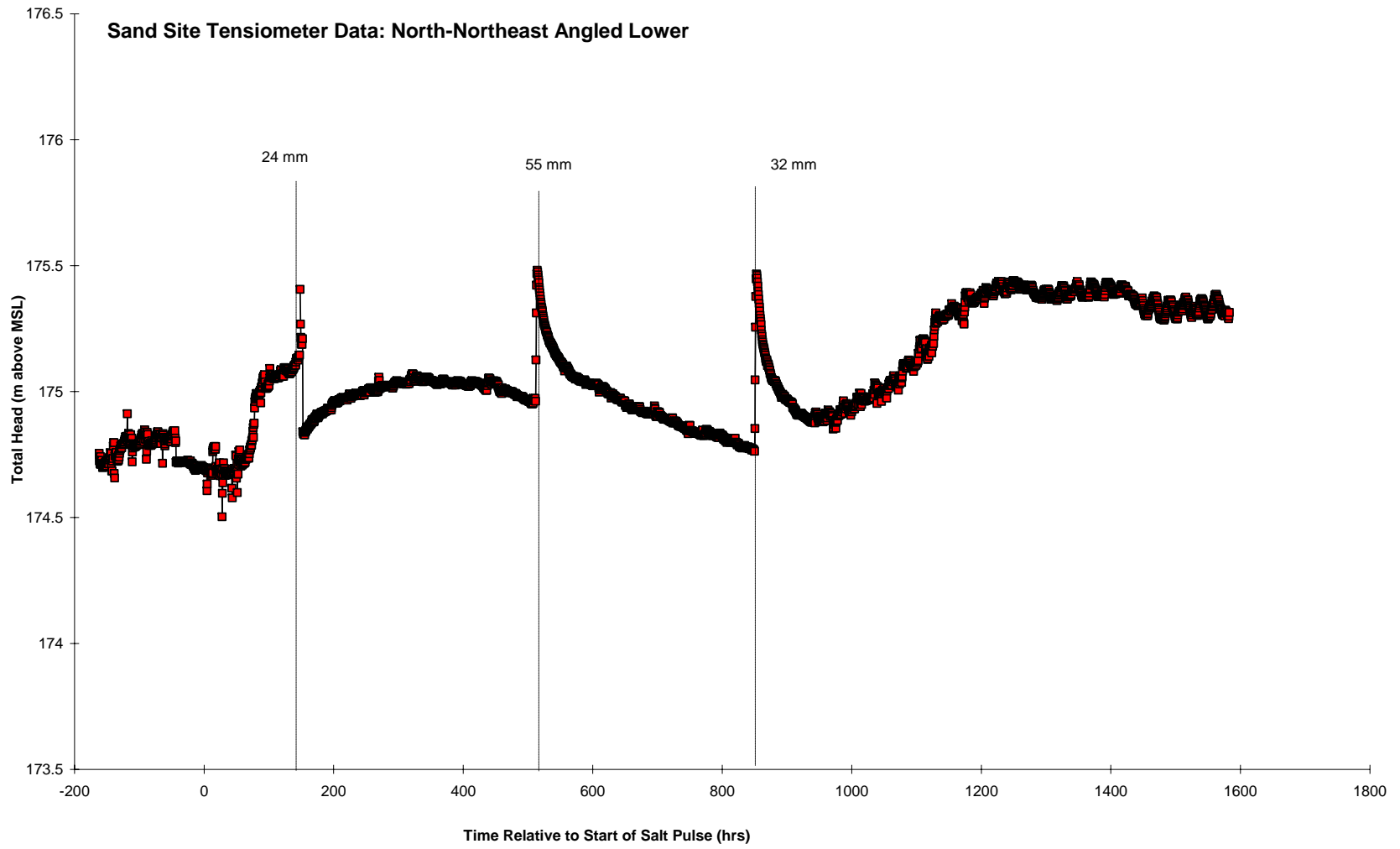
207

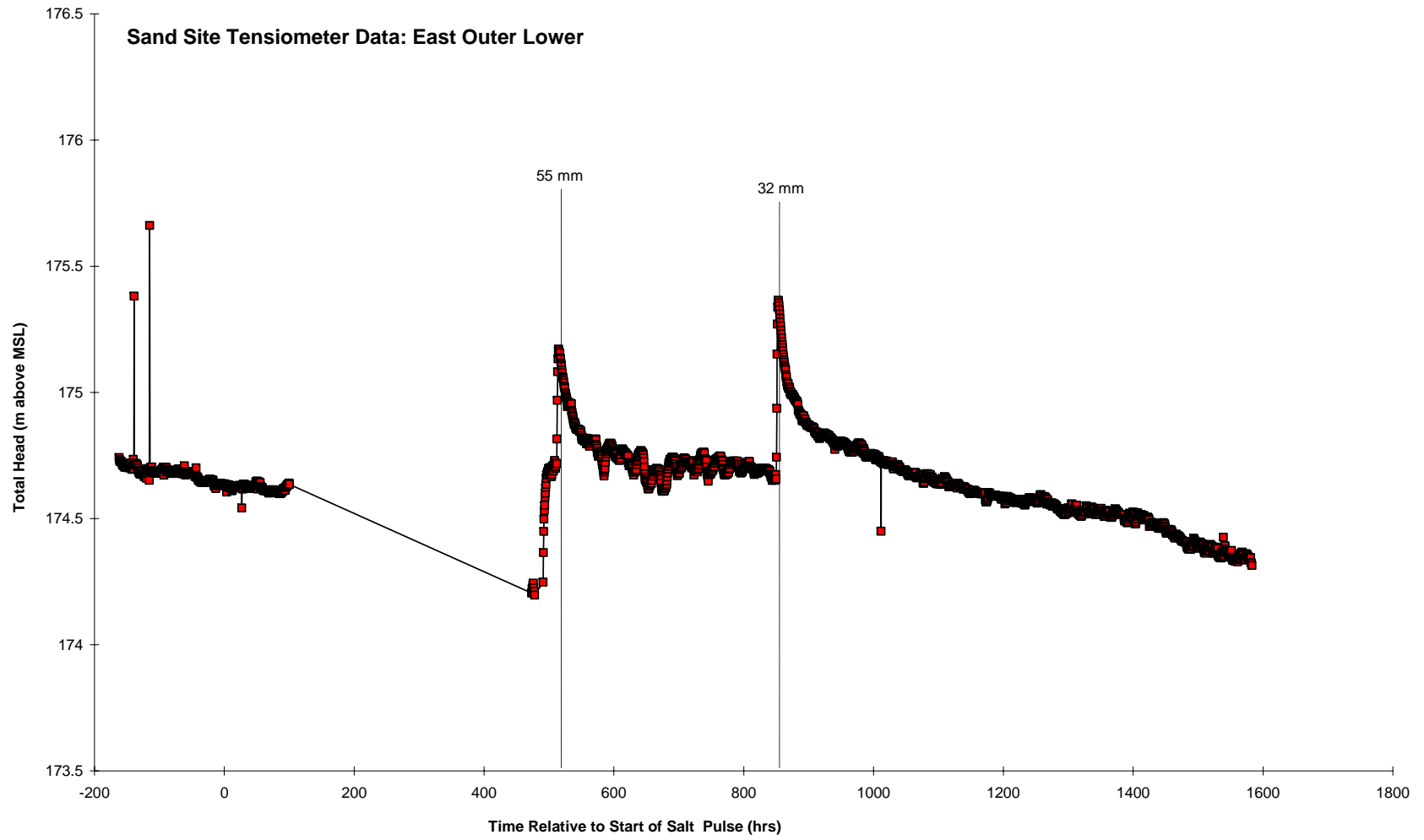


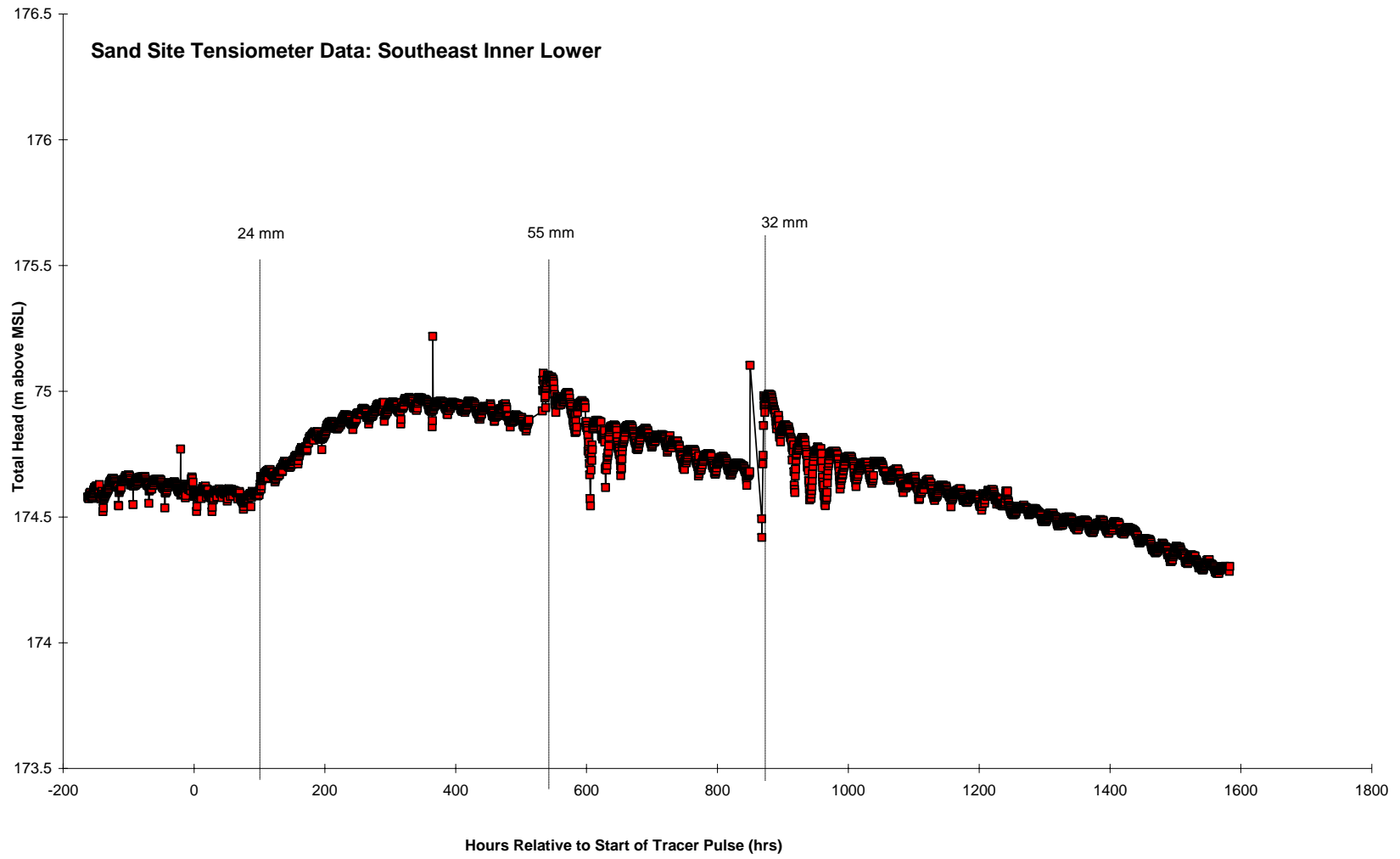


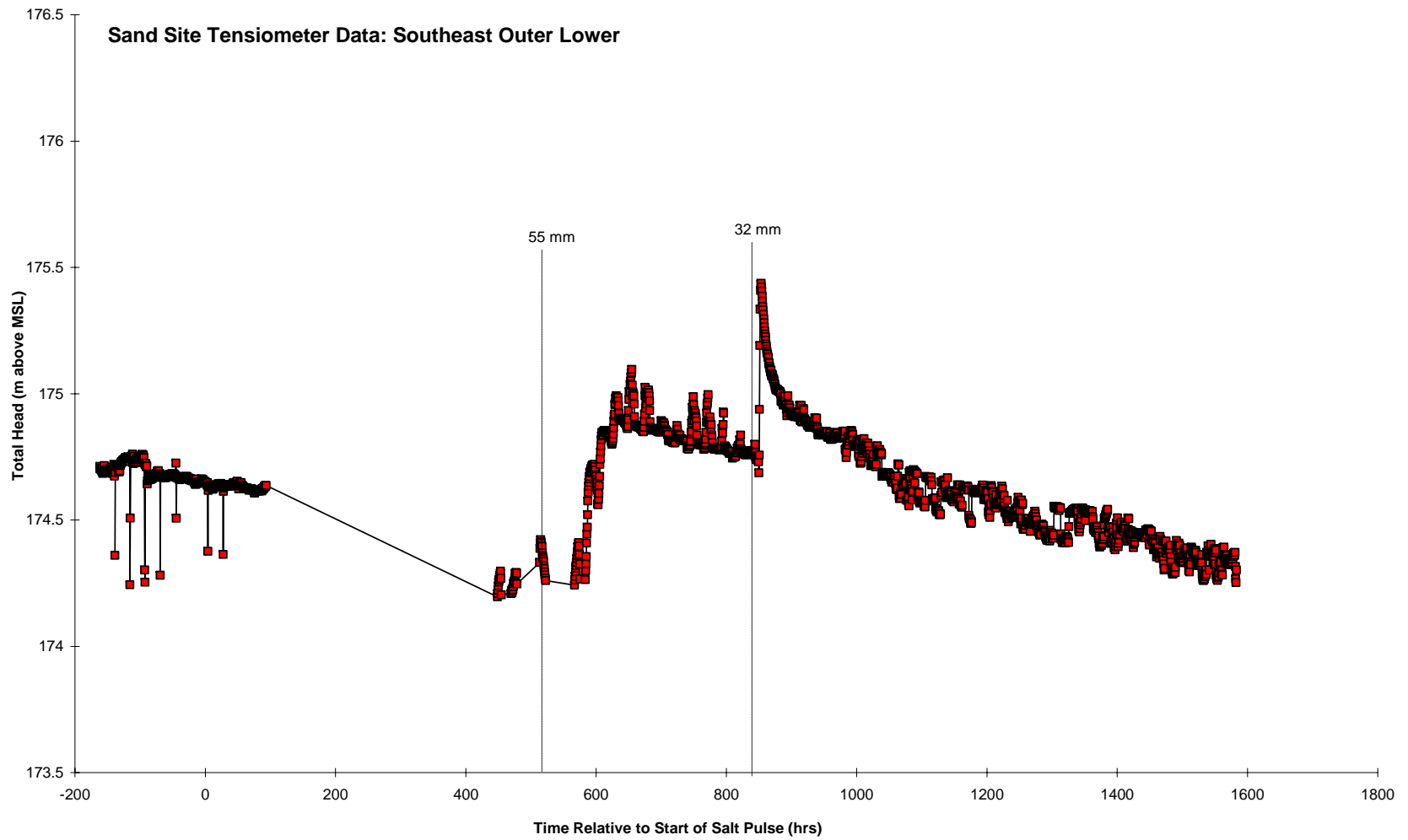


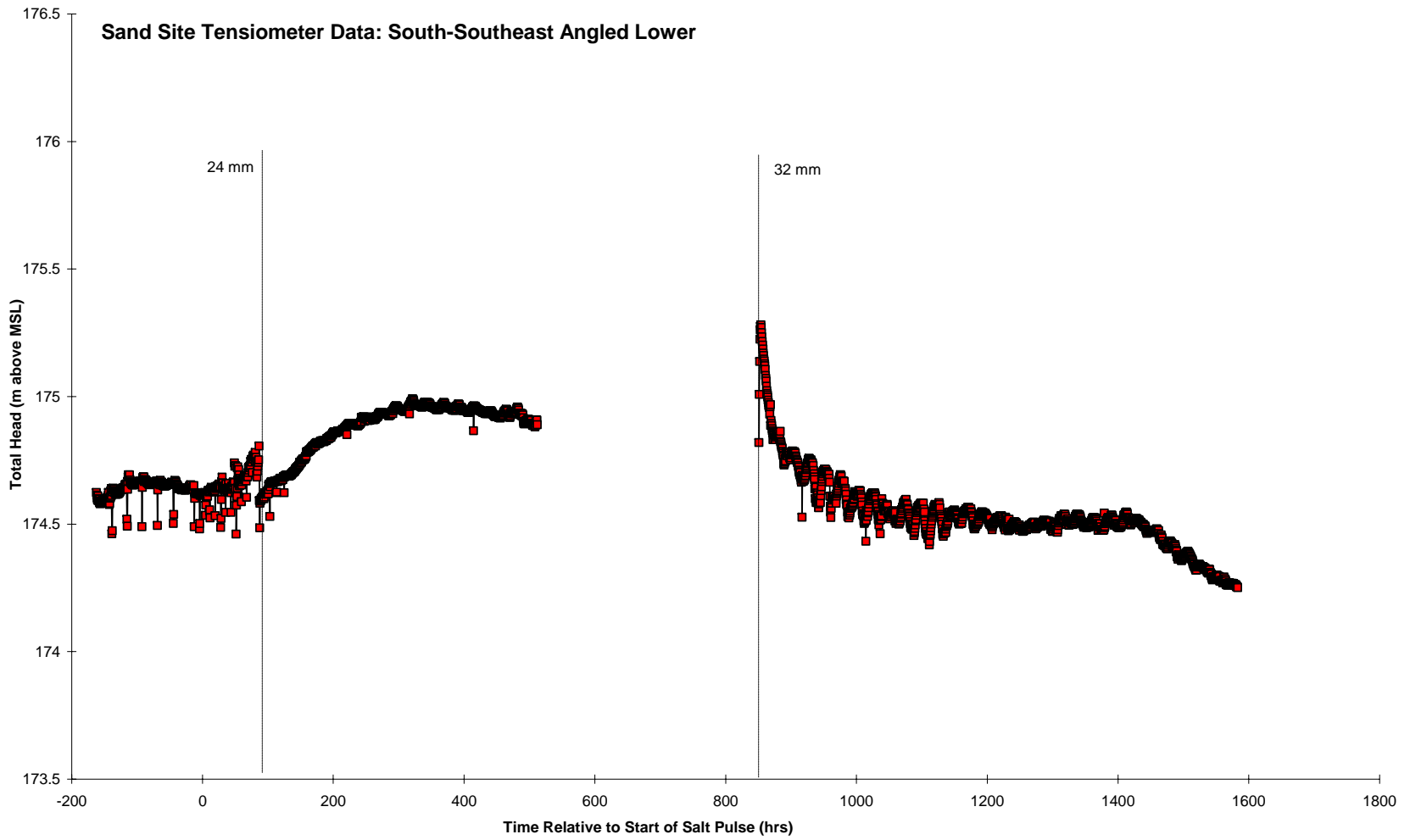


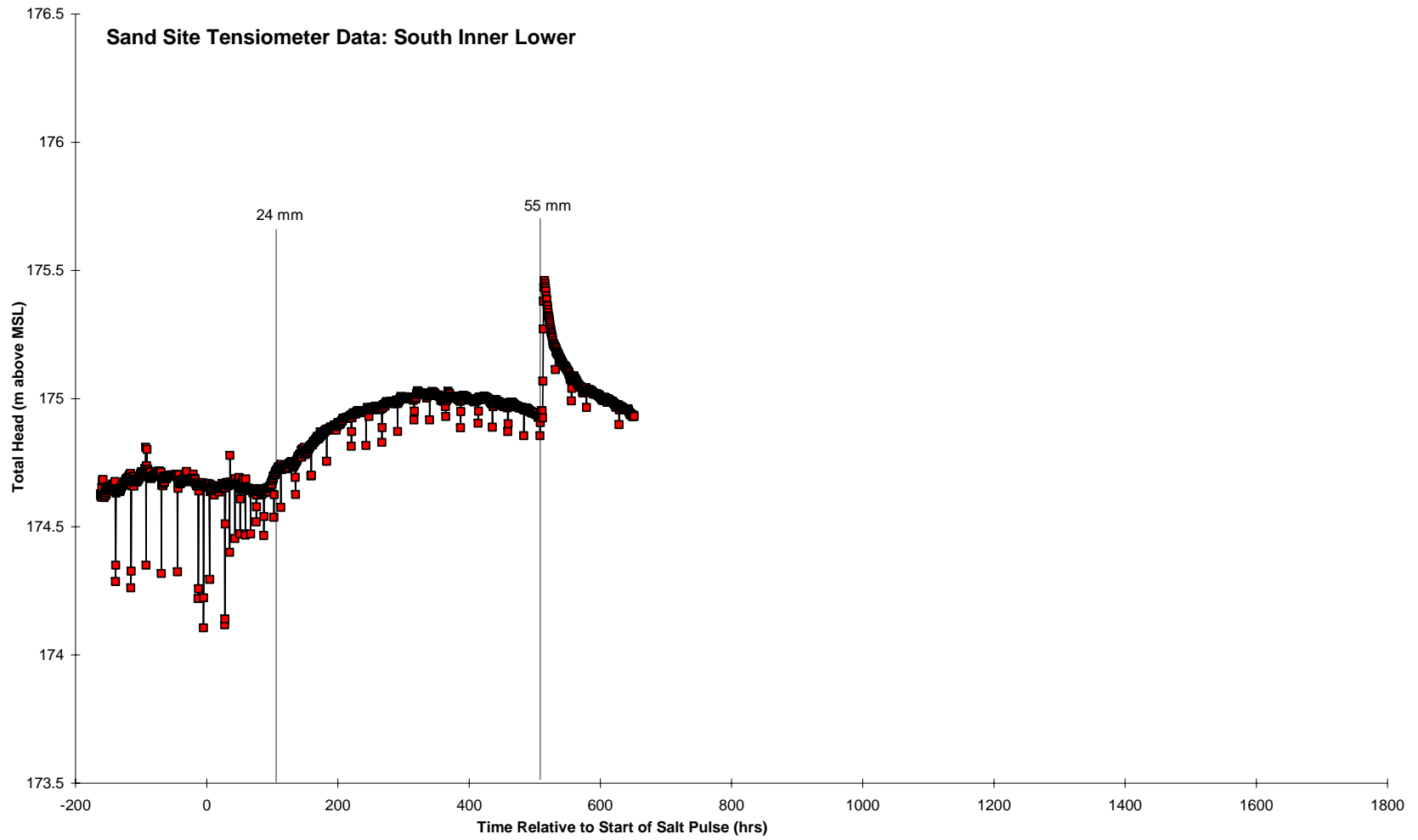


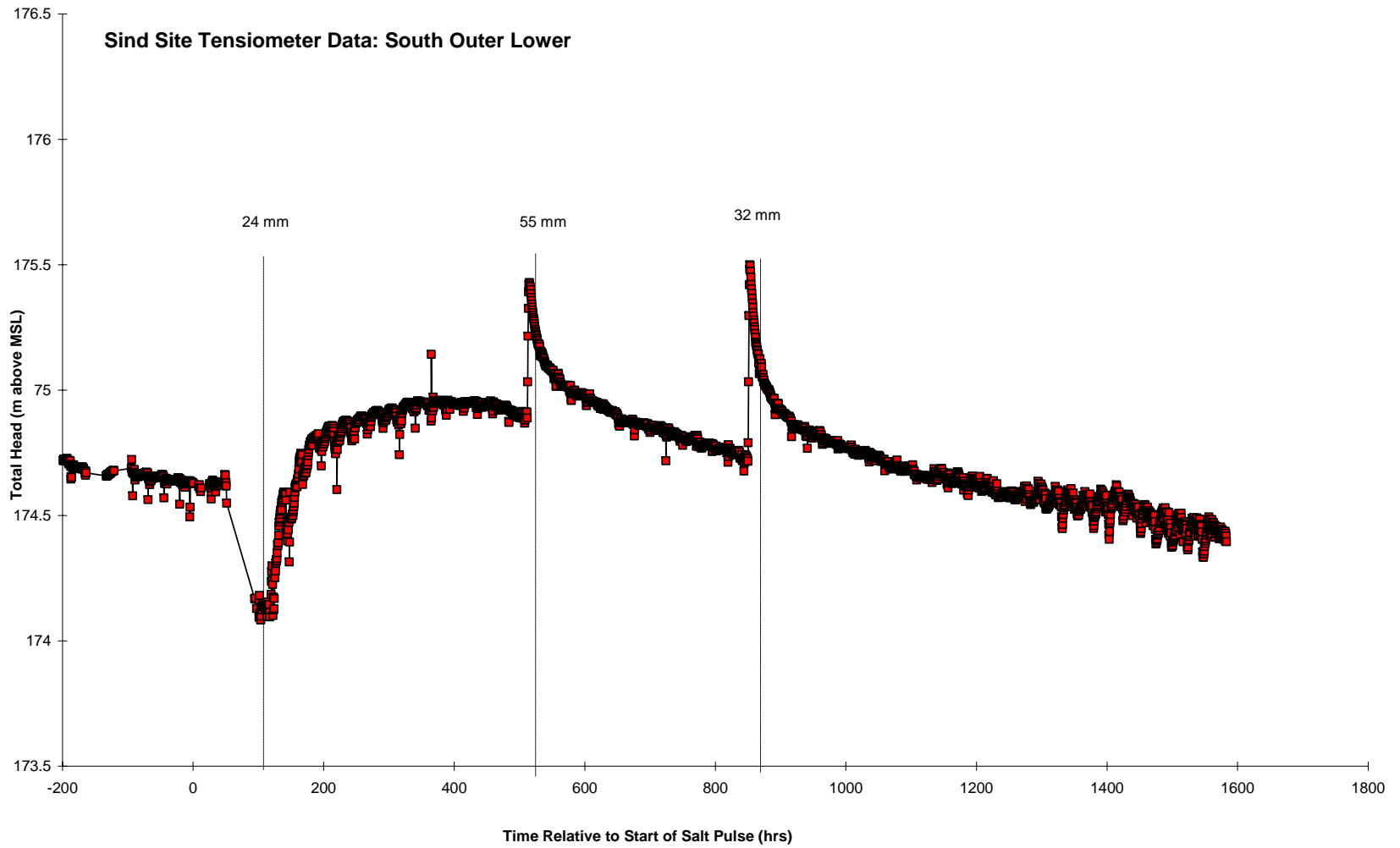


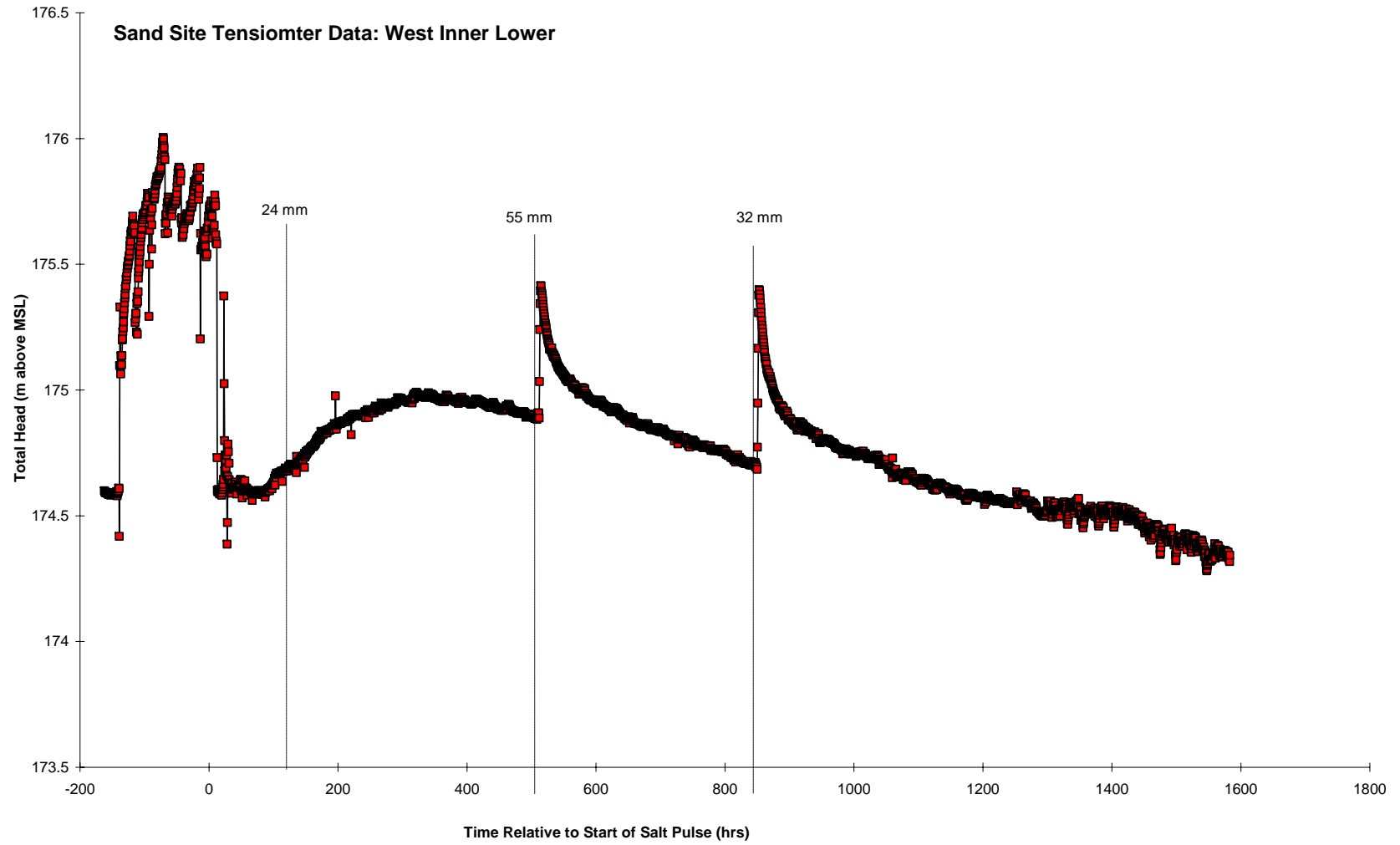


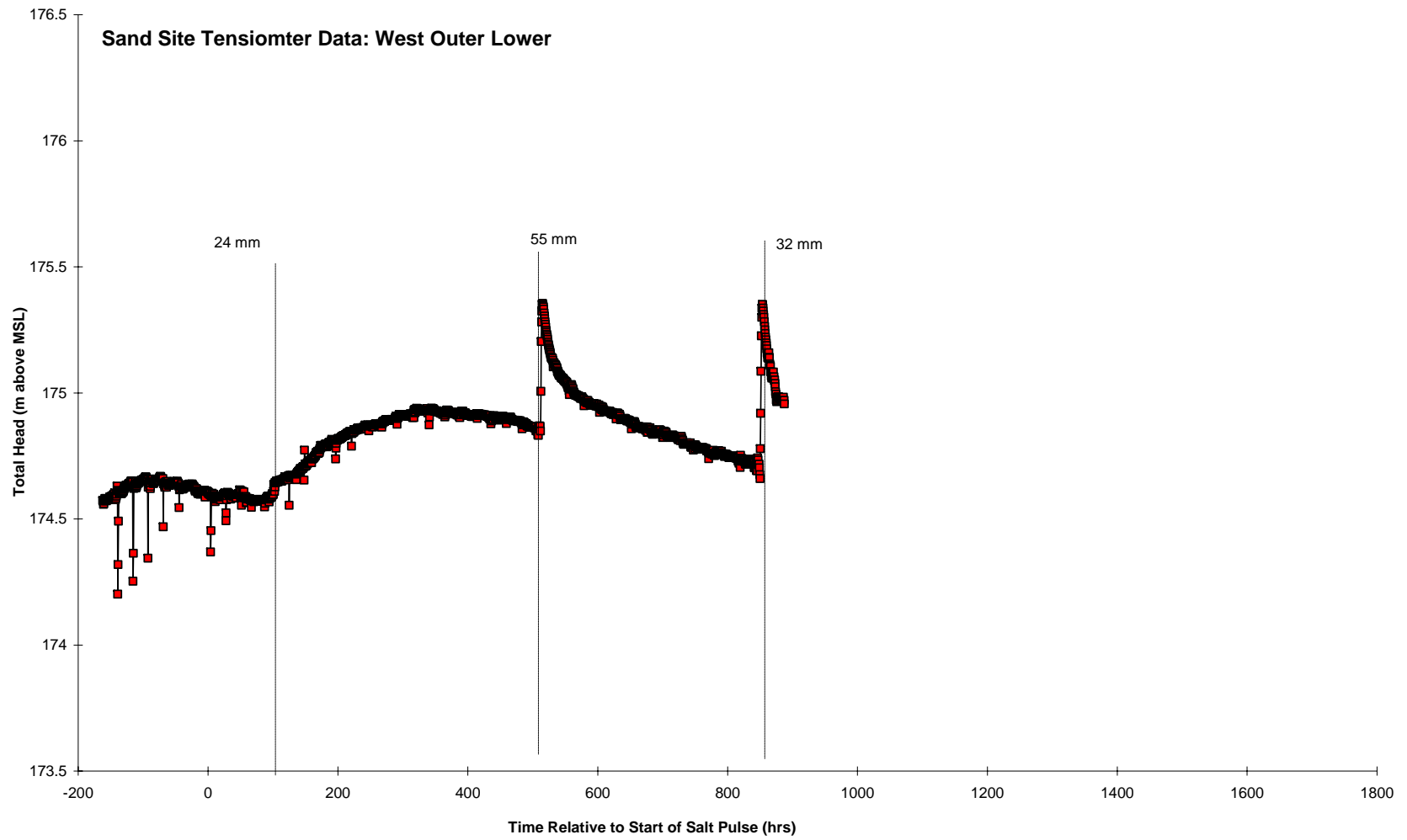


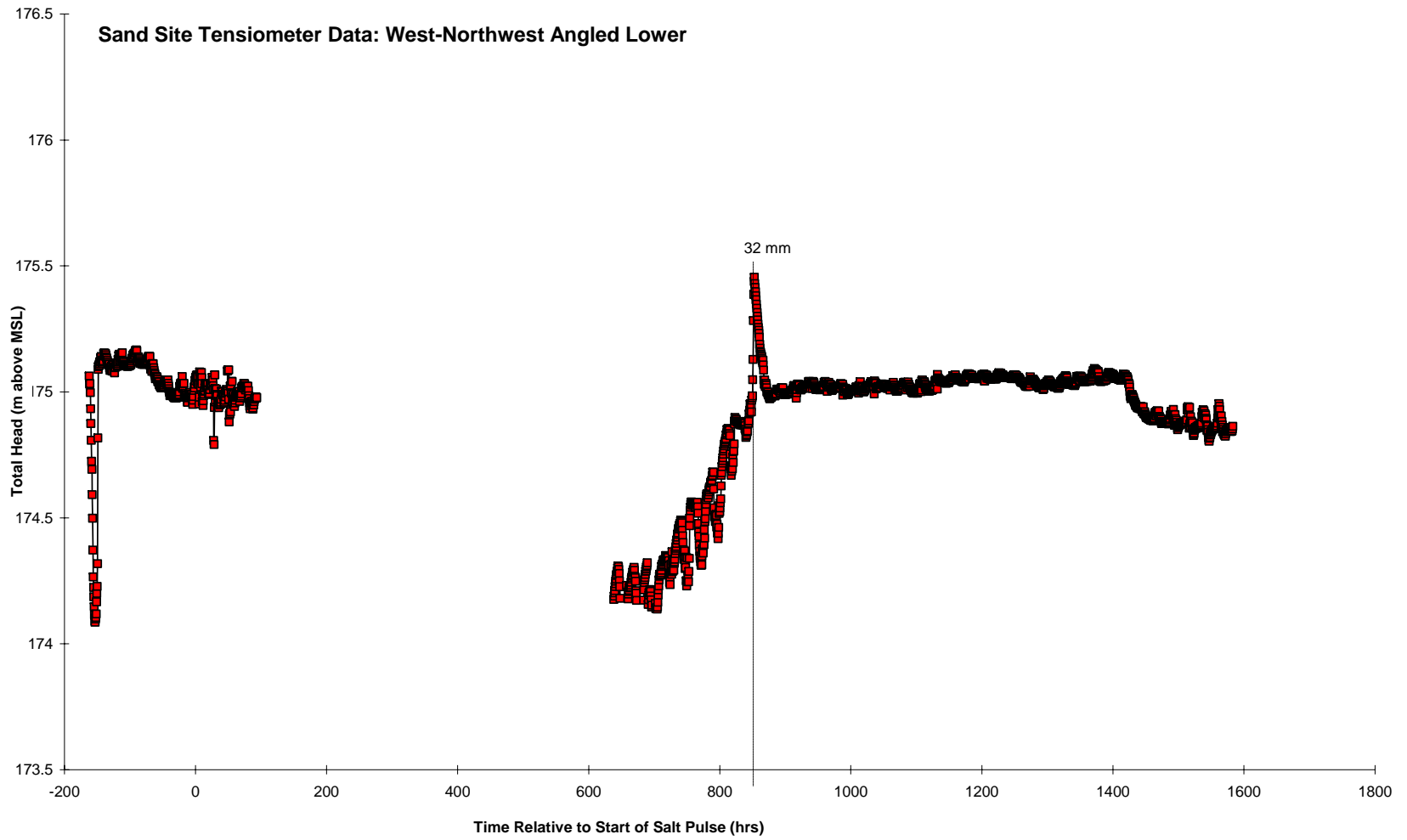


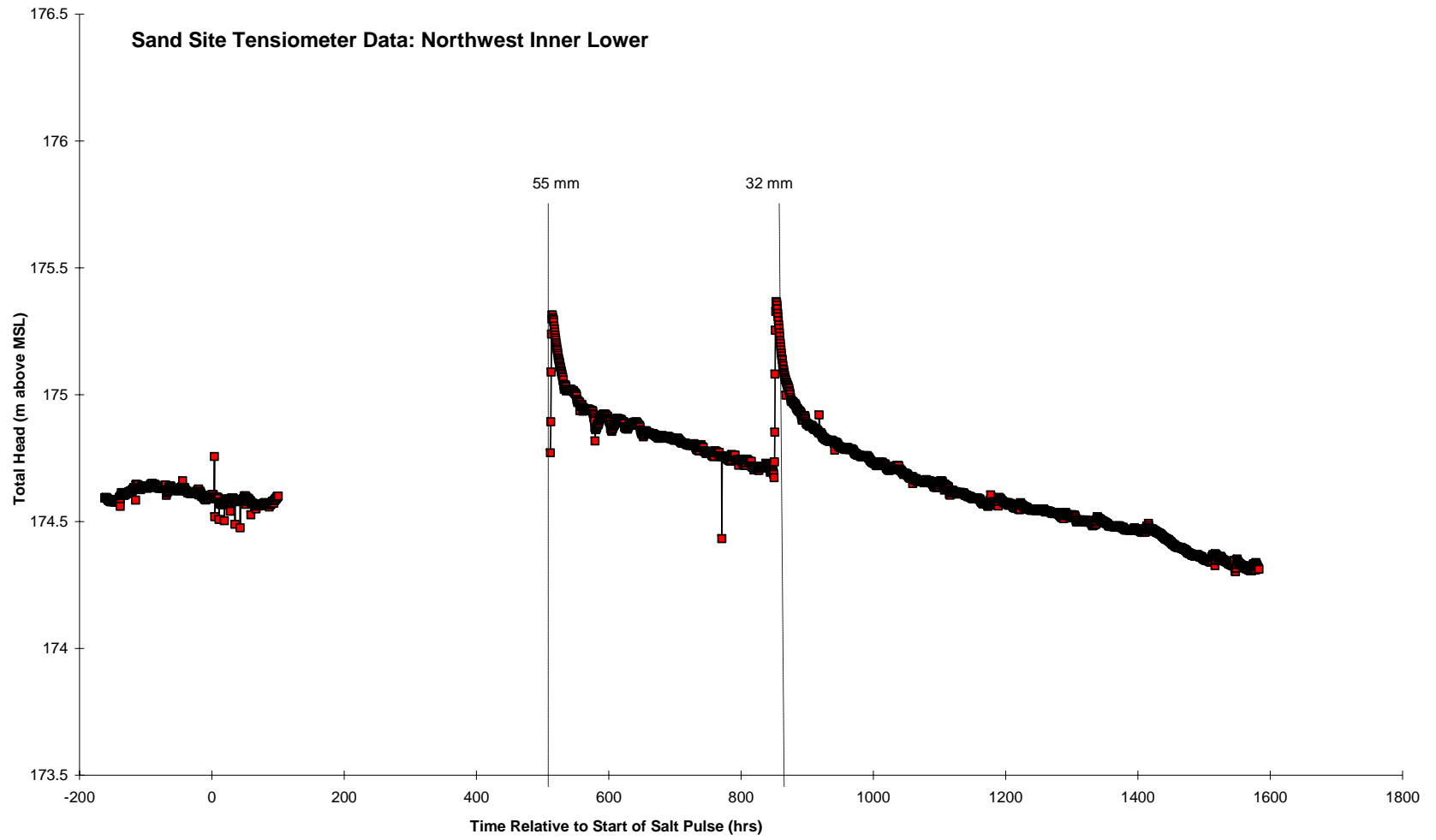












This page intentionally left blank.

Appendix F. Dye Pulse and Site Excavation

<u>Section</u>	<u>Page</u>
F.1 Dye Pulse	224
F.2 Excavation methods	224
F.3 Clay Site Excavation	224
F.4 Biological Macropores	226
F.5 Results	226

The dye pulse and subsequent excavation of the Clay Site provided the means to verify hypothesized fast transport pathways, zones of preferential flow, and the direct observation of the subsurface geology (see Appendix A). The excavation process, as well as observations concerning the heterogeneities and macropores that impacted the dye tracer transport is discussed. Throughout this appendix, reference is made to photographs (Plates) in Appendix G which provide a photographic record of the excavation process.

F.1 Dye Pulse

At 5:30 p.m., August 15, 2004, a 4.0 g/L solution of FD&C red dye #3 was prepared by adding 12.0 kg of powdered dye to 800 gallons of water in the reservoir tanks at the Clay Site. The dye was introduced into the infiltrometer without stopping infiltration (Plate 13).

At 08:30 a.m., August 17, an additional 1.4 kg dye was added to the remaining 650 gallons, resulting in a final concentration of 4.5 g/L. At 11:30 a.m., August 20, with 400 gallons of dyed water remaining in the reservoir tanks, all infiltration at the Clay Site was terminated. Flow at the Sand Site, where no dye had been introduced, was also terminated at this time.

F.2 Excavation Methods

Excavation of the Clay Site was begun on August 22, and completed on August 27. The site was excavated by trackhoe to remove large quantities of material and by hand tools to allow detailed examination. Excavation of the south half of the infiltrometer surface was begun by hand (Plates 17 and 18) and continued with the trackhoe to excavate a circular trench between the inner and outer sampling rings (see Plates 21 to 23). The trench was widened inward until it met the infiltrometer surface (Plate 24). The resulting 2 m wide by 2 m high cake shaped pillar was then excavated by hand tools (Plates 25 to 39).

Excavation continued with trackhoe excavation of one to two foot layers followed by had tool excavation and detailed inspection of exposed surfaces. Throughout the excavation process, the sides of the pit were sloped resulting in a pit significantly larger than the instrumented site. The final size of the excavation was approximately 20 m across at the top, sloping to a 5.5 m diameter floor at a depth of approximately 6 m. An additional pit measuring 1.5 m by 2 m was excavated by the trackhoe in the bottom of the pit (Plates 100 to 102). After photographing, and mapping, the pit was refilled with the excavated materials.

F.3 Clay Site Excavation

During hand excavation of the infiltration surface, red dye saturated soils indicated that the majority of dye was captured by the organic growth in the first foot of soil (Plate 19). Below this depth the dye appeared as a mottled pink to red color (Plate 20). The lack of dye stain in the walls of the circular trench at a width of 1 m and to a depth of 1.5 m deep between the inner and outer sampling rings (Plate 22) indicated an absence of dye flow in this region (Plate 41). At this point, the excavation cut into the blocky structured clays of the HS Unit 4. The excavation was widened to a 6 m diameter and the remaining pillar under the infiltrometer was excavated by hand (Plate 27). As the pillar was dissected, it was apparent that virtually all the flow from the infiltrometer was directed vertically through HS Units 5 and 4 (topsoil and blocky structured

clays) through fractures, root tubes, and wormholes (Plates 28 to 39). During this excavation period, a dye-filled wormhole was observed to directly intersect with the East-Northeast Angled Upper sampling point (Plate 30). Excavation by trackhoe was resumed after the central pillar was completely excavated by hand tools. The pit was widened to approximately 6 m with a depth of 2 m (Plate 43) where the bedded, oxidized clays of HS Unit 3 were intersected. Dye stain indicated that the flow was still predominantly vertical through fractures and macropores beneath the infiltrometer, though flow paths began to spread horizontally along bedding planes (Plate 54).

At a depth of 2.1 m, a 2 cm by 3 cm crayfish hole filled with dyed water was exposed (Plate 40). Additionally hand excavation of the floor revealed dye stain in numerous fractures and in thin silty sand stringers (Plates 44 and 45). The matrix surrounding dye stained macropores was also slightly stained. This depth was the upper boundary of oxidized clays containing carbonate filled fractures. Many of the carbonate deposits encountered were stained a light pink color indicating further lateral spread on the dye plume. During excavation of the media, standing water was observed in fractures and macropores at 2 m depth shortly after excavation. Subsequent excavation revealed that the water table dropped to a 6 m depth over a 48 hour period.

Excavation by trackhoe and hand continued through the remaining oxidized, bedded clays (HS Unit 3) where the presence of dye indicated further lateral spread. The clay colors gradually but irregularly changed with depth from yellow to brownish gray and to gray indicating the presence of the unoxidized clays of HS Unit 2 (Plates 50 to 53). Within this sequence, stained crayfish and fractures were very commonly observed along with stained sandy zones (Plates 52, 56, and 73).

In close proximity to sampling point West Outer Lower, a sand stringer at 2.8 m was discovered, which seeped dyed water after exposure (Plate 77). Further excavation revealed connection to a large silty sand body (mixture of HS Units 4 and 6) located in the northwest quadrant of the site and apparently deposited within the oxidized silty clays of HS Unit 3 (Plate 76).

Dye stain was observed within the unoxidized gray clay of HS Unit 2, encountered at about 3.0 m below the ground surface. Some dye stained crayfish burrows were observed within the upper 1 m (approximately 3.2 m bgs) of this unit (Plate 83) and no burrows, stained or not, were observed deeper than this.

Excavation of HS Unit 2 revealed that this unit is thinly bedded (beds of clay 1 to 3 cm thick separated by very thin silt beds), horizontal and vertical fractures filled with fine sand and boarded with yellow (reduction) rims up to 1 to 2 cm thick, and small scale deformation features (Plates 50 to 54). Excavation into this unit revealed instances of saturated sand stringers. At this depth, the dyed water had been diluted to the extent that the dye was almost imperceptible.

The last major unit, the massive unoxidized clay of HS Unit 1, was encountered at depths between 3.4 m to 5 m. This unit exhibited isolated sand channels and stringers (Plate 102), random cobble and pebble inclusions (Plate 102), and deformation features (Plate 53). The depth of this unit at the Clay Site is unknown, but extends at least to 5.5 m, which is the deepest point of excavation. Bedding planes that were otherwise invisible in excavated exposures became very apparent in trackhoe samples that were deformed during excavation (Plate 66). The beds,

measuring 2 to 4 cm thick, parted along very thin planes of fine sand and silt. A secondary dye pulse (Plate 55) initiated in HS Unit 1 (approximately 3 m), and resultant dye stain within these bedding planes confirmed that flow along these planes was possible (Plate 103).

During the excavation, large sample cores were taken from most units for later hydrologic laboratory analysis (Plates 60 to 67 and 95 to 99).

In addition to the bedding heterogeneity discussed in Appendix A and the features discussed above, a large silty sand body in the northwest quadrant of the site (Plates 74 and 94) was exposed during excavation (HS Unit 6) along with seemingly isolated sand channels and stringers that were encountered at all depths (Plates 44, 52, and 102 and Figure F-1). Another feature worth noting is the greater abundance of layered oxidized clays containing thin interbeds of carbonate in the south and southeast section of the site and the greater number of silty sand zones in the northwest quadrant of the site.

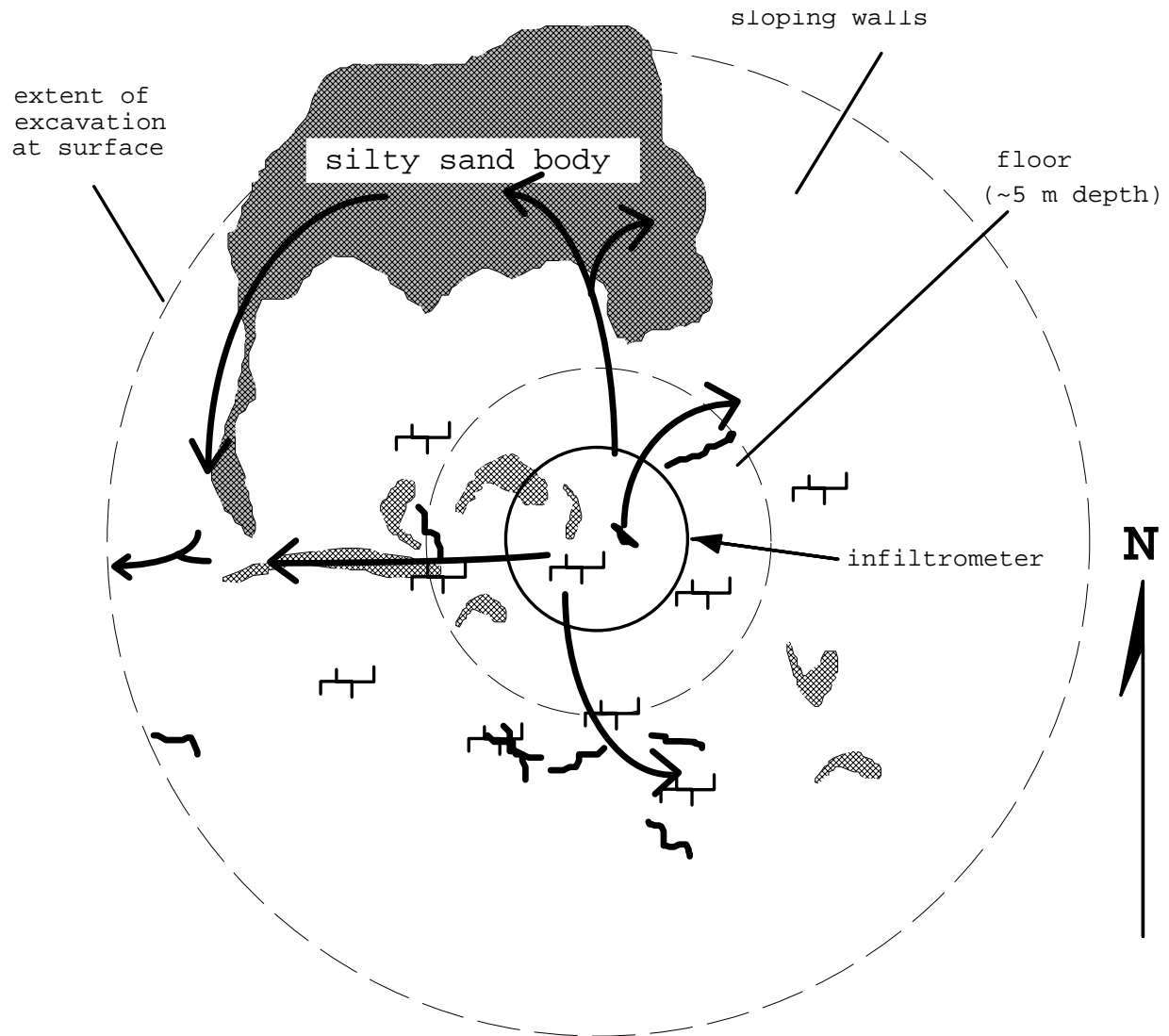
F.4 Biological Macropores

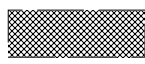
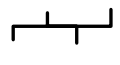
As noted above, biological macropores produced major flow pathways (Figure F-1). Root and wormholes were ubiquitous throughout the first 2 m of the excavation. Crayfish burrows appeared in many cases to follow pre-existing fractures in the bedded clays. Complexes of crayfish burrows stained with red dye (Plate 82) were found at depths from just below the surface to 3.2 m (Plate 83). A fifteen minute cursory inspection of the surrounding field surface discovered three instances of crayfish burrows (Plates 104 to 109).

F.5 Results

Dye tracer

Dye movement was observed through the top soils and loess (Hydrostratigraphic Unit 5) and underlying blocky structured silty clays (Hydrostratigraphic Unit 4) via fractures, root holes, crayfish burrows, and worm holes. Dye movement was vertical through these units, with no evidence of lateral spread encountered during the excavation. The East-Northeast Angled Upper sensor pack, approximately 2 m below the infiltrometer ring, was directly intercepted by a worm hole beginning just beneath the infiltrometer surface. The soil water sampler at that location was inoperable, but the wormhole and sampling site contained dark red dye (Plate 30). Forty-two minutes after the introduction of the salt pulse, Ci/Co ratios from the TDR trace at that sampling point went almost instantaneously from 0 to off scale (greater than .45) indicating that the Cl⁻ tracer transport via this fast transport pathway reached a depth of 2 m at high concentration in less than one hour (Figure D12). Concentrations of Cl⁻ tracer traveling this same path may have spread laterally through the bedded clays of HS Unit 3 and contributed to the early arrival of high concentrations at the Northeast Inner Lower sensor pack. The relative fast attenuation of Cl⁻ concentrations from this area may be due to the fast arrival of clean infiltrated water through the wormhole following the termination of the Cl⁻ tracer pulse.



-  : preferential flow through sand stringers(Unit 6)
-  : active flow through fractures and bedding planes
-  : major flowpaths
-  : major biological macropores

10 m

Figure F-1. Plan view of major biological macropores, fractures, and zones of preferential flow found during excavation at the Clay Site. Noted features are integrated over the depth of the excavation.

Biologically Produced Macropores

Biologically produced macropores were a major factor in transport at the Clay Site. Ubiquitous wormholes (Plates 29, 30, 31, and 39), root holes (Plates 31 to 34), and crayfish burrows (Plates 80 to 84) transported dye past the depths of the oxidized bedded clays (HS Unit 3) and into the layered unoxidized clays (HS Unit 2) near the deepest extent of the excavation. The lack of dyed transport pathways on the outside walls of the initial trench dug around the infiltrometer (Plate 23) and the preponderance of dyed root and wormholes observed while dissecting the pillar beneath the infiltrometer also attest to the importance of biologically produced macropores in aiding vertical flow through the upper three hydrostratigraphic units. The low salinity concentrations encountered at sampling points in the south, southwestern, and southeastern quadrants of the site, and the corresponding large number of dyed macropores in the same region suggest that the majority of the tracers passed through these macropores while completely bypassing the sensor packs.

In order to gain a rough estimate of potential flow through macropores, Poiseuille's Law was used to calculate the flux through tubes of diameters approximating those of the observed macropores. Application of this law to this situation requires simplifying assumptions such as laminar flow conditions, a horizontal straight tube, a circular cross-section, a completely filled tube, and a known pressure gradient. Despite the fact that none of these assumptions are met in this situation, application of the Poiseuille Law using conservative estimates for pressure head gradients provides a feel for the potential carrying capacity of the observed macropores. Poiseuille Law can be written as follows:

$$Q = -\frac{\pi R^4}{8\mu} \frac{\Delta P}{\Delta x}$$

Where Q is the volumetric flow rate [L^3T^{-1}], R is the radius of the tube [L], μ is the viscosity of water [$ML^{-1}T^{-1}$], and ΔP is the pressure drop over the distance Δx .

Table F1 summarizes a range of calculated flow rates for a variety of pore dimensions and gradients while Table F2 gives the calculated volumetric flow as a percentage of the maximum measured infiltration rate. As expected numerous root holes are required to accommodate the measured maximum infiltration rate through the infiltrometer at gradients of .01 and .1, while one crayfish hole with 2 cm \times 3 cm dimensions with a gradient of .1 could carry about 9% of the flow from the infiltrometer. At a gradient of 1 a worm hole could carry about 2% of the infiltrometer flow while the crayfish hole could handle 500 times that flow rate. This exercise shows, as one might guess, that the transport potential of the crayfish hole is significant compared to the other types of macropores observed at the site.

The Hagen-Poiseuille equation: $q = -\frac{N \rho_w g R^2}{\mu} \nabla h$, where

N = a dimensionless shape factor,

R = diameter of passage,

ρ_w = density of water, and

g = acceleration of gravity

For a circular tube, this becomes:

$$q = -\frac{\rho_w g r^2}{8\mu} \nabla h \quad \text{where } \begin{array}{l} r = \text{tube radius} \\ \text{all others as above} \end{array}$$

To approximate pore tortuosity and roughness, we used a conservative equation of:

$$q = -\frac{\rho_w g r^2}{12\mu} \nabla h. \quad \text{The results for a range of pore sizes and } \nabla h \text{'s:}$$

Table F-1. Potential Fluxes Through Various Size Bioturbated Passages at Three Possible Gradients

Biological Macropore Type	Approximate Radius r (m)	Calculated Volumetric Flow Rate Q at .01 Gradient (liters/min)	Calculated Volumetric Flow Rate Q at .10 Gradient (liters/min)	Calculated Volumetric Flow Rate Q at 1.00 Gradient (liters/min)
Root	0.0005	2.45E-13	1.4726E-07	8.84E-03
Root	0.001	3.93E-12	2.3562E-06	1.41E-01
Root	0.0015	1.99E-11	1.1928E-05	7.16E-01
Worm	0.002	6.28E-11	3.7699E-05	2.26E+00
Crayfish	0.015	1.99E-07	0.11928235	7.16E+03

Biological Macropore Type	Percentage of Maximum Infiltration (1.4 liters/min) .01 Gradient	Percentage of Maximum Infiltration (1.4 liters/min) .1 Gradient	Percentage of Maximum Infiltration (1.4 liters/min) 1.0 Gradient
Root	1.76E-11	1.06E-05	6.34E-01
Root	2.82E-10	1.69E-04	1.01E+01
Root	1.43E-09	8.56E-04	5.13E+01
Worm	4.51E-09	2.70E-03	1.62E+02
Crayfish	1.43E-05	8.56E+00	5.13E+05

$\nabla h = .01$:

Biological Macropore Type	r (m)	μ (kg/ms)	q(m/s)	Q (m3/s)	Qinfl (maximum)	% of Maximum Q
very small root	0.0005	9E-07	0.002286	1.795E-09	3.1678E-05	0.01
small root	0.001	9E-07	0.009144	2.873E-08	3.1678E-05	0.09
Wormhole	0.0015	9E-07	0.020575	1.454E-07	3.1678E-05	0.46
medium root	0.002	9E-07	0.036577	4.596E-07	3.1678E-05	1.45
crayfish burrow	0.015	9E-07	2.057466	0.0014543	3.1678E-05	4591.04

$\nabla h = .1$:

Biological Macropore Type	r	μ	q(m/s)	Q (m3/s)	Qinfl (maximum)	% of Maximum Q
very small root	0.0005	9E-07	0.022861	1.795E-08	3.1678E-05	0.06
small root	0.001	9E-07	0.091443	2.873E-07	3.1678E-05	0.91
wormhole	0.0015	9E-07	0.205747	1.454E-06	3.1678E-05	4.59
medium root	0.002	9E-07	0.365772	4.596E-06	3.1678E-05	14.51
crayfish burrow	0.015	9E-07	20.57466	0.0145434	3.1678E-05	45910.41

$\nabla h = 1$:

Biological Macropore Type	r	μ	q(m/s)	Q (m3/s)	Qinfl (maximum)	% of Maximum Q
very small root	0.0005	9E-07	0.228607	1.795E-07	3.1678E-05	0.57
small root	0.001	9E-07	0.91443	2.873E-06	3.1678E-05	9.07
wormhole	0.0015	9E-07	2.057466	1.454E-05	3.1678E-05	45.91
medium root	0.002	9E-07	3.657718	4.596E-05	3.1678E-05	145.10
crayfish burrow	0.015	9E-07	205.7466	0.1454337	3.1678E-05	459104.08

Appendix G. Plates



Plate 1. View of the Clay and Sand Sites in early July, 1994. The Clay Site and Paddys Run Creek are to the right, the Sand Site is to the left. Between the two site are the main water supply tanks.



Plate 2. The Sand Site showing staked instrumentation boreholes, the infiltrrometer, and the two 1900 L water supply tanks at each site.



Plate 3. Main water supply tanks (9468 L each). The water filter manifold is in the foreground between the rows of 55 gal. drums.



Plate 4. Soil water suction lysimeters (solution samplers) prior to installation. The samplers are taped to the 3/8" PVC pipe used to protect the TDR coaxial signal transmission cable.



Plate 5. Instrument installation at the Clay Site by FERMCO and Sandia Laboratory personnel.



Plate 6. Instrument borehole auguring and instrument installation.



Plate 7. The Sand Site with instrument array installed. The white piping (arrows) are tensiometers at sampling locations.



Plate 8. Installation of TDR and tensiometer transducer array. The transducer multiplexers and datalogger station are contained in the gray box with solar panel in center of picture. A TDR system is being assembled at left.



Plate 9. The Clay Site with tensiometers and TDR systems in place. The tensiometers at some sensor packs are covered with aluminized insulation. The two site supply tanks at left have not yet been plumbed to the infiltrrometer.



Plate 10. The fully operational Clay Site. Aluminum cloth sunscreens shield TDR stations from the summer sun.



Plate 11. Water supply manifold from site supply tanks to the infiltrometer.



Plate 12. View of the infiltrometer water supply manifold and float valves.



Plate 13. Introduction of the dye tracer at the Clay Site on August 15, 1994. 1514 L of dye solution were infiltrated into the site in 90 hrs.



Plate 14. Dye pulse spreading across infiltrtrometer.



Plate 15. Disassembly of the Clay Site on the morning of August 22, 1994, after termination of dye pulse and before start of excavation.



Plate 16. Dye stain on the infiltration surface after infiltrometer removal.



Plate 17 (above). Initial hand excavation of infiltrometer surface.



Plate 18 (right). Hand excavation of South half of the surface inside the Clay Site infiltrometer.



Plate 19. Excavated South half of the Clay Site infiltrrometer surface. Note the significant dye capture in the organic-rich topsoil.



Plate 20. Excavated South half of the Clay Site infiltrrometer surface. Note the dye capture in the organic-rich topsoils (unit 5) and the preferential movement into the beginning of the blocky structured sandy silts (unit 4).



Plate 21. Beginning of trench between inner and outer rings of the instrumentation array.



Plate 22. Backhoe trenching between inner and outer sampling rings.



Plate 23. Completed trench between inner and outer sampling rings. No dye was found on either the inner or outer walls of this trench.



Plate 24. Enlargement of the trench towards the infiltrometer surface. A partially excavated angled instrument pack is circled.

Plate 25 (right). Beginning of excavation of the pillar under the infiltrometer.



Plate 26 (below). Backhoe excavation between the infiltrometer and the outer sampling ring.





Plate 27 (above). Remaining pillar under the infiltrometer surface. The white feature at the bottom center of the infiltrometer is the top of the sand pack of the East-Northeast Upper sensor pack.



Plate 28 (right). Dye-stained matrix following worm hole transport pathway to the East-Northeast Upper sensor pack.

Plate 29 (right). Worm hole filled with red dye in pillar under infiltrometer.



Plate 30 (below). Worm hole filled with red dye intercepted by the East-Northeast Lower sensor pack. The Cl⁻ tracer pulse arrived in 42 min. and in high concentration at this sensor pack.



Plate 31 (right). Dye stained fractures and root and worm holes through unit 4 in the pillar underneath the infiltrometer.



Plate 32 (left). Dye stained root holes and fractures in unit 4.



Plate 33. Excavation of the pillar under the infiltrometer showing dye stained fracture surfaces.



Plate 34. Dye stained matrix surrounding root hole.



Plate 35. Dye stained 2 cm by 3 cm crayfish burrow (arrow) .3 m below surface in pillar beneath infiltrometer.



Plate 36 (above). Dye stained preferential flowpaths in pillar beneath infiltrometer. Note the light-colored bands of carbonate deposits at base of pillar (unit 3).



Plate 37 (right). Dye stained root holes and matrix in unit 4.

Plate 38 (right). Dye flow-paths along fracture planes and root casts in unit 4 beneath infiltrometer pillar.



Plate 39 (below). Worm hole in unit 5 just beneath infiltrometer surface.





Plate 40. Dye stained crayfish burrow at approximately 2.2 m depth in layered oxidized clays of unit 3.



Plate 41. Unstained exterior walls and floor of excavation at the outer sampling ring and a depth of approximately 1.3 m.



Plate 42. Morning prayers led by Keith, the Lugubrious.



Plate 43. Backhoe excavation and sloping of pit sides.



Plate 44 (above). Numerous macropores, sandy zones of preferential flow, and dye stained fractures indicated by 4" x 6" notecards at approximately 2.2 m depth in oxidized layered clays of unit 3.

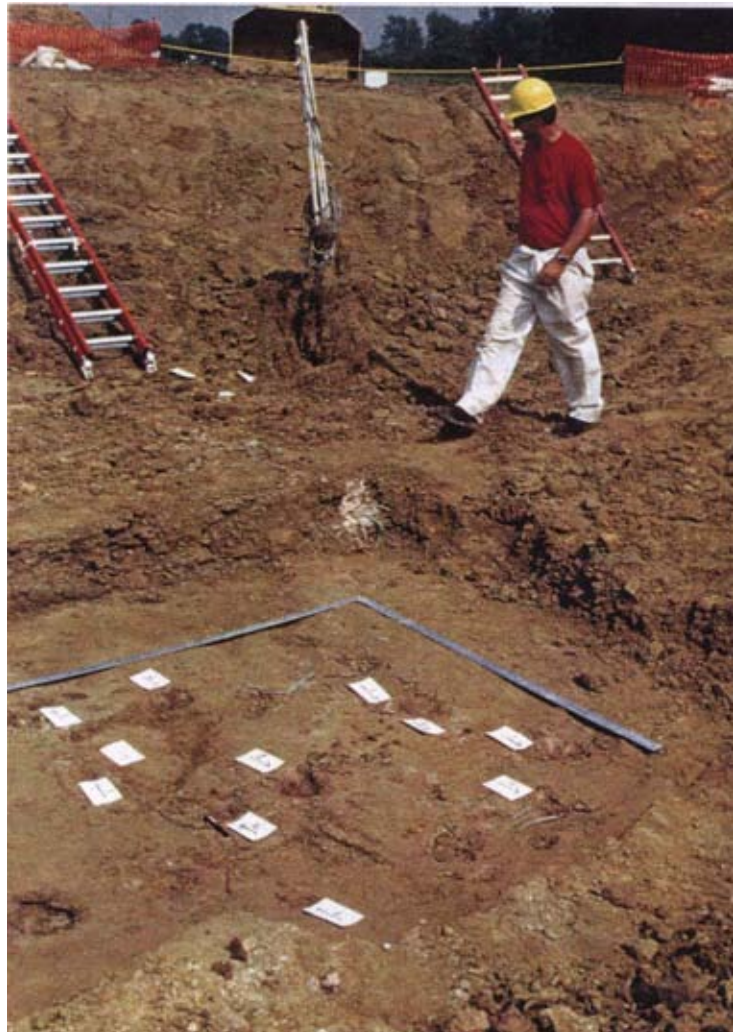


Plate 45 (right). Macropores, zones of preferential flow and active fractures at approximately 2.2 m depth in oxidized layered clays of unit 3.



Plate 46. Widening and deepening of excavation.



Plate 47. Note cards indicate macropores, fractures, and thin sandy beds at approximately 2.5 m depth. Note the layered oxidized clays and carbonate layers in the vertical exposure



Plate 48. Deepening the excavation to the top of the layered unoxidized clays of Unit 2.



Plate 49. Hand excavation into the unoxidized, layered clays of unit 2. The PVC tubing and cables of an upper and lower instrument pack are visible to the left. Note the column of bentonite surrounding the tubing and protruding above the excavated surface.



Plate 50. Oxidized fracture surface in the unoxidized layered clays of unit 2.



Plate 51. Unoxidized layered clays of unit 2. Note the oxidized fracture surfaces and bedding planes.



Plate 52. Tight bedding in the layered unoxidized clays of unit 2. A small sandy zone is visible in the lower center of the plate.



Plate 53. Deformation features in the massive unoxidized clays of unit 1.

Plate 54 (right). Large vertical and horizontal fractures in layered oxidized clays of unit 3.



Plate 55 (below). Secondary Dye infiltration event performed at top of Unit 1 (massive unoxidized clays) at approximately 3.2 m bgs.



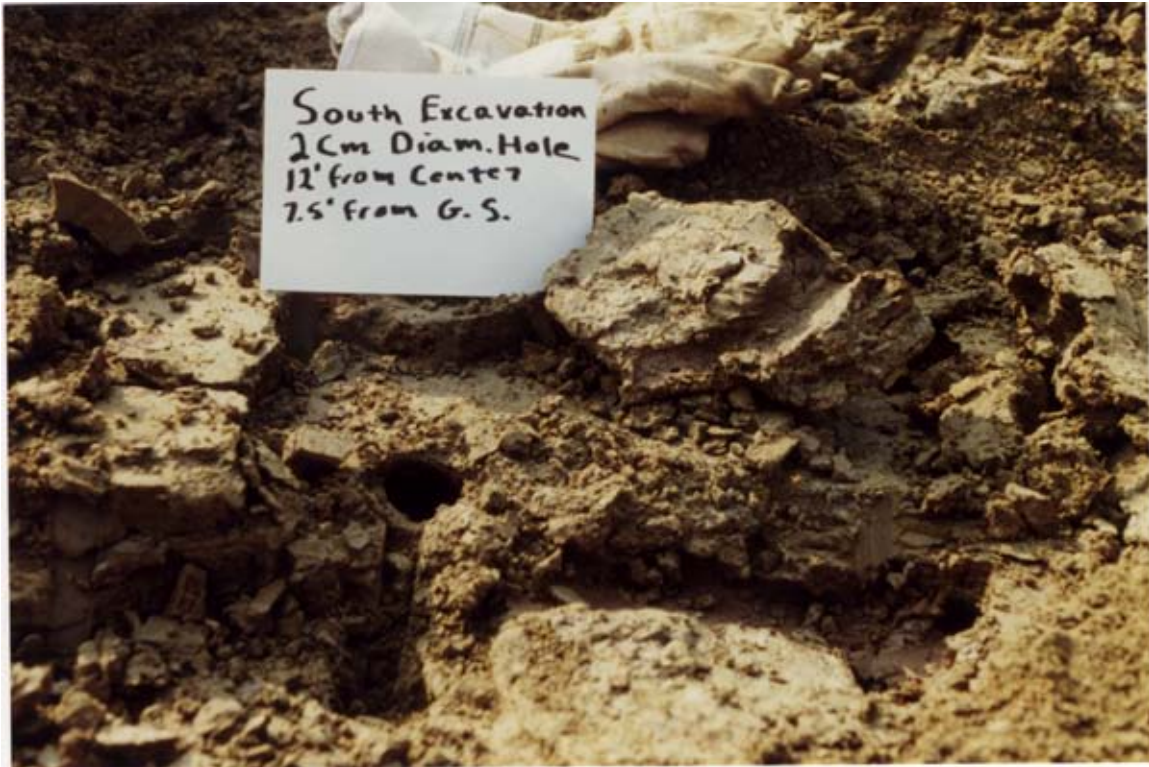


Plate 56. Crayfish burrows in South face of excavation.



Plate 57. Hand excavated transect through strata in south face of excavation.

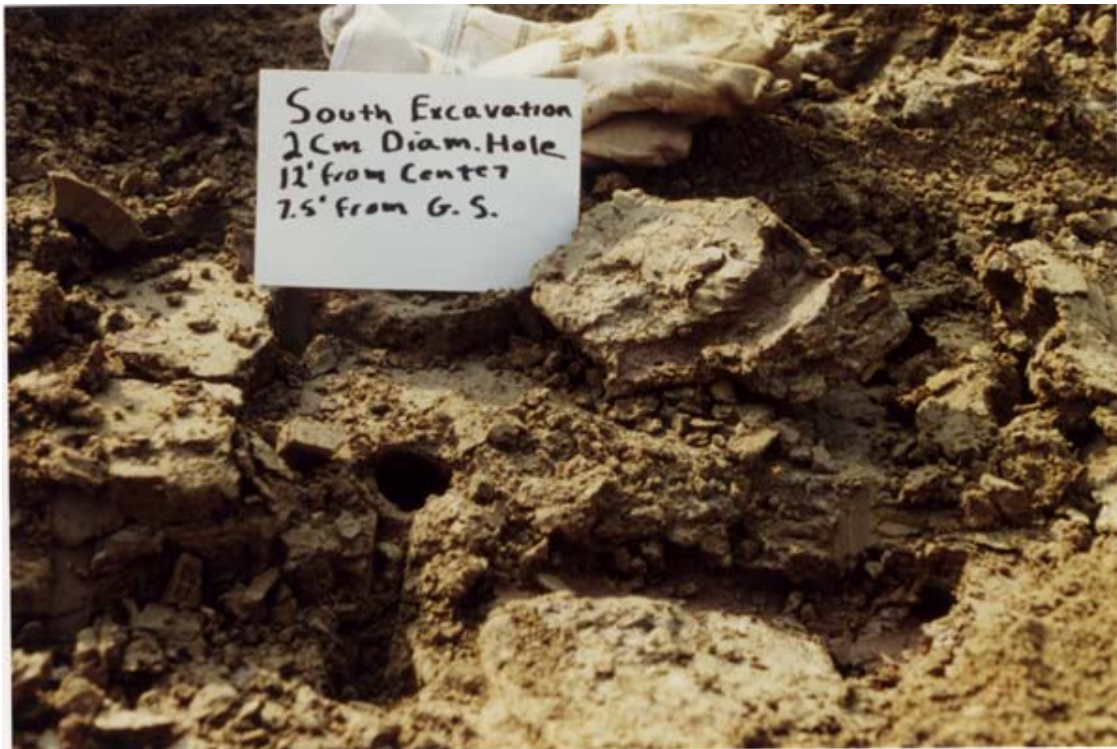


Plate 58. Terraced hand excavation of sloping sides of the excavated pit.



Plate 59. Backhoe excavation of the sloping sides. The blue tarp was put in place to prevent impacts to the secondary dye pulse (Plate 55).



Plate 60. Emplacement of a 30 cm diameter plastic pipe used to obtain cores from unit 2.



Plate 61. Backhoe used to press pipe into media for core samples.



Plate 62. Pipe pressed into clays to obtain undisturbed core samples.



Plate 63. First four core samplers in place.



Plate 64 (above). Close-up of first four core samplers before removal.



Plate 65 (right). Removal of sample cores with backhoe.



Plate 66 (above). Core removed from unit 2. Deformation of this unit resulted in shearing of beds along thin silty to sandy beds.



Plate 67 (right). Excavation after core samples removed.



Plate 68. Vertical fracture in Unit 2 (layered unoxidized clays) filled with silt and fine to medium sands.



Plate 69. Continued deepening and widening the excavation, morning of August 26, 1994.



Plate 70. Terracing of sides with hand tools.



Plate 71. Dye stained fractures and crayfish burrows (arrows) in unit 3. The depth is approximately 2.3 m. The crayfish burrows appear to follow pre-existing fractures.



Plate 72. Mud crack casts in oxidized, layered clays of unit 3.



Plate 73. Pink dyed thin carbonate layers between the beds of unit 2 (unoxidized layered clays).
Depth approximately 3 m.



Plate 74. Close-up of the large, silty sand body in the Northwest quadrant of the site.



Plate 75. Large filled macropore in the silty sand body in the Northwest quadrant of the site. The macropore is between the note card and the film container cap.



Plate 76. View of the excavation sides from the center of the excavation facing West. The West Outer Lower sensor pack is at the left. A portion of the large silty sand body deposited between the layered clay units can be seen in the vertical face at the center of the photograph.



Plate 77. Pink dye can just be seen in the bottom of the trench at the West Outer Lower sensor pack. The water was moving through a sand stringer originating in the silty sand body in the Northwest quadrant.



Plate 78 (above). Close-up of the pink water emerging from the sand stringer at the West outer Lower sensor pack.



Plate 79 (right). Beds of unit 3 (oxidized layered clays). Slightly dyed carbonate deposits (arrows) were found between beds and in fractures.



Plate 80. Pink dyed crayfish burrow at approximately 2 m depth.



Plate 81. Crayfish burrow in Unit 3 (oxidized layered clays).



Plate 82. Compiles of crayfish burrows in Unit 3 at South of site. Depth approximately 2.5 m.



Plate 83. Crayfish burrow in unit 2 (unoxidized layered clays) at a depth of approximately 3 m.



Plate 84 (above). Large crayfish burrow at 75° angle from vertical, just below surface at far West-edge of the excavation. This burrow dropped down at least 1.1 m before orienting horizontally toward the center of the site.



Plate 85 (right). Transect from layered unoxidized clays to surface at South of excavation.

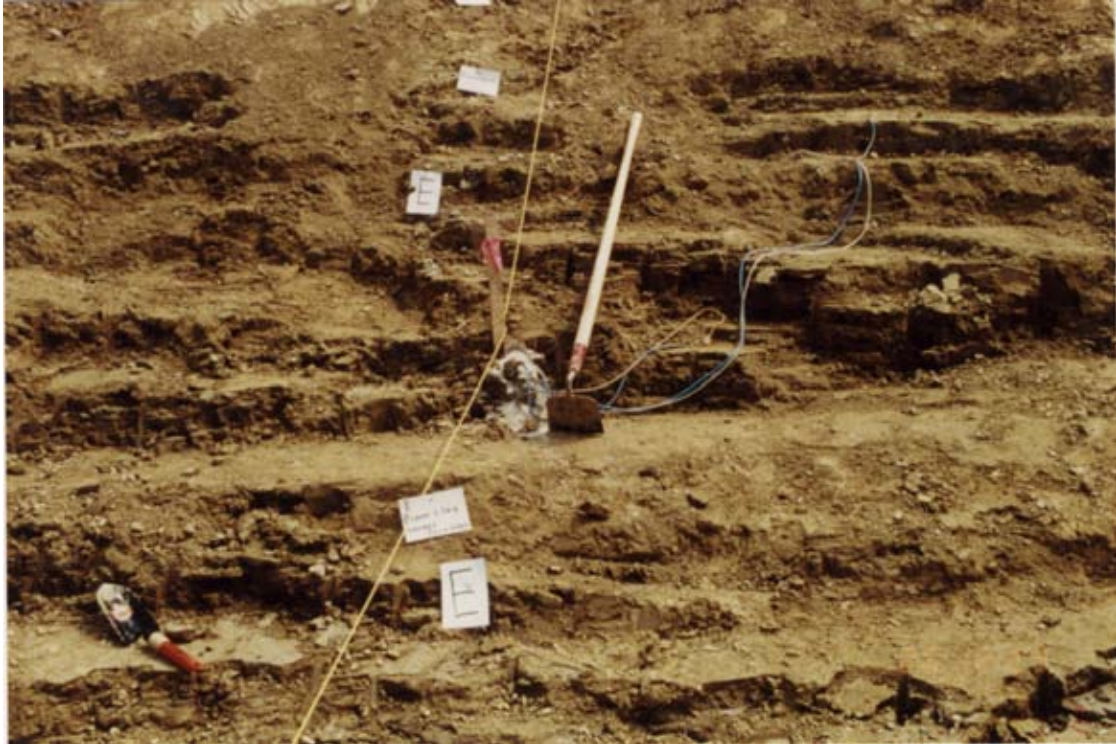


Plate 86. Hand terracing of east side of the excavation. Light-colored sand from a sensor pack can be seen in the center of the plate.



Plate 87. View of the excavation at noon, August 26, 1994. Facing North. Excavated material can be seen in a large pile behind the bulldozer. The silty sand body in the Northwest quadrant is outlined.



Plate 88. View of the excavation on August 26, 1994, facing northeast.



Plate 89. View of the excavation at noon on August 26, 1994, facing east.



Plate 90. View of the excavation at noon on August 26, 1994, facing southeast.



Plate 91. View of the excavation at noon on August 26, 1994, facing south.



Plate 92. View of the excavation at noon on August 26, 1994, facing southwest.



Plate 93. View of the excavation at noon on August 26, 1994, facing west.

Plate 94 (right). View of the sand body in the northwest quadrant of the site at noon, August 26, 1994.



Plate 95 (below). More core sampling by backhoe.





Plate 96. View of a finished vertical core sample.



Plate 97. Horizontal insertion of a core sampler by backhoe.



Plate 98. Extracted horizontal core from unit 3.



Plate 99. Close-up of extracted horizontal core.

Plate 100 (right). Backhoe gouge into the massive unoxidized clays of unit 1.



Plate 101 (left). Backhoe gouge into the massive unoxidized clays of unit 1.

Plate 102 (right). Gravels, cobbles, and sand inclusion in unit 1. The depth is approximately 6 m.



Plate 103 (below). Dye in fracture plane of a backhoe-excavated sample from the massive unoxidized clays of Unit 1.



Plate 104 (right). Covered opening of crayfish burrow #1 at surface.



Plate 105 (below). Crayfish burrow #1 15 cm below the surface.





Plate 106. Covered surface opening of crayfish burrow #2.



Plate 107. Crayfish burrow #2.



Plate 108. Crayfish burrow #3, the third surface opening of a crayfish burrow found in a cursory 15 min. examination of the field surrounding the infiltration sites.



Plate 109. Crayfish burrow #3.



Plate 110. Clay and Sand Sites after termination of the TPCTs. The view is facing East-Southeast towards Paddy's Run and the main FERMCO plant. The large dirt mound in the center of the photo was excavated from the Clay Site.

DISTRIBUTION:

1	1350	J.R. Brainard 06313
1	1138	R.J. Glass 06326
1	8523	Central Technical Files
2	4414	Technical Library